Institut für Theorie der Kondensierten Materie
Karlsruhe Institute of Technology

Coherent Defects in Superconducting Circuits

Zur Erlangung des akademischen Grades eines
DOKTORS DER NATURWISSENSCHAFTEN
von der Fakultät für Physik des
Karlsruher Instituts für Technologie

genehmigte

Dissertation

von

Dipl. Phys. Clemens Müller
aus Rottweil

To my mother

Introduction

During the last two decades, research into devices and architectures intended for quantum computation has strongly improved our understanding of the fundamental processes in quantum mechanics. Especially in solid-state system, great progress has been made in the understanding and characterization of the interaction of quantum systems with their environment. This interaction leads to decoherence in the time-evolution of the state of a quantum system and is present in all solid-state devices. However, not all of these effects are fully understood yet.

One such open problem is connected with the observation of coherent defect states in superconducting circuits. These defects manifest themselves as anti-crossings in spectroscopic data, illustrating their high degree of coherence and strong interactions with the underlying circuit. It can be shown that they are genuine two-level systems and reside most probably inside the circuits Josephson junctions. These two-level states (TLS) are in general detrimental to the operation of the circuits, since they open additional decoherence channels and, due to their strong interaction with the circuit, modify its dynamics significantly. On the other hand they might prove useful for quantum computation tasks themselves, as their coherence time often exceeds the fabricated artificial qubits by more than one order of magnitude. Their microscopic origin remains unclear. Many different possibilities have been proposed, but no definite answer has been reached. Also, their possible connection to the ubiquitous $1/f$-noise in solid-state systems, thought to stem from ensembles of incoherent TLS, is unclear.

In this thesis, we show a study of the effects of coherent and incoherent TLS on the operation of superconducting circuits. One goal was the understanding of the effect such TLS have on the coherence properties of the circuits. We developed theory describing this interaction in all relevant parameter regimes. The second goal was to reach a better understanding of their microscopic nature and the nature of their interaction with the circuit in order to either reduce the number of TLS already in fabrication or utilize them directly for quantum manipulation. We focus mostly on TLS in superconducting phase qubits, since they are most often observed in these circuits. We were able to put strong constraints on several microscopic models for TLS, which marks a large step forward towards understanding their nature. Additionally we developed a method to directly manipulate the state of individual TLS, which can be used to probe their quantum mechanical properties directly.

In most of this work, we have greatly profited from a very fruitful collaboration with the experimental group of Prof. Alexey V. Ustinov at KIT. We will show a great variety of experimental data that has been measured in this group, and without which, this thesis would not have been possible in this form.

This thesis is divided into five chapters:

We start with a motivation, where we introduce the physics of two-level defects and explain their general role in the modeling of decoherence. We then go on to describe coherent defects, as they are often found in superconducting circuits, and shortly present several possible microscopic models.

Chapter one intends to give an introduction into the general theoretical background. The superconducting phase qubit is described in detail and its Hamiltonian derived from the circuit diagram. A short overview on the treatment of decoherence - the interaction with an environment - in quantum systems is provided. We then introduce Floquet theory and how we can use it to model driven systems including dissipation. As an aside from the thesis' main theme, we then establish the notion of geometric quantum computation using non-abelian holonomies, with the aim of realizing them in superconducting systems.

The second chapter deals with the identification of the microscopic origin of coherent TLS using spectroscopic data. We first show the experimental data and identify the underlying physical processes. This data is then used for a high precision comparison with several existing microscopic models leading to severe constraints on the parameters of the models.

The following chapter three develops a method to directly manipulate the state of individual TLS. We show results from an experiment demonstrating this control to investigate the coherence of two single TLS and try to speculate on some microscopic explanation of the data.

In the fourth chapter, we focus on the description of interaction effects when a qubit is interacting with additional two-level quantum systems. Here we treat the two cases of weak and strong qubit-TLS coupling separately. We characterize the interaction in terms of effective decoherence rates and also treat ensemble effects, arising when the qubit is resonant with several TLS. This gives us a starting point to briefly discuss the collective physics of quantum meta-materials formed e.g., by ensembles of qubits coupled to a common transmission line resonator.

Finally, in chapter five, we give a brief introduction on how to realize holonomic gates in superconducting systems. We propose a physical realization and show how to implement the adiabatic gate sequence.

The conclusions then summarizes the main findings and gives a short outlook on future research.

An appendix provides details of calculations and gives additional information on the described methods. A list of publications is also given there.

For ease of notation we use the convention $\hbar = k_B = 1$.

Contents

Motivation

We start this thesis by motivating our interest in defect systems in superconducting devices. We then give a short introduction into two-level systems as a general noise-model, explaining the ubiquitous $1/f$-noise found in solid state systems. In the following we motivate our interest in coherent two-level systems, as they are found especially in superconducting qubits, and give a short overview of possible microscopic explanations.

General

The miniaturization of traditional electronic circuits has led to great advances in computational power and complexity. But further progress in this field might meet with a major challenge in the next years. As the dimensions of the circuits become ever smaller, quantum effects will begin to influence their operation. Already, in state-of the art MOSFET transistors, special efforts are required to keep the errors due to quantum tunneling in manageable bounds.

Properly harnessed, quantum effects do not have to be detrimental towards the desired operations. The proposal of a quantum computer relies on quantum mechanical two-level system and their controllable coherent interaction to achieve exponential speedup for certain computational tasks [1].

Much effort has been devoted in the last two decades towards designing and characterizing the individual building blocks of a possible quantum computer. Theses quantum bits, or qubits, have been realized in a large variety of different physical systems. Among the candidates for possible architectures for quantum computation are photons in fibers or photonic crystals [2], single ions in electromagnetic traps [3], neutral atoms in optical crystals [4] and superconducting circuits [5–7], among others. Each of these architectures shows particular advantages and challenges, founded in the nature of the underlying physical systems. A regularly updated list of recent progress for the different architectures can be found online at Ref. [8].

Even when not focusing on the goal of quantum computation, the research in this area has greatly improved our understanding of the underlying fundamental processes. The predictions of quantum mechanics were tested and confirmed with very high accuracy in many different systems. For example, experimental tests of the Bell inequalities have been performed in various different physical realizations (cf. e.g., Refs. [9–11]), and their violation has been confirmed in every situation tested to date. This demonstrates the non-local nature of entanglement in quantum mechanics.

In this thesis, we focus on the particular realization of qubits in superconducting circuits. A particular challenge in this field are the inevitable interactions of the circuits with their environment. This chapter first establishes the ideas behind using superconducting circuits for quantum applications. We then introduce a special kind of environment often observed in solid-state system, namely ensembles of two-level systems (TLS). We end the chapter by explaining about coherent TLS, as they are often observed in operation of superconducting quantum systems.

Superconducting Quantum Circuits

Superconducting circuits are realized as nano-scale thin-film circuits on a substrate. They offer the natural advantage of dissipation-less operation, due to superconductivity, and intrinsic scalability. The scalability is partly due to synergy effects from the large body of experience gained in standard integrated circuit design and fabrication. Many of the methods originally developed for fabrication of semiconductor electronics are also applicable for superconducting circuits.

Superconducting electronics already find wide applications e.g. as single photon detectors, small bandwidth radiation detectors or ultra-sensitive magnetometers. For these applications they are operated in the semi-classical regime, i.e., where the discrete structure of quantum mechanics does not yet play a strong role. We are interested in using superconducting devices in the deep quantum regime, where the single level energy is the largest energy scale.

Most common circuit elements (e.g. resistors, capacitances and inductances) are linear elements, i.e., their current-voltage characteristics are linear functions. This means that the Hamiltonian of a circuit made out of linear elements will always be a quadratic function and the potential will be harmonic. The energy levels of such systems will then be equidistant. In trying to design qubits, we need to introduce anharmonicity in the potentials, which will lead to non-equidistant level-splitting. If the difference in the energy-splitting between the levels is large enough, we can focus on a single transition and describe the circuit effectively by only two levels. This pair of levels will then form the qubit. In order to introduce such anharmonicity, we have to insert non-linear elements into the circuits.

The only non-dissipative non-linear circuit element we know is a Josephson tunnel junction. It is formed when two superconducting contacts are separated by a thin tunneling barrier. The macroscopic equations determining the behavior of such a Josephson junction are [12]

$$
\begin{aligned}
I &= I_C \, \sin \phi \,, \\
V &= \frac{\Phi_0}{2\pi} \, \dot{\phi} \,,
\end{aligned}
\tag{0.1}
$$

where I_C is the maximum super-current the junction can carry before switching into a resistive state, V is the voltage across the junction and $\phi = \phi_1 - \phi_2$ is the

phase difference of the condensate wave-functions on the two sides of the junction. $\Phi_0 = h/2e$ is the superconducting flux quantum. The first of these Josephson relation describes that the magnitude of the super-current flowing across such a tunnel junction depends on the phase difference across the junction in a non-linear way, while the second shows that this phase difference will change when applying a voltage to the junction. Combining the two relations we see that for an applied voltage, the supercurrent across the junction will oscillate with a frequency which is proportional to the applied voltage. Modern quantum metrology makes use of the Josephson relations to define a voltage-standard based solely on natural constants, via frequency measurements of the Josephson oscillations.

Using the anharmonicity supplied by Josephson junctions, many non-linear superconducting circuits have been designed. For qubit applications there are three main types of circuits, the charge type [5], flux type [6] and phase type [7]. Many variations of these basic designs have been built, mainly with the goal to make the circuits insensitive to certain aspects of the environment (cf. e.g., Refs. [13, 14]). The junction non-linearity may also be employed for other purposes, e.g., to build tune-able microwave oscillators [15] or parametric amplifiers [16].

One problem when employing Josephson junctions in the circuits is, that they potentially introduce additional decoherence sources into the circuit. The insulating oxide commonly used to form the junctions tunneling barrier is an amorphous material and as such, is subject to dynamical disorder on the atomic scale. In the following we introduce a model how this kind of disorder may lead to dissipation, namely tunneling two-level systems.

Two-Level Systems and $1/f$- Noise

One of the main drawbacks of solid state quantum systems is their inevitable interaction with their environment. This interaction leads to decay in the coherent time evolution towards a state of thermal equilibrium with the environmental degrees of freedom. Such a process is called decoherence and is in general detrimental to the desired operation of the system. On the other hand, the study of the environment has lead to strong increase in the understanding of many microscopic effects in the solid state.

Many of the physical quantities influencing the operation of superconducting circuits show slow fluctuations with a power-spectrum that scales like $1/f$, where f is the frequency of the fluctuations. This fact is actually not limited to quantum systems. Such spectra can also be observed e.g., in the flood levels of the river Nile over the scope of the last decades as well as in the power spectra of music and spoken language [17]. Our interest however is focused more towards noise in the electronic properties of the circuits, such as magnetic flux or critical current.

A standard explanation for such a $1/f$ power spectrum gives the so-called Dutta-Horn model [18]. This model assumes a large group of microscopic two-level systems whose fluctuations correspond to the modulations of the physical quantity of interest.

The noise spectrum of each TLS at low frequencies is then given by a Lorentzian with the width γ corresponding to its switching rate. For a statistical ensemble of two-level systems, the resulting low-frequency noise spectrum is given by the weighted sum of the single contributions

$$S_{TLS} = \int \mathrm{d}\gamma \, P(\gamma) \, \frac{\gamma}{\gamma^2 + f^2} \qquad (0.2)$$

where the switching rates γ are distributed with probabilities $P(\gamma)$. For tunneling TLS this distribution is $\propto 1/\gamma$ and the resulting low-frequency noise spectrum shows $1/f$ frequency dependence.
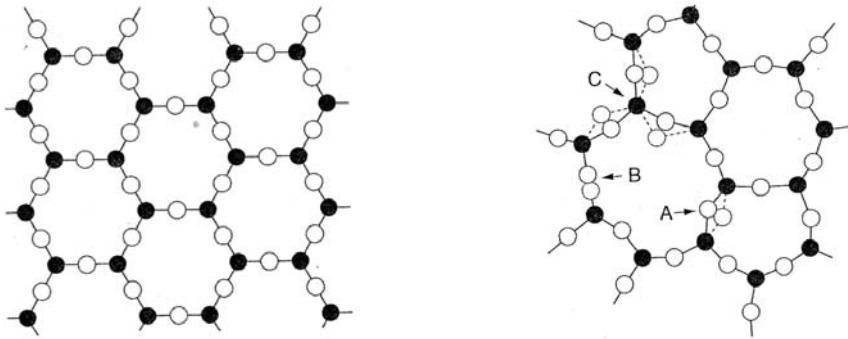

Figure 0.1.: *Illustration of tunneling systems in an amorphous solid. The left picture show the structure of crystalline SiO_2 (quartz glas) while the right panel shows its amorphous configuration. In the amorphous phase single atoms or groups of atoms may have more than one metastable position between which tunneling is possible. This picture gives a natural explanation of the observation of tunneling systems in glasses and amorphous materials [19–21].*

Ensembles of such tunneling two-level systems have been used as a model to explain interesting physics before. Most prominent is the case of the anomalous low-temperature heat-capacity and sound attenuation properties in glasses [19, 20], which can be derived from the properties of low-energy tunneling TLS. For an amorphous or glassy material, the appearance of such tunneling defects follows naturally, as is illustrated in Fig. 0.1. Today, ensembles of TLS are a standard model for decoherence in a wide range of different physical systems, such as micro-mechanical oscillators [22, 23], microwave resonators [24] and superconducting qubits [25, 26].

A commonly employed model describing tunneling two-level systems is illustrated in Fig. 0.2. A double well with asymmetry $\epsilon_0 = E_1 - E_2$ is separated by a tunneling barrier of height V. This system can be described by the Hamiltonian

$$\hat{H} = \frac{1}{2}\epsilon_0\sigma_z + \frac{1}{2}\Delta_0\sigma_x \,, \qquad (0.3)$$

where the tunneling matrix element $\Delta_0 \propto \mathrm{e}^{-V}$ and the σ are pauli-matrices. The
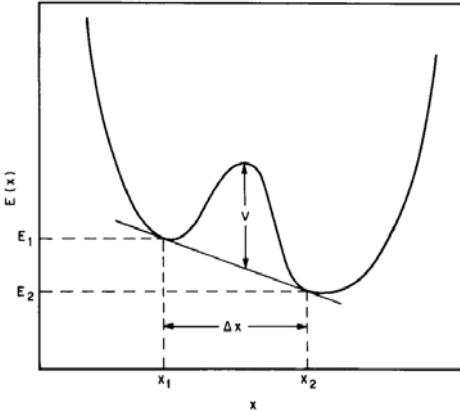
Figure 0.2.: *Double well potential of a tunneling two-level system. Two wells are separated by a potential barrier V, through which tunneling takes place. States in the wells have energies E_1 and E_2. Figure from [20].*
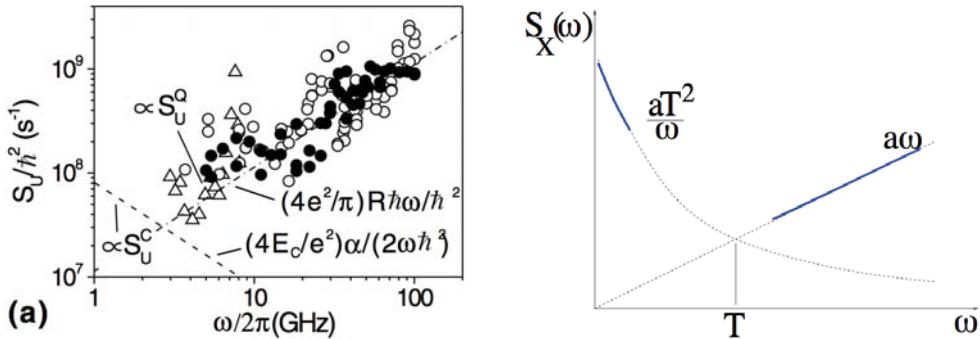

Figure 0.3.: *A possible connection between noise at low- and high-frequencies in charge qubits was found in Ref. [27]. The left figure shows the experimental data. The noise spectra cross at a frequency corresponding to the temperature of the experiment. If an ensemble of two-level systems is responsible for both the low- and high-frequency parts of the noise, this connection follows naturally [25]. Right figure from [28].*

level-splitting of this system is then given by $\epsilon = \sqrt{\epsilon_0^2 + \Delta_0^2}$. For weak tunneling systems we assume $\epsilon_0 \gg \Delta_0$, so that $\epsilon \approx \epsilon_0$ [21]. The fluctuating behavior of the TLS now depends on the ratio of temperature T and level-splitting ϵ. In the thermally activated regime, $T \gg \epsilon$, the TLS will switch randomly with the switching rate γ determined by the tunneling element Δ_0. For normal distributed tunnel barriers V, this behavior leads to the $1/f$-type low-frequency noise (cf. Eq. (0.2)). For the opposite situation, $T \ll \epsilon$, however, the TLS dynamics are not influenced by temperature and they can show coherent behavior.

Recently, in experiments on Josephson charge qubits, a possible connection be-

tween the low-frequency $1/f$-noise and the high-frequency ohmic noise in the circuit was found [27]. The interpolation of the noise-spectra in the two regimes was shown to cross at an energy corresponding to the temperature of the experiment. As was demonstrated in Ref. [25], this behavior follows naturally if an ensemble of TLS is at the same time responsible for the the low- and high-frequency components of the noise. Such an ensemble would consist of TLS of both very small level-splitting $\epsilon \ll T$ and very high-energy, possibly coherent TLS with $\epsilon \gg T$.

Coherent Two-Level Defects
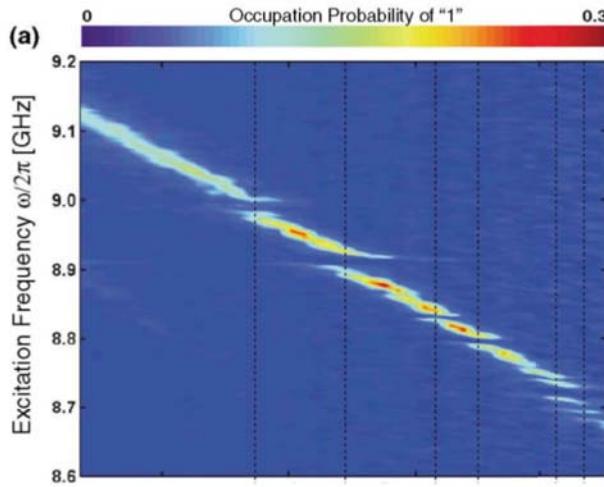
Figure 0.4.: *Spectroscopy of a superconducting phase qubit. The line indicates the resonance frequency of the qubit transition as a function of external flux bias. At certain values of the flux bias (dotted lines), we see pronounced anticrossings indicating that the qubit is resonant with an additional coherent quantum system. Figure from [29]*

Previously, we introduced ensembles of TLS as a phenomenological model of noise properties in solids. A possibly different kind of two-level system is often observed in spectroscopy of superconducting qubits. Fig. 0.4 shows the results of such an experiment [29, 30]. Spectroscopy probes the steady state of the system under driving and as such enables one to map out the energies of the Hamiltonian of a system. The line visible in Fig. 0.4 indicates the level splitting of a superconducting phase qubit as a function of flux bias. At certain frequencies and bias fluxes (indicated by dotted lines), the spectrum shows characteristic anti-crossings. Such features are indicative of additional quantum systems being resonantly coupled to the circuit at these points. They are also observed in other kinds of superconducting qubits, namely in flux [31] and charge [32] qubits.

It can be shown that these defects are formed as genuine two-level, or at least strongly anharmonic systems [31, 33]. Their coherence times often exceed that of the qubits by more than one order of magnitude [34, 35]. For this reason they have been proposed as naturally formed qubits [36] and their possible use as a quantum memory was demonstrated [34]. In general they are considered detrimental to the qubit's operation, since their strong interaction with the circuit will heavily influence the qubit operation [37] and possibly open additional channels of decoherence [38].

The microscopic origin of these defects is still unclear. Since they are most often observed in phase qubits, which have the largest Josephson junctions in all species of superconducting qubit, they are thought to reside in the tunnel barrier of the junctions. A large number of theoretical models have been proposed in order to account for the experimental observations [39]. There are several possibilities how a microscopic defect might interact with a superconducting circuit.
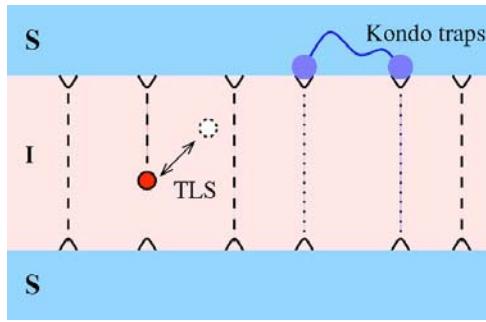

Figure 0.5.: *Illustration of channel blocking and Kondo-like traps. Atoms moving inside the tunnel barrier might modify the transparency of the junction, blocking and unblocking single conduction channels. Kondo impurities sitting near the junction surface might also be responsible for a change in transparency. Figure from [40].*

Most theoretical attention was devoted to the possibility that the TLS changes the critical current through the Josephson junction. This might be understood as a simple atomic rearrangement due to tunneling of single atoms or groups of atoms [41] or as Kondo-like traps near the surface of the Josephson junction which would modulate its transparency [40]. These two models are illustrated in Fig. 0.5.

An alternative explanation for a modulation of the critical current involves an impurity level inside the junction, interacting with the superconducting leads and forming an Andreev bound-state [42, 43]. Fig. 0.6 gives an illustration of this process.

In a different microscopic model, the TLS is formed by an electric dipole [44, 45]. Its dipole moment would then interact with the electric field across the junction and by this process influence the circuits operation. The microscopic picture would again be a tunneling system along the lines depicted in Fig. 0.5, now additionally with an associated moving charge.

Another possibility has the TLS formed by a magnetic moment, e.g., a single large
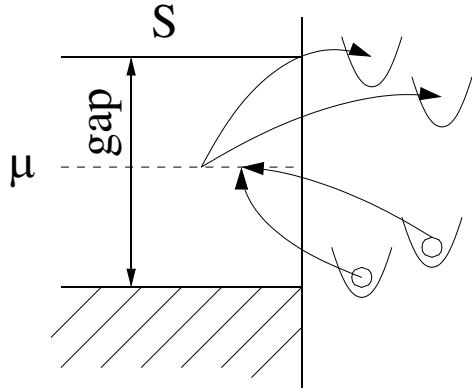
Figure 0.6.: *Illustration of an Andreev-level fluctuator [42, 43]. An impurity level μ inside the gap is hybridized by the interaction with the superconducting leads and forms a pair of Andreev bound states.*

spin on the surface of the superconductor [46, 47]. Such a magnetic dipole generates a magnetic flux which would interact with any inductive circuit element.

Despite the many possible microscopic models, no definite conclusion has been reached to date concerning the physical nature of the coherent TLS in superconducting circuits. A further remaining challenge is their possible connection to the low-frequency noise observed in nearly all solid-state systems.

1. Theoretical Background

This chapter lays the theoretical groundwork for all the following ones. We start with an introduction into quantum circuit theory, explaining the principles of how to derive a Hamiltonian from an electrical circuit diagram. After this, we give an overview of the quantum mechanical treatment of dissipative systems, starting with the phenomenological Bloch equations and moving on to the more rigorous Bloch-Redfield description. In a quantum optics context, the Lindblad equations are a standard tool to describe lossy processes. We introduce them, give the connection to the Bloch-Redfield equations and define their respective areas of applicability. Then we give a short introduction into Floquet theory and how to incorporate it for dissipative systems. The last part introduces holonomies in quantum mechanics and shortly motivates how one can use them to implement geometric fault-tolerant quantum computation.

Introduction

In this chapter we give a short overview of the main theoretical toolbox that will be used throughout this work. We start by deriving the Hamiltonian of a superconducting phase qubit from the circuit diagram. The method applied here has proven very powerful in designing and understanding superconducting quantum enabled devices. It relies on the use of Kirchhoff's equations to derive the classical Lagrangian of the circuit. After performing a Legendre transform one then imposes canonical commutation relations on the until then classical variables to arrive at the Hamiltonian. We demonstrate this on a very simple circuit, the superconducting phase qubit. In App. A we consider some more complicated situations.

We then move on to discuss the treatment of decoherence in quantum systems. Starting with phenomenological descriptions we go on to try and give a more microscopic picture of dissipative processes. To this end we show the calculation of transition rates with the Golden Rule equation before moving on to the more rigorous treatment of dissipation in the density matrix description via the Bloch-Redfield equations. In this framework we identify the relevant rates in the dynamics and solve the problem for the simplest imaginable system, a two-level atom coupled to a bath. Due to their wide applicability in decohering systems we also show the Lindblad equations and discuss their connections with the previous examples.

Next we give a short introduction on Floquet theory, which simplifies the description of periodically driven systems. We introduce the relevant quantities and discuss the theories application to dissipative systems. Again we illustrate the theory by

applying it to the problem of a driven two-level atom.

In the last part we introduce the concepts of holonomies in quantum mechanics, with a special focus on their possible application in the field of quantum computation.

1.1. Quantum Circuit Theory

In the field of superconducting quantum systems, we often talk about the correspondence of our systems with their quantum optics analogue, namely atoms and cavities. The main difference in the superconducting case is, that our systems are realized as nanoscale circuits and their properties are engineered to correspond to a known natural system or even yield new physics. In order to understand and design these systems, one has to understand the properties of the circuit elements. In this section we will give an example of how to derive a Hamiltonian from a circuit diagram. We will use the circuit of the superconducting phase qubit [7, 30], since defect states are most often observed in this system.

The procedure is as follows: We use Kirchhoff's equations to derive the (classical) equations of motion for the voltages and currents in the circuit. From the equations of motion we can deduce the Lagrangian and finally arrive via a Legendre transformation at the Hamiltonian function describing the circuit. We then impose canonical commutation relations on the phases and their conjugate momenta to find the Hamiltonian describing the quantum dynamics of the system. We end the section with some words on the experimental parameters and the operation of a superconducting phase qubit.

1.1.1. Circuit Diagram and Kirchhoff Equations

The circuit diagram of a superconducting phase qubit including the control circuitry is shown in Fig. 1.1. The phase qubit itself in green is given by a superconducting ring of inductance L interrupted by a single Josephson junction. The junction is described by its Josephson energy $E_J = \frac{\Phi_0}{2\pi} I_C$, where I_C is its critical current, as well as the junctions capacitance C. The external controls are drawn in blue. The circuit can be controlled by an applied external magnetic flux through the loop Φ_{Ext} as well as by a voltage V_G, which is coupled to the circuit via the gate capacitor C_G.

For the circuit depicted in Fig. 1.1 we have four circuit elements, the Josephson junction with Josephson energy E_J, the junction capacitance C, the loop inductance L and the gate capacitance C_G. Each circuit element is described by a pair of variables $\{\Phi_n, V_n\}$. Here Φ_n is the flux corresponding to the phase drop ϕ_n across that part of the circuit and we have $\Phi_n = (\Phi_0/2\pi)\,\phi_n$. $V_n = \dot{\Phi}_n$ gives the voltage over this circuit element. We can identify three closed loops in the circuit of Fig. 1.1, which will allow us to reduce the number of independent pairs of variables to one. We do this by means of the second rule of Kirchhoff, $\sum V = \sum V_{Ext}$, which relates the fact that the sum off all voltages in a loop has to be equal to the sum of the
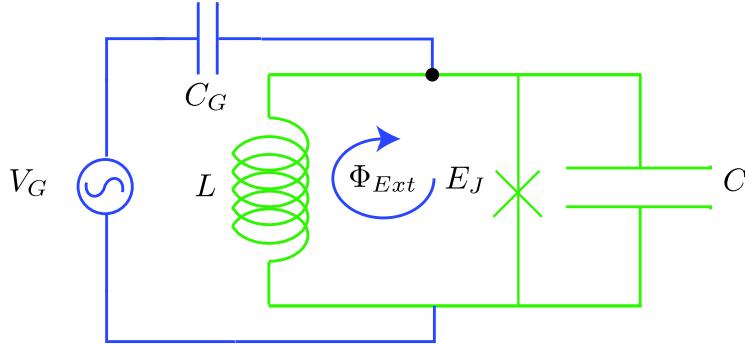
Figure 1.1.: *Circuit diagram of a superconducting phase qubit. The qubit in green consists of a superconducting ring of inductance L interrupted by a Josephson junction with Josephson energy E_J and capacitance C. It can be manipulated by an applied external magnetic flux Φ_{Ext} through the loop and a gate voltage V_G coupled capacitively via the capacitor C_G. At the point marked by the black dot, we evaluate the current balance to arrive at the equations of motion for the circuit.*

external voltage sources in the same loop. In our circuit, we have two source terms, the gate voltage V_G and the external flux Φ_{Ext}. As dynamical variables, we choose the phase Φ across the junction and the respective voltage V. For the remaining variables, we get

$$
\begin{aligned}
\dot{\Phi}_G &= -\dot{\Phi} + V_G \,, \\
\dot{\Phi}_L &= \ \ \dot{\Phi} - \dot{\Phi}_{Ext} \,, \\
\dot{\Phi}_C &= \ \ \dot{\Phi} \,,
\end{aligned}
\tag{1.1}
$$

where Φ_G corresponds to the phase drop across the gate capacitor C_G, Φ_L to the the phase across the inductance, Φ_C to the phase drop across the junction capacitance and Φ_{Ext} is the applied external flux.

We then use the current balance at one point in the circuit by applying the first rule of Kirchhoff, $\sum I = 0$, which is essentially a manifestation of the continuity equation. We choose the point marked by a black dot in Fig. 1.1 and get

$$
C_G \left(\dot{V}_G - \ddot{\Phi} \right) = C\ddot{\Phi} + I_C \sin\left(\frac{2\pi}{\Phi_0}\Phi\right) + \frac{1}{L} \left(\Phi - \Phi_{Ext} \right) \,,
\tag{1.2}
$$

where we already inserted the relations Eq. (1.1).

1.1.2. Circuit Hamiltonian

The Eq. (1.2) is the classical equation of motion for the voltages and phases in this circuit and as such has to follow from a Lagrangian $\mathcal{L}$ via the Euler-Lagrange equations $\frac{\mathrm{d}}{\mathrm{d}t}\frac{\partial \mathcal{L}}{\partial \dot{q}} = \frac{\partial \mathcal{L}}{\partial q}$. As canonical variables we choose the phase ϕ across the

junction and its time derivative $\dot{\phi}$. In these variables, we can deduce the Lagrangian in the proper units as

$$\mathcal{L}(\phi, \dot{\phi}) = \frac{1}{2} C_G \left(\frac{\Phi_0}{2\pi}\right)^2 \left(U_G - \dot{\phi}\right)^2 + \frac{1}{2} C \left(\frac{\Phi_0}{2\pi}\right)^2 \dot{\phi}^2$$
$$+ E_J \cos\phi - \frac{1}{2L} \left(\frac{\Phi_0}{2\pi}\right)^2 (\phi - \phi_{Ext})^2 , \tag{1.3}$$

where we defined the dimensionless gate voltage as $U_G = (2\pi/\Phi_0) \, V_G$. From this Lagrangian we calculate the canonical momentum

$$p = \frac{\partial \mathcal{L}}{\partial \dot{\phi}} = \left(\frac{\Phi_0}{2\pi}\right)^2 \left(C\dot{\phi} - C_G \left(U_G - \dot{\phi}\right)\right) , \tag{1.4}$$

which corresponds to the charge on the capacitor C and we define $p = 2e\,q$ with the dimensionless charge q. We then perform the Legendre transform to arrive at the Hamiltonian function of the circuit

$$\mathcal{H} = p\,\dot{\phi} - \mathcal{L}$$
$$= -\frac{2e^2 n_G^2}{C_G} + \frac{2e^2 (q - n_G)^2}{C_\Sigma} - E_J \cos\phi + \frac{1}{2L} \left(\frac{\Phi_0}{2\pi}\right)^2 (\phi - \phi_{Ext})^2 , \tag{1.5}$$

where we introduced the dimensionless charge on the gate capacitor by $n_G = C_G V_G/2e$ and the total capacitance $C_\Sigma = C + C_G \approx C$. The first term in Eq. (1.5) does not contribute to the dynamics and can be neglected. We now identify the charge q and the phase ϕ as operators and impose canonical commutation relations, $[\hat{q}, \hat{\phi}] = \mathrm{i}$, to finally arrive at the Hamiltonian

$$\hat{H} = E_C \left(\hat{q} - n_G\right)^2 + E_L \left(\hat{\phi} - \phi_{Ext}\right)^2 - E_J \cos\hat{\phi} \tag{1.6}$$

where we defined the charging energy $E_C = 2e^2/C$, the inductive energy $E_L = 1/(2L)(\Phi_0/2\pi)^2$ and the Josephson energy $E_J = I_C(\Phi_0/2\pi)$.

If we neglect the Josephson energy E_J in Eq. (1.6), i.e. we neglect the nonlinear Josephson element in the circuit Fig. 1.1, this Hamiltonian describes a simple harmonic LC oscillator with its mass given by the capacitance C and the potential defined by the inductivity L. By adding the Josephson term, the potential becomes no longer harmonic. The Hamiltonian thus describes the motion of a particle of mass $\propto C$ in an anharmonic potential defined by

$$U(\hat{\phi}) = E_L \left(\hat{\phi} - \phi_{Ext}\right)^2 - E_J \cos\hat{\phi} . \tag{1.7}$$
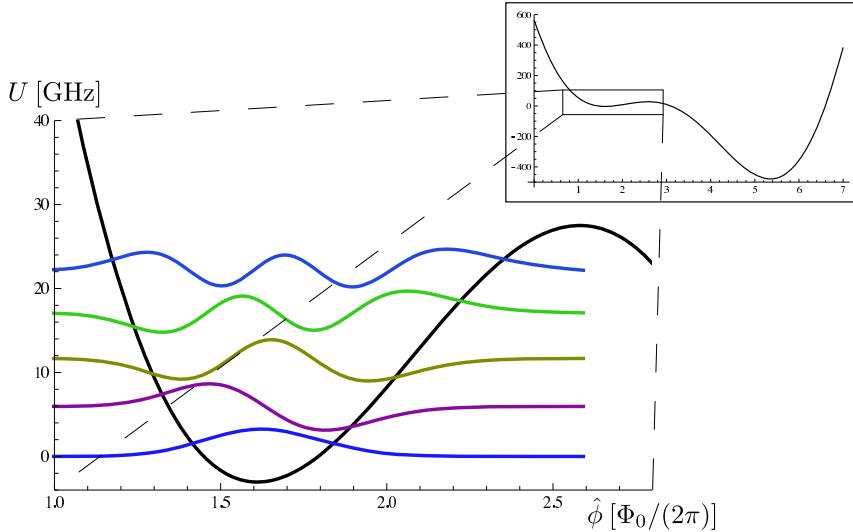
Figure 1.2.: *Plot of the potential U of a superconducting phase qubit with circuit parameters taken from Ref. [37]. The main figure shows the region of the shallow potential well, relevant for qubit operation. To the right of this we find another, deeper well used for qubit readout. The full potential with the same parameters is depicted in the inset. The lines show the five lowest qubit circuit eigenstates, with the offset given by their respective energies. Zero energy is defined by the energy of the lowest eigenstate in the shallow well and the picture shows the situation for an external flux Φ_{Ext} corresponding to a qubit splitting of $\epsilon_{01}/2\pi = 6$ GHz.*

1.1.3. The Superconducting Phase Qubit

In the parameter regime relevant for phase qubit operation, we have $E_L > E_J \gg E_C$. The potential is then mainly harmonic $\propto E_L \hat{\phi}^2$ with small variations due to the Josephson term $\propto E_J \cos \hat{\phi}$. These variations in turn are still big compared to the kinetic energy scale E_C, so that the dynamics are confined to the minima of the $\cos \hat{\phi}$ function. The circuit is then biased such that the lowest two wells of the potential are strongly asymmetric, with a deep well on one side and a shallow on the other side. It is this shallow well that is used for qubit operation. Since it is so flat, the anharmonicity is more pronounced, allowing for a good separation of level splittings between individual states, a situation necessary for qubit operation.

Fig. 1.2 shows the potential of a phase qubit circuit in the experimentally relevant parameter regime. The inset shows the full potential with the shallow well, relevant for qubit operations, on the left and the deep well, used for qubit readout, on the right. The main figure shows a zoom into the left well. Lines indicate the five lowest energy eigenfunctions in this well, with their respective offset defined by the eigenenergies. The lowest two of these eigenfunctions are used as the logical qubit states.

The circuit can be manipulated via the gate voltage V_G and the magnetic flux

Φ_{Ext}. Qualitatively speaking, the application of a constant magnetic flux to the loop changes the zero-point of the harmonic contribution to the potential Eq. (1.7). The anharmonic term $\propto \cos\hat{\phi}$ will not be affected by this, and therefore the application of an external flux changes the shape of the potential minima. This modification of the potential will then in turn influence the shape and energy of the eigenfunctions in each well. We will quantify this statement in the following.

To illustrate the operation of the phase qubit circuit as a qubit, i.e. an artificial two-level system, we have to restrict the Hamiltonian Eq. (1.6) to the two lowest energy eigenstates of the shallow potential well. To demonstrate how it is possible to manipulate the system, we include the coupling to the external circuitry. From Eq. (1.6) we see that the external voltage couples to the charge operator as $\propto n_G\hat{q}$ and that the magnetic flux couples to the phase operator as $\propto \phi_{Ext}\hat{\phi}$. To determine the effect of manipulations, we therefore have to find the correct representation for the operators $\hat{q}$ and $\hat{\phi}$ in the qubit two-state basis. Focusing on the shallow potential well in Fig. 1.2, we restrict ourselves to a region in $\hat{\phi}$-space around its minimum, as depicted in Fig. 1.2. We first express the qubit operators as

$$\hat{q} = \mathrm{i}\left(\hat{a}^\dagger - \hat{a}\right) \quad , \quad \hat{\phi} = \hat{a}^\dagger + \hat{a}\,, \tag{1.8}$$

where $\hat{a}$ is the usual annihilation operator for harmonic oscillator eigenstates. Since the circuit potential is anharmonic, these are not the eigenstates of the qubit circuit. But, because the anharmonicity is weak, they are sufficiently close, so that this representation serves as a good starting point.

To find the expressions for the operators $\hat{q}$ and $\hat{\phi}$ in the qubit eigenbasis, we can now either perform a calculation in perturbation theory using a third order approximation of the qubit potential [48] or solve the Schrödinger equation numerically for the exact eigenfunctions of the circuit Hamiltonian Eq. (1.6). Restricting ourselves to the circuits two lowest energy eigenstates, we find

$$\hat{q} = q_\perp\sigma_y \quad , \quad \hat{\phi} = \phi_\perp\sigma_x + \phi_\|\sigma_z\,, \tag{1.9}$$

with the numerical factors $q_\perp, \phi_\perp \approx 1$ and $\phi_\| \ll 1$. Since the shape of the potential Eq. (1.7) and thus its eigenfunctions depends on the chosen flux bias point, the value of these constants is also weakly dependent on the external flux Φ_{Ext} through the qubit loop.

As we see from Eq. (1.9), the phase operator $\hat{\phi}$ acquires a longitudinal component $\propto \sigma_z$ while the charge operator $\hat{q}$ does not. The physical reason for this is simple to understand from the circuits diagram. Longitudinal components of the operators correspond to different average values of the corresponding observables in the different eigenstates. For the phase operator $\hat{\phi}$ the average value is proportional to the super-current through the ring. An average value of the charge operator $\hat{q}$, on the other hand, would correspond to a DC voltage across the Josephson junction, a situation which is prevented by the superconducting ring serving as an inductive shunt.

For the full qubit circuit Hamiltonian Eq. (1.6) in the two-level approximation we then find

$$\hat{H} = \frac{1}{2}\epsilon_{01}\sigma_z + \frac{1}{2}v_G n_G \sigma_y + \frac{1}{2}v_{\phi,\perp}\phi_{Ext}\sigma_x + \frac{1}{2}v_{\phi,\parallel}\phi_{Ext}\sigma_z \,, \qquad (1.10)$$

where ϵ_{01} is the level-splitting of the two lowest energy levels at the chosen flux bias and the σ are pauli-matrices. The coupling strengths v depend on the circuit parameters and are also weakly dependent on flux bias (for more details, cf. Ch. 2). From this expression we see that changing the flux bias determines the level-splitting of the qubit, while its state can be manipulated by either oscillating magnetic or electric fields.

Readout of the phase qubits state traditionally involves tilting the potential by an applied external bias flux for some fixed time, such that all states but the ground-state tunnel from the shallow left to the deep right well. The states in the two different wells differ by a large amount of circulating current through the loop, which can then be detected using a SQUID magnetometer on the same chip [29, 30].

1.2. Description of Dissipative Quantum Systems

One of the major challenges of solid state systems for quantum engineering is their inevitable coupling to the environment. This coupling leads to a time evolution involving degrees of freedom over which no control is possible. Tracing out these additional degrees of freedom, the probability of remaining in one of the controllable states will decay with time. Such effects are classified as decoherence.

In classical systems, the treatment of dissipation often involves additional energy non-conserving terms in the equations of motion. Similarly, in quantum mechanics, incorporating dissipative effects in the theory gives non-unitary time-evolution operators, which account for the loss of coherence and therefore time-reversal symmetry.

The most successful treatments of decoherence in quantum mechanics are based on effective master equations derived from a system-bath approach. In this picture, the system, whose time-evolution we are interested in, is coupled weakly to a bath of infinitely many modes. After tracing over the degrees of freedom of the environment, one acquires the effective dynamics of the system under the influence of the bath. The effects of the coupling of the system to the environment can in most cases be characterized as fluctuations in some parameter of the system, e.g., the magnetic flux through a loop. It is then the spectrum of these fluctuations which will determine the effect they have on the dynamics of the quantum system: High frequency fluctuations will lead to energy exchange processes while low frequency fluctuations will lead to a randomized dynamical phase and thus dephasing.

Here we give a short introduction into two methods which are commonly used to treat the problems of decoherence, namely the Bloch-Redfield and the Lindblad equations. As a starting point we introduce the phenomenological Bloch equations and then show how to use Fermi's Golden Rule to calculate transition rates between discrete states. We then show the Bloch-Redfield and Lindblad equations and discuss

their respective areas of applicability. Finally we discuss under which conditions the two treatments are equivalent and point out some finer points in their usage.

1.2.1. Bloch Equations and Golden Rule

One of the earliest descriptions of dissipation in quantum mechanics are the phenomenological equations F. Bloch introduced in 1946 to describe the decay of the magnetization in a material to which a magnetic field is applied [49]. We assume here a constant magnetic field in z-direction, defining an equilibrium magnetization M_0, and a time-varying field in x and y-direction. The dynamic equations for the magnetization $\vec{M}$ are given by

$$\frac{\mathrm{d}}{\mathrm{d}t}\vec{M} = -\vec{B} \times \vec{M} - \gamma_1 (M_z - M_0)\, \hat{e}_z - \gamma_2 (M_x \hat{e}_x + M_y \hat{e}_y) \tag{1.11}$$

where the $\hat{e}_i$ are unit-vectors in i-direction. The first term on the rhs of Eq. (1.11) describes the precession of the magnetization $\vec{M}$ around the direction of the applied magnetic field $\vec{B}$. The second term introduces the decay of the z-component of the magnetization M_z to its equilibrium value M_0 with the rate γ_1 while the third term gives the decay of the x- and y-components to zero with time constant γ_2.

If we identify the magnetization with the direction of a single spin $\frac{1}{2}$, we can rewrite the Bloch equations (1.11) as equations for the spins density matrix ρ as

$$\begin{aligned}
\dot{\rho}_{00} &= -\gamma_\uparrow \rho_{00} + \gamma_\downarrow \rho_{11}\,, \\
\dot{\rho}_{11} &= \gamma_\uparrow \rho_{00} - \gamma_\downarrow \rho_{11}\,, \\
\dot{\rho}_{01} &= -\mathrm{i}B_\perp \rho_{01} - \gamma_2 \rho_{01}\,,
\end{aligned} \tag{1.12}$$

where we define $\gamma_1 = \gamma_\downarrow + \gamma_\uparrow$ and used the fact that $\rho_{00} + \rho_{11} = 1$. From the thermal steady-state occupation $\langle \rho_{th} \rangle = (\gamma_\downarrow - \gamma_\uparrow)/(\gamma_\downarrow + \gamma_\uparrow)$ we find $\gamma_{\downarrow/\uparrow} = 1/2\,\gamma_1 (1 \pm \langle \rho_{th} \rangle)$. The decay rate of the off-diagonal elements is given by γ_2. Due to preservation of positivity of the density matrix ρ, we can conclude that $\gamma_2 \geq 1/2\,\gamma_1$ with possible additional contributions not originating from energy decay. We write $\gamma_2 = 1/2\gamma_1 + \gamma_\varphi$ where γ_φ is called pure dephasing rate.

The rates γ in the Eqs. (1.11) and (1.12) are still purely phenomenological. Next we will show the simplest microscopic picture describing decay processes, the so called Golden Rule decay.

Golden Rule

We take a general system coupled weakly to an infinitely large bath. We describe it by the Hamiltonian

$$\hat{H} = \hat{H}_S + \hat{H}_I + \hat{H}_B\,, \tag{1.13}$$

where $\hat{H}_S$ describes the dynamics of the system, $\hat{H}_B$ the dynamics of the bath and $\hat{H}_I$ the interaction between the two. For the interaction Hamiltonian we take the

general form

$$\hat{H}_I = \hat{z}\,\hat{X}\,, \tag{1.14}$$

where $\hat{z}$ is an operator of the system and $\hat{X}$ is an operator of the bath. To arrive at the Golden Rule expression, we now calculate the time-evolution assuming weak coupling to the bath. Specifically, we are interested in the probability of a transition from an initial state $|n\rangle$ to a final state $|m\rangle$ under the influence of coupling to the bath.

We start by evaluating the probability P_{if}^{nm} of a transitions between the states $|i,n\rangle$ and $|f,m\rangle$, where $|n/m\rangle$ denotes initial and final state of the system and $|i/f\rangle$ the states of the bath. The coupling $\hat{H}_I$ we treat as a perturbation. Changing into the interaction picture, we get in leading order of the interaction Hamiltonian

$$P_{if}^{nm}(t) = \left| -\mathrm{i}\int_0^t \mathrm{d}t'\,\langle i,n|\,\mathrm{e}^{-\mathrm{i}(\hat{H}_S+\hat{H}_B)t'}\,\hat{z}\,\hat{X}\mathrm{e}^{\mathrm{i}(\hat{H}_S+\hat{H}_B)t'}\,|m,f\rangle \right|^2\,, \tag{1.15}$$

where we include time evolution due to both the system $\propto \hat{H}_S$ and the bath $\propto \hat{H}_B$. Taking the square explicitly and separating the matrix elements for system and bath, we get

$$P_{if}^{nm}(t) = |z_{nm}|^2 \int \mathrm{d}t'\mathrm{d}t''\,\langle i|\,\hat{X}(t')\,|f\rangle\,\langle f|\,\hat{X}(t'')\,|i\rangle\,\mathrm{e}^{-\mathrm{i}\omega_{nm}(t'-t'')}\,, \tag{1.16}$$

where $z_{nm} = \langle n|\,\hat{z}\,|m\rangle$ and $\hat{X}(t) = \mathrm{e}^{-\mathrm{i}\hat{H}_B t}\hat{X}\mathrm{e}^{\mathrm{i}\hat{H}_B t}$. We are not interested in the final state of the bath, so we can sum this equation over all possible bath states $|f\rangle$. As the initial bath state we assume a thermal distribution ρ_{th} and finally arrive at the probability to be in the state $|m\rangle$ at time t when at time $t=0$ the system was in the initial state $|n\rangle$ as

$$P_{nm}(t) = t^2\,|z_{nm}|^2 \int_{-\infty}^{\infty} \mathrm{d}\omega\,C_X(\omega)\,\mathrm{sinc}^2\frac{(\omega-\omega_{nm})t}{2}\,, \tag{1.17}$$

where the sinc-function is defined by $\mathrm{sinc}(x) = \sin x/x$. The unsymmetrized correlation function of the bath coupling operator $\hat{X}$ is given by

$$C_X(\omega) = \int_{-\infty}^{\infty} \frac{\mathrm{d}t}{2\pi}\,\mathrm{e}^{\mathrm{i}\omega t}\left\langle \hat{X}(t)\hat{X}(0)\right\rangle\,. \tag{1.18}$$

Further details on this calculation might be found e.g., in Ref. [50]. Under the condition that the correlation function $C_X(\omega)$ is a smooth function around the transition frequency ω_{nm}, we can approximate the sinc-function by a delta-peak. The frequency range in which the correlation function should be smooth has to be determined carefully. More exactly the required size will be given self consistently by the resulting rate. The validity of this approximation will be discussed later in more detail (cf. Sec. 4.2). Using this approximation, we get $\partial_t P_{nm}(t) = \Gamma_{n\to m}$ with the

transition rate

$$\Gamma_{n \to m} = |z_{nm}|^2 \, C_X(\omega = \omega_{nm}) \,, \tag{1.19}$$

the standard Golden Rule result.

Above equation allows for an intuitive interpretation of the role of the bath in the decoherence. For a relaxation process, $E_n > E_m$, the bath correlation function is probed at positive frequency $\omega_{nm} > 0$. It here gives a measure of the ability of the bath to absorb energy at this frequency. For an excitation process on the other hand, $E_n < E_m$, the bath is probed at negative frequency $\omega_{nm} < 0$, representing its ability to emit energy. For a bath at thermal equilibrium we find

$$C(-\omega) = \mathrm{e}^{-\omega/T} \, C(\omega) \,. \tag{1.20}$$

This relation expresses the fact, that the occupation probability of states in the bath at frequency ω is distributed according to Boltzmann's law.

1.2.2. Bloch-Redfield Equations

The phenomenological equations (1.11) have later been put on a sound theoretical footing by Bloch and Redfield in independent works [51, 52]. The treatment developed there allows for description of decoherence of a general system coupled weakly to a thermal bath. We only shortly motivate the derivation of these so-called Bloch-Redfield equations here. Then we use the equations to define relevant decoherence rates and discuss their regime of applicability and common methods of solving them. We illustrate the effects of decoherence by solving for the time-evolution of a single two-level system coupled to a bath. A more complete derivation and discussion of the Bloch-Redfield equations can be found in Ref. [50].

We again start from a general system described by the Hamiltonian Eq. (1.13) and interacting with a thermal bath via the interaction term Eq. (1.14). Instead of calculating the time-evolution of the states, as was done to obtain the Golden Rule Eq. (1.19), we now consider the evolution of the systems reduced density matrix ρ. We again move into the interaction picture and first formulate the equations of motion for the complete density matrix ρ_{tot}, describing system and bath. We then trace over the bath degrees of freedom, assuming weak system-bath coupling, so that the density matrix factorizes at all times, $\rho_{tot}(t) = \rho(t)\rho_B$, where ρ_B describes the bath. We take the bath to be infinitely large, such that the interaction does not change its state significantly and we can describe it at all times by a thermal distribution $\rho_B = \rho_{th}$. In second order of the system-bath coupling we get

$$\partial_t \rho^{(i)} = - \int_0^t \mathrm{d}t' \, Tr_B \left\{ \left[\hat{H}_I^{(i)}(t), \left[\hat{H}_I^{(i)}(t'), \rho^{(i)}(t')\rho_{th} \right] \right] \right\} \tag{1.21}$$

where the superscript (i) denotes quantities in the interaction picture. Transforming

this equation back into the Schrödinger picture we find

$$\partial_t \rho(t) - \mathrm{i} \left[\rho(t), \hat{H}_S \right] =$$
$$- \int_0^t \mathrm{d}\tau \left\langle \hat{X}(\tau)\hat{X}(0) \right\rangle \left\{ \hat{z} \mathrm{e}^{-\mathrm{i}\hat{H}_S\tau} \hat{z} \rho(t') \mathrm{e}^{\mathrm{i}\hat{H}_S\tau} - \mathrm{e}^{-\mathrm{i}\hat{H}_S\tau} \hat{z} \rho(t') \mathrm{e}^{\mathrm{i}\hat{H}_S\tau} \hat{z} \right\} + \mathrm{h.c.} \,,$$

(1.22)

where we changed integration variables to $\tau = t - t'$. In this equation, the evolution of the system at time t is influenced by all previous times t'. One possibility to make the dynamics local in time is the so called Redfield approximation. For this we take the bath to be short correlated, so that the correlator $\left\langle \hat{X}(t)\hat{X}(0) \right\rangle$ decays quickly. We assume weak coupling to the bath, so that the time evolution of the system on the time-scale of the bath correlations is governed completely by the coherent evolution $\propto \mathrm{e}^{-\mathrm{i}\hat{H}_S t}$. We can then replace the density matrix at time $t' = t - \tau$ in Eq. (1.22) by

$$\rho(t') \approx \mathrm{e}^{-\mathrm{i}\hat{H}_S\tau} \rho(t) \mathrm{e}^{\mathrm{i}\hat{H}_S\tau} \,,$$

(1.23)

which makes the evolution local in time. The dynamics of the systems density matrix elements $\rho_{nm} = \langle n | \rho | m \rangle$ in its eigenbasis $\{|n\rangle\}$ is then described by the Bloch-Redfield equations:

$$\dot{\rho}_{nm} - \mathrm{i}\omega_{nm}\rho_{nm} = \sum_{lk} \mathcal{R}_{nmlk}\, \rho_{lk} \,,$$

(1.24)

with the Redfield tensor defined by

$$\mathcal{R}_{nmlk} = \Lambda_{kmnl} + \Lambda_{lnmk}^* - \sum_j \left(\Lambda_{njjl}\delta_{mk} + \Lambda_{mjjk}^*\delta_{nl} \right) \,.$$

(1.25)

The terms $\mathcal{R}_{nmlk}$ can be interpreted as the rates with which the density matrix element ρ_{lk} decays into the element ρ_{nm}. The Λ terms are here given by Golden Rule like equations

$$\Lambda_{nmlk} = z_{nm}\, z_{lk}\, Q_X(\omega = \omega_{kl}) \,,$$

(1.26)

with the matrix elements of the system coupling operator $z_{nm} = \langle n | \hat{z} | m \rangle$ and the energy difference between states $|n\rangle$ and $|m\rangle$ defined by $\omega_{nm} = \epsilon_n - \epsilon_m$. The function Q_X is defined as the Laplace transform of the correlator of $\hat{X}$,

$$Q_X(\omega) = \int_0^\infty \mathrm{d}t\, \mathrm{e}^{-\mathrm{i}\omega t} \left\langle \hat{X}(t)\hat{X}(0) \right\rangle \,,$$

(1.27)

and is in general complex valued. The imaginary part of this function will give additional contributions to the dynamic evolution, the Lamb shifts. In the following, we neglect these energy renormalisation effects. We can then again use the bath correlation function $C_X(\omega)$ by identifying $\mathcal{R}\left\{ Q_X(\omega) \right\} = 1/2\, C_X(\omega)$.

In the derivation of the rate Eq. (1.26), we made a similar assumption about the smoothness of the function Q_X as in the derivation of the Golden Rule result Eq. (1.19). In order for the above formulation to hold, Q_X has to be flat on the scale of the resulting rate Λ.

To check the validity of the approximations used in deriving the Redfield tensor, one has to calculate the resulting dissipative rates Γ governing the system dynamics and compare them to the time-scales of the coherent time-evolution of the undisturbed system, ω_{nm}, and to the bath correlation time τ_B. The Boch-Redfield equations are valid for $\Gamma \ll \omega_{nm}, 1/\tau_B$.

The Redfield tensor as defined in Eq. (1.25) is a tensor of 4th rank and as such very unwieldy to treat. For calculation one normally moves into the so-called super-operator space, where the Redfield tensor is of rank two and the density matrix is a vector. The Eq. (1.24) can then be formulated as a simple matrix equation and solutions are easy to find by standard diagonalization methods. To construct the super-operator, we can use the properties of the tensor product to derive

$$\mathrm{vec}(\hat{A}\hat{X}\hat{B}) = \left(\hat{A} \otimes \hat{B}^T\right)\mathrm{vec}(\hat{X}), \tag{1.28}$$

where the symbol $\otimes$ denotes the tensor product. Here $\hat{A}$, $\hat{B}$ and $\hat{X}$ all are matrices in normal Hilbert space. This provides us with a relation between any equation of the form $\hat{A}\hat{X}\hat{B}$ to an equation where the super-operator $\left(\hat{A} \otimes \hat{B}^T\right)$ acts on the vectorized form of the matrix $\hat{X}$. As an example, we write the dynamic equations as

$$\dot{\rho} = \mathcal{L}\rho, \tag{1.29}$$

with the Liouvillian $\mathcal{L}$ describing the complete dynamics. The formal solution to Eq. (1.29) is simply $\rho(t) = \mathrm{e}^{\mathcal{L}t}\rho(0)$. Now we apply the transformation Eq. (1.28) to get the super-operator description of this problem as

$$\mathrm{vec}(\dot{\rho}) = (\mathcal{L} \otimes \mathbb{1})\,\mathrm{vec}(\rho), \tag{1.30}$$

the solution of which can be easily obtained by diagonalization of the super-operator $(\mathcal{L} \otimes \mathbb{1})$.

Transition Rates

Writing down the Bloch-Redfield equations (1.24) for the occupation probabilities of the eigenstates, i.e. the diagonal matrix elements of the reduced density matrix ρ, one can define the transition rates $\Gamma_{n \to m} = -\mathcal{R}_{mmnn}$. Using the definition Eq. (1.25), we find

$$\Gamma_{n \to m} = |z_{nm}|^2 C_X(\omega = \omega_{nm}), \tag{1.31}$$

the same as for the Golden Rule calculation Eq. (1.19).

Dephasing Rates

Dephasing describes the decay of the off-diagonal elements of the density matrix. For $n \neq m$, we define $\rho_{nm}(t) = \mathrm{e}^{-\mathrm{i}\omega_{nm}t}\bar{\rho}_{nm}(t)$, thus separating the time-evolution into a fast and a slow evolving part. From Eq. (1.24) we get the time-evolution of the slow part as

$$\dot{\bar{\rho}}_{nm} = \sum_{lk} \mathcal{R}_{nmlk}\, \bar{\rho}_{lk}\, \mathrm{e}^{-\mathrm{i}(\omega_{lk}-\omega_{nm})t}\,. \tag{1.32}$$

Assuming non-degenerate transitions, $\omega_{nm} \neq \omega_{lk}$ for $nm \neq lk$, we can perform a rotating wave approximation and neglect all the fast rotating terms in Eq. (1.32) to arrive at

$$\dot{\rho}_{nm} = (\mathcal{R}_{nmnm} + \mathrm{i}\omega_{nm})\,\rho_{nm} \tag{1.33}$$

i.e., the decay of the off-diagonal elements are purely governed by a single element of the Redfield tensor. We define this as the dephasing rate of the off-diagonal element of the density matrix ρ_{nm},

$$\begin{aligned}
\Gamma_{2,nm} &= -\mathcal{R}_{nmnm} \\
&= \frac{1}{2}\left[\sum_{k\neq n}\Gamma_{n\to k} + \sum_{k\neq m}\Gamma_{m\to k}\right] + \frac{1}{2}\left(z_{nn} - z_{mm}\right)^2 C_X(\omega = 0)\,. \tag{1.34}
\end{aligned}$$

Here, the first term gives the contributions to the off-diagonals decay due to environment induced transitions in the system. The second term, called pure dephasing, is due to processes in which no energy is exchanged between the system and the bath and is therefore proportional to the bath correlation function at zero frequency.

This second term can also be derived by a semi-classical argument, which we show in the following. From Eq. (1.33) we see that the off-diagonal elements of the density matrix ρ_{nm} show oscillations at frequency ω_{nm}. We assume now the systems energy levels to be influenced by some classical fluctuating parameter X of the environment. We can write $\omega_{nm} = \omega_{nm}^{(0)} + (z_{nn} - z_{mm})\,X$, where $\omega_{nm}^{(0)}$ is the undisturbed value of the splitting and the $z_{nn} = \partial E_n/\partial X$ define the sensitivity of the energy of the state $|n\rangle$ on the value of the parameter X. The additional phase acquired at time t due to the environment is then given by

$$\Delta\varphi(t) = (z_{nn} - z_{mm})\int_0^t \mathrm{d}t'\, X(t')\,. \tag{1.35}$$

In an experiment, many measurements will be taken, each corresponding to a different realization of the parameter X and therefore to a different dynamical phase. Averaging over the measurements will result in an effective decay of the off-diagonals as $\rho_{nm}(t) \propto f(t)$. We perform the average over the fluctuations of the environmental parameter X assuming a gaussian distribution, i.e. $\langle\exp\{\mathrm{i}\Delta\varphi\}\rangle =$

$\exp\{-1/2\,\langle\Delta\varphi^2\rangle\}$, and calculate the decay function for free induction decay as

$$f(t) = \exp\left(-\frac{t^2}{2}(z_{nn} - z_{mm})^2 \int_{-\infty}^{\infty} \mathrm{d}\omega\, C_X(\omega)\, \mathrm{sinc}^2\frac{\omega t}{2}\right). \qquad (1.36)$$

For a sufficiently flat correlation function around $\omega = 0$ we can again replace the sinc-function by a delta peak and get simple exponential decay with the same rate as in the Bloch-Redfield treatment Eq. (1.34).

For $1/f$-noise, i.e. a noise spectrum of the form $S(\omega) \propto 1/\omega$, the pure dephasing rate seems to diverge. In this case one has to realize, that the lowest frequencies a given experiment is sensitive to are defined by the inverse total time t_{tot} of the experiment. This fact introduces an infrared cutoff $\omega_{IR} = 2\pi/t_{tot}$ into the integral in Eq. (1.36) and assures convergence of the expression.

Secular Approximation

The full Eq. (1.24) can quickly become very hard to solve. For a general n-level system, the Redfield tensor Eq. (1.25) in super-operator form is given by a $n^2 \times n^2$-matrix. For most physical problems, in which the application of the Bloch-Redfield equations is feasible, we are in the situation where the individual level-splittings $\omega_{nm} = \epsilon_n - \epsilon_m$ are much larger than all rates $\mathcal{R}$ appearing in the Redfield tensor. In this case we can apply the so-called secular approximation to the tensor, which decouples the time-evolution of each off-diagonal element of the density matrix from every other element. The dynamics of each off-diagonal ρ_{nm} is then given by an equation of the form Eq. (1.33). This approximation formally correspond to a rotating wave approximation in the elements of the Redfield tensor. The tensor in super-operator space can then be written in block-diagonal form, for a particular ordering of the density matrix elements.

Liouvillian Degeneracy

When taking the secular approximation, one has to be careful about possible degeneracies in the Redfield-tensor. More specifically, the possible degeneracies can appear in the transition frequencies between different levels as $\omega_{nm} = \omega_{lk}$ for $nm \neq lk$. This kind of degeneracy is know as Liouvillian degeneracy and can only appear in multi-level systems.

As soon as the size of the level-splittings ω_{nm} becomes comparable to the relevant rates $\mathcal{R}$, we can no longer neglect the tensor elements connecting the off-diagonals corresponding to the degenerate transitions. In the example above, we would have to include the element $\mathcal{R}_{nmlk}$ also in secular approximation.

Dissipative Two-Level System

Now we want to give an example of a Bloch-Redfield treatment of a dissipative system. The simplest possible model in which decoherence plays a role is a single

two-level system coupled to a bath. We describe it by the Hamiltonian

$$\hat{H} = \frac{1}{2}\epsilon_0\sigma_z + \frac{1}{2}\beta\left(\sin\theta\,\sigma_z + \cos\theta\,\sigma_x\right)\hat{X} + \hat{H}_{Bath}\,, \qquad (1.37)$$

where ϵ_0 is the TLS level-splitting, β defines the coupling strength to the bath operator $\hat{X}$ and the angle θ depends on the microscopics of the TLS-bath interaction. We will again not explicitly specify the bath Hamiltonian $\hat{H}_{Bath}$, but only characterize it via a correlation function. The Bloch-Redfield equations for a single two-level system in secular approximation take the particularly simple form

$$\dot{\rho} = \begin{pmatrix} \mathcal{R}_{0000} & \mathcal{R}_{0011} & 0 & 0 \\ \mathcal{R}_{1100} & \mathcal{R}_{1111} & 0 & 0 \\ 0 & 0 & \mathcal{R}_{0101} - i\epsilon_0 & 0 \\ 0 & 0 & 0 & \mathcal{R}_{1010} + i\epsilon_0 \end{pmatrix}\begin{pmatrix} \rho_{00} \\ \rho_{11} \\ \rho_{01} \\ \rho_{10} \end{pmatrix}. \qquad (1.38)$$

In this case, they reduce to the above stated Bloch-equations for the density matrix of a single spin, Eq. (1.12). We can then easily identify the rates appearing in the phenomenological Bloch-equations Eq. (1.12) as

$$\gamma_\downarrow = \mathcal{R}_{1100} = \frac{1}{4}\beta_\perp^2 C_X(\omega = \epsilon_0)\,,$$

$$\gamma_\uparrow = \mathcal{R}_{0011} = \frac{1}{4}\beta_\perp^2 C_X(\omega = -\epsilon_0)\,,$$

$$\gamma_1 = \mathcal{R}_{1100} + \mathcal{R}_{0011} = \frac{1}{2}\beta_\perp^2 S_X(\omega = \epsilon_0)\,,$$

$$\gamma_2 = \mathcal{R}_{0101} = \mathcal{R}_{1010} = \frac{1}{2}\gamma_1 + \frac{1}{4}\beta_\parallel^2 S_X(\omega = 0) \qquad (1.39)$$

where $\gamma_1 = \gamma_\downarrow + \gamma_\uparrow$ as defined above and we define transversal and longitudinal bath coupling as $\beta_\perp = \beta\cos\theta$ and $\beta_\parallel = \beta\sin\theta$. The symmetrized correlation function is defined by $S(\omega) = 1/2(C(\omega) + C(-\omega))$. Again we see the two contribution to the dephasing rate γ_2, the first part due to relaxation γ_1 and the second part due to pure dephasing $\propto S_X(0)$.

Fig. 1.3 illustrates the effects of dissipation on the time evolution of a single two-level system. We assumed purely transversal coupling to the bath, $\gamma_2 = 1/2\gamma_1$, and zero-temperature. The blue line shows the decay $\propto e^{-\gamma_1 t}$ of the expectation value $\langle\sigma_z\rangle$ for an initially excited state. The red line shows the decay of the expectation value $\langle\sigma_x\rangle$ for the initial state $\langle\sigma_x(t=0)\rangle = 1$. We see oscillations with frequency ϵ_0 which decay to zero with time constant $\gamma_2 = 1/2\gamma_1$.

1.2.3. Lindblad Equations

In quantum optical systems, the standard theoretical tool to treat decoherence are the so-called Lindblad equations [53, 54]. The equations in Lindblad form are given
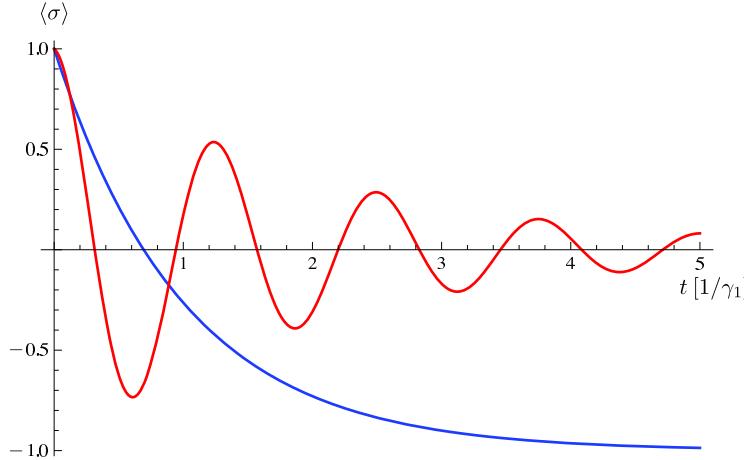
Figure 1.3.: *Illustration of dissipation in a two-level system. The lines show the decay of the expectation value of σ_z (blue line) and σ_x (red line) as a function of time for different initial states. For the blue line, the initial state is characterized by $\langle\sigma_z(t=0)\rangle = 1$, for the red line it is given by $\langle\sigma_x(t=0)\rangle = 1$. Parameters are (in units of γ_1): $\gamma_2 = 1/2$ and $\epsilon_0 = 5$.*

by

$$\dot{\rho} = -\mathrm{i}\left[\hat{H}, \rho\right] + \sum_n \Gamma_n \left(L_n \rho L_n^\dagger - \frac{1}{2}\left\{L_n L_n^\dagger, \rho\right\}\right), \tag{1.40}$$

where the sum is over all possible channels of decoherence with respective rates $\Gamma_n \geq 0$. The L_n are system operators corresponding to the individual decoherence channels. For example, relaxation in a two-level system would be described by the operator σ_-, inducing transitions from the excited state to the ground-state. Pure dephasing in this system can be described by the operator σ_z, which changes the level splitting of the two-level system. The rates Γ_n in Eq. (1.40) have to be determined for each channel individually, e.g. by means of the Golden Rule Eq. (1.19).

The validity range of these equations is similar to the Bloch-Redfield equations discussed earlier. They rely on weak coupling to the bath $\Gamma_n \ll \omega_{nm}$, where the ω_{nm} represent the frequencies relevant in the coherent evolution of the system. Also, the baths have to be infinitely large, so that they are always in equilibrium, and they have to obey Markovian dynamics, i.e., their correlation time has to be small. The exact form of these requirements depends on the approximations made when deriving the rates Γ_n in Eq. (1.40).

1.2.4. Applicability

There exists a common misconception, namely that the Lindblad equations of the form Eq. (1.40) are the only possible description of dissipative processes in quantum mechanics. The reason for this is, that, as Lindblad showed in Ref. [54], the equations in Lindblad form are the most general form of a dissipative master equation

with constant coefficients which does not violate positivity of the density matrix at any time during the evolution. This is often thought to imply that, for any physically sensible master equation, one has to be able to write it in Lindblad form. The Bloch-Redfield equations, as given in Eq. (1.24) do in general not fulfill this condition. However, as can be shown [55], in most relevant situations, possible violations of positivity of the density matrix are restricted to time scales which are small compared to or of the order of the bath-correlation time τ_B. For such small times, the validity of a Bloch-Redfield treatment is anyhow questionable (cf. the above discussion on their validity). In this case, also a Lindblad-type calculation has to be done very carefully, since most definitions of transitions rates Γ depend on times larger than the bath correlation time τ_B. These difficulties can be avoided when treating the coefficients in the master equation as time-dependent on the time-scale of the bath correlations, i.e. during this time they change smoothly from zero to some finite value. For long times we then have again constant coefficients and both types of equation will preserve positivity. A discussion of these points is provided in Ref. [55].

Another important difference between the two treatments comes about when treating strongly coupled systems, where each of the individual systems is coupled to a bath. The standard formulation of the Lindblad equations treats the systems separately and assumes independent decoherence channels for each one. Strong coupling between two systems might however change the energy landscape significantly compared to the uncoupled case. As we see in Eq. (1.19), any transition rates are proportional to the spectrum of the environment at the frequency of the transition. If these frequency is very different in the uncoupled as compared to the coupled case, the contribution to decoherence from each channel might also change significantly. This happens if the spectrum of the environment is not smooth on the scale of the coupling strength. In this case one has to formulate the Lindblad equations for the coupled system directly and can no longer use the results from the uncoupled case. The Bloch-Redfield equations on the other hand are already written in the eigenbasis of the coupled system and automatically incorporate any such modifications of the coupling to the baths. In the later parts of this thesis we give some discussion on this point (cf. Sec. 4.6).

For most applications we consider in this thesis, the two treatments are equivalent and the Bloch-Redfield equation could be written in in Lindblad form without loosing any vital information. We use both types of treatment for different applications in the scope of this work.

The Lindblad equations, Eq. (1.40), are very convenient and easy to implement for numerical calculations. They are at heart phenomenological equations, and we can identify the rates Γ_n of the individual decay channels with independently measured experimental rates for the individual systems (cf. Ch. 2 and Ch. 3).

The Bloch-Redfield equations, Eq. (1.24), on the other hand, allow for an intuitive understanding of the microscopics of the decoherence processes. We therefore prefer them for analytical treatments concerned with the origin of dissipation (cf. Ch. 4).

1.3. Floquet Theory

In this section we introduce Floquet theory as a means to treat periodically time-dependent problems in quantum mechanics. We start by introducing the formalism and defining all relevant quantities. In the second part, we apply the theory to an exactly solvable model, a single two-level system under driving. This example illustrates the techniques and arguments used in later chapters. More details on the formalism and additional examples may be found in Ref. [56].

1.3.1. Formalism

Floquet theory applies to the solution of periodically time dependent problems. The Floquet theorem (cf. e.g., [57]) states that there exist solutions to any periodically time-dependent differential equation which have the same periodicity as the original problem.

We start by assuming a time-dependent Hamiltonian with period T and $\hat{H}(t) = \hat{H}(t + T)$ and defining solutions $|\Psi(t)\rangle$ of the time-dependent Schrödinger equation

$$\mathrm{i}\, \partial_t \, |\Psi(t)\rangle = \hat{H}(t) \, |\Psi(t)\rangle \;. \tag{1.41}$$

According to Floquet's theorem there exist solutions to this equation which have the form

$$|\Psi(t)\rangle = \mathrm{e}^{-\mathrm{i}\epsilon t} \, |\phi(t)\rangle \;, \tag{1.42}$$

where the functions $|\phi(t)\rangle$ are the time-periodic Floquet modes. They obey the relation

$$|\phi(t + T)\rangle = |\phi(t)\rangle \;, \tag{1.43}$$

i.e. they show the same periodicity as the Hamiltonian. The quantities ϵ in Eq. (1.42) are a set of real parameters, called the quasi-energies. They are uniquely defined only up to multiples of the driving frequency $\omega = 2\pi/T$. This definition is in formal analogy to Bloch's theory in solid state physics. Bloch theory defines solutions to a Hamiltonian periodic in space which have the same periodicity and can be characterized by a quasi-momentum. In fact, Bloch theory in real space is equivalent to Floquet theory in time.

Since the Floquet states $|\phi\rangle$ and the Hamiltonian $\hat{H}$ are both periodic in time with period ω, we can write them as a Fourier-series. We define

$$|\phi(t)\rangle = \sum_n \mathrm{e}^{-\mathrm{i}n\omega t} \, |\phi_n\rangle \;, \qquad \hat{H}(t) = \sum_n \mathrm{e}^{-\mathrm{i}n\omega t} \, \hat{H}_n \;, \tag{1.44}$$

with time-independent coefficients $|\phi_n\rangle$ and $\hat{H}_n$. We now use the relations Eq. (1.42) and Eq. (1.44) to write down the Schrödinger equation for the Fourier-coefficients

$$\sum_n (\epsilon + n\omega) \, |\phi_n\rangle \, \mathrm{e}^{-\mathrm{i}n\omega t} \mathrm{e}^{-\mathrm{i}\epsilon t} = \sum_{k,l} \hat{H}_k \, |\phi_l\rangle \, \mathrm{e}^{-\mathrm{i}(k+l)\omega t} \mathrm{e}^{-\mathrm{i}\epsilon t} \;. \tag{1.45}$$

In this equation we can compare the coefficients on both sides to get the determining equation for the Floquet states as

$$(\epsilon + n\omega)\,|\phi_n\rangle = \sum_k \hat{H}_k\,|\phi_{n-k}\rangle\;, \tag{1.46}$$

which has the form of a time independent Schrödinger equation. Eq. (1.46) will be the starting point when treating periodically driven systems. Note that we did not use second quantization of the driving here, the number n stems from the Fourier-decomposition of the periodic problem.

As is clear from the definition Eq. (1.44), each of the coefficients $|\phi_n\rangle$ is a d-dimensional vector, where d is the original dimensionality of the problem. Eq. (1.46) determines how states with different index n are connected to each other due to the periodic driving. In treating the periodicity, we have therefore increased the effective dimension of our problem. The advantage of Floquet theory is, that for most problems the Fourier-series of the Hamiltonian, Eq. (1.44) can be well approximated by only a finite number of coefficients.

1.3.2. Two-Level System under Driving

As the simplest possible example, we consider the case of a two-level atom interacting with a monochromatic laser field. Assuming dipolar interaction between atom and light, we have the Hamiltonian

$$\hat{H} = \frac{1}{2}\epsilon_0\sigma_z + \mu E_0 \sin\left(\omega t + \varphi\right)\sigma_x\;, \tag{1.47}$$

where ϵ_0 is the level splitting of the atom, μ its dipole moment in direction of the electric field and E_0 the electric field strength at the position of the atom. The laser field has frequency ω and phase φ. The σ are pauli-matrices describing the two states of the atom.

Without loss of generality, we can set $\phi = \pi/2$ and write the driving field as a superposition of circularly polarized fields. The interaction becomes then

$$\hat{H}_I = \frac{1}{2}\Omega\left(\sigma_+ + \sigma_-\right)\left(\mathrm{e}^{\mathrm{i}\omega t} + \mathrm{e}^{-\mathrm{i}\omega t}\right) \tag{1.48}$$

where we defined the coupling strength $\Omega = \mu E_0$. Here the terms $\propto \sigma_-\mathrm{e}^{\mathrm{i}\omega t}$ and $\propto \sigma_+\mathrm{e}^{-\mathrm{i}\omega t}$ correspond to energy conserving processes (simultaneous excitation / relaxation of the atom and absorption / emission of a laser photon) and the terms $\propto \sigma_-\mathrm{e}^{-\mathrm{i}\omega t}$ and $\propto \sigma_+\mathrm{e}^{\mathrm{i}\omega t}$ to energy non-conserving processes (simultaneous relaxation / excitation of the atom and absorption / emission of a photon) Neglecting the non-conserving terms in the rotating wave approximation (RWA) leads us to the total Hamiltonian

$$\hat{H} = \frac{1}{2}\epsilon_0\sigma_z + \frac{1}{2}\Omega\left(\sigma_-\mathrm{e}^{\mathrm{i}\omega t} + \sigma_+\mathrm{e}^{-\mathrm{i}\omega t}\right)\;. \tag{1.49}$$

This problem is well know under the name of Rabi-Hamiltonian and proves to be exactly solvable. We determine the Fourier coefficients of the Hamiltonian as

$$\hat{H}_0 = \frac{1}{2}\epsilon_0\sigma_z\,, \qquad \hat{H}_{\pm 1} = \frac{1}{2}\Omega\sigma_{\mp}\,, \tag{1.50}$$

and use them to write the equation for the Floquet modes

$$(\epsilon + n\omega)\ket{\phi_n} = \frac{1}{2}\epsilon_0\sigma_z\ket{\phi_n} + \frac{1}{2}\Omega\left(\sigma_-\ket{\phi_{n+1}} + \sigma_+\ket{\phi_{n-1}}\right)\,. \tag{1.51}$$

This equation illustrates how states from Floquet mode $\ket{\phi_n}$ are connected to states from the mode $\ket{\phi_{n\pm 1}}$. No additional modes play a role in the dynamics since we assume monochromatic driving and performed the rotating wave approximation.
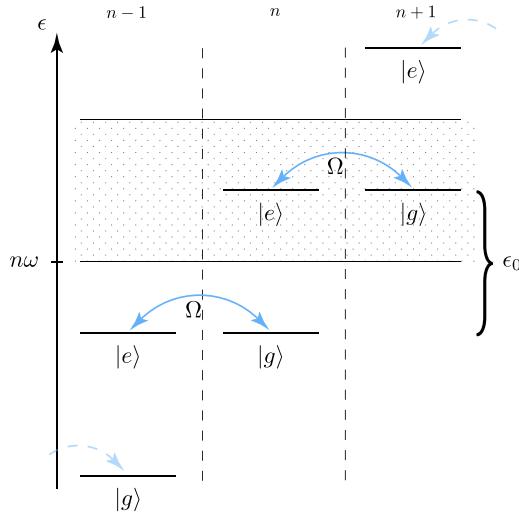
Figure 1.4.: *Illustration of the level structure of a periodically driven two-level system for the case of exactly resonant driving $\omega = \epsilon_0$. $\ket{g/e}$ denote ground- and excited state of the TLS. Since $\epsilon_0 \gg \Omega$, the dynamics is restricted to the doublets coupled via the driving field with strength Ω. The dotted area indicates a single Brillouin-zone of size ω in the quasi-energies. Each BZ contains a total of two-states.*

In Fig. 1.4 we illustrate the level structure described by Eq. (1.51) for the case of exactly resonant driving $\epsilon_0 = \omega$. The columns labeled by the number n indicate the states in the n-th Floquet mode. The operators $\sigma_{\pm}$ connect states in different modes with the coupling strength Ω. We see that the level structure is periodic with the mode number n. Similar to the situation in Bloch theory, we can then restrict ourselves to a single Brillouin-zone (BZ) in energy to describe the dynamics. The width of the first BZ is given by the driving frequency ω. The dotted area in Fig. 1.4 indicates one possible choice for the first BZ. The Hamiltonian restricted to

this Brillouin zone reads

$$\hat{H}_{BZ} = \frac{1}{2} \begin{pmatrix} -\delta\omega & \Omega \\ \Omega & \delta\omega \end{pmatrix}, \tag{1.52}$$

where the states used to write down Eq (1.52) are the TLS ground- and excited states of different Floquet modes $|e_n\rangle$ and $|g_{n+1}\rangle$. Here we labeled the states with an index denoting their Floquet mode n. We defined the detuning between the atomic transition and the laser field $\delta\omega = \epsilon_0 - \omega$ and measure the energies relative to the middle of the first BZ. The eigenstates of this Hamiltonian are

$$|\phi_+\rangle = \sin\frac{\xi}{2} \, |e_n\rangle + \cos\frac{\xi}{2} \, |g_{n+1}\rangle \,,$$
$$|\phi_-\rangle = \cos\frac{\xi}{2} \, |e_n\rangle - \sin\frac{\xi}{2} \, |g_{n+1}\rangle \,, \tag{1.53}$$

with the mixing angle $\tan\xi = \Omega/\delta\omega$. Their energies are given by

$$\epsilon_\pm = \pm\frac{1}{2}\sqrt{\Omega^2 + \delta\omega^2} \,, \tag{1.54}$$

so that the two states are split in energy by the Rabi-frequency $\Omega_R = \sqrt{\Omega^2 + \delta\omega^2}$.
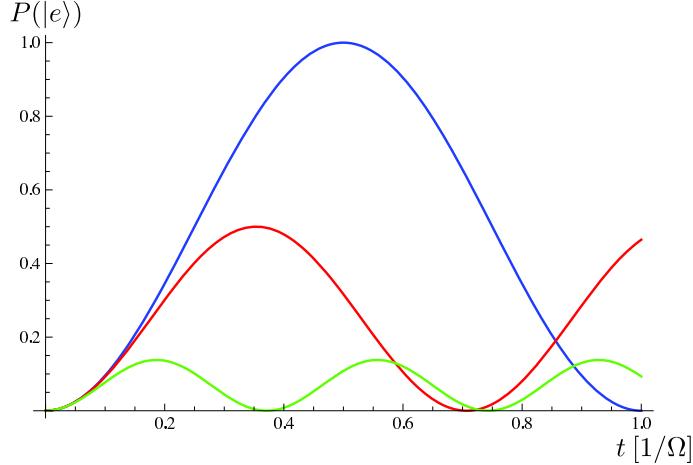
Figure 1.5.: *Rabi oscillations of a single periodically driven two-level system. We plot the probability $P(|e\rangle)$ of the TLS to be in the excited state $|e\rangle$ as a function of time for different values of detuning $\delta\omega$ between TLS and laser field. The blue line corresponds to zero detuning, $\epsilon_0 = \omega$, while the red line is calculated for a detuning of $\delta\omega = \Omega$ and the green line is for $\delta\omega = 2.5\,\Omega$.*

Solving for the time-evolution of the Hamiltonian Eq. (1.52), we get the so called Rabi-oscillations between ground- and excited state of the two-level system with frequency Ω_R. The amplitude of the oscillations also depends on the coupling strength and detuning as $\propto \Omega^2/(\Omega^2 + \delta\omega^2)$. Fig. 1.5 shows the excitation prob-

ability $P(|e\rangle) = |\langle\phi(t)|\,|e\rangle|^2$ for the initial state $|\phi(t=0)\rangle = |g\rangle$ as a function of time. The colors indicate different values of the detuning $\delta\omega$.

It should be noted that the same Hamiltonian Eq. (1.52) can be obtained from simply transforming the original problem Eq. (1.49) into a frame rotating with the driving frequency ω or by treating the driving field in second quantization. We show this alternative approach in Ch. 3.

If we do not apply the RWA to the original problem Eq. (1.47), the determining equation for the Floquet modes, Eq. (1.51), acquires an additional term of the form $1/2\,\Omega\,(\sigma_- |\phi_{n-1}\rangle + \sigma_+ |\phi_{n+1}\rangle)$. In the level diagram, Fig. 1.5, these expressions connect the states $|g_n\rangle$ with the states $|e_{n+1}\rangle$. In the resulting dynamics, an infinite set of Floquet modes will now play a role. For illustration we show the Hamiltonian without RWA for the first BZ, but including now also the two nearest states connected by energy non-conserving terms. Exactly in resonance, $\delta\omega = 0$, we get

$$\hat{H} = \frac{1}{2}\begin{pmatrix} 4\epsilon_0 & \Omega & 0 & 0 \\ \Omega & 0 & \Omega & 0 \\ 0 & \Omega & 0 & \Omega \\ 0 & 0 & \Omega & -4\epsilon_0 \end{pmatrix}, \tag{1.55}$$

where the states used are now $\{|e_{n+2}\rangle, |g_{n+1}\rangle, |e_n\rangle, |g_{n-1}\rangle\}$. Comparing with Eq. (1.52) in RWA, we see that the added states are far detuned. Under the condition $\Omega \ll \epsilon_0, \omega$ their effect will only be a shift in the energy of the states $|e_n\rangle$ and $|g_{n+1}\rangle$ in the first BZ.

Since the problem is fully periodic in the Floquet modes n, we see that, independent of the strength of the driving Ω, we will always find only two states in the first Brillouin-zone. It is these states that describe the dynamics.

1.4. Holonomic Gates for Quantum Computation

Until now, we have mainly discussed the problem of decoherence for the manipulation of quantum systems. Another problem arises from the necessity of manipulation and control of parameters. Since in quantum computation gates are non-discrete, small errors in preparation and execution of control pulses might accumulate. The precision necessary for fault tolerant quantum computing is therefore of the order of at least 10^4 gate operations per error [1], and as of yet far from experimental realization. The main problems lie in the timing of control pulses and in the exact control of their magnitude.

As a possible solution to this problem, geometric quantum computation was proposed [58]. This scheme depends on the generation of geometric phases in order to manipulate the states of the qubits. In this case, the unitary transformations depend only on the path taken in parameter space and not on their exact timing. Additionally, possible random fluctuation of the control parameters will cancel to first order [59], also providing a measure of protection from decoherence.

In mathematics, the term holonomy describes a measure of the extent in which parallel transport of a vector along a closed curve in parameter space fails to preserve the geometric properties of the vector. Therefore any geometric manipulation, in which a state vector acquires a phase due to a periodic change in the Hamiltonian, can be described as a holonomy. More importantly this same effect can be used to effect arbitrary rotations in degenerate subspaces of the total Hamiltonian.

In this part we first give a short introduction into the notion of holonomies in quantum mechanics. We start with a general time-dependent Hamiltonian and motivate how a periodic change in the system can lead to non-trivial time evolution. We then introduce the tripod Hamiltonian, a system in which holonomic gates can be realized. In Ch. 5 we show how we can realize this Hamiltonian in a physical system built out of superconducting qubits.

1.4.1. Geometric Phases and Holonomies

Here we give a simple picture on how to understand the concepts of geometric phases and holonomies in quantum mechanics. We start from the Schrödinger equation for a time-dependent problem

$$\mathrm{i}\partial_t \ket{\Psi} = \hat{H}(t) \ket{\Psi} \,, \tag{1.56}$$

where we use the description of the time-dependent Hamiltonian

$$\hat{H}(t) = \sum_n E_n(t) \ket{n(t)} \bra{n(t)} \,, \tag{1.57}$$

which is diagonal in the basis of the instantaneous eigenstates $\ket{n(t)}$ and has instantaneous eigenvalues $E_n(t)$. We want to find the Schrödinger equation for the state $\ket{\Phi}$ defined in the time-independent basis $\{n_0\}$ as

$$\ket{\Phi} = \hat{U}(t) \ket{\Psi} = \sum_n c_n \ket{n_0} \,, \tag{1.58}$$

where we defined the unitary transformation

$$\hat{U}(t) = \sum_n \ket{n(t)} \bra{n_0} \,. \tag{1.59}$$

For ease of reading we do not write all explicit time-dependences in the following, and instead indicate time-independent quantities by the subscript 0. The Schrödinger equation for $\ket{\Phi}$ can again be brought in the standard Schrödinger form Eq. (1.56), now with the transformed Hamiltonian

$$\hat{H}' = \hat{U}\hat{H}\hat{U}^{-1} + \mathrm{i}\,\dot{\hat{U}}\hat{U}^{-1} \,. \tag{1.60}$$

Writing this operator explicitly in the basis of the time-independent states $\{n_0\}$, we get

$$\hat{H}' = \sum_n E_n |n_0\rangle \langle n_0| + i \sum_{n,m} |n_0\rangle \langle \partial_t n | m\rangle \langle m_0| \tag{1.61}$$

where we write $|\partial_t n\rangle = \partial_t |n\rangle$. We will now focus on the second term of Eq. (1.61), since it describes the effects due to the evolution of the Hamiltonian in time. The diagonal parts in this term, $n = m$, give an additional contribution $\Delta\varphi$ to the dynamical phase φ a state acquires during its time evolution. The off-diagonal parts, $n \neq m$, on the other hand induce transitions between the basis states $\{|n_0\rangle\}$, and for strong time-dependence of the Hamiltonian (non-adiabatic driving) will lead to Landau-Zener tunneling, i.e. transitions between the systems eigenstates.

We now take the Hamiltonian to explicitly depend on a set of parameters $\vec{R}$, which in turn change in time. We have $\hat{H}(t) = \hat{H}(\vec{R}(t))$, and can then write

$$\partial_t |n\rangle = \partial_t \vec{R} \frac{\partial |n\rangle}{\partial R} = \dot{\vec{R}} |\partial_R n\rangle \ , \tag{1.62}$$

which describes the change of the basis vector $|n\rangle$ when transported in parameter space along the path defined by the change in the parameter vector $\vec{R}$.

Assuming a cyclic time evolution of $\vec{R}$, i.e. $\vec{R}(0) = \vec{R}(T)$ for some period T, the additional dynamical phase $\Delta\varphi$ acquired by the state $|n_0\rangle$ during one cycle of $\vec{R}(t)$ can be found as

$$\Delta\varphi = \int_0^T dt \, \dot{\vec{R}} \langle \partial_R n | n\rangle = \int_{R(0)}^{R(T)} dR \, \langle \partial_R n | n\rangle \ , \tag{1.63}$$

which we identify as the total area the change in $|n\rangle$ describes in the parameter space of $\vec{R}$. We call this contribution the geometric phase or in the case of adiabatic evolution the Berry's phase. This result determines the geometric phase a state acquires as the difference in the state vector after it is transported along a full cycle in parameter space, i.e. the holonomy.

In most cases, especially for slow rate of change of the Hamiltonian, we can safely neglect the off-diagonal terms in $\hat{H}'$. However, for a degenerate subspace of states, spanned e.g., by the two states $\{|n\rangle, |m\rangle\}$ with $E_n = E_m$, these terms will introduce transition between the states $|n\rangle$ and $|m\rangle$. The off-diagonal terms in Eq. (1.61) now determine the state evolution in this two-dimensional subspace. The transition matrix elements, relevant for the time-evolution are given by

$$A_{nm} = i \langle \partial_R n | m\rangle \ . \tag{1.64}$$

The time evolution operator acting on this subspace can then be calculated as

$$\hat{U}_H = \mathcal{T} \exp\{\oint dR \, \hat{A}\} \ , \tag{1.65}$$

where the symbol $\mathcal{T}$ indicates the time ordered product and the matrix $\hat{A}$ has entries defined by Eq. (1.64). The symbol $\oint$ denotes integration along a full cycle in parameter space. In general the matrices $\hat{A}$ do not commute with themselves at different times, thus the non-abelian nature of the holonomy $\hat{U}_H$.

1.4.2. The Tripod Hamiltonian

One such time-dependent Hamiltonian, in which non-abelian geometric phases can be observed, is given by the much studied tripod Hamiltonian

$$\hat{H} = \begin{pmatrix} \Delta & \Omega_1 & \Omega_2 & \Omega_3 \\ \Omega_1^* & 0 & 0 & 0 \\ \Omega_2^* & 0 & 0 & 0 \\ \Omega_3^* & 0 & 0 & 0 \end{pmatrix}, \tag{1.66}$$

where the Ω_i are control parameters (usually referred to as Rabi-frequencies) and can be changed in time. The Hamiltonian Eq. (1.66) describes a single state $|0\rangle$ of energy Δ coupled via the Rabi-frequencies Ω to three other, degenerate states $|n\rangle$, $n = 1, 2, 3$. The first proposal to observe non-Abelian transformations in trapped ions was based on Hamiltonian (1.66) (cf. [60, 61]). In ion-trap systems this Hamiltonian describes e.g., a single metastable excited state of an atom coupled via laser fields to three stable states of the same atom.

The tripod Hamiltonian has two non-degenerate eigenstates, usually referred to as *bright* states at energies $\epsilon_{1/2} = 1/2 \left(\Delta \pm \sqrt{\Delta^2 + 4|\Omega_1|^2 + 4|\Omega_2|^2 + 4|\Omega_3|^2} \right)$. More importantly, one also finds a degenerate zero-energy subspace $\mathcal{E}$ spanned by two *dark* states. To achieve a holonomy, the system is initially prepared in this zero-energy subspace $\mathcal{E}(t = 0)$. Upon changing the Hamiltonian cyclic in time $\hat{H}(T) = \hat{H}(0)$, the system will remain in the initial subspace $\mathcal{E}(T) = \mathcal{E}(0)$, under the condition that the change happens adiabatically slow. The initial state, however, will have undergone a non-trivial $U(2)$ transformation in the subspace, which is our holonomy. A specific example of such a transformation will be provided in Ch. 5.

One might note that the degenerate subspace $\mathcal{E}$ which we will use to realize a holonomic gate is not the ground-state of the Hamiltonian Eq. (1.66), and might therefore be affected by decoherence. The important thing to note here, is that the dark states $|d\rangle_n$ will at any time during the evolution be a mixed state of the three originally zero-energy states $|n\rangle$, used to write down the Hamiltonian Eq. (1.66). For adiabatic evolution, the subspace $\mathcal{E}$ is isolated from the bright states, and the only relevant decoherence channels are the ones acting on the original basis states $|n\rangle$, i.e. the degenerate ground-states of the system. This situation is however not applicable to all implementations of the tripod Hamiltonian. It is equally possible that the states $|n\rangle$ are not the ground-states of the system and then the time-evolution will be affected by decoherence.

2. Comparison of Defect Models

The microscopic origin of the coherent two-level defects found in superconducting circuits still remains unclear. In this chapter we will show how we can use spectroscopic data to learn about the exact form of the interaction between the qubit and the TLS. To this end, we will first introduce spectroscopy and use experimental data acquired on a phase qubit to demonstrate the relevant transitions. From this knowledge we then move on towards extracting parameters by performing a high-accuracy fit of the data to a general theoretical model. This results provide insight into the nature of the coupling between a qubit and a microscopic defect and therefore into the TLS microscopics.

Introduction

A key limiting factor of superconducting quantum coherent devices is that they suffer from decoherence induced by their weak but non-negligible interaction with the environment [62], the details of which are still not completely understood. The theoretical modeling of these interactions has greatly advanced our understanding of fundamental processes in the environment [26, 63] and led to improved designs for increased coherence times, e.g., by engineering 'sweet-spots' or insensitivity to particular aspects of the environment [13, 14]. Despite these advances, not all effects of the environment are understood.

When studying superconducting qubits spectroscopically, one often finds clear signatures of level anti-crossings at certain frequencies [29–31, 37, 45, 64]. These anti-crossings indicate intrinsic, microscopic two-level systems being coupled coherently to the qubit circuit. In general, ensembles of two-level microscopic defects are believed to be responsible for loss in a wide variety of systems (cf. Sec. 4.2), including phase- and flux-based superconducting qubits [25], microwave resonators [24] and even nano-mechanical oscillators [22, 23]. They are also a model system for the anomalous behavior of the heat capacity and sound attenuation in amorphous and spin-glass systems at low-temperature [19–21]. In solid state systems they serve as a standard model for the low-frequency part of the noise spectrum, since ensembles of tunneling two-level systems will show a $1/f$-noise spectrum at low-frequencies [18].

In superconducting systems, the exact microscopic nature of these intrinsic two-level systems remains unknown. It has been shown that they are coherent and due to their relatively long coherence times can potentially be used to store and retrieve quantum information [34]. Also coherent two-level systems are considered detrimental to the qubits operation, since they can introduce additional channels of decoher-

ence [38, 65] and will change the response of the qubit strongly (cf. Sec. 4.3). Also, it has been suggested to use the TLS themselves as naturally formed qubits [36], for which one would need to be able to tailor their properties. Therefore, acquiring a more in-depth understanding of their microscopic nature is essential.

In several experiments [31, 33, 34], it has been observed that, for strongly coupled defects, the coupling term is mainly transverse ($\propto \sigma_x \tau_x$, involving pure qubit-defect energy exchange) with minimal longitudinal ($\propto \sigma_z \tau_z$, phase shift inducing) component. Since different microscopics correspond to different physical nature of the coupling between qubit and TLS, this will also change the exact form of the coupling. In this chapter, we will show a high precision comparison between experimental data and a general theoretical model with the goal to shed light on the exact form of the coupling operator between qubits and two-level defects. We obtain quantitative estimates of the longitudinal and transverse coupling components and compare these results to existing theoretical models for intrinsic two-level systems.

The chapter is organized as follows: First, we introduce the Hamiltonian used to describe the system. It is composed of a three level phase qubit coupled to a two-level defect. The form of the coupling between the two depends on the microscopic nature of the TLS. We give a detailed description of the TLS models we will consider in the later evaluation. Second, we show results from spectroscopy of this system. The experiments we consider were performed in the group of Alexey Ustinov at KIT. In these experiments, a relatively high microwave power was used for the driving, resulting in dynamics which include higher qubit levels. We apply our model to the data and use it to identify the relevant transitions. We then use this information to illustrate how we can use this date to learn about the form of the interaction between qubit and TLS. The last part is dedicated to a comparison of the experimental data with several coupling models. We show results from high-precision fits to the data and use their results to give bounds on the parameters of the microscopic models for the TLS.

2.1. System and Defect Models

Here we start by introducing the components of our subsequent analysis. We first give the Hamiltonian of the system, consisting of the phase qubit circuit and a TLS. As we show in the next section, it is no longer sufficient to use a two-level description of the qubit to account for the experimental data. We therefore explain how to include higher levels in the qubit circuit and then give details about how to model the coupling to the TLS. Several physical mechanisms of the coupling are possible, each corresponding to different microscopic models of the TLS. In the last part of the section, we give a detailed explanation of the defect models we will later use in our analysis of the origin of the coupling.

2.1.1. Hamiltonian

We describe the system by the Hamiltonian

$$\hat{H} = \hat{H}_q + \hat{H}_f + \hat{H}_I + \hat{H}_{Bath}\,, \tag{2.1}$$

where $\hat{H}_q$ describes the qubit circuit, $\hat{H}_f$ the TLS and $\hat{H}_I$ the interaction between them. The bath operator $\hat{H}_{Bath}$ describes both the coupling of the two systems to thermal baths as well as the baths internal dynamics. We will not specify $\hat{H}_{Bath}$ in this chapter and instead describe the decoherence dynamics by a simplified Lindblad-type equation characterized by independent relaxation and dephasing rates (cf. Sec. 1.2).

The TLS is described here simply as a generic two-level system with its characteristic level splitting ϵ_f

$$\hat{H}_f = -\frac{1}{2}\tau_z \epsilon_f\,, \tag{2.2}$$

where τ is a pauli matrix.

The phase qubit circuit was already introduced in Sec. 1.1. It is given by the circuit depicted in Fig. 1.1. We derive the Hamiltonian for that circuit and get

$$\hat{H}_q = E_C \left(\hat{q} - n_G\right)^2 + E_L \left(\hat{\phi} - \phi_{\text{Ext}}\right)^2 - E_J \cos \hat{\phi}\,, \tag{2.3}$$

with the three energy scales charging energy $E_C = 2e^2/C$, inductive energy $E_L = 1/(2L)(\Phi_0/2\pi)^2$ and Josephson energy $E_J = I_C \Phi_0/2\pi$. Here, I_C is tht critical current of the circuits Josephson junction, C is the qubit's capacitance, L the inductance of the superconducting ring and $\Phi_0 = 2e/h$ is the superconducting flux quantum. Eq. (2.3) describes an anharmonic oscillator with dynamical variables given by the phase difference across the Josephson junction $\hat{\phi}$ and its conjugate momentum $\hat{q}$, corresponding to the number of cooper pairs tunneled across the junction, with $[\hat{q}, \hat{\phi}] = i$. We can manipulate the circuit via two external variables, the phase corresponding to the external flux through the loop $\phi_{Ext} = \Phi_{Ext}\, 2\pi/\Phi_0$ and the dimensionless gate charge $n_G = C_G\, V_G$.

The main idea behind the coupling between the qubit and the TLS is now, that the TLS is a microscopic defect somewhere inside or near the qubit circuit. If the states of the TLS now correspond to different values in one of the parameters of the Hamiltonian Eq. (2.3), their dynamics will automatically be coupled.

Looking at the circuit Hamiltonian Eq. (2.3), we see that such a coupling can have three different origins: (i) a variation in the critical current I_C of the Josephson junction, (ii) a variation in the external flux Φ_{Ext} through the qubit loop and (iii) a variation of the gate charge n_G. We will give possible microscopic explanations for these different coupling in the following.

2.1.2. Defect Models

Here we will specify the form of the coupling operator $\hat{H}_I$ in Eq. (2.1). For each possibility we will give details on possible microscopic pictures of the TLS and specify the origin of parameters of the models.

We assume linear coupling between qubit and TLS and can write the general form

$$\hat{H}_I = v\,\hat{o}\left(\sin\theta\,\tau_z + \cos\theta\,\tau_x\right), \tag{2.4}$$

where $\hat{o}$ is an operator of the qubit (to be specified below) and $\sin\theta\,\tau_z + \cos\theta\,\tau_x$ is the most general form of a two-level system operator. The coupling strength v finally determines the strength of the interaction.

The angle $\theta \in [0, \pi]$ in Eq. (2.4) characterizes the relation between the TLS eigenbasis, in which the Eqs. (2.4) and (2.2) are written, and the *physical* TLS basis. The physical TLS basis we define as the basis where the interaction between qubit and TLS is diagonal, meaning that the states in this basis correspond to different microscopic values of whatever qubit parameter the TLS couples to, e.g., critical current of the Josephson junction, external magnetic flux through the qubit loop or applied gate charge. Finding θ thus gives information on these physical states. In this basis the TLS is described by (cf. Fig. 0.2)

$$\hat{H}_f = -\frac{1}{2}\epsilon_0\tilde{\tau}_z - \frac{1}{2}\Delta_0\tilde{\tau}_x, \tag{2.5}$$

with the asymmetry energy $\epsilon_0 = \sin\theta\,\epsilon_f$ and the tunneling matrix element $\Delta_0 = \cos\theta\,\epsilon_f$. Therefore, an angle of $\theta = \pi/2$ corresponds to exact degeneracy of the TLS-states in the physical basis.

Coupling via Critical Current I_C

This kind of qubit-defect coupling received most attention from theory groups in the last years. In this case, the state of the TLS will modulate the critical current of the Josephson junction. In Eq. (2.3), we can then write $E_J = E_J^{(0)} + \delta E_J$, where δE_J will depend on the state of the TLS. For the coupling operator we find

$$\hat{H}_{I,c} = v_c\,\cos\hat{\phi}\left(\sin\theta_c\,\tau_z + \cos\theta_c\,\tau_x\right), \tag{2.6}$$

with $v_c = \delta I_c\Phi_0/2\pi$. Determining the strength of the coupling will therefore tell us the magnitude of the change in critical current as induced by the TLS.

There is a large number of possible microscopic TLS models, which correspond to a change in critical current (cf. e.g., Refs. [40–43]). We will focus our analysis on only two of them. The first one is probably the conceptually simplest one, in which the microscopic picture of the TLS is that of a single atom or a group of atoms tunneling between two metastable positions in the amorphous dielectric of the Josephson junction (cf. Fig. 0.1). This is the standard model of tunneling two-level systems observed e.g., in glasses [19, 20]. The change in critical current upon

transition between the two physical TLS states can be understood as blocking and unblocking of single conduction channels in the circuits Josephson junction [41].

The second model by de Sousa et al. [43] assumes a single impurity level of energy ϵ_d inside the Josephson junction interacting with one of the leads. This system is described by the Hamiltonian

$$\hat{H} = \hat{H}_0 + \hat{H}_{BCS} + \hat{H}_I \,, \tag{2.7}$$

with the impurity level $\hat{H}_0 = \sum_\sigma \epsilon_d \hat{d}_\sigma^\dagger \hat{d}_\sigma$, the BCS Hamiltonian H_{BCS} describing the superconducting lead and H_I describing the interaction between impurity level and lead. The operator $\hat{d}_\sigma^\dagger$ is a fermionic creation operator acting on the impurity. The BCS Hamiltonian is given by

$$\hat{H}_{BCS} = \sum_{k,\sigma} \epsilon_k \hat{c}_{k,\sigma}^\dagger \hat{c}_{k,\sigma} + \sum_k \Delta_{BCS} c_{k,\uparrow}^\dagger c_{-k,\downarrow}^\dagger + \text{h.c.} \,, \tag{2.8}$$

where $c_{k,\sigma}^\dagger$ generates a conduction electron in the superconductor and Δ_{BCS} is the superconducting gap ($\Delta_{\text{BCS}} \approx 300\ \mu\text{eV}$ for thin Al-films). The interaction part describes hopping between the impurity level and the lead and can be written as

$$\hat{H}_I = \sum_{k,\sigma} V_k \hat{d}_\sigma^\dagger \hat{c}_{k,\sigma} + \text{h.c.} \,, \tag{2.9}$$

with the hopping matrix element V_k. For impurity energies inside the superconducting gap, $|\epsilon_d| < \Delta_{BCS}$, this hybridization leads to the formation of a pair of Andreev bound states at energies $\pm E_b$. The energies E_b can be found as solutions to the equation

$$E_b^2 \left(1 + \frac{2\gamma}{\sqrt{\Delta_{\text{BCS}}^2 - E_b^2}} \right) - \epsilon_d^2 - \gamma^2 = 0 \,, \tag{2.10}$$

where we defined a hybridization parameter $\gamma \propto \langle V_k^2 \rangle$, characterizing the strength of the interaction between the impurity and leads. This pair of Andreev bound states will form what is called an Andreev level fluctuator (ALF), which will interact with the qubit. The two physical states of the ALF correspond to the occupation of the two different Andreev levels with energies $\pm E_b$. Occupation of each of these levels will modify the critical current of the junction. Since the energies of the two states are different, the critical current will in general be different for either one of the levels occupied.

Identifying such an ALF with the two-level systems observed in spectroscopy, we find the relation between the energies $\epsilon_f = 2E_b$. In this model we can write the interaction between qubit and ALF as

$$\hat{H}_{I,c} = v_c \cos \hat{\phi} \left((a_+ - a_-)\tau_z + 2\sqrt{a_+ a_-}\tau_x \right) \,, \tag{2.11}$$

where the amplitudes $a_\pm$ are given by

$$a_\pm = \frac{(\Delta_{\mathrm{BCS}}^2 - E_b^2)\left[(\epsilon_d \pm E_b)^2 + \gamma^2\right]}{2\left[(2\Delta_{\mathrm{BCS}}^2 - E_b^2)(\epsilon_d^2 + \gamma^2) - E_b^4\right]}\,. \tag{2.12}$$

We can thus identify

$$2\sqrt{a_+ a_-} = \cos\theta_c\,,$$
$$(a_+ - a_-) = \sin\theta_c\,. \tag{2.13}$$

Inserting then Eq. (2.10) into Eq. (2.12) we can express the amplitudes $a_\pm$ as function of only one unknown variable, the impurity level energy ϵ_d. The relations Eq. (2.13) therefore connect the angle θ_c in this model to the impurity level energy ϵ_d. The change in critical current δI_C can again be found through the coupling strength v_c.

Coupling via Magnetic Flux Φ_{Ext}

In this case, the physical states of the TLS correspond to different values of the external flux through the qubit loop. By writing $\phi_{Ext} = \phi_{Ext}^{(0)} + \delta\phi_{Ext}$, we find for the coupling operator

$$\hat{H}_{I,\phi} = v_\phi\,\hat{\phi}\,\left(\sin\theta_\phi\,\tau_z + \cos\theta_\phi\,\tau_x\right)\,, \tag{2.14}$$

with the coupling strength $v_\phi = E_L\,\delta\phi_{Ext}$.

The microscopic picture would be of a large magnetic moment somewhere on the surface of the superconducting wire of the qubit circuit. The TLS states would then be defined by the direction of the magnetic field induced by the supercurrent in the circuit. This model is motivated by the recent discoveries of large densities of free spins on the surfaces of metals and superconductors [46, 47].

In order to extract the necessary value of the magnetic moment, we assume the magnetic moment to be located on the surface of the current carrying wire in the phase qubit circuit. The magnetic field on the surface of a wire of radius R is given by

$$B_\parallel = \frac{\mu_0}{2\pi}\frac{I}{R}\,, \tag{2.15}$$

with the current I through the wire and the direction of the field parallel to the wire surface. The interaction energy of a magnetic moment μ in a magnetic field is

$$U = -\vec{\mu}\cdot\vec{B}\,, \tag{2.16}$$

so the energy difference for the two possible orientations of the moment (parallel and anti-parallel to the field) is given by

$$\delta E = 2\mu B\,. \tag{2.17}$$

A switching magnetic moment μ will induce a change in magnetic flux $\delta\Phi$ through a nearby ring. In order to calculate this change, we make use of Newton's third law. A change $\delta\Phi$ in the magnetic flux through the loop will induce an electromotive force due to Lenz' rule, which in turn gives a change in the energy of the electromagnetic field of

$$\delta E = I\delta\Phi\,, \tag{2.18}$$

where I is again the current through the circuit. We compare the two energies Eq. (2.17) and Eq. (2.18) and find the magnitude of the magnetic moment needed for a change in magnetic flux $\delta\Phi$ as

$$\mu = \frac{\pi R}{\mu_0}\delta\Phi\,, \tag{2.19}$$

where we can identify $\delta\Phi = \Phi_0/(2\pi)\,\delta\phi_{Ext}$.

Coupling via Charge n_G

The last possibility is the coupling of the state of the TLS to the electric field across the circuits Josephson junction. In this case the TLS would be formed as a microscopic dipole [44, 45] inside the dielectric of the junction. Again this can be associated with the tunneling of a single atom or group of atoms between two metastable positions in the standard tunneling model [19, 20].

We write the coupling Hamiltonian

$$\hat{H}_{I,q} = v_q\,\hat{q}\,\left(\sin\theta_q\,\tau_z + \cos\theta_q\,\tau_x\right)\,, \tag{2.20}$$

where the coupling strength v_q can now be connected to the dipole strength $d_\perp$ across the junction.

We can determine the dipole size from a semiclassical argument [45]. For this we identify the coupling strength v_q with the interaction energy of the dipole $\vec{d}$ in the electric field of the junction $\vec{E}$. The electric field is purely perpendicular to the junction surface and can be written as $E_\perp = V/x$, with the voltage V and the junction thickness x. We then find

$$v_q = \vec{d}\cdot\vec{E} = q\frac{d_\perp}{x}V\,, \tag{2.21}$$

where $d_\perp$ is the dipole size perpendicular to the junction and q is its charge. We now need to determine the strength of the electric field across the junction. For this we make a harmonic approximation of the qubit Hamiltonian

$$\hat{H}_q \approx \frac{\Phi^2}{2L} + \frac{Q^2}{2C}\,, \tag{2.22}$$

with the variables magnetic flux $\Phi = \Phi_0/(2\pi)\hat{\phi}$ and charge $Q = 2e\hat{q}$. We then assume

the qubit to be in the ground-state with the energy $1/2 \, \epsilon_{01} = 1/2\hbar\omega_0$ with $\omega_0 = 1/\sqrt{LC}$ and apply the equipartition theorem to get the average phase amplitude

$$\Phi = \sqrt{\frac{1}{2}\hbar\omega_0 L} = \sqrt{\frac{\hbar}{2C\omega_0}} \, . \tag{2.23}$$

The phase Φ in the ground-state will be oscillating with the frequency ω_0. We make use of the second Josephson relation $\dot{\Phi} = V$ to get the voltage across the junction

$$V = \omega_0 \Phi = \sqrt{\frac{\hbar\omega_0}{2C}} \tag{2.24}$$

where we alrady used Eq. (2.23). Plugging Eq. (2.24) into Eq. (2.21) we finally get

$$v_q = n_q \frac{d_\perp}{x} \sqrt{E_C \, \epsilon_{01}} \, , \tag{2.25}$$

with the dipole charge in units of cooper pairs $n_q = q/2e$ and the circuits charging energy E_C as defined above. Using this equation we can extract the fractional dipole size $d_\perp/x$.

The coupling operator $\hat{q}$ has a special role in these equations. For a harmonic system, $E_J = 0$, all three operators $\hat{\phi}$, $\cos\hat{\phi}$ and $\hat{q}$ would be purely transversal in the eigenbasis of the Hamiltonian Eq. (2.3). Due to the anharmonicity $\propto E_J$, the operator $\hat{\phi}$ and therefore also $\cos\hat{\phi}$ acquire longitudinal corrections $\propto \hat{a}^\dagger\hat{a}$ in the qubits eigenbasis. The operator $\hat{q}$ on the other hand, always stays purely transversal, inducing transitions in the systems without any associated energy shift. Physically this is easy to understand. Since the electric field across the junctions is proportional to $\hat{q}$, a longitudinal component in $\hat{q}$ would correspond to different values of average electric field across the junction in the different qubit states. Since the junction is shunted by a superconducting loop, such an average voltage cannot be present.

2.2. Defect Spectroscopy

In this section we show the results from a spectroscopy experiment on a phase qubit circuit coupled strongly to a TLS [33]. The experiment was performed in the group of Alexey Ustinov at KIT and we were asked to help in interpretation of the data. In this experiment a relatively high incident microwave power was used and multi-photon effects could be observed. We show results from theoretical calculations using Floquet theory to account for the strong driving and and a Lindblad-type master equation to treat decoherence. This theoretical description enables us to identify the relevant states of the coupled system involved in the dynamics. Using this knowledge, we motivate how we can use the experimental data to learn about the detailed form of the interaction between qubit circuit and TLS.

In a spectroscopy experiment, one probes the steady state of the system under

driving. The goal is to map out the states of the system at different bias points. For a phase qubit, the external bias is given by the external flux Φ_{Ext} through the qubit loop. One then applies a microwave pulse via the voltage port for a sufficiently long time $t \gg \gamma$, so that all transient phenomena have decayed. γ represents here all relevant decoherence rates in the system. The state of the qubit is then measured as a function of microwave frequency and flux bias. If the applied driving is resonant with a transition in the system, the steady state will be a superposition of initial and final state. If at least one of the two states is visible in the measurement channel, spectroscopy will give a signal.

A word is in order here concerning the measurement in a phase qubit circuit. In the parameter regime of interest, the circuits potential consists of two wells, one of which is very shallow. Operation of the circuit takes place in this anharmonic shallow well, containing normally of the order of five to ten energy levels [48]. The two lowest energy states in this well form a macroscopic two-level system (our qubit). In order to readout the state of the qubit, the potential barrier between the two wells is lowered to allow the excited states of the shallow well to tunnel into the deeper well. States in the two wells differ by a large amount of persistent current through the loop, which can be detected by measuring the switching current of a measurement SQUID located on the same chip. Such a measurement thus distinguishes between the ground state and all other, excited states of the qubit circuit and yields the overall excitation probability for the qubit or the probability not to be in the ground state.

When considering a phase qubit which is weakly driven and/or weakly coupled to a TLS, it is common to model the qubit circuit as a two-level system and to use the rotating-wave-approximation. For the experiment described here, neither of the above approximations are valid and one must use a formalism which takes into account an arbitrary number of qubit states as well as multi-photon processes. This allows us to describe the experiment over a wide parameter range without knowing which effects are important *a priori*. Several techniques exist for treating a driving field when the perturbation is no longer "weak" [66–68]. We employ a numerical expansion in the Floquet basis [57, 69] as this allows us to include arbitrary multi-photon processes together with decoherence (cf. Sec. 1.3). The inclusion of higher lying states in the qubit can be achieved via direct diagonalization of the exact qubit potential in Eq. (2.3), or by using an anharmonic approximation [34, 48].

In the parameter regime explored in the experiment, it is sufficient to describe the qubit using only the lowest three energy levels. The TLS energy splitting ϵ_f is obtained from the spectroscopic data. For the purpose of describing the experiment, we write the coupling term between qubit and TLS as $v_\perp \hat{q} \cdot \hat{\tau}_x$, where the operator $\hat{q}$ is proportional to the charge and therefore the electric field across the qubit circuit's Josephson junction. The operator $\hat{\tau}_x$ is the Pauli matrix in x-direction acting on the two-level system, inducing transitions of the state of the TLS. We use this type of coupling here since the charge operator $\hat{q}$ has no longitudinal components and therefore the above coupling term is purely transversal. Transversal coupling is the minimal requirement in order to explain the experimental findings of anti-crossings

at certain frequencies. Later we will give a detailed analysis of the type of coupling present in the system, we first want to show the general features here.
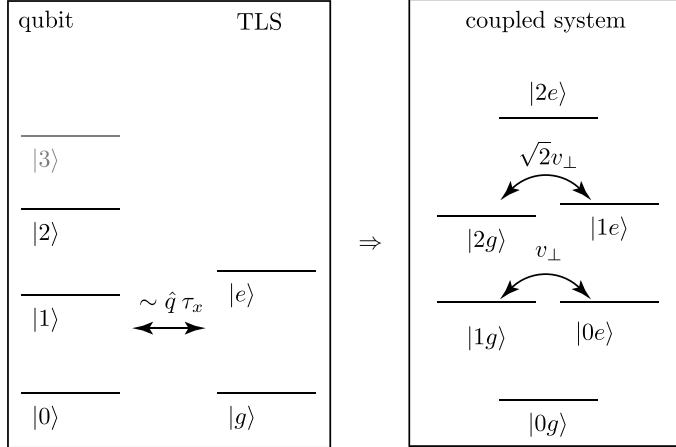
Figure 2.1.: *Illustration of the level structure of the coupled system of three-level phase qubit circuit and two-level defect. The coupling is chosen to be purely transversal $\propto v_\perp \hat{q} \, \tau_x$. Due to the properties of the operator $\hat{q} \sim \mathrm{i}\left(\hat{a}^\dagger - \hat{a}\right)$, the coupling between the higher levels $|1e\rangle$ and $|2g\rangle$ acquires the factor $\sqrt{2}$.*

The full Hamiltonian is then given by

$$\hat{H} = \epsilon_{01} \left|1\right\rangle \left\langle 1\right| + \left(\epsilon_{01} + \epsilon_{12}\right) \left|2\right\rangle \left\langle 2\right| + \frac{1}{2}\epsilon_f \tau_z + \frac{1}{2}v_\perp \, \hat{q} \cdot \tau_x \,. \tag{2.26}$$

The charge operator $\hat{q}$ can be written in the harmonic oscillator basis as $\propto \mathrm{i}(\hat{a}^\dagger - \hat{a})$, where $\hat{a}$, $\hat{a}^\dagger$ are the usual annihilation and creation operators. In the exact qubit eigenbasis $|n\rangle$, used to write down Eq. (2.26), this operator will acquire corrections of the form $|n\rangle \langle n+2|$. To obtain the energy splittings ϵ_{01} and ϵ_{12} in this basis, we solve for the eigenstates and eigenvalues of the Hamiltonian numerically using the exact potential of the phase qubit circuit. The state of the TLS is described by its ground state $|g\rangle$ and excited state $|e\rangle$. The energies are defined relative to the energy of the ground state of the coupled qubit-TLS system $|0g\rangle$. Fig. 2.1 gives an illustration of the level structure of the Hamiltonian Eq. (2.26).

The system is coupled to an external microwave drive at frequency ω_d with the coupling Hamiltonian

$$\hat{H}_I = \frac{1}{2}V_q \, \hat{q} \cos \omega_d t \,, \tag{2.27}$$

where the coupling constant V_q is proportional to the microwave amplitude and we define the generalized n-photon Rabi frequency $\Omega_q^{(n)} \propto V_q^n$ on resonance.

To describe the effects of decoherence in the system, we use a simple Lindblad model [53, 54], with relaxation and dephasing rates taken from independent measurements of both qubit and TLS (cf. Sec.1.2.3). The dynamical equations for the

reduced density matrix ρ of the system (consisting of qubit and TLS) are given by

$$\dot{\rho} = i\left[\rho, \hat{H}\right] + \sum_n \Gamma_n \left(L_n \rho L_n^\dagger - \frac{1}{2}\left\{L_n L_n^\dagger, \rho\right\}\right) \tag{2.28}$$

where the sum is over all possible channels of decoherence with the respective rates Γ_j. The L_n are the operators corresponding to each decoherence channel, e.g., pure dephasing of the qubit is described by the number operator $\hat{a}^\dagger \hat{a}$ while relaxation of the qubit is described by the annihilation operator $\hat{a}$. The term in Eq. (2.28) responsible for relaxation acting on the qubit is then given by

$$\Gamma_\downarrow \left(\hat{a}\rho\hat{a}^\dagger - \frac{1}{2}\hat{a}\hat{a}^\dagger \rho - \frac{1}{2}\rho\hat{a}\hat{a}^\dagger\right) , \tag{2.29}$$

where the rate $\Gamma_\downarrow$ can be calculated using e.g., the Golden Rule Eq. (1.19). This formalism in principle enables us to include an arbitrary number of qubit levels without changing the structure of the theory.

The experiments in the group of Alexey Ustinov were performed with a phase qubit circuit which has a critical current of $I_C \approx 1.1$ μA, a capacitance of $C = 850$ fF and an inductance of $L = 720$ pH. The qubit circuit is biased such that the frequency of its lowest lying transition is close to the resonance frequency of a particular TLS. The studied TLS has a level splitting of $\epsilon_f/2\pi \approx 7.845$ GHz and is coupled to the qubit with a transversal coupling strength $v_\perp/2\pi \approx 21$ MHz. We use the above values in the modeling of the spectroscopy experiment, later we will give more exact values obtained from the fitting. In the full numerical model of the system, we use the values of $T_1^{(q)} = 120$ ns and $T_1^{(f)} = 715$ ns for the relaxation rates of the qubit and TLS, respectively. Dephasing rates , determined from Ramsey fringes, are found to be $T_2^{(q)} = 90$ ns for the qubit and $T_2^{(f)} = 110$ ns for the TLS.

2.2.1. Two-Photon Spectroscopy of a Four-Level System

We initially present results from driving the qubit with a relatively low microwave power (Fig. 2.2), corresponding to a qubit Rabi-frequency of $\Omega_q^{(1)}/2\pi \approx 4$ MHz and focusing on the range near resonance $\epsilon_{01} \approx \epsilon_f$. In this parameter regime, it is sufficient to approximate the qubit circuit by a two-level system and we can write the Hamiltonian

$$\hat{H} \approx \frac{1}{2}\epsilon_{01}\sigma_z + \frac{1}{2}\epsilon_f\tau_z + \frac{1}{2}v_\perp\sigma_y\tau_x \tag{2.30}$$

with Pauli matrices for the qubit σ and for the TLS τ. A sketch of the level structure at resonance including the relevant transitions is shown in the inset of Fig. 2.2. Here we define the hybridized eigenstates $|1-\rangle = \cos(\xi/2)|0e\rangle - \sin(\xi/2)|1g\rangle$ and $|1+\rangle = \sin(\xi/2)|0e\rangle + \cos(\xi/2)|1g\rangle$, where $\tan\xi = v_\perp/(\epsilon_{01} - \epsilon_f)$ varies with flux bias. The coupling term $\hat{\sigma}_y\hat{\tau}_x$ is formally equivalent to the previously described transversal coupling since in the two-level basis of the qubit circuit we have $\hat{q} = \sigma_y$.
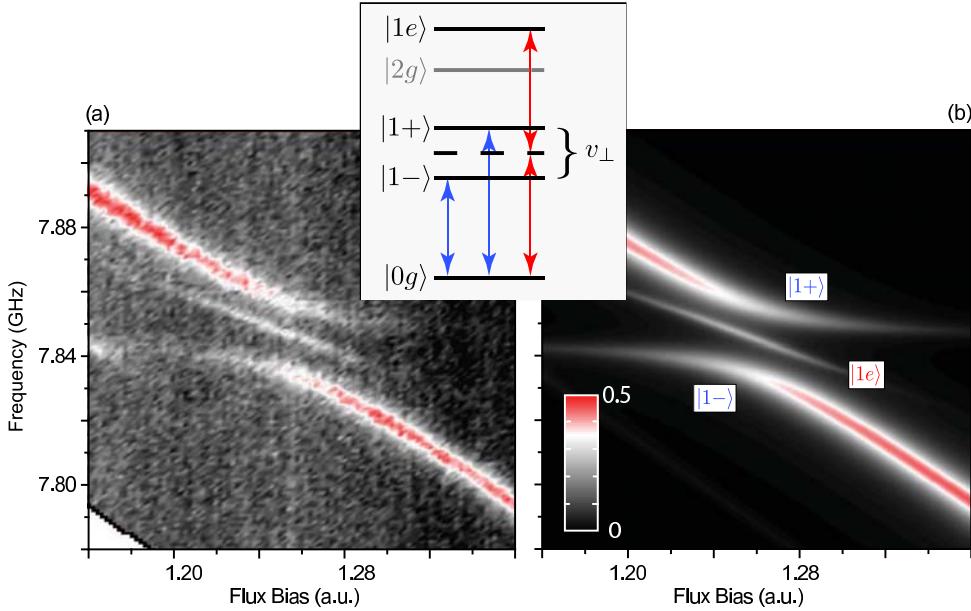
Figure 2.2.: *Experimental **(a)** and theoretical **(b)** spectroscopic scans as a function of flux bias and drive frequency, showing both the anti-crossing due to single-photon transitions and the resonance line associated with the weaker two-photon transition. The color-scale indicates the probability to find the qubit not in the ground state. We use the same color-scale for both plots. **Inset:** Energy level structure of the qubit/TLS system in resonance $\epsilon_{01} = \epsilon_f$ including the hybridized states $|1\pm\rangle$, which are split by the coupling $v_\perp$. As well as the usual single-photon transitions (between $|0g\rangle$ and $|1\pm\rangle$, indicated by blue arrows), a two-photon transition is allowed between the states $|1e\rangle$ and $|0g\rangle$ (red arrows).*

The experimental data in Fig. 2.2 (a) shows a characteristic level anti-crossing associated with the qubit-TLS resonance, $\epsilon_{01} \approx \epsilon_f$, with coupling strength $v_\perp/2\pi = 21$ MHz. An additional spectroscopic line can be seen in the middle of the qubit-TLS anti-crossing. We identify this line as a two-photon transition from the ground-state $|0g\rangle$ to the excited state $|1e\rangle$, indicated by red arrows in the inset of Fig. 2.2.

In Fig. 2.2 (b) we show the result of a theoretical treatment of the system, calculating the time dependence of the system's density matrix including decoherence. System parameters are taken from the measurements as described above. As can be seen, the numerics reproduce the experimental data with high accuracy.

The position of the two-photon line in the middle of the anti-crossing gives a first indication about the strength of a possible longitudinal coupling $\sim \hat{\sigma}_z\hat{\tau}_z$ between qubit and TLS. Fig. 2.3 gives an indication how a purely longitudinal coupling term in the Hamiltonian Eq. (2.30) would change the level structure. Such a coupling would shift the states with an even number of excitation (i.e., $|0g\rangle$ and $|1e\rangle$) in one direction, while the states with an odd number of excitation (i.e., the states
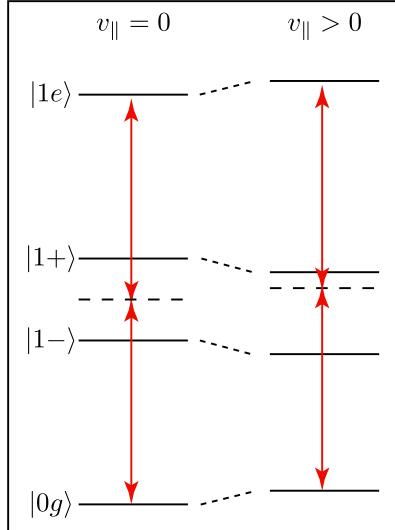
Figure 2.3.: *Illustration of the effect of a purely longitudinal coupling term $\propto v_{\parallel}\,\sigma_z\tau_z$ on the spectrum of the coupled system for exact resonance $\epsilon_{01} = \epsilon_f$. For $v_{\parallel} = 0$ we have the situation depicted also in Fig. 2.2, where the two-photon $|0g\rangle \leftrightarrow |1e\rangle$ transition is exactly in the middle of the first order anti-crossing. For $v_{\parallel} \neq 0$ on the other hand, all states with an even number of excitation ($|0g\rangle$ and $|1e\rangle$ in this illustration) are shifted in energy in one direction, while the states with an odd number of excitations (these are the states $|1\pm\rangle$ here) are shifted in the other direction. The two-photon $|0g\rangle \leftrightarrow |1e\rangle$ transitions is then shifted away from the middle of the anti-crossing.*

$|1\pm\rangle$) would be shifted in the other direction. Due to the lack of a zero energy standard, this effect could not be distinguished if only one-photon transitions are permitted. But it will shift the position of a two-photon $|0g\rangle \leftrightarrow |1e\rangle$ transition relative to the first order anti-crossing. Through the presence of the two-photon line near the middle of the anti-crossing, we can thus conclude (i) the TLS is a two-level or at least strongly anharmonic system and (ii) longitudinal coupling between qubit circuit and TLS is small in our system. Exactly how small a possible longitudinal coupling is and what this means for the microscopic origin of the coupling, will be clarified in the next section.

Very similar features have been observed in a related system, namely a superconducting flux qubit [31], which suggests that these strongly coupled TLS have the same origin in both flux and phase qubits, even though the degrees of freedom being manipulated are different. Additional evidence against the TLS being an harmonic object (as would result from an ensemble of two-level systems forming an effective TLS [38], Sec. 4.3, for example) is provided by experiments trying to pump two excitations resonantly into the TLS [70, 71], similar to the protocol used in Ref. [34].

## 2.2.2. Two-Photon Spectroscopy at Strong Excitation
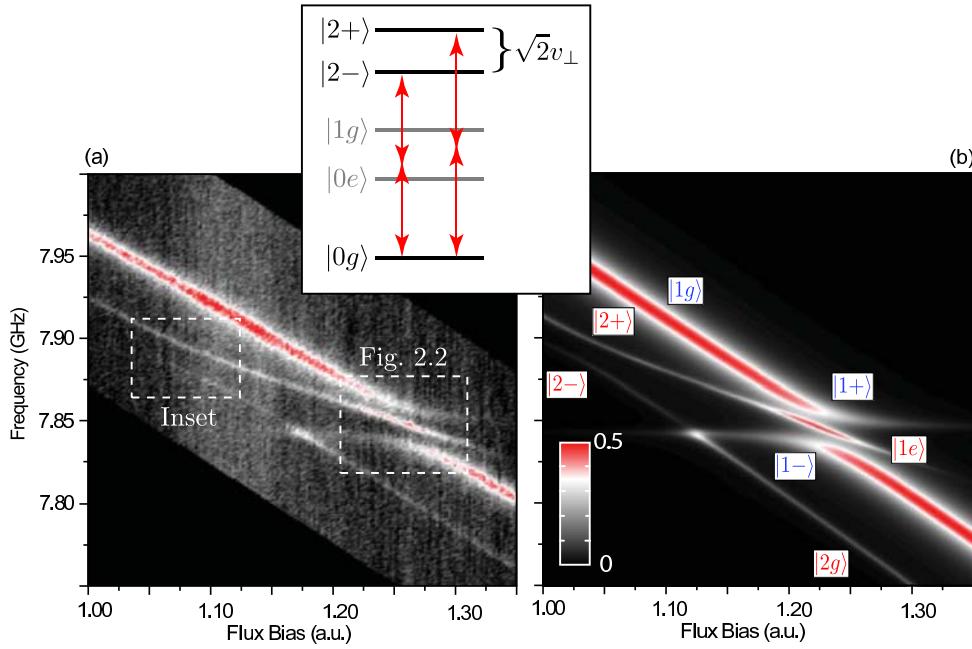
Figure 2.4.: *At higher microwave powers and over a wider region of parameter space, processes involving higher lying states of the qubit become important. We again show experimental **(a)** and theoretical **(b)** spectroscopic scan as a function of flux bias, showing both the transitions to the hybridized states $|1\pm\rangle$ (as per Fig. 2.2) and the states $|2\pm\rangle$. The color-scale is the same for both graphs. **Inset:** Level structure including higher lying states of the qubit including further hybridized states which can be excited via a two-photon process, as indicated.*

In addition to the structure around the qubit-TLS anti-crossing, at higher power $(\Omega_q^{(1)}/2\pi \approx 7 \text{ MHz})$ we find additional features at lower flux bias, shown in Fig. 2.4. We observe a weaker line running parallel to the single-photon qubit transition, showing an additional anti-crossing with the $|0g\rangle \leftrightarrow |1e\rangle$ line, indicated by the lefthand dashed box on the figure. From their power dependence, both these lines can be identified as two-photon transitions.

To explain the spectral features of Fig. 2.4 (a), it is now essential to include the third level of the qubit circuit in the treatment. A sketch of the level structure around this second anti-crossing is again shown in the inset of Fig. 2.4. Possible transitions are indicated by arrows. Due to the anharmonicity in the qubit circuit, the transition between the levels $|1\rangle \leftrightarrow |2\rangle$ is detuned from the qubit transition $|0\rangle \leftrightarrow |1\rangle$ by the amount $\Delta = \epsilon_{12} - \epsilon_{01} < 0$. At the chosen range of flux bias, our circuit has an anharmonicity $|\Delta| \sim 100$ MHz. We therefore identify this weaker, parallel line as the two-photon $|0g\rangle \leftrightarrow |2g\rangle$ transition, detuned from the first transition line by the amount $|\Delta|/2 \sim 50$ MHz due to its two-photon nature. The anti-crossing in the left

dashed box is due to the coupling between qubit and TLS $\sim \hat{q} \cdot \hat{\tau}_x$, which hybridizes the states $|1e\rangle$ and $|2g\rangle$. The coupling strength is increased by a factor $\sqrt{2}$ due to the properties of the momentum operator and the magnitude of the anti-crossing is given by $\sqrt{2}v_\perp/2 \approx 15$ MHz (where the additional factor of two results from the two-photon process). Fig. 2.4 (b) shows the result of a numerical calculation. The theory is in very good agreement with the experimental data over all parameter regimes.
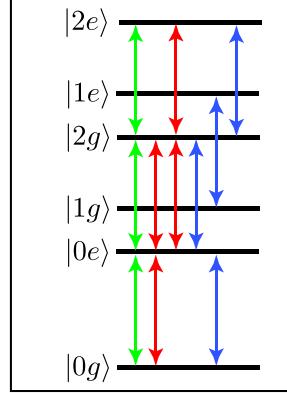

Figure 2.5.: *Level structure of the coupled system at the point of high symmetry $\epsilon_f = 1/2\epsilon_{02} = \omega_D$. The driving frequency is resonant to induce one-photon (blue), two-photon (red) and three-photon transitions (green) at this point.*

An additional feature can be identified in the spectroscopic scan of Fig. 2.4 (a) at a flux bias of ~ 1.175 and microwave frequency resonant with the TLF $\omega_d \approx \epsilon_f \approx \frac{1}{2}\epsilon_{02}$. Here, the two-photon $|0g\rangle \leftrightarrow |2g\rangle$ line crosses the one photon $|0g\rangle \leftrightarrow |0e\rangle$ transition. This is an area of high symmetry in the spectrum as is illustrated in Fig. 2.5, resulting in strongly enhanced absorption. The asymmetric nature of this effect is well reproduced by the numerics (Fig. 2.4 (b)).

2.2.3. Single-Photon Spectroscopy of Higher States

As a further confirmation that the left anti-crossing of Fig. 2.4 indeed represents the coupling between the states $|1e\rangle$ and $|2g\rangle$, we probed these higher lying states directly with a single-photon transition. The experimental results are presented in Fig. 2.6 (a) where one can clearly see the anti-crossing at doubled resonance frequency ~ 15.7 GHz with a magnitude now of $\sqrt{2}v_\perp \sim 30$ MHz. When approximating the shallow well using the third order anharmonic oscillator potential [48], the transition $|0\rangle \leftrightarrow |2\rangle$ is forbidden. However, when treating the anharmonicity exactly, there is a finite matrix element in the momentum operator $\hat{q}$ corresponding to this transition. Fig. 2.6 (b) shows the results of a theoretical calculation and the inset gives a sketch of the level structure including the transitions induced by the microwave drive.
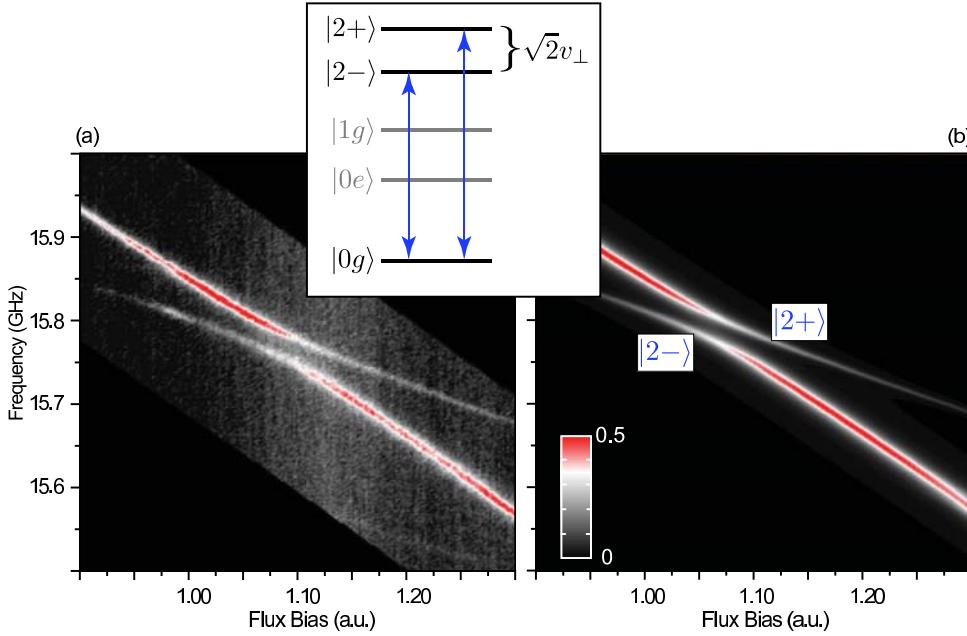
Figure 2.6.: *Using higher frequency excitations, the hybridized states $|2\pm\rangle$ can be directly excited via a one-photon process. Experimental **(a)** and theoretical **(b)** spectrum showing the clear anti-crossing due to the $|0g\rangle \leftrightarrow |2\pm\rangle$ transition. The color-scale is the same for both graphs. **(Inset)** The corresponding energy level diagram shows this direct transition which is typically ignored within the usual simplified models of such a system.*

2.3. Evaluation of Defect Models

In this section we present a detailed evaluation of the spectroscopic data shown previously, with the goal of understanding the microscopic nature of the TLS. As we have seen in Sec. 2.1.2 coupling between qubit and TLS can be mediated by three different kinds of interaction. Therefore we will perform a high-precision fit of the spectroscopic data to the three different theoretical models. From this fit we will extract model parameters describing the microscopics of the interaction between the defect state and the qubit circuit. This will finally allow us to place bounds on the validity of the individual defect models [39].

We first introduce the theoretical model and identify the parameters of the fit, before we shortly explain the procedure. In the second part we show the results of the fitting for two different TLS on the same qubit chip. For each of the possible models introduced in Sec. 2.1.2 we will give the value of relevant parameters and discuss the models applicability.
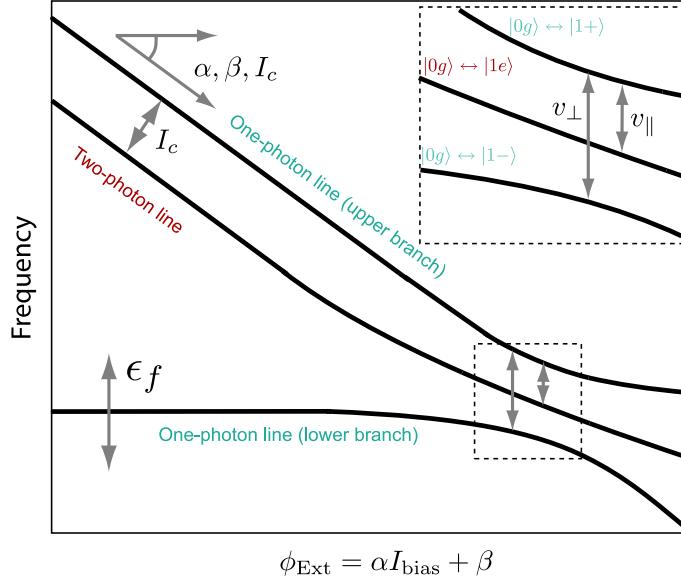
Figure 2.7.: *Anatomy of a qubit-TLS anti-crossing in the high power regime. The overall slope of the spectral lines, their position and the spacing between one- and two-photon features allows us to calibrate the system, even for several independent fitting parameters (see text). The separation and asymmetry of the lines, within the anti-crossing itself, allows us to estimate the transverse and longitudinal components of the coupling operator, respectively. The arrows indicate the influence of each of the fitting parameters on the form of the spectrum. Since they are largely independent, we can perform a simultaneous fit to a model containing all six of them.*

2.3.1. Fitting Model

We start by identifying the relevant fitting parameters of the microscopic models. The system is described by the total Hamiltonian Eq. (2.1). For the qubit part we take again the full qubit Hamiltonian Eq. (2.3), characterized by the three energy scales of charging energy $E_C = e^2/(2C)$, inductive energy $E_L = 1/(2L) (\Phi_0/2\pi)^2$ and Josephson energy $E_J = I_C \Phi_0/(2\pi)$. The capacitance C and inductance L of the circuit are defined by the circuit design and are not expected to change over time. The critical current I_C on the other hand, is a property of the amorphous insulating layer in the Josephson junction. It is know to degrade over time and we will use it as a fitting parameter in the model. The external flux Φ_{Ext} is generated via a flux coil on chip. In experiment only the bias current applied to the coil is measured with no way of directly determining the flux through the loop We here assume a linear flux-current relation of the form $\Phi_{Ext} = \alpha I_{\text{bias}} + \beta$, with the fabrication dependent parameters α and β. The TLS is described as a generic two-level system by Eq. (2.2) with the level splitting ϵ_f.

As discussed in Sec. 2.1.2, the coupling between qubit and TLS can be mediated by These three situations are described by the generic coupling Hamiltonians (cf.

Eq. (2.4)),

$$H_I = v \, \hat{o} \left(\cos \theta \, \tau_x + \sin \theta \, \tau_z \right) \tag{2.31}$$

where $\hat{o} = \hat{q}$, $\hat{\phi}$ or $\cos \hat{\phi}$ depending on the nature of the coupling and v parameterize its strength. The angle $\theta \in [0, \pi]$ finally gives additional information on the states of the TLS in a particular microscopic model.

In order to compare the various coupling models later, we define the transverse $v_\perp$ and longitudinal $v_\parallel$ coupling in the qubit $\{|0\rangle, |1\rangle\}$ basis as

$$\begin{aligned} 2\, v_\perp &= v \cos \theta \left(\langle 1| \, \hat{o} \, |0\rangle + \langle 0| \, \hat{o} \, |1\rangle \right) , \\ 2\, v_\parallel &= v \sin \theta \left(\langle 1| \, \hat{o} \, |1\rangle - \langle 0| \, \hat{o} \, |0\rangle \right) , \end{aligned} \tag{2.32}$$

where the qubit component of the coupling term $\hat{o}$ is defined as in Eq. (2.31).

Our theoretical model, Eq. (2.1), is described by a total of six independent parameters. Three parameters describe the qubit circuit and its tuning via the external flux: the critical current I_c of the qubits Josephson junction and the parameters α and β describing the local generation of flux on chip and its coupling to the qubit loop. The TLS is described by its level splitting ϵ_f and the interaction between qubit and TLS via v and θ. Fig. 2.7 shows an illustration of the spectrum of the model and the influences of the different parameters. Since their effects on the spectrum, as indicated by arrows in Fig. 2.7, are all largely independent, this allows us to perform a fit to all six parameters simultaneously.

For the circuit capacitance C and inductance L we take the design values of $C = 850$ fF and $L = 720$ pH. To account for fabrication variation, we repeated the fitting procedure with a $\pm 5\%$ tolerance in both L and C, resulting in no significant variation in the TLS parameter estimates (although I_c, α and β vary accordingly).

To shed light on the nature of the interaction between qubit and two-level defect, we need to determine the values of v and θ in Eq. (2.31). To this end, take the data from a series of spectroscopy experiments on a superconducting phase qubit strongly coupled to a TLS, at varying microwave power [33], cf. Fig. 2.2 and Fig. 2.4. Performing spectroscopy at both low- and high-power allows us to use a combination of single- and two-photon transitions to obtain spectral lines which are sensitive to the nature of the qubit-TLS coupling. Additionally we use date from 'swap-spectroscopy', where an additional swap between qubit and TLS is performed before readout, effectively measuring the state of the TLS.

We prepare the experimental data by extracting the frequencies of the various transitions. To this end we fit each spectroscopic trace with Lorentzian functions and take the center frequency as frequency of a certain transition. We then numerically diagonalize our model, Eq. (2.1), using the six independent parameters detailed above and fit these results to the experimental data.

It is important to note that, since we are limited here to spectroscopic data, the results presented here are only sensitive to purely transversal $\propto \sigma_x \tau_x$ and purely longitudinal $\propto \sigma_z \tau_z$ coupling terms. Mixed terms $\propto \sigma_z \tau_x$ or $\propto \sigma_x \tau_z$ are not visible

in the steady state of the system but would only show in experiments probing the systems dynamics.

2.3.2. Parameters of Defect Models

Here we give the results for the fitting procedure and discuss them in light of the different microscopic models. We used data in spectroscopy of two different TLS located in the vicinity and interacting with the same phase qubit circuit. For one of them (called TLS1 in the following) the amount of data available was higher, resulting in lower uncertainties of the fitting results.
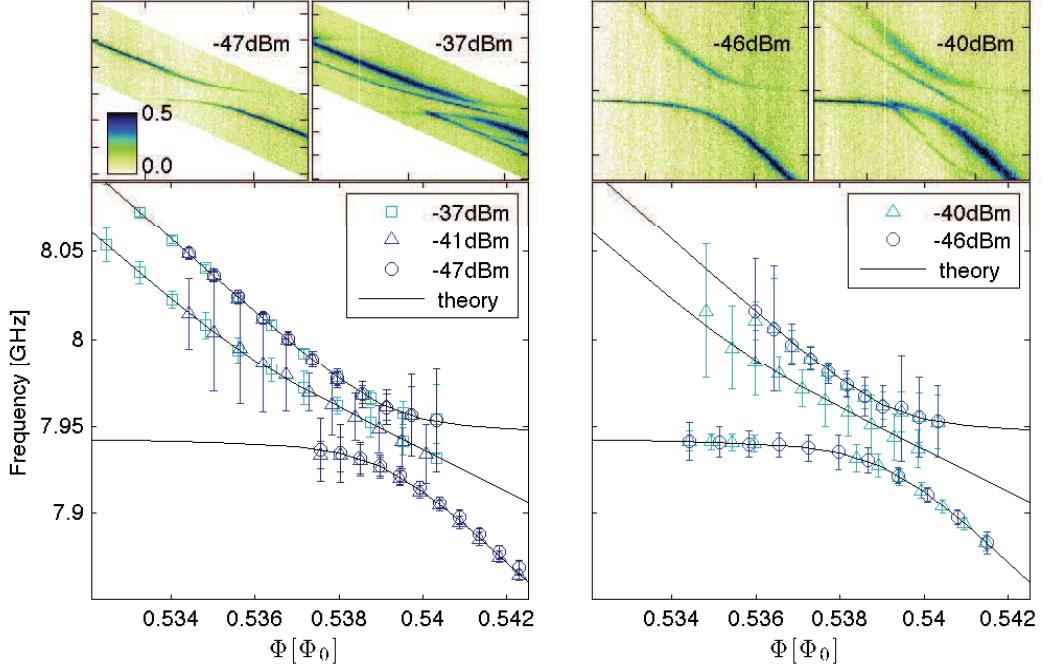
Figure 2.8.: *Peak positions obtained for **(a)** qubit spectroscopy and **(b)** swap spectroscopy. For clarity, only 10% of the dataset is shown. The error bars give the 1-σ confidence interval for the fitted peak positions. The theoretical curves show the relevant transition frequencies for the coupled qubit-TLS system obtained via fitting the extracted peak positions (see text). Inserts show examples of the (normalized) escape probability as a function of excitation frequency and bias flux, from which the peak positions are extracted.*

Fig. 2.8 shows fitting results and original spectroscopy pictures for TLS1. On the left side we see results from standard spectroscopy, measuring the steady state of the qubit under driving. Upper panels show the real spectroscopy data, from which the transitions peak positions were extracted. Data points in the lower panel show these peak positions together with their $1 - \sigma$ confidence interval. Only 10% of the

TLS1	ϵ_f	$v_\perp$	$v_\parallel$	χ_r^2
$H_{I,c}$	7944.38 ± 0.08	35.52 ± 0.13	0.27 ± 0.12	0.997
$H_{I,\phi}$	7944.41 ± 0.08	35.55 ± 0.09	0.23 ± 0.12	0.997
$H_{I,q}$	7944.49 ± 0.08	35.65 ± 0.08	$----$	0.998
TLS2	ϵ_f	$v_\perp$	$v_\parallel$	χ_r^2
$H_{I,c}$	7734.4 ± 0.3	23.3 ± 0.2	0.5 ± 0.2	0.992
$H_{I,\phi}$	7734.5 ± 0.2	23.3 ± 0.2	0.5 ± 0.2	0.992
$H_{I,q}$	7734.0 ± 0.2	23.2 ± 0.2	$----$	0.994

Table 2.1.: *Estimates for the TLS resonance frequency and qubit-TLS coupling which were obtained from the fitting procedure, including 1-σ uncertainties. The parameters for two different TLSs on the same chip are shown and all values are in MHz. The reduced χ^2 value is also given for each fit, showing good convergence with minimal over-fitting.*

dataset is shown here. The lines are from the theoretical model using the parameters obtained from the fitting. The right side shows the same but for swap-spectroscopy, where effectively the state of the TLS is measured [34, 35].

Tab. 2.1 shows the fitting results for the two TLS under consideration. For each TLS we give its level splitting ϵ_f, and transversal $v_\perp$ and longitudinal $v_\parallel$ coupling strength as defined above, and we provide the values for each of the three coupling models described in Sec. 2.1.2. Since the momentum operator $\hat{q}$ has no longitudinal components, we do not have any information on longitudinal coupling in this case. We will now discuss these results in the light of several existing models describing the microscopic origin of such TLSs.

For this we will calculate parameters values, describing the microscopics in a particular picture. When using numerical values which have an associated uncertainty, we always assume linear error regression. This means, that given a function $f = f(\{\lambda_n\})$ of a set of parameters $\{\lambda_n\}$, the total error of this function is given by

$$\delta f = \sum_n \delta\lambda_n \frac{\partial f}{\partial \lambda_n} \,, \tag{2.33}$$

with the error $\delta\lambda_n$ of the parameter λ_n. Details of the calculations with each step written explicitly can be found in App. B

Critical Current Variation δI_C

For a TLS changing the transparency of the junction along the lines of Ref. [41] we obtain estimates for the change in critical current δI_c:

$$\delta I_{c,1} = 693 \pm 5 \text{ pA}\,, \qquad \delta I_{c,2} = 447 \pm 7 \text{ pA}\,, \tag{2.34}$$

where the subscript 1/2 denotes results for TLS1 / TLS2, respectively. The total critical current is obtained from our fitting procedure

$$I_{c,1} = 984 \pm 2 \text{ nA}\,, \qquad I_{c,2} = 976 \pm 1 \text{ nA}\,. \tag{2.35}$$

The change in critical current is therefore of the order of 0.1%, well within reasonable bounds. The angle θ_c for this coupling can be found as

$$\tan \theta_{c,1} = 0.04 \pm 0.02\,, \qquad \tan \theta_{c,2} = 0.12 \pm 0.05 \tag{2.36}$$

Using these estimates for the angle θ we can place further constraints on the physical states of the microscopic model (cf. Sec. 2.1.2). Using the above estimates yields

$$\epsilon_{0,1} = 0.34 \pm 0.16 \text{ GHz}\,, \qquad \Delta_{0,1} = 7.937 \pm 0.007 \text{ GHz}\,,$$
$$\epsilon_{0,2} = 0.97 \pm 0.38 \text{ GHz}\,, \qquad \Delta_{0,2} = 7.89 \pm 0.05 \text{ GHz}\,. \tag{2.37}$$

giving two nearly degenerate states coupled by a large tunneling element for both TLS. We can therefore conclude that for a TLS modulating the junction transparency and via this the critical current of the circuit, that the physical states of such a defect have to be nearly degenerate to account for the data.

Alternatively, the model of de Sousa et al. [43] assumes an impurity level in the junction which, via hybridization with the Cooper-pairs in the superconductor, forms an Andreev bound state with energy inside the gap.

For the same values of $v_\perp$ and $v_\parallel$ used before, we here get a change in critical current of

$$\delta I_{c,1} \leq 1.46 \pm 0.01 \text{ nA}\,, \qquad \delta I_{c,2} \leq 0.94 \pm 0.01 \text{ nA}\,. \tag{2.38}$$

Here we can only give bounds on the values of δI_C since the equations describing the models have multiple solutions. We show here the values with the largest magnitude. For details on the solutions, we refer the reader to App. B. We can also calculate the impurity level energy ϵ_d as

$$\epsilon_{d,1} \leq 101.6 \pm 46.5 \text{ MHz}\,, \qquad \epsilon_{d,2} \leq 278.4 \pm 109.6 \text{ MHz}\,, \tag{2.39}$$

very close to the Fermi edge. Such a small impurity energy is a consequence of the small longitudinal coupling, $\theta_c \approx 0$. Again we can conclude that this parameters are acceptable within the microscopic model, but they place strong constraints on the realization in the observed defects.

Magnetic Flux Change $\delta\Phi_{Ext}$

If the state of the TLS modulates the value of the magnetic flux threading the superconducting loop, we can extract the change of magnetic flux $\delta\Phi_{Ext}$ from the coupling strength v_ϕ. We get

$$\delta\phi_{Ext,1} = 232.5 \pm 1.2\mu\Phi_0 \,, \qquad \delta\phi_{Ext,2} = 151.5 \pm 2.5\mu\Phi_0 \,, \tag{2.40}$$

in units of the flux quantum Φ_0. For the TLS orientation angle θ_ϕ we calculate

$$\tan\theta_{\phi,1} = 0.04 \pm 0.02 \,, \qquad \tan\theta_{\phi,2} = 0.14 \pm 0.06 \,, \tag{2.41}$$

which gives similar results for the TLS physical states as we have seen before (cf. Eq. (2.37)), i.e. strongly degenerate states dominated by the tunneling element.

Assuming the fluctuations in the external flux result from a magnetic moment μ on the surface of the superconducting loop of wire-thickness $R \propto 1 \ \mu$m, we get

$$\mu_1 = 129700 \pm \ \ 700 \, \mu_B \,, \qquad \mu_2 = \ \ 84500 \pm 1400 \, \mu_B \,, \tag{2.42}$$

in units of the electron magnetic moment μ_B.

No physical microscopic system is known to us which would spontaneously generate such a strong magnetic moment. We can therefore exclude the possibility that the coherent TLS observed in qubit spectroscopy are of magnetic nature.

Electric Dipole d

Analogous to our description in Sec. 2.1.2, we calculate the fractional size d of the aligned dipole moment in the direction of the electric field as

$$d/x = v_\perp\sqrt{\frac{2C}{e^2\epsilon_{01}}} \,, \tag{2.43}$$

where x ist the thickness of the junction, C its capacitance and e the electron charge. Here we already assumed the dipole to have a charge of $q = e$, i.e. $n_q = 1$. The qubit level splitting ϵ_{01} is taken in resonance with the TLS ($\epsilon_{01} = \epsilon_f$) and $v_\perp$ is the transversal coupling strength from the fitting.

For the two TLSs under consideration we obtain

$$d_1/x = 0.0837 \pm 0.0002 \,, \qquad d_2/x = 0.0551 \pm 0.0004 \,, \tag{2.44}$$

For a junction thickness x of $\propto$ nm, this results in an aligned dipole-size of the order of atomic distances, as would be expected for tunneling systems in amorphous materials.

Since the momentum operator $\hat{q}$ has no diagonal component, such a dipole interaction would not lead to any longitudinal component $\propto \sigma_z\tau_z$ in the coupling operator. Spectroscopy therefore provides no direct measure of the orientation θ_q of

the charge-dipole and we cannot give a value of the longitudinal coupling strength $v_\parallel$ in Tab. 2.1. This restriction stems from the use of spectroscopic date for our evaluation. Determining additional components of this form requires experiments which probe the dynamical properties of the system [72].

The data so far was compatible with a small longitudinal coupling (as seen above from fitting to flux or critical current coupling, cf. Tab. 2.1), but the resulting coupling strength $v_\parallel$ is comparable to the uncertainties and therefore we cannot rule out a pure charge-dipole. In such a case, a small longitudinal coupling component may also stem from a variation in the junction potential along the lines of Ref. [73]. A linear combination of the different coupling models, Eq. (2.31), is therefore also possible.

Conclusions

In this chapter we have shown how one can use data from spectroscopy experiments to try to identify the physical origin of the anti-crossings which are frequently observed in qubit spectra. Our analysis of the data on two strongly coupled TLS provided bounds on the parameters of several microscopic models. Specifically the models of a magnetic impurity on the surface of the superconductor can be excluded since no known physical model can account for the necessary magnitude of magnetic moment. For the models describing coupling via modulation of the critical current, we can give bounds on the magnitude of variation in I_C. We get additional information on the orientation of the TLS, resulting in a strongly symmetric TLS for the tunneling model or a very small impurity energy for an Andreev level fluctuator. If the TLS would be formed by a microscopic dipole, we can conclude that the size of the dipole would be of the order of atomic distances, a result which is consistent with the models of atomic tunneling systems.

Unfortunately, the results are not yet fully conclusive as to the nature of the TLS. Additional experiments are required to fully probe the form of the interaction. Possibilities include performing Hamiltonian characterization of the coupling along the lines introduced in Ref. [72]. This procedure enables one to probe relative phases between different terms in the Hamiltonian. Since we are driving the circuit via the voltage port $\propto \hat{q}$, this would provide us with a built-in phase reference.

3. Direct Control of Individual Defects

In this chapter we are going to present a method to directly address and control individual two-level defects inside a phase qubit circuit. This work was motivated by experiments on driving Rabi-oscillations in a qubit while tuning the qubit around resonance with a single strongly coupled defect. The resulting asymmetric response can be understood when including the higher lying levels in the phase qubit circuit. A similar effect enables one to directly manipulate the TLS when driving it resonantly while the qubit is detuned. We start the chapter by introducing the original experiment and giving a theoretical explanation of the observed effects. This theory is then adapted to explain the direct driving of TLS's. In the end we again show experimental results and speculate on some possible explanations.

Introduction

As we have seen previously, the exact microscopic nature of the coherent defects appearing in superconducting qubits is still unclear. On the one hand, they strongly influence the dynamics of the qubit circuit and are therefore considered detrimental towards using the qubits for quantum information processing. But on the other hand it has been found that their coherence properties (T_1 and T_2 times) are often much better than for the qubit itself. It thus has been proposed to use the TLS themselves as naturally formed qubits [36] and their usability as a quantum memory has been demonstrated [34].

In order to use the defects as a resource, it is desirable to have a possibility to address them directly, without involving excitations of the qubit circuit. In this chapter we show a method of direct manipulation of the state of individual TLS. This work was motivated by experiments probing the response of a phase qubit which was resonantly driven with microwaves while tuning it around resonance with a single strongly coupled TLS [37]. The resulting spectrum was strongly asymmetric with respect to detuning with the TLS and we show theory calculations explaining the asymmetry. Based on this results, we develop a method which allows one to directly manipulate individual TLS and again show experimental results where this method was used in order to measure the decoherence properties of single TLS. The data obtained in these measurements does not follow the standard theories, so in the last part, we will shortly speculate on possible explanations.

3.1. Rabi-Spectroscopy

In an experiment in the group of Alexey Ustinov, a phase qubit was driven by resonant microwaves to induce Rabi-oscillations while tuning it around resonance with a single strongly coupled two-level defect. The resulting oscillations in the time domain were analyzed by Fourier-transformation in order to detect their frequencies [37]. The experimental results are shown in Fig. 3.1.
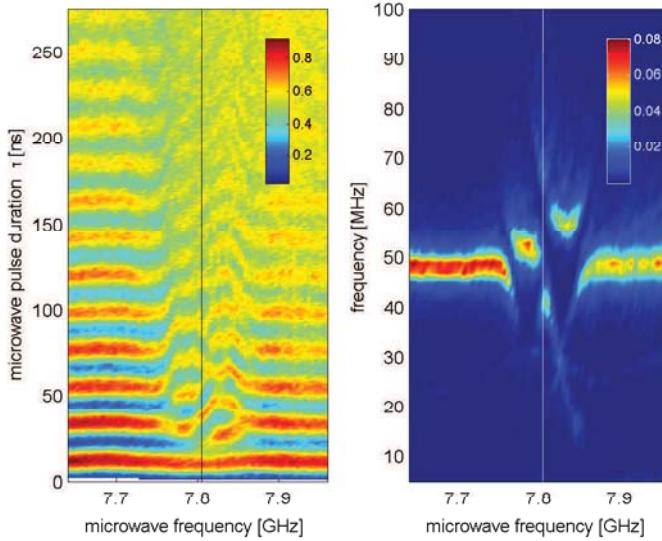
Figure 3.1.: *Experimental results from Rabi-spectroscopy. Resonance with the TLS is indicated by vertical lines. The left panel shows the time evolution of the excited state population of the qubit as a function of qubit frequency. The right panel shows the Fourier-transform of this data. A clear asymmetry with respect to detuning to the TLS is observed.*

One can see that far out of resonance (for detuning between qubit and TLS much larger than their coupling strength), ordinary Rabi-oscillations with a frequency of about 50 MHz are observed. Near resonance, the oscillations are becoming more complicated and from the Fourier-transform it becomes clear that more than on distinct frequency is involved. Perhaps the most striking feature of the data is the asymmetry of the frequency-components with respect to detuning with the TLS.

In experiment, the level-splitting of the probed TLS was at $\epsilon_f/2\pi = 7.805$ GHz and its coupling to the qubit had a strength of $v_\perp/2\pi = 25$ MHz. The qubit circuit itself had a critical current of $I_C = 1$ μA, capacitance of $C = 800 \times 10^{-15}$ F and inductance $L = 720 \times 10^{-12}$ H.

3.2. Theory - Rabi-Oscillations in the Coupled System

In this section we give the theory necessary to describe the observed effects. We start with what we call the *minimal* model needed to describe Rabi-oscillations in the coupled system. In this model, the response will be symmetric with respect to detuning, therefore not accounting for the experimental data. We then move on to show three different possible explanations for the observed asymmetry. However, only one of these explanation will be needed to fully account for the observed effect and we will show in the end our results, fully reproducing the experimental data without the need for any free parameters.

3.2.1. System - Minimal Model

We describe the experiment by the following Hamiltonian

$$\hat{H} = \hat{H}_S + \hat{H}_D + \hat{H}_I \,, \tag{3.1}$$

where $\hat{H}_S$ describes the system, consisting of qubit and coupled TLS, H_D the microwave driving and H_I the interaction with the driving.

First we present what we call the *minimal* model for Rabi-oscillations in the coupled system. $\hat{H}_S$ is then given by

$$\hat{H}_S = \frac{1}{2}\epsilon_{01}\sigma_z + \frac{1}{2}\epsilon_f\tau_z + \frac{1}{2}v_\perp\left(\sigma_+\tau_- + \sigma_-\tau_+\right) \,, \tag{3.2}$$

where σ and τ are pauli-matrices for qubit and TLS respectively, ϵ_{01} is the qubit level splitting between ground and first excited state, ϵ_f the level splitting of the TLS and $v_\perp$ is their transversal coupling strength. We have already performed a rotating wave approximation to get rid of the fast rotating terms in the coupling part of the Hamiltonian Eq. (3.2). The driving field is described by

$$\hat{H}_D = \omega_D\hat{a}^\dagger\hat{a} \,, \tag{3.3}$$

with the driving frequency ω_D and the photon annihilation operator $\hat{a}$. Similar to the situation in the experiment, we choose the driving to be resonant with the qubit $\omega_D = \epsilon_{01}$. Finally, the interaction with the driving field is only to the qubit. In the RWA we get

$$\hat{H}_I = \frac{1}{2}\Omega_{q,0}\left(\sigma_-\hat{a}^\dagger + \sigma_+\hat{a}\right) \,, \tag{3.4}$$

with the bare qubit coupling strength $\Omega_{q,0}$. We consider the parameter regime where the level splittings are much bigger than the couplings $\epsilon_f, \epsilon_{01} \gg v_\perp, \Omega_q$ and the qubit and TLS are near resonance $\delta\omega = \epsilon_f - \epsilon_{01} \ll \epsilon_{01}, \epsilon_f$

Rabi oscillations in this minimal model have been considered before, see e.g., Refs. [74, 75], and no asymmetry with respect to detuning was found. This minimal

model will therefore not be sufficient to explain the experimental findings of [37]. It is, however, instructional to review the physics of Rabi-oscillations in this coupled system before moving on to more complicated situations.

In Sec. 1.3 we showed the Floquet approach to periodically driven systems. Here we will show an alternative description, based on treating the driving field in second quantization as written above. As will become clear in the following, this approach leads to the same results as a Floquet theory description.

We go into the dressed states basis

$$
\begin{aligned}
|0\rangle &= |0g\rangle \otimes |n+1\rangle \; , \\
|1\rangle &= |1g\rangle \otimes |n\rangle \; , \\
|2\rangle &= |0e\rangle \otimes |n\rangle \; , \\
|3\rangle &= |1e\rangle \otimes |n-1\rangle \; , \tag{3.5}
\end{aligned}
$$

where $|0/1\rangle$ denotes ground- and first excited state of the qubit and $|g/e\rangle$ ground and excited state for the TLS. $|n\rangle$ is the microwave Fock state with n photons. In this basis, the Hamiltonian looks like

$$
\hat{H}_n = \frac{1}{2} \begin{pmatrix} -\delta\omega & \Omega_q & 0 & 0 \\ \Omega_q & -\delta\omega & v_\perp & 0 \\ 0 & v_\perp & \delta\omega & \Omega_q \\ 0 & 0 & \Omega_q & \delta\omega \end{pmatrix} \; , \tag{3.6}
$$

where $\delta\omega$ is the detuning between qubit and TLS and $\Omega_q = \sqrt{n}\,\Omega_{q,0}$. The energies in eq. (3.6) are measured from the energy of n photons $= n\epsilon_{01}$ and the full Hamiltonian is block-diagonal with parts of the form (3.6) for every photon number n. The level structure of one of the blocks (3.6) is depicted in Fig. 3.2.
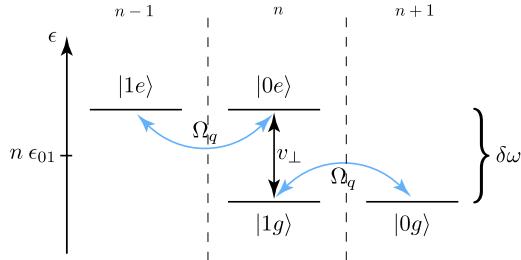
Figure 3.2.: *Dressed states for a two level qubit coupled to a TLS and driving resonantly with the qubit $\omega_D = \epsilon_{01}$. This illustration shows one multiplett of levels for n photons. This picture is repeated periodically for every n, separated in energy by the qubit splitting $\epsilon_{01} = \omega_D \gg \delta\omega, v_\perp, \Omega_q$*

Fig. 3.2 shows one multiplett of four levels of the full Hamiltonian. This picture is repeated periodically for every photon number n, and each multiplett is separated from the next by an energy difference of $\epsilon_{01} = \omega_D \gg \delta\omega, v_\perp, \Omega_q$. Because of this

hierarchy of energies, the dynamics will be restricted to each of the multipletts, and no transitions between separate multiplets will take place. Additionally we consider the limit of large photon numbers n where $\sqrt{n} \approx \sqrt{n \pm 1}$ and in this limit the dynamics inside each multiplett is equivalent. It is therefore sufficient for the description of Rabi-oscillations in this system to only consider one multiplett (3.6).

The choice of describing the driving as a fully quantized field as in Eq. (3.3) is actually not necessary in this case. Since the driving is strong, the description as a classical field (with $\hat{H}_I = 1/2\Omega_q \sigma_x \cos \omega_D t$) would be justified. In the classical description, we would move into the frame rotating at the driving frequency ω_D and obtain the same Hamiltonian Eq. (3.6) and therefore the same physics. As mentioned already, a description using Floquet theory of the driving also gives the same results.

In order to describe the dynamics of the driven oscillations we consider the time-evolution of a general system, described by the Hamiltonian $\hat{H}$. The stationary Schrödinger equation tells us that the state vector $|\psi\rangle$ evolves in time as

$$|\Psi(t)\rangle = \sum_i c_i e^{-i\epsilon_i t} |i\rangle \ , \tag{3.7}$$

where ϵ_i are the eigenvalues and $|i\rangle$ the eigenstates of the Hamiltonian $\hat{H}$. The coefficients c_i are defined by the initial condition $|\Psi(0)\rangle = \sum_i c_i |i\rangle = |\Psi\rangle_i$. We then re-express the eigenstates in a new set of basis vectors $\{|k\rangle\}$, which will represent the measurement basis (i.e. the basis in which the measurment operator is diagonal). We get

$$\begin{aligned} |\Psi(t)\rangle &= \sum_i \sum_k c_i e^{-i\epsilon_i t} |k\rangle \langle k |i\rangle \\ &= \sum_{i,k} a_{i,k} e^{-i\epsilon_i t} |k\rangle \ , \end{aligned} \tag{3.8}$$

with the coefficients $a_{i,k} = c_i \langle k |i\rangle$. A measurement of an operator $\hat{A}$ then gives

$$\langle \Psi(t)| \hat{A} |\Psi(t)\rangle = \sum_{i,j,k} a_{i,k}^* a_{j,k} e^{-i(\epsilon_j - \epsilon_i)} \langle k| \hat{A} |k\rangle \ , \tag{3.9}$$

where we already used the fact that the operator $\hat{A}$ is diagonal in the measurement basis $\{|k\rangle\}$. The result (3.9) allows for an easy interpretation of measurements: The observable $\hat{A}$ will show oscillations at frequencies $\omega_{ij} = \epsilon_j - \epsilon_i$ with amplitudes given by $\sum_k a_{i,k}^* a_{j,k} \langle k| \hat{A} |k\rangle$.

We therefore calculate the eigenenergies and transitions frequencies of the dressed state Hamiltonian eq. (3.6). For exact resonance between qubit and TLS, $\delta\omega = 0$,
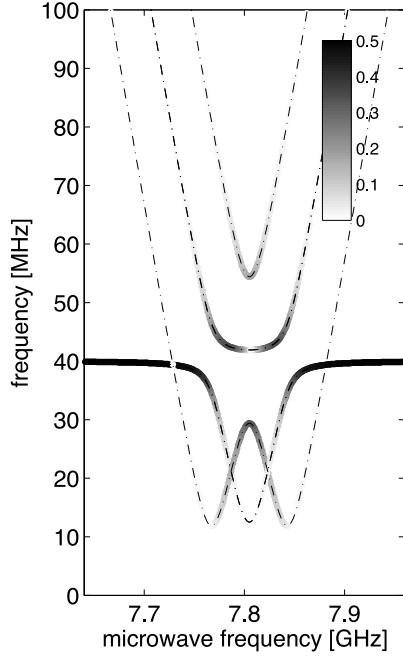
Figure 3.3.: *Spectrum of possible transitions in the minimal model eq. (3.6), consisting of a two-level qubit transversally coupled to a TLS. Greyscale intensity denotes the weight of the respective Fourier-components in the time evolution of the system. The spectrum is symmetric with respect to detuning (the TLS resonance frequency is at $\epsilon_f/2\pi = 7.805$ GHz.)*

we get

$$\epsilon_0 = -\frac{1}{4}\left(v_\perp + \sqrt{v_\perp^2 + 4\Omega_q^2}\right), \qquad \epsilon_1 = -\frac{1}{4}\left(v_\perp - \sqrt{v_\perp^2 + 4\Omega_q^2}\right),$$

$$\epsilon_2 = \frac{1}{4}\left(v_\perp - \sqrt{v_\perp^2 + 4\Omega_q^2}\right), \qquad \epsilon_3 = \frac{1}{4}\left(v_\perp + \sqrt{v_\perp^2 + 4\Omega_q^2}\right). \qquad (3.10)$$

The transitions frequencies ω_{ij} for transitions between level i and j are then

$$\omega_{01} = \omega_{23} = \frac{1}{2}\sqrt{v_\perp^2 + 4\Omega_q^2},$$

$$\omega_{02} = \omega_{13} = \frac{1}{2}v_\perp,$$

$$\omega_{03} = \frac{1}{2}\left(v_\perp + \sqrt{v_\perp^2 + 4\Omega_q^2}\right),$$

$$\omega_{12} = \frac{1}{2}\left(v_\perp - \sqrt{v_\perp^2 + 4\Omega_q^2}\right). \qquad (3.11)$$

We see that in the minimal model we have a total of four distinct transition frequencies since two of the transitions are twofold degenerate.

Fig. 3.3 shows the spectrum of possible transitions of the Hamiltonian (3.6) as a

function of qubit level-splitting. Two of the transitions lines are twofold degenerate over the whole range of detunings and the spectrum is symmetric with respect to resonance with the TLS. The greyscale intensity of the transitions in Fig. 3.3 indicate the spectral weight of the respective Fourier components in the time evolution of a measurement of the qubit population, i.e. the expectation value of the operator σ_z, and for an initial state of $|\Psi\rangle_i = |0g\rangle$, both qubit and TLS in their respective ground-state. They can also be calculated exactly, but the formula are lengthy and would not contribute to clarification, so we do not show them.

The symmetry of the response in Fig. 3.3 is owed to the degeneracy of transitions mentioned earlier. The Fourier weight of these degenerate transition is actually non-symmetric, meaning that on each side of resonance one of the two degenerate transitions is excited and contributes to the Fourier spectrum. Only due to their degeneracy is the response in the minimal model symmetric.

3.2.2. Asymmetry - Possible Explanations

Analyzing the origin of the asymmetric response of the coupled system, we discovered three different possible explanations. Only one of them will be needed to explain the results in the end, but we shortly show them all in order to give the whole picture. In each case we initially consider the eigenspectrum of the Hamiltonian at zero detuning ($\epsilon_{01} = \epsilon_f$) and identify how the initial degeneracies in the transition frequencies of the minimal model can be lifted. Due to the selectivity of the Fourier response, a lifting of this degeneracy will lead to an asymmetry with respect to detuning.

Longitudinal Coupling between Qubit and TLS

The minimal model assumes only transversal coupling $\propto \sigma_x \tau_x$ between qubit and TLS, since this kind of coupling is easily identifiable in the qubit spectrum (cf. Ch. 2) and because it is expected to give the strongest contribution to the Rabi-spectrum since it facilitates energy exchange between the two systems. If we assume a longitudinal coupling term $\propto \sigma_z \tau_z$, the Hamiltonian in the dressed state basis looks like

$$\hat{H}_\parallel = \frac{1}{2} \begin{pmatrix} -\delta\omega + v_\parallel & \Omega_q & 0 & 0 \\ \Omega_q & -\delta\omega - v_\parallel & v_\perp & 0 \\ 0 & v_\perp & \delta\omega - v_\parallel & \Omega_q \\ 0 & 0 & \Omega_q & \delta\omega + v_\parallel \end{pmatrix}, \tag{3.12}$$

where $v_\parallel$ is the strength of the longitudinal coupling. Calculating again eigenenergies for this Hamiltonian, we get

$$\begin{aligned} \epsilon_{0/1} &= -\frac{1}{4} \left(v_\perp \pm \sqrt{v_+^2 + 4\Omega_q^2} \right), \\ \epsilon_{2/3} &= \frac{1}{4} \left(v_\perp \mp \sqrt{v_-^2 + 4\Omega_q^2} \right), \end{aligned} \tag{3.13}$$

with $v_\pm = v_\perp \pm 2v_\parallel$. We see that $v_\parallel \neq 0$, effectively meaning $v_+ \neq v_-$, will result in six distinct transition frequencies. and the symmetry of the response will be broken.

Direct Driving of the TLS

The experiment uses driving of the qubit circuit via the microwave voltage port of the circuit (cf. Fig. 1.1). Since it was assumed that the TLS is a microscopic defect sitting in the vicinity of the qubit circuit (possibly inside the JJ), the driving field in the minimal model couples only to the qubit and not directly to the TLS. Assuming the TLS does also couple *directly* to the microwave, we get an additional term in the Hamiltonian of the form

$$\hat{H}_{I,f} = \frac{1}{2}\Omega_f^d \left(\tau_- \hat{a}^\dagger + \tau_+ \hat{a}\right) , \tag{3.14}$$

where Ω_f^d is the strength of the direct driving and we already performed the RWA. In the dressed state basis we then have

$$\hat{H}_d = \frac{1}{2} \begin{pmatrix} -\delta\omega & \Omega_q & \Omega_f^d & 0 \\ \Omega_q & -\delta\omega & v_\perp & \Omega_f^d \\ \Omega_f^d & v_\perp & \delta\omega & \Omega_q \\ 0 & \Omega_f^d & \Omega_q & \delta\omega \end{pmatrix} . \tag{3.15}$$

The eigenenergies of this Hamiltonian at zero detuning can be calculated as

$$\epsilon_{0/1} = -\frac{1}{4}\left(v_\perp \pm \sqrt{v_\perp^2 + 4\Omega_-^2}\right) ,$$

$$\epsilon_{2/3} = \frac{1}{4}\left(v_\perp \pm \sqrt{v_\perp^2 + 4\Omega_+^2}\right) , \tag{3.16}$$

with $\Omega_\pm = \Omega_q \pm \Omega_f^d$. Again $\Omega_f^d \neq 0$, meaning $\Omega_+ \neq \Omega_-$, lifts the degeneracy of the transitions and leads to an asymmetry in the response.

Influence of Higher Qubit Levels

For the minimal model we assumed the qubit to be a perfect two-level system. As we have seen before, a phase qubit is actually not a natural two-level system, but instead an anharmonic oscillator (cf. Ch. 2). Important for using this circuit as a qubit is the ratio of the anharmonicity Δ, i.e. the energy difference between the $0-1$ level-splitting and the $1-2$ level-splitting, to other energy scales in the system (coupling v, driving strength Ω). The anharmonicity Δ is here defined as $\Delta = \epsilon_{01} - \epsilon_{12}$. As long as Δ is large compared to these other parameters, we are justified in using a two-level description.

The qubit used in the experiment had an anharmonicity of roughly $\Delta/2\pi \approx 100$ MHz while the driving strength on the qubit was already $\Omega/2\pi \approx 50$ MHz. It is therefore natural to assume that higher qubit levels will play a role in the dynamics.
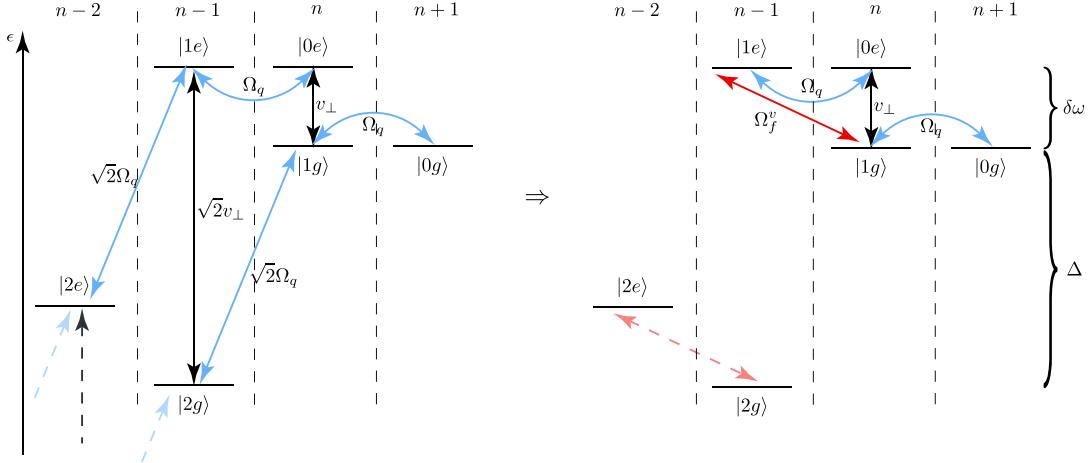
Figure 3.4.: *Dressed states of the coupled system for driving resonant with the qubit $0-1$ level splitting $\omega_D = \epsilon_{01}$. A Raman-like second order transition via virtual excitation of the $|2g\rangle$ state leads to an effective direct coupling of the TLS to the microwave field with coupling strength $\Omega_f^v = v_\perp \Omega_q / \Delta$.*

Fig. 3.4 shows the level structure of the coupled system when including higher qubit levels. The coupling operator σ_x of the qubit has been replaced with the momentum operator $\hat{q} = \mathrm{i}\,(\hat{b}^\dagger - \hat{b})$ of an anharmonic oscillator. Due to the properties of the oscillator annhihilation and creation operators $\hat{b}$, the matrix-elements connecting to higher qubit levels get stronger by a factor $\sqrt{m}$, where m is the qubit state. Assuming the higher levels are still not directly excited (i.e. the dynamics is still confined to to lowest four levels) we can identify an effective direct matrix element coupling the TLS to the microwave drive via virtual transition to the $|2g\rangle$ state. Its strength can be calculated by second order perturbation theory.

Reducing ourselves again to the effective four-level dynamics, we can express the Hamiltonian in the dressed state picture now by

$$
\hat{H}_v = \frac{1}{2}
\begin{pmatrix}
-\delta\omega & \Omega_q & 0 & 0 \\
\Omega_q & -\delta\omega & v_\perp & \Omega_f^v \\
0 & v_\perp & \delta\omega & \Omega_q \\
0 & \Omega_f^v & \Omega_q & \delta\omega
\end{pmatrix},
\tag{3.17}
$$

with the effective direct coupling strength $\Omega_f^v = v_\perp \Omega_q / \Delta$.

The eigenvalues of Eq. (3.17) can in principle be calculated analytically, but the expressions are again very lengthy. We instead give in Fig. 3.5 the spectrum of possible transitions including the respective Fourier weights for the time evolution of the qubit population according to the reduced four-level Hamiltonian as a function of detuning between qubit and TLS. One can clearly see the asymmetry of the response due to the different Fourier weights left and right of resonance. A similar picture also holds for the two previous possibilities.
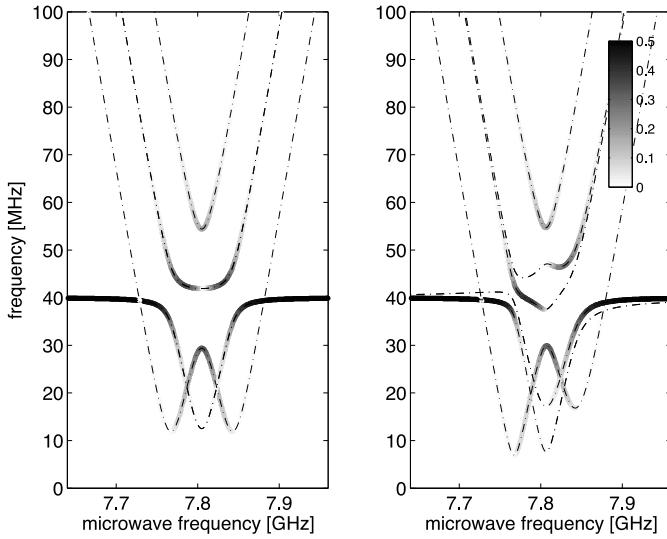
Figure 3.5.: *Spectrum of possible transitions in the coupled system of qubit and TLS (dashed dotted lines). Grayscale intensity denotes visibility of individual transitions in the Rabi-spectrum. The left picture is calculated using the minimal model eq. (3.6), the right picture when taking into account the second order transition via higher qubit levels. For the other possible models of the asymmetry, longitudinal coupling and direct driving, a similar picture holds. The TLS resonance frequency is at $\epsilon_f/2\pi = 7.805$ GHz.*

3.2.3. Asymmetry - Results

We have presented three different explanations for the experimentally observed asymmetry in the Rabi-spectroscopy. The conceptually simplest explanation, since it does not require any additional parameters, is the third one, effective direct driving due to higher lying qubit levels. This effect will also be always present, and its strength mainly depends on the ratio of the driving strength Ω to the anharmonicity Δ for the given circuit. For the other possibilities we would need additional parameters, that have to be determined from the experimental results.

From other experiments [31, 33] we know that the strength of longitudinal coupling to coherent defects is normally small compared to the transversal coupling (cf. also Ch. 2). In order to explain the experimental data, we would need comparable longitudinal and transversal couplings $v_\perp \approx v_\parallel$, and this effect therefore seems unlikely.

Most models of TLS (cf. Ch. 2) assume them to reside in the amorphous dielectric layer of one of the circuits Josephson junctions. In this case the microscopic defect would mainly see the circuits dynamics and not the direct effects of the voltage drive. In order to explain the experimental findings we would need a direct coupling strength of the order of $\Omega_f^d \approx 0.1\Omega_q$. From dimensional considerations we would expect a ratio of Ω_q/Ω_f^d closer to 100 (cf. App. A).

For an effective coupling of the TLS to the driving via higher qubit levels, no additional parameters are needed. For a simulation of the experiments we are actually already near the parameter region, where the second order perturbation theory is no longer valid, since the qubit Rabi-frequency Ω_q is no longer small compared to the anharmonicity Δ.
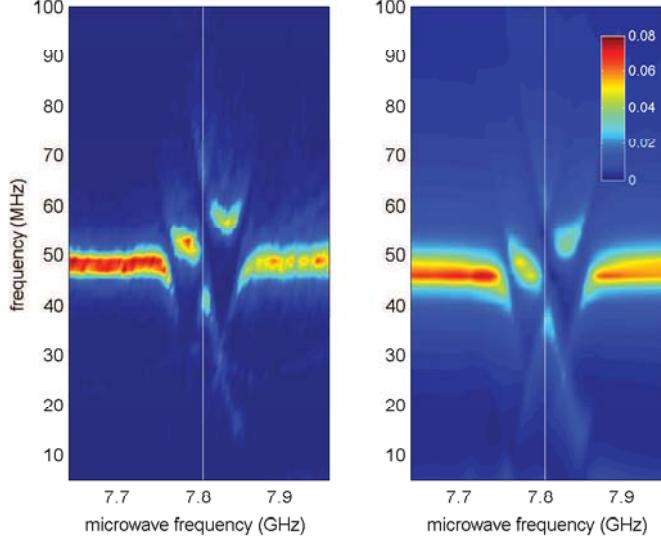
Figure 3.6.: *Experimental (left) and theoretical (right) Rabi-spectroscopy. The theoretical plot was obtained calculating the full six-level dynamics of three-level qubit coupled to a TLS. All parameters of the calculation were determined in independent experiments. The vertical white line denotes resonance with the TLS.*

Fig. 3.6 shows a comparison of the experimental Rabi-spectroscopy data and the results of a theoretical calculation taking into account the full six-level dynamics of a three-level phase qubit coupled to a single TLS. Decoherence on both qubit and TLS has been included in a standard Lindblad approach (cf. Sec. 1.2). No fitting was needed, all parameters of the system have been determined in independent experiments. The theory gives a remarkably good agreement with the experimental data and we can conclude that we do not need either longitudinal coupling between qubit and TLS or direct coupling of the TLS to the microwave field in order to reproduce the experiment [37].

3.3. Direct Driving of TLS

As we have seen in the previous part, the intrinsic coupling of the TLS to the qubit circuit can lead to an effective direct driving of the defect by the microwave field. We now show how this effect can be used to directly control the state of an individual TLS without exciting the phase qubit circuit and therefore effectively use the TLS

as a new qubit [35, 36, 76]. To this end, we first develop the theory to explain the effect of indirectly driving the TLS without participation of the qubit circuit. We then show results from an experiment where this effect was utilized in order to measure the coherence properties of individual TLS. The results do not follow the expectations developed from standard theory. In the next chapter we show this theory and also speculate on possible explanation of this data.

3.3.1. Direct Driving - Theory

In the previous part we analyzed the situation, where the driving field is resonant with the qubit $0 - 1$ transition, i.e. $\omega_D = \epsilon_{01}$. This driving frequency was chosen in order to induce Rabi-oscillations in the phase qubit.

If the microwave would directly couple to the defect, driving Rabi-oscillations of the TLS would also simply involve tuning the microwave to be resonant with the TLS splitting ϵ_f. Since we have seen that virtual excitations of higher lying qubit levels can lead to an *effective* direct coupling of the TLS to the microwave, we might expect this simple picture to still hold.
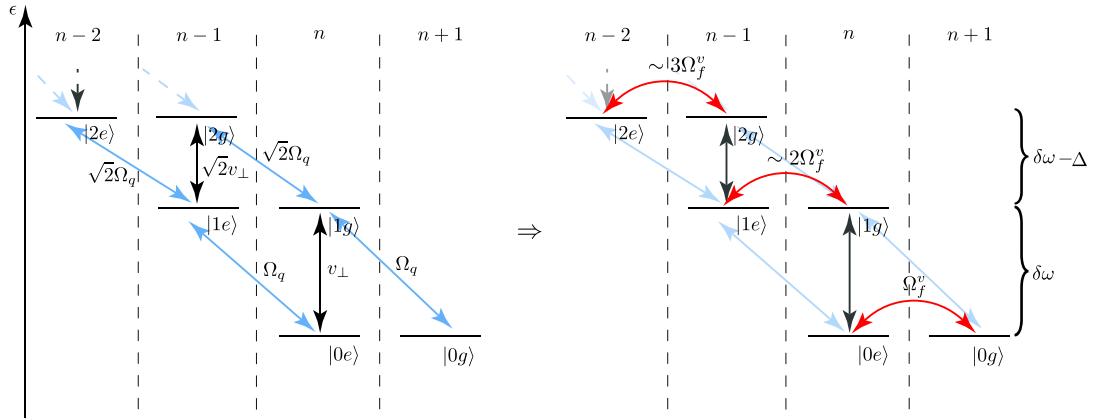

Figure 3.7.: *Dressed states of the coupled system for driving resonant with the TLS level splitting $\omega_D = \epsilon_f$. Via second order processes, the TLS can be driven quasi-directly with a driving strength of $\Omega_f^v = v_\perp \Omega_q / \delta\omega$.*

Fig. 3.7 shows the level structure of the coupled system when now driving resonantly with the TLS transition frequency $\omega_D = \epsilon_f$. The TLS can be driven again via a second order process involving virtual excitation of the qubit. For the qubit circuit in its ground-state $|0\rangle$, the effective driving strength is given by $\Omega_f^v = v_\perp \Omega_q / \delta\Omega$. Since we can only couple the TLS indirectly via the qubit circuit to the driving field, we additionally have to bias the qubit circuit such that no excitations of the phase qubit can take place $\delta\omega \gg \Omega_q$. Note, that the effective driving strength is stronger if the phase qubit circuit is also excited. For the qubit in the first excited state $|1\rangle$, the effective TLS Rabi-frequency is given by $2v_\perp \Omega_q / (\delta\omega - \Delta) \gtrsim 2\Omega_f^v$. Due to the

negative anharmonicity ($\epsilon_{12} < \epsilon_{01}$) of the phase qubit circuit, this effect becomes even more pronounced for higher qubit excitations.

3.3.2. Probing the Coherence of Individual TLS

The method of directly controlling individual coherent TLS we developed above has been applied by the group of Alexey Ustinov in an experiment with the the goal to directly probe the coherence properties of individual TLS [35].
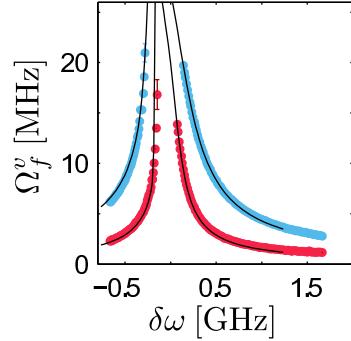

Figure 3.8.: *Effective Rabi-frequency Ω_f^v of a directly driven TLS as a function of detuning $\delta\omega$. The two curves correspond to different microwave powers. The lines give the expectation as calculated from theory involving up to five higher levels in the qubit circuit.*

Fig. 3.8 shows the effective Rabi-frequency when driving an individual TLS via the phase qubit circuit. The TLS here was coupled to the qubit with a coupling strength of $v_\perp/2\pi = 23$ MHz. The dots in blue and red are two measurements with different microwave power, i.e. different qubit driving Ω_q. The lines give the expectations as calculated from theory following Fig. 3.7. In these calculations, the system dynamics for a TLS coupled to a five-level qubit circuit was calculated and the oscillation frequency of the TLS extracted.

In the experiment, first the coherence times of a TLS was measured as a function of its detuning $\delta\omega = \epsilon_f - \epsilon_q$ from the qubit. The measurements of the relaxation time T_1 is shown in Fig. 3.9. Far out of resonance, the intrinsic T_1 of the TLS is measured. Near resonance we will have an influence from the coherent coupling to the qubit and the measured T_1 will be changed (cf. Sec. 4.3). Since the relaxation time of the qubit ($T_1^q = 110$ ns) is much shorter than for the TLS ($T_1^f = 410$ ns), we expect a dip in the measured rate. Note, however, the asymmetry of the decrease in Fig. 3.9. It is not centered around zero detuning ($\delta\omega = \epsilon_f - \epsilon_{01}$, TLS and phase qubit $0 - 1$ transitions resonant), but around lower detunings $\delta\omega < 0$.

In a next step, the temperature dependence of the relaxation and dephasing time was measured up to temperatures of the order of the TLS level-splitting. The results are shown in Fig. 3.10. During the evolution time, the qubit was constantly detuned at a fixed working point of $\delta\omega = -0.5$ GHz. The data is well fitted by a
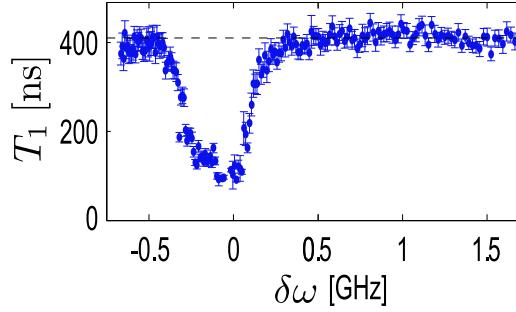
Figure 3.9.: *Relaxation time T_1 of a TLS as a function of its detuning $\delta\omega = \epsilon_f - \epsilon_{01}$ from the qubit resonance. For this TLS, its intrinsic relaxation time was around $T_1^f = 410$ ns, while the qubit relaxation time is about $T_1^q = 110$ ns. A decrease of effective T_1 near resonance is expected (cf. Ch. 4) but centered around zero detuning.*
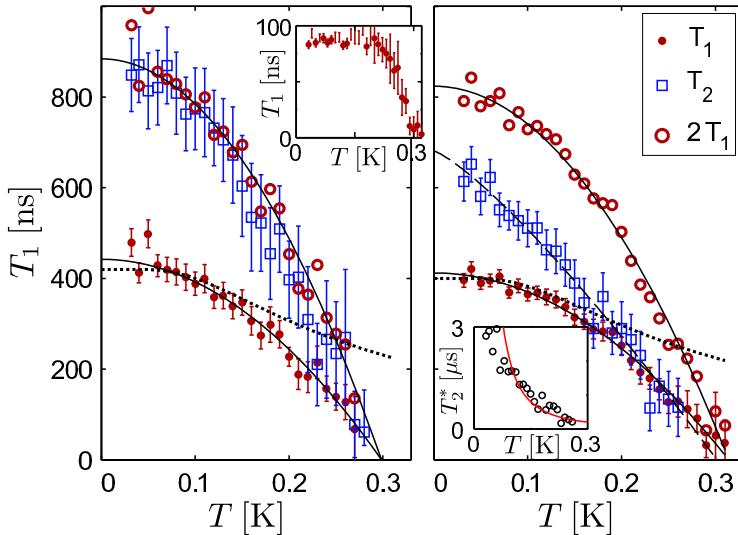
Figure 3.10.: *Relaxation time T_1 of two different TLS as a function of temperature. During these measurements, the qubit was biased at a detuning of $\delta\omega/2\pi = -500$ MHz. The lines are a fit to a quadratic dependence $T_1 = a - bT^2$, with $a, b > 0$. The left inset shows the same data for the qubit for comparison. The left TLS is T_1-limited at all temperatures, while the right one has additional contributions from pure dephasing. The right insets shows the dependence of the slow noise contributions on temperature.*

quadratic dependence on temperature $T_1 = a - bT^2$, with $a, b > 0$ (solid lines). From standard theory for an infinite bath at thermal equilibrium [77], one would expect a dependence of $T_1 \propto \tanh(\omega/2T)$ (dotted lines). For comparison, the temperature dependence of the qubits relaxation time is shown in the upper left inset. While it also does not fully obey the expected dependence, it shows qualitatively similar

behavior. The left TLS is T_1-limited at all temperatures, i.e. its dephasing time $T_2 = 2T_1$. The right TLS shows additional contributions from pure dephasing. After a one-pulse echo sequence, T_1-limited behavior is recovered. The right inset in Fig. 3.10 shows the temperature dependence of the extracted pure dephasing time T_2^* of the right TLS. It decays as roughly $1/T^2$ as is expected for low-frequency noise stemming from ensembles of two-level systems [25].

In Ch. 4 we show theory calculating the effective decoherence rates for interacting quantum systems. As we will show there, we expect the TLS relaxation time T_1 to be a symmetric function around resonance with the qubit, assuming the qubit dynamics to be restricted to its lowest two levels. We also do not expect the interaction to change the temperature dependence in a qualitative way. The experimental data clearly shows results not compatible with these claims. In Sec. 4.5 we will therefore speculate on some possible explanations.

Conclusions

In this chapter we have developed a method to manipulate the state of individual two-level defects coupled to a phase qubit. The method relies on virtual excitation of higher lying qubit states to indirectly drive the TLS via second order Raman-like processes. For very strong excitation, this method will eventually be equivalent to driving via a classical anharmonic oscillator. In the parameter regime we consider here however, the qubit state is still restricted to the shallow well in its potential and the discrete level structure is important. We note that the effectiveness of the indirect driving scheme (i.e. the resulting effective Rabi-frequency) can be improved by first exciting the qubit before driving the TLS. This improvement is however limited by qubit relaxation, which again destroys the possible gain.

4. Effects of Qubit-TLS Interaction

Coupling between a qubit and other quantum systems will strongly modify the resulting dynamics. The nature and strength of this coupling will determine if the effects are purely dissipative or may lead to coherent exchange of excitation. When the two systems are both coherent and in resonance, oscillations will transfer excitations between them and even out of resonance, a strong influence on the qubits coherence properties is expected.

In this chapter we give an overview of the effects two-level systems may have on the time evolution of a qubit. We mainly characterize these effects by calculating the modified relaxation rate Γ_1 near resonance with individual or several two-level defects and differentiate between the cases of weak and strong coupling. We give expressions for the effective relaxation rate for the cases when the qubit is near resonance with a single or several TLS as well as for TLS ensembles. Motivated by experimental results on direct driving of single defects, we also show calculations on interaction with multi-level systems. The chapter closes with some remarks on collective effects which might be observable in quantum meta-materials.

Introduction

If a qubit is coupled to any additional quantum system, this coupling is expected to change the time evolution of the qubit significantly. It is both the nature of this coupling as well as its strength that will determine the actual effects on the dynamics. For transversal coupling, the qubit can exchange energy with the TLS. In the weak coupling limit, this will manifest as relaxation into the thermal ground-state while for stronger coupling one can observe coherent oscillations where the energy is continuously exchanged between the two systems. Longitudinal coupling on the other hand will give a contribution to the qubits level-splitting and, depending on the internal dynamics of the TLS, lead to a randomization of the dynamical phase in the evolution, a process which is called pure dephasing.

In this chapter we analyze the properties of a qubit coupled to defect two-level systems and, in particular, their influence on the relaxation process. We start for the case of weak coupling between qubit and TLS. In this case we can use an effective bath approach, where the internal dynamics of the TLS will only incoherently act on the qubit via effective bath correlations. This regime has been the focus of extensive studies in the past (cf. e.g., Refs. [18, 25, 65]) and it can be shown that an ensemble

of weakly coupled TLS might be responsible for both the low- and high-frequency noise component of the environment. We will only only give the main result in the derivation to show the influence of weakly coupled TLS on the qubit dynamics. We then move on to the regime of strong coupling, in which the TLS will influence the coherent dynamics of the qubit.

To this end, we first consider a single TLS coupled resonantly to the qubit, i.e., with its energy splitting close to that of the qubit. In this regime the TLS strongly affects the qubit's dynamics, and we observe two effects: (i) coherent oscillations with the excitation energy going back and forth between the qubit and the TLS; (ii) the decay to the ground state due to the energy relaxation in either the TLS or the qubit. The oscillations themselves also show decay, dominated by dephasing processes. We describe the oscillation and relaxation processes and determine the relevant time scales.

Further, we discuss the dynamics of a qubit coupled to a collection of TLS's. Our motivation is based on the following observations from the analysis of the experimental data: a) strongly coupled TLS's (*strongly coupled* refers to a strong qubit-TLS coupling) were observed experimentally in phase qubits with large-area junctions [29, 30, 34]. In these qubits the T_1 time shows rather regular behavior as a function of the energy splitting of the qubit (in the regions between the avoided level crossings, which arise in resonance with the strongly coupled TLS's); b) in smaller phase and flux qubits the T_1 time often shows a seemingly random behavior as a function of the energy splitting of the qubit [27, 63, 78]; c) the strong coupling observed in Refs. [29, 30, 34] requires a microscopic explanation. For instance, a large dipole moment of the TLS, ed, is needed to account for the data, where d is of the order of the width of the tunnel barrier and e is the electron charge; d) experiments [46] suggest a very high density of (spin) fluctuators on the surface of superconductors.

Based on these observations we speculate about a possible microscopic picture of the fluctuations, which could be consistent with these observations: First, one could expect in the analysis of the dependence of T_1 on the level splitting that the contribution of each fluctuator is peaked near its level splitting (when it is resonant with the qubit and can absorb its energy efficiently). Further, one might assume that for a large collection of spectrally dense TLS's (that is with a dense distribution of the level splittings), the corresponding peaks overlap strongly, and the resulting T_1-energy curve is smooth (even though for a dense distribution the contributions of the TLS's are not necessarily independent). Indeed, this general picture is consistent with the data: in charge and flux qubits, with smaller-area junctions, the TLS's are not spectrally dense, and resonances with single TLS's can be resolved in the dependence of the relaxation rate on the level splitting. This may look as a seemingly random collection of peaks. In contrast, in phase qubits, with large-area junctions, there are many TLS's (for instance, the TLS's could be located in the junctions so that their number would scale with the junction area); thus the spectral distribution of their level splittings is dense and almost continuous. This may produce a smooth T_1-vs.-energy curve. Furthermore, one can speculate about

the structure of the fluctuator bath. Suggested scenarios of the microscopic nature of the fluctuators find it difficult to explain the existence of the strongly coupled TLS's, which were observed, for instance, in the qubit spectroscopy via the avoided level crossings [29, 30, 34].

In this picture each TLS is only coupled to the qubit, and they are essentially decoupled from each other. For each of them the coupling to the qubit is much weaker than observed in experiments [29, 30, 34]. For a dense uniform distribution of the TLS's splittings, usual relaxation of the qubit takes place. However, as we find below, if the level splittings of the TLS's accumulate close to some energy value (which may be a consequence of the microscopic nature of the TLS's), as far as the qubit's dynamics is concerned the situation is equivalent to a single strongly coupled TLS. Thus, in our picture, weakly coupled TLS's may conspire to emulate a strongly coupled TLS, visible, e.g., via qubit spectroscopy. Note, however, also the results of Ref. [31, 70, 71] pointing towards single strongly coupled TLS's.

To demonstrate this kind of behavior, we further study the regime, where two or more fluctuators are in resonance with the qubit. Our main observation in this case is that the fluctuators form a single effective TLS with stronger coupling to the qubit. For a collection of many TLS's with a low spectral density, we estimate the statistical characteristics (by averaging over the possible spectral distributions) of the random relaxation rate of the qubit and estimate corrections to this statistics due to the resonances that involve multiple TLS's. Finally, we discuss collections of spectrally dense TLS's. In this case we identify two regimes. If the TLS's are distributed homogeneously in the spectrum, they form a continuum, to which the qubit relaxes, and the dynamics is described by a simple exponential decay. If, however, a sufficiently strong local fluctuation of the spectral density of TLS's occurs, the situation resembles again that with a single, strongly coupled fluctuator. This may explain the origin of the strongly coupled TLS's observed in the experiment.

In the previous chapter we have shown experimental data obtained by directly probing the coherence of individual defect two-level systems (cf. Sec. 3.3.2). This data can not be explained by the theory developed so far. As we have seen in the previous chapters, concerned with defects in superconducting phase qubits, the description of a phase qubit circuit as a two-level system is often not sufficient to account for experiments. Motivated by this, we extend our previous calculations to coupling between TLS and multi-level systems. Specifically we show results for a single TLS coupled to a three level phase qubit and explain how such an interaction could explain the experimental data.

The chapter ends with some words on collective effects that might be observed in so-called superconducting quantum meta-materials. These materials consist of many superconducting qubits coupled to a common resonator mode. Due to the coupling to a shared degree of freedom, these qubits might show collective behavior, where excitations are shared coherently by many individual systems. One such collective effect, that might be observable in superconducting systems, is the appearance of super- and sub-radiant states. We will discuss the origin of this effect in detail and provide some

4.1. Description of the System

We consider a system described by the following Hamiltonian

$$\hat{H} = -\frac{1}{2}\, \epsilon_{01}\, \sigma_z - \frac{1}{2} \sum_n \epsilon_{f,n}\, \tau_{z,n}$$

$$+ \frac{1}{2}\, (\cos\eta\, \sigma_z + \sin\eta\, \sigma_x) \sum_n v_n\, (\cos\theta_n\, \tau_{z,n} + \sin\theta_n\, \tau_{x,n})$$

$$+ \hat{H}_{\text{Bath}}\,. \tag{4.1}$$

The first term, the Hamiltonian of the qubit in its eigenbasis reads $\hat{H}_q = -\frac{1}{2}\,\epsilon_{01}\,\sigma_z$, where ϵ_{01} is the level splitting between the ground and the excited state, and σ_z is the Pauli matrix. Similarly, the Hamiltonian of the n-th TLS in its eigenbasis reads $\hat{H}_{f,n} = -\frac{1}{2}\,\epsilon_{f,n}\,\tau_{z,n}$. Here we write a general coupling term between two two-level systems. The mixing angles η, θ are defined by the microscopic origin of the interaction between qubit and TLS (cf. Ch. 2). Later we will consider special cases of this coupling leading to different effects in the interaction. Most important will be purely transverse coupling $\propto v_\perp \sigma_x \tau_x$, leading to energy exchange between qubit and TLS, and purely longitudinal coupling $\propto v_\parallel \sigma_z \tau_z$, meaning that the level splitting of one system depends on the state of the other. Here we have defined the coupling strengths $v_\perp = \sin\eta\,\sin\theta$ and $v_\parallel = \cos\eta\,\cos\theta$. In this model all TLSs interact with the qubit, but not with each other. This assumption is reasonable, since the TLS's are microscopic objects distributed over, e.g., the whole area of the Josephson junction. Thus, they typically are located far from each other, but interact with the large qubit. The term $\hat{H}_{\text{Bath}}$ describes the coupling of each TLS and of the qubit to their respective baths. We model the environment of the qubit and of the TLSs as a set of baths characterized by the variables X_i and coupling constants β_i (specific examples are provided below).

In the course of describing the dissipative dynamics, many different decoherence rates will play a role. It is useful to reduce those rates, when possible, to the 'fundamental' ones, i.e., those characterizing the decoupled TLS's and the qubit and their coupling to respective baths. Each fluctuator is thus characterized by its own relaxation rate $\gamma_1^{f,n}$ and by the pure dephasing rate $\gamma_\varphi^{f,n}$, with the total dephasing rate given by $\gamma_2^{f,n} = (1/2)\gamma_1^{f,n} + \gamma_\varphi^{f,n}$. We define these rates below and later also discuss the generalization for the case of a non-Markovian environment. Also the qubit is characterized by its intrinsic (not related to TLS) relaxation rate γ_1^q and the pure dephasing rate γ_φ^q. Again $\gamma_2^q = (1/2)\gamma_1^q + \gamma_\varphi^q$. In what follows the mentioned rates are treated as 'fundamental'. All the other rates, emerging in the coupled system of the qubit and fluctuators, are denoted by capital letters Γ.

4.2. Weak Qubit-TLS Coupling

Assuming weak coupling between the qubit and the TLS, we can describe the resulting dynamics in an effective bath picture. For this we separate the system into three parts and treat the dynamics in two steps. In each step we only consider one pair of system parts interacting perturbatively. The first pair consists of the thermal baths coupled to the TLSs. They induce dissipative dynamics in the TLS which we describe by the characteristic rates. The dressed TLS (dressed with the induced decoherence) then serve as our new bath influencing the qubit. This enables us to formulate an effective TLS-bath correlation function which will give the description of the qubit decoherence. The effective bath picture is valid as long as the qubit-TLS coupling is weak compared to the resulting decoherence rates. At the end of this section we will quantify this statement by comparing the results of the effective bath description with a full Bloch-Redfield treatment of the coupled system.

4.2.1. TLS Dynamics

As a first step, we only consider the dynamics of the individual TLS due to their coupling to thermal baths. The model in this case is a simple two-level system coupled to a heat bath

$$\hat{H}_n = \frac{1}{2}\epsilon_{f,n}\tau_{z,n} + \hat{H}_{Bath} \, . \tag{4.2}$$

We assume each individual TLS coupled to independent baths by the Hamiltonian

$$\hat{H}_{Bath} = \frac{1}{2}\sum_n \left(\beta_\perp^{f,n}\tau_{x,n} + \beta_\parallel^{f,n}\tau_{z,n} \right) \hat{X}_n \, , \tag{4.3}$$

with the bath operator $\hat{X}$ and the coupling strengths β. Here we include transversal ($\perp$) as well as longitudinal ($\parallel$) coupling to a bath. Here we are only interested in the TLS induced decoherence of the qubit, so we do not consider a direct coupling of the qubit to any thermal bath.

Solving the Bloch-Redfield equations for the model Eq. (4.2) with the coupling Hamiltonian Eq. (4.3) we get the standard rates (cf. Sec. 1.2)

$$\gamma_1^{f,n} = \frac{1}{2}(\beta_\perp^{f,n})^2 S_{X_n}(\omega = \epsilon_{f,n}) \, ,$$
$$\gamma_2^{f,n} = \frac{1}{2}\gamma_1^{f,n} + \frac{1}{2}(\beta_\parallel^{f,n})^2 S_{X_n}(\omega = 0) \, , \tag{4.4}$$

with the symmetrized correlation function of the bath operator $\hat{X}$, $S_X(\omega) = \frac{1}{2}(C_X(\omega) + C_X(-\omega))$. The same results follow from a simple Golden Rule treatment (cf. Sec. 1.2). Note that in Eq. (4.3) we assumed both the transversal and the longitudinal coupling to a common bath operator $\hat{X}_n$. As we can see from Eq. (4.4) the relevant frequency ranges are very different. The transversal coupling probes the environment at frequencies corresponding to the level splitting while the longitudinal part

is sensitive to the bath dynamics at very low frequencies ≈ 0. We here assume the operator $\hat{X}_n$ to include both low- and high-frequency degrees of freedom.

4.2.2. Effective Bath Description - TLS Correlation Function

In the next step, we consider the TLSs to act as an effective bath acting on the qubit. The model is again a simple two-level system coupled to a heat bath

$$\hat{H} = \frac{1}{2}\epsilon_{01}\sigma_z + \hat{H}_{Bath,eff} \,. \tag{4.5}$$

We can then again use the Golden Rule to calculate effective qubit decoherence rates. The effective bath coupling operator is given by

$$H_{Bath,eff} = \frac{1}{2}\left(\cos\eta\,\sigma_z + \sin\eta\,\sigma_x\right)\sum_n v_n \hat{Y}_n \,, \tag{4.6}$$

with $\hat{Y}_n = (\cos\theta_n\,\tau_z + \sin\theta_n\,\tau_x)$. In order to obtain the effective qubit dynamics, we have to evaluate the correlation function C_Y of the TLS operator $\hat{Y}$, which is coupling to the qubit

$$C_Y(\omega) = \int_{-\infty}^{\infty} dt\, e^{i\omega t}\left\langle \hat{Y}(t)\hat{Y}(0)\right\rangle \,, \tag{4.7}$$

which can be a nontrivial problem. However, we already solved the TLS dynamics due to its coupling to a thermal bath and this knowledge enables us to evaluate the correlation function Eq. (4.7) using the so called Quantum Regression Theorem (QRT) [53]. The QRT states, that, assuming separability of the system-environment density matrix at all times, any correlation function of the form Eq. (4.7) can be calculated using the formula

$$\left\langle \hat{Y}(t)\hat{Y}(0)\right\rangle = Tr\left\{\hat{Y}(0)\,e^{\mathcal{L}t}\,\hat{Y}(0)\rho(t)\right\} \,, \tag{4.8}$$

for $t > 0$. For $t < 0$ a similar equation holds. Here $\rho(t)$ is the systems density matrix in the Schrödinger picture and the dissipative influence of the baths are accounted for by the Liouvillian super-operator $\mathcal{L}$ (cf. Sec. 1.2).

The effective TLS-bath correlation function for one TLS is then found as

$$\begin{aligned}
C_{f,n}(\omega) = {}& \cos^2\theta_n \frac{1}{\cosh^2\left(\frac{\epsilon_{f,n}}{2T}\right)} \frac{2\gamma_1^{f,n}}{(\gamma_1^{f,n})^2 + \omega^2} \\
& + \sin^2\theta_n \frac{1 + \tanh\left(\frac{\epsilon_{f,n}}{2T}\right)}{2} \frac{2\gamma_2^{f,n}}{(\gamma_2^{f,n})^2 + (\omega - \epsilon_{f,n})^2} \\
& + \sin^2\theta_n \frac{1 - \tanh\left(\frac{\epsilon_{f,n}}{2T}\right)}{2} \frac{2\gamma_2^{f,n}}{(\gamma_2^{f,n})^2 + (\omega + \epsilon_{f,n})^2} \,,
\end{aligned} \tag{4.9}$$

i.e., Lorentzians of width $\gamma_2^{f,n}$ around frequencies corresponding to the TLS level-splitting $\pm\epsilon_{f,n}$ and of width $\gamma_1^{f,n}$ around zero.

The decoherence rates of the qubit due to its coupling to the non-interacting TLS are then calculated by

$$\Gamma_1^q = \frac{1}{2} \sum_n v_n^2 \sin^2 \eta \, S_{f,n}(\omega = \epsilon_{01}) \,,$$

$$\Gamma_2^q = \frac{1}{2}\Gamma_1^q + \frac{1}{2} \sum_n v_n^2 \cos^2 \eta \, S_{f,n}(\omega = 0) \,, \tag{4.10}$$

plus possible direct rates $\gamma_{1/2}^q$ due to an eventual coupling to an independent (not consisting of TLS) bath. Here S_f is again the symmetrized correlation function of the TLS $S_f = 1/2(C_f(\omega) + C_f(-\omega))$.

The Eqs. (4.9) and (4.10) show how an ensemble of TLS could account for the low- as well as the high-frequency part of the noise spectrum. Low-frequency systems, where $\epsilon_{f,n} \leq T$, will contribute mostly to dephasing due to random thermal flipping of their state. Because of the purely longitudinal coupling term $\propto v_\parallel \sigma_z \tau_{z,n}$ this fluctuating dynamics will randomize the qubit level-splitting and therefore randomize the dynamical phase it acquires during its evolution. This is expressed by the Lorentzian of width $\gamma_1^{f,n}$ around zero frequency in Eq. (4.9). Standard theory shows, that a superposition of Lorentzians around zero frequency with a log-uniform distribution of widths, $P(\gamma_1) \propto 1/\gamma_1$, naturally expected for tunneling TLS, leads to the experimentally measured $1/f$-noise spectrum [18]. On the other end, high-frequency TLS, with $\epsilon_{f,n} \ll T, \gamma_2^{f,n}$ can, due to the purely transversal coupling $\propto v_\perp \sigma_x \tau_x$, exchange energy with the qubit and therefore flip its state. The resonance condition for this process is smeared by the dephasing acting on the TLS, effectively broadening the resonance by the dephasing rate $\gamma_2^{f,n}$. They will therefore each contribute a Lorentzian around their level-splitting $\epsilon_{f,n}$ of width $\gamma_2^{f,n}$ to the noise spectrum. It was shown in Ref. [25] that for certain distributions of TLS parameters, which for tunneling TLS follow naturally, the experimental data can be accounted for.

4.2.3. Range of Validity

The effect of the TLS bath on the qubit for this weak coupling case is simply one of inducing decoherence. Since these effects generally understood, we will in the following give a short discussion on the range of validity of the approximations made to obtain the above result. There are two main assumptions whose justification we will consider in detail: (i) the use of the TLS correlation function Eq. (4.9) for a Golden Rule calculation and (ii) the assumption of weak coupling between qubit and TLS. For both cases we will give the exact range where the approximations break down by comparing the above Golden Rule results with a more exact treatment of directly solving the Bloch-Redfield equations for the coupled system of qubit and TLS.

We chose the particularly simple case of a single TLS coupled only transversally to the qubit $\eta = \theta = 0$, and qubit and TLS in resonance $\epsilon_{01} = \epsilon_f$. We also assume the TLS to be coupled transversally to a bath, $\beta_\parallel^f = 0$ and temperature equal to zero. This will make the following calculations much simpler without changing any of the conclusions we may draw.

For the qubit resonant with a single high frequency TLS ($\epsilon_f \gg \gamma_2^f$) and zero temperature, we find a particularly simple expression for the effective relaxation rate in the effective bath picture

$$\Gamma_1^q = v_\perp^2/\gamma_2^f = 2v_\perp^2/\gamma_1^f \,, \tag{4.11}$$

with $v_\perp = \sin\eta \sin\theta \, v$ as defined above and we used the fact that for no longitudinal coupling to the bath, $\beta_\parallel^f = 0$, we have $\gamma_2^f = 1/2\gamma_1^f$.

We also formulate and solve the Bloch-Redfield equations (1.24) for this case and extract the qubit relaxation rate from the dynamics of the expectation value $\langle \sigma_z \rangle$. As the initial state in the evolution, we choose the TLS excited and the qubit in its ground-state.

Small Bath Coupling - Singular Correlation Function
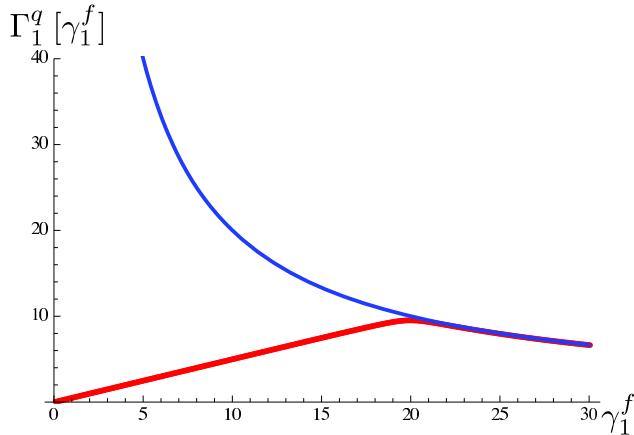
Figure 4.1.: *Effective qubit relaxation rate Γ_1^q as a function of TLS relaxation rate γ_1^f. The blue curve shows the standard Golden Rule result, $\Gamma_1^q \propto 1/\gamma_1^f$ while the red curve is calculated solving the full Bloch-Redfield equations for the coupled system. One can see that for small TLS relaxation, i.e., small width of the TLS correlation function Eq. (4.9), the Golden Rule result overestimates the relaxation. For stronger TLS decoherence, both methods agree well. The boundary is given exactly when the effective qubit rate Γ_1^q for the Golden Rule result gets bigger then the width of the correlation function. Parameters in this plot (in units of γ_1^f): $\epsilon_q = \epsilon_f = 100$, $v_\perp = 10$, $T = 0$.*

In the derivation of the standard Golden Rule rates of the form Eq. (4.4), it is

assumed, that the correlation function $C(\omega)$ is a constant or at least smooth function of energy in an area around the frequency at which it is evaluated (cf. Sec. 1.2). The range of smoothness has to be determined self-consistently depending on the resulting rate. One can say that the resulting rate gives the time-scale on which the bath correlations are probed. If they are sufficiently well behaved on this time-scale, the Golden Rule results holds.

However, looking at the effective TLS-bath correlation function $C_f(\omega)$, Eq. (4.9), we note that it consist of Lorentzians whose widths are given by the TLS dissipation rates $\gamma_{1/2}^f$. These rates in turn depend on the coupling strength between TLS and the thermal bath β_f and can therefore be small.

Fig. 4.1 shows the effective qubit relaxation rate Γ_1^q as a function of intrinsic TLS relaxation rate γ_1^f for small γ_1^f calculated using the Golden Rule result Eq. (4.10) (blue) and from the solution of the Bloch-Redfield equations (red). We see that the Golden Rule result Eq. (4.11) starts to deviate from the Bloch-Redfield calculations at the point $\gamma_1^f = 2v_\perp$. For bigger values of the TLS relaxation rate, both results agree very well. For $\gamma_1^f < 2v_\perp$ however, the Bloch-Redfield result follows $\Gamma_1^q = 1/2\gamma_1^f$, a result that will become clear in the next section. The problem here is the above mentioned behavior of the effective TLS-bath correlation function Eq. (4.9). For $\gamma_1^f < v_\perp$ its width becomes smaller than the resulting qubit rate Γ_1^q and we can no longer use the simple Golden Rule result Eq. (4.10). In the Bloch-Redfield calculations however, this assumption is not necessary, since there we consider the full coupled system of qubit and TLS coupled to a single bath.

Strong Qubit-TLS Coupling - Coherent Dynamics

The second assumption concerns the coupling strength between qubit and TLS. It is clear from the beginning that in order for the Golden Rule result Eq. (4.10) to hold, the coupling has to be small. It is our purpose now to quantify the word small by again comparing the Golden Rule with the results from a full Bloch-Redfield treatment.

In Fig. 4.2 we show this comparison. We plot the effective qubit relaxation rate Γ_1^q as a function of qubit-TS coupling strength $v_\perp$. We again see excellent agreement of the two methods up to $v_\perp = 1/2\gamma_1^f$. At this point the resulting effective qubit rate is given by $\Gamma_1^q = 1/2\gamma_1^f$. From this point on, the coupling between qubit and TLS is stronger than the induced decoherence and therefore coherent effects of the coupling will become important in the dynamics. It is then essential to no longer treat qubit and TLS as individual systems but to consider the full dynamics of the coupled system.

In this respect, the two limiting cases we have considered here are equivalent. For both small γ_1^f and large $v_\perp$, the region of validity of the Golden Rule treatment is given by $\gamma_1^f < 2v_\perp$, i.e. when the coupling between qubit and TLS does not yet play a role in the dynamical evolution, meaning that the intrinsic decoherence is stronger than any coherent part of the shared Hamiltonian. In the following, we will consider the opposite case, when the coupling $v_\perp$ is bigger than all intrinsic decoherence rates
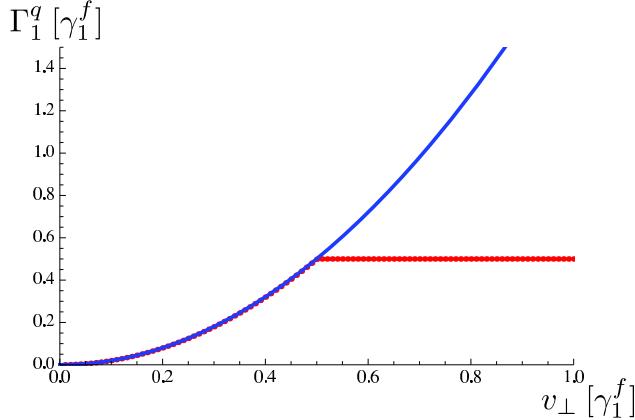
Figure 4.2.: *Qubit relaxation rate Γ_1^q as a function of qubit-TLS coupling strength $v_\perp$. The blue curve is again the results from a Golden rule treatment with the TLS as an effective bath while the red curve is obtained via solving the Bloch-Redfield equations for the coupled system. As soon as the effective rate Γ_1^q is bigger than the coupling strength $v_\perp$, the Golden Rule result is no longer valid. In this case the coupling becomes coherent and plays a role in the dynamics and it becomes important to consider the full coupled system. Parameters in this plot (in units of γ_1^f): $\epsilon_q = \epsilon_f = 100$, $T = 0$.*

γ in the system.

4.3. Coherent Qubit-TLS Coupling

In the previous section we have seen that the effective bath description of a qubit coupled to TLS is valid in only a small parameter range where the dissipation is still stronger than the coupling. To treat the full dynamics for arbitrary coupling we have to resort to a calculation of the full Bloch-Redfield equations for the coupled system, which can be very involved. In this section we will give analytical results for the case of purely transverse coupling between qubit and TLS, i.e., $\eta = \theta_n = \pi/2$ and therefore $v_{\perp,n} = v_n$. We note that the physical qubit-TLS interaction (e.g., a charge-charge coupling) would typically produce also other coupling terms in the qubits's eigenbasis (longitudinal and mixed terms; cf. the discussion of the purely longitudinal coupling $\propto \sigma_z \tau_z$ relevant for the dephasing by $1/f$ noise, e.g., in Refs [65, 79] and the discussion on defect models in Ch. 2). However, for our purposes (description of relaxation and transfer of excitations) the transverse coupling is most relevant since it gives rise to spin-flip processes between the qubit and TLS's.

To this end, we write down and solve the Bloch-Redfield equations [51, 52] for the coupled system of qubit and TLSs.

Strong coupling to fluctuators as a source of decoherence of a qubit was the focus of research in the past, cf., e.g., Refs. [80–82]. These works concentrated, however, on single-level fluctuators, i.e., an electron jumping back and forth between a continuum

and a localized level. Such a system maps onto an over-damped dissipative two-level system [83]. In contrast, here we study the effect of strong coupling to underdamped (coherent) two-level fluctuators.

4.3.1. Qubit Coupled to a Single TLS

As a first step, we consider a system of a qubit and a single TLS.

$$\hat{H} = -\frac{1}{2}\,\epsilon_{01}\,\sigma_z - \frac{1}{2}\,\epsilon_f\,\tau_z + \frac{1}{2}\,v_\perp\,\sigma_x\,\tau_x + \hat{H}_{\mathrm{Bath}}\;. \tag{4.12}$$

We restrict ourselves to the regime $\epsilon_{01} \approx \epsilon_f \gg v_\perp$ where the transversal interaction is relevant. We denote with $|0/1\rangle$ the ground- and first excited state of the qubit, width $|g/e\rangle$ ground- and excited state of the TLS. Then the ground state $\approx |0g\rangle$ and the highest energy level $\approx |1e\rangle$ are only slightly affected by the coupling. On the other hand the states $|1g\rangle$ and $|0e\rangle$ form an almost degenerate doublet. The coupling $v_\perp$ lifts the degeneracy to form the two eigenstates $|1-\rangle = -\cos\frac{\xi}{2}\,|0e\rangle + \sin\frac{\xi}{2}\,|1g\rangle$ and $|1+\rangle = \sin\frac{\xi}{2}\,|0e\rangle + \cos\frac{\xi}{2}\,|1g\rangle$ (cf. Fig. 4.3). Here we introduced the angle $\tan\xi = v_\perp/\delta\omega$ where $\delta\omega \equiv \epsilon_{01} - \epsilon_f$ is the detuning between the qubit and the TLS. The energy splitting between the levels $|1+\rangle$ and $|1-\rangle$ is given by $\omega_{osc} = \sqrt{v_\perp^2 + \delta\omega^2}$.
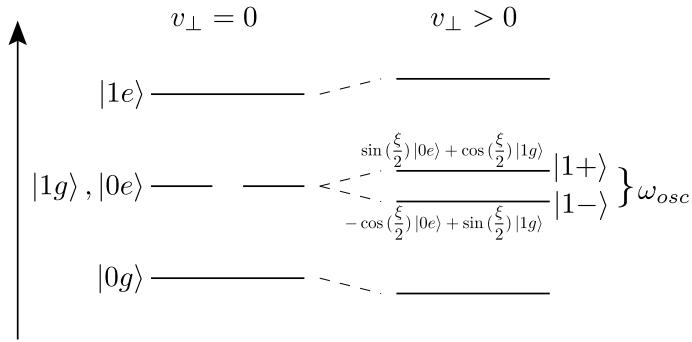
Figure 4.3.: *Level structure of the coupled qubit-TLS system in resonance $\delta\omega = 0$. For $v_\perp = 0$ the middle levels form a degenerate doublet. The coupling lifts the degeneracy and splits the levels by the oscillation frequency $\omega_{osc} = \sqrt{v_\perp^2 + \delta\omega^2}$.*

Transverse TLS-Bath Coupling

First, we consider the simplest case, in which only the TLS is coupled to a dissipative bath and this coupling is transverse. The coupling operator in Eq. (4.12) takes the form

$$\hat{H}_{\mathrm{Bath}} = \frac{1}{2}\beta_{f,\perp}\,\tau_x \cdot \hat{X}_{f,\perp}\;, \tag{4.13}$$

where the bath variable $\hat{X}_{f,\perp}$ is characterized by the (non-symmetrized) correlation function $C_{f,\perp}(t) \equiv \left\langle \hat{X}_{f,\perp}(t)\hat{X}_{f,\perp}(0) \right\rangle$. In thermal equilibrium we have $C_{f,\perp}(-\omega) = e^{-\omega/T}C_{f,\perp}(\omega)$. We first assume here that $T \ll \epsilon_f$, i.e., that the temperature is effectively zero, so that we can neglect excitations.

We introduce the rate

$$\gamma_1^f = \frac{1}{2}\,\beta_{f,\perp}^2\,S_{f,\perp}(\omega \approx \epsilon_{01}) = \gamma_{\downarrow}^f + \gamma_{\uparrow}^f\,, \tag{4.14}$$

which is the intrinsic relaxation rate of the fluctuator and given by the sum of relaxation and excitation rate $\gamma_{\uparrow/\downarrow}^f$ in the two-level system. Here we introduced the symmetrized correlation function $S_{f,\perp}(\omega) = 1/2(C_{f,\perp}(\omega) + C_{f,\perp}(-\omega))$. For $T \to 0$ excitations are exponentially suppressed, $\gamma_{\uparrow}^f = 0$ and therefore

$$\gamma_1^f(T=0) = \gamma_{\downarrow}^f = \frac{1}{4}\,\beta_{f,\perp}^2 C_{f,\perp}(\omega \approx \epsilon_{01})\,. \tag{4.15}$$

We solve the Bloch-Redfield equations [51, 52] for the coupled system using the secular approximation. As the initial condition we take the qubit in the excited state and the TLS in its thermal equilibrium state. Tracing out the TLS's degrees of freedom we find the dynamics of $\langle \sigma_z \rangle$ (Fig. 4.4).
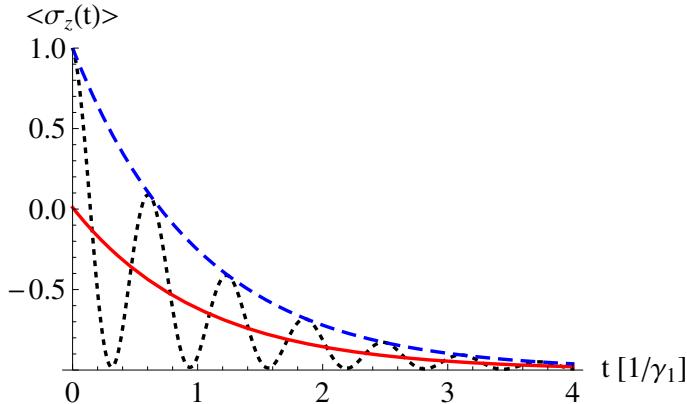
Figure 4.4.: $\langle \sigma_z \rangle$ *as a function of time in units of the inverse TLS relaxation rate γ_1^f for the case of the qubit exactly in resonance with the TLS (dotted black line). One observes oscillations with frequency ω_{osc}. The solid red curve gives the decay averaged over the oscillations, characterized by a_{av} and Γ_{av} and the dashed blue curve shows the envelope described by a_{env} and Γ_{env}. Parameters in this plot are (in units of γ_1^f): $\epsilon_{01} = \epsilon_f = 100, v_{\perp} = 10, T = 0$.*

For the expectation value $\langle \sigma_z \rangle$ we find the following expression

$$\begin{aligned}\langle \sigma_z(t) \rangle &= \langle \sigma_z \rangle_{\infty} + a_{\downarrow,-}\,e^{-\Gamma_{\downarrow,-}\,t} + a_{\downarrow,+}\,e^{-\Gamma_{\downarrow,+}\,t} \\ &\quad + a_{osc}\cos(\omega_{osc}t)e^{-\Gamma_{osc}\,t}\,,\end{aligned} \tag{4.16}$$
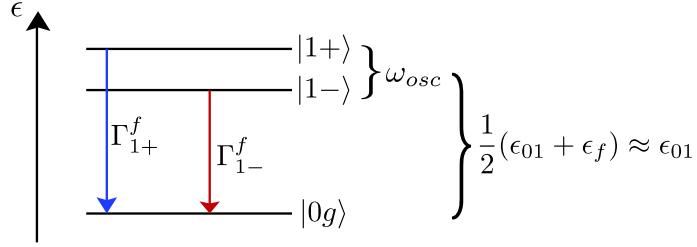
Figure 4.5.: *Level-structure of the coupled qubit-fluctuator system in the simplest case where only the TLS couples to a heat bath and the temperature is small (no excitations). The rates Γ^f_{1-} and Γ^f_{1+} in Eq. (4.19) lead from levels $|1-\rangle$ and $|1+\rangle$ respectively to the ground state $|0g\rangle$. The excited state $|1e\rangle$ is not included in this illustration.*

where $\langle \sigma_z \rangle_\infty = -1$ is the zero-temperature equilibrium value. We can separate the rhs of Eq. (4.16) into damped oscillations, with decay rate Γ_{osc}, and a purely decaying part. The amplitude and the decay rate of the oscillating part are given by

$$a_{osc} = \frac{v_\perp^2}{v_\perp^2 + \delta\omega^2} \; , \tag{4.17}$$

$$\Gamma_{osc} = \frac{1}{2}\gamma^f_\downarrow \; . \tag{4.18}$$

We observe that the decay rate of the oscillations, Γ_{osc}, is independent of the coupling strength $v_\perp$ and of the detuning $\delta\omega$. Note that the physics considered here is only relevant near the resonance $\epsilon_f \approx \epsilon_{01}$, and we assume that the spectrum $C_{f,\perp}(\omega)$ is sufficiently smooth in this region, so that $C_{f,\perp}(\epsilon_f) \approx C_{f,\perp}(\epsilon_{01})$.

For the purely decaying part we find

$$a_{\downarrow,-} = 2\sin^4\frac{\xi}{2} \; , a_{\downarrow,+} = 2\cos^4\frac{\xi}{2} \; ,$$

$$\Gamma_{\downarrow,-} = \Gamma^f_{1-} = \cos^2\frac{\xi}{2}\gamma^f_\downarrow \; , \Gamma_{\downarrow,+} = \Gamma^f_{1+} = \sin^2\frac{\xi}{2}\gamma^f_\downarrow \; , \tag{4.19}$$

where Γ^f_{1-} and Γ^f_{1+} are the rates with which the states $|1-\rangle$ and $|1+\rangle$ decay into the ground state $|0g\rangle$ (cf. Fig. 4.5).

As we can see, the decay law for $\langle \sigma_z(t) \rangle - \langle \sigma_z \rangle_\infty$ is given by a sum of several exponents. It is sometimes useful, e.g., for comparison with experiments where no fitting to a specific decay law was performed, to define a single decay rate for the whole process. If a function $f(t)$ decays from $f(t=0) = a$ to $f(t \to \infty) = 0$, we can define the single decay rate Γ from $\int_0^\infty f(t)dt = a/\Gamma$.

We can introduce the single decay rate in two different ways, either effectively averaging over the oscillations or including all parts and describing the envelope curve (cf. Fig. 4.4). In the first case, averaging over the oscillations, we choose

$f(t) = a_{\downarrow,-}\, e^{-\Gamma_{\downarrow,-}\, t} + a_{\downarrow,+}\, e^{-\Gamma_{\downarrow,+}\, t}$ and obtain for the amplitude and the decay rate

$$a_{av} = a_{\downarrow,-} + a_{\downarrow,+} = 1 + \frac{\delta\omega^2}{v_\perp^2 + \delta\omega^2} \ , \tag{4.20}$$

$$\Gamma_{av} = \frac{a_{\downarrow,-} + a_{\downarrow,+}}{\frac{a_{\downarrow,-}}{\Gamma_{\downarrow,-}} + \frac{a_{\downarrow,+}}{\Gamma_{\downarrow,+}}}$$

$$= \frac{1}{2}\, \gamma_\downarrow^f \, \frac{v_\perp^2\,(v_\perp^2 + 2\delta\omega^2)}{v_\perp^4 + 5v_\perp^2\,\delta\omega^2 + 4\delta\omega^4} \ . \tag{4.21}$$

This gives a quasi-Lorentzian line-shape of $\Gamma_{av}(\delta\omega)$ with the width of the order of the coupling $v_\perp$ and the maximum value at resonance of $\Gamma_{av}(\delta\omega = 0) = \frac{1}{2}\,\gamma_\downarrow^f$.
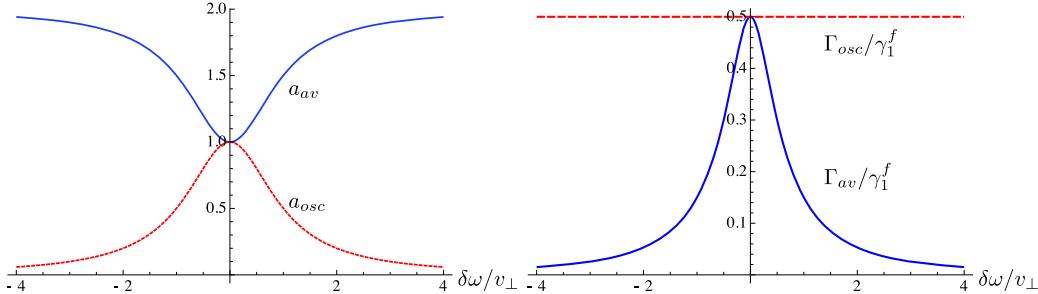
Figure 4.6.: *Amplitudes a and rates Γ for the decay of the oscillating (dashed red) and purely decaying (solid blue) part of the qubit's $\langle\sigma_z\rangle$ as a function of the detuning $\delta\omega$ between the qubit and fluctuator. The detuning is taken in units of the coupling $v_\perp$ and temperature is zero.*

Fig. 4.6 shows the amplitudes and rates characterizing the decay of the oscillations (dashed red) and of the purely decaying part (solid blue) of the qubits $\langle\sigma_z\rangle$.

To describe the envelope we choose $f(t) = a_{\downarrow,-}\, e^{-\Gamma_{\downarrow,-}\, t} + a_{\downarrow,+}\, e^{-\Gamma_{\downarrow,+}\, t} + a_{osc}\, e^{-\Gamma_{osc}\, t}$ (cf. Fig. 4.4). This gives

$$\Gamma_{env} = \frac{a_{\downarrow,-} + a_{\downarrow,+} + a_{osc}}{\frac{a_{\downarrow,-}}{\Gamma_{\downarrow,-}} + \frac{a_{\downarrow,+}}{\Gamma_{\downarrow,+}} + \frac{a_{osc}}{\Gamma_{osc}}}$$

$$= \frac{1}{2}\, \gamma_\downarrow^f \, \frac{2v_\perp^2\,(v_\perp^2 + \delta\omega^2)}{2v_\perp^4 + 5v_\perp^2\,\delta\omega^2 + 4\delta\omega^4} \ , \tag{4.22}$$

with amplitude $a_{env} = a_{\downarrow,-} + a_{\downarrow,+} + a_{osc} = 2$. This again gives a quasi-Lorentzian peak with height $\Gamma_{env}(\delta\omega = 0) = \frac{1}{2}\,\gamma_\downarrow^f$ and width similar to that of Eq. (4.21).

For finite temperature, the TLS's in the initial state has a finite probability according to the Boltzmann distribution to be in the excited state. Also, the excitation

rate $\gamma_\uparrow^f$ is now finite and we get additional contributions to the Redfield tensor

$$\Gamma_{-1} = \cos^2\left(\xi/2\right)\gamma_\uparrow^f,$$
$$\Gamma_{+1} = \sin^2\left(\xi/2\right)\gamma_\uparrow^f, \tag{4.23}$$

corresponding to excitations from the ground-state $|0g\rangle$ to the states $|1-\rangle$ and $|1+\rangle$ respectively.

Calculating the expectation value of $\langle\sigma_z\rangle$ we get the same form as eq. 4.16. The amplitudes and rates for the purely decaying part are now given by

$$a_{\downarrow,-} = (1+a)\sin^4\frac{\xi}{2}, \qquad a_{\downarrow,+} = (1+a)\cos^4\frac{\xi}{2}$$

$$\Gamma_{\downarrow,-} = \Gamma_{1-} + \Gamma_{-1} = \cos^2\frac{\xi}{2}\,\gamma_1^f$$

$$\Gamma_{\downarrow,+} = \Gamma_{1+} + \Gamma_{+1} = \sin^2\frac{\xi}{2}\,\gamma_1^f \tag{4.24}$$

while the purely oscillating part gives

$$a_{osc} = (1+a)\cos^2\frac{\xi}{2}\sin^2\frac{\xi}{2}$$

$$\Gamma_{osc} = \frac{1}{2}(\Gamma_{\downarrow,-} + \Gamma_{\downarrow,+}) = \frac{1}{2}\gamma_1^f \tag{4.25}$$

where we introduced the thermal factor $a = \tanh\left(\epsilon_{01}/2T\right)$. The decay of the oscillations is again independent of the coupling between qubit and TLS.

The average decay rate Γ_{av} for finite temperature has the same form as equation (4.21), now with $\gamma_\downarrow^f$ replaced by the general TLS relaxation rate γ_1^f. Its amplitude can be found to be

$$a_{av} = \frac{1}{2}(1+a)\left(1 + \frac{\delta\omega^2}{v_\perp^2 + \delta\omega^2}\right) \tag{4.26}$$

the same as eq. (4.20) but with a thermal prefactor due to the different initial condition. For the envelope of the decay, the same reasoning holds.

The results presented above are valid in the regime when the coupling between the qubit and the TLS is stronger then the decay rates due to the interaction with the bath, $v_\perp \gg \gamma_1^f$. In the opposite limit the Golden-Rule results hold, with the relaxation rate $\sim v_\perp^2/\gamma_1^f$ (cf. Refs. [80, 82, 84]).

General Coupling to the Baths

We now provide the results for the general case, when both the qubit and TLS are coupled to heat baths. The coupling in Eq. (4.12) is given by

$$\hat{H}_{\text{Bath}} = \frac{1}{2} \left(\beta_{f,\parallel} \, \tau_z \cdot \hat{X}_{f,\parallel} + \beta_{f,\perp} \, \tau_x \cdot \hat{X}_{f,\perp} \right)$$
$$+ \frac{1}{2} \left(\beta_{q,\parallel} \, \sigma_z \cdot \hat{X}_{q,\parallel} + \beta_{q,\perp} \, \sigma_x \cdot \hat{X}_{q,\perp} \right) . \tag{4.27}$$

It includes both transverse ($\perp$) and longitudinal ($\parallel$) coupling for both the qubit and the fluctuator. First, the temperature T is again assumed to be well below the level splitting $\epsilon_{01} \approx \epsilon_f$ so that we can neglect excitation processes from the ground state. Here, we used different bath operators for transversal and longitudinal degrees of freedom. This is because physically their relevant dynamics are very different. For longitudinal coupling to the bath, the low-frequency dynamics of the environment will be important, while for transversal coupling, it is the high-frequency components which will enter the dynamics. Assuming both types of spectrum for a single bath, we could also use coupled to a common environment as in Eq. (4.3).

We specify now the main ingredients of the Bloch-Redfield tensor of the problem. As in Eq. (4.19) the relaxation rates from the states $|1-\rangle$ and $|1+\rangle$ to the ground state due to the transverse coupling of the fluctuator are given by

$$\Gamma^f_{1-} = \cos^2 \frac{\xi}{2} \, \gamma^f_{\downarrow} , \qquad \Gamma^f_{1+} = \sin^2 \frac{\xi}{2} \, \gamma^f_{\downarrow} ,$$
$$\gamma^f_{\downarrow} = \frac{1}{4} \, \beta^2_{f,\perp} \, C_{f,\perp}(\omega \approx \epsilon_{01}) . \tag{4.28}$$

Similarly the transverse qubit coupling gives rise to new rates,

$$\Gamma^q_{1-} = \sin^2 \frac{\xi}{2} \, \gamma^q_{\downarrow} , \qquad \Gamma^q_{1+} = \cos^2 \frac{\xi}{2} \, \gamma^q_{\downarrow} ,$$
$$\gamma^q_{\downarrow} = \frac{1}{4} \, \beta^2_{q,\perp} \, C_{q,\perp}(\omega \approx \epsilon_{01}) . \tag{4.29}$$

The longitudinal coupling to the baths, $\propto \sigma_z, \tau_z$, gives two types of additional rates in the Redfield tensor, a pure dephasing rate, Γ_φ, and the transition rates between the states $|1-\rangle$ and $|1+\rangle$,

$$\Gamma^f_\varphi = \cos^2 \xi \, \gamma^f_\varphi$$
$$\Gamma^f_{-+} = \frac{1}{4} \, \beta^2_{f,\parallel} \, \sin^2 \xi \, C_{f,\parallel} \left(-\omega_{osc} \right)$$
$$\Gamma^f_{+-} = \frac{1}{4} \, \beta^2_{f,\parallel} \, \sin^2 \xi \, C_{f,\parallel} \left(\omega_{osc} \right) ,$$

where γ_φ^f is the pure dephasing rate of the TLS:

$$\gamma_\varphi^f = \frac{1}{2}\,\beta_{f,\|}^2\,S_{f,\|}\,(\omega = 0)\ . \tag{4.30}$$

Here $S_{f,\|}(\omega) = \frac{1}{2}\left(C_{f,\|}(\omega) + C_{f,\|}(-\omega)\right)$ is the symmetrized correlation function.

Similarly, the rates due to the qubit's longitudinal coupling to the bath are given by

$$\begin{aligned}
\Gamma_\varphi^q &= \cos^2 \xi\,\gamma_\varphi^q, \\
\Gamma_{-+}^q &= \frac{1}{4}\,\beta_{q,\|}^2\,\sin^2 \xi\,C_{q,\|}\,(-\omega_{osc})\,, \\
\Gamma_{+-}^q &= \frac{1}{4}\,\beta_{q,\|}^2\,\sin^2 \xi\,C_{q,\|}\,(\omega_{osc})\,, \\
\gamma_\varphi^q &= \frac{1}{2}\,\beta_{q,\|}^2\,S_{q,\|}\,(\omega = 0)\,.
\end{aligned} \tag{4.31}$$

Fig. 4.7 gives an illustration of the processes involved in the formation of the Redfield tensor when still neglecting excitations.
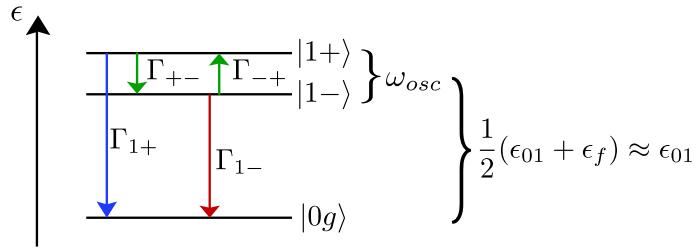
Figure 4.7.: *Illustration of the relevant transition processes in the general case of arbitrary coupling of the qubit and fluctuator to a heat bath and still small temperature. In addition to the transitions from the central levels $|1-\rangle$, $|1+\rangle$ to the ground state $|0g\rangle$ with the rates Γ_{1-} and Γ_{1+}, we now also have transitions between the two central levels with the rates Γ_{12} and Γ_{21}. The excited state $|1e\rangle$ is again omitted in the illustration.*

For $\langle \sigma_z(t) \rangle$ we again obtain the decay law (4.16). The amplitude of the oscillating part, a_{osc}, is still given by Eq. (4.17). The decay rate of the oscillations is, however, modified:

$$\Gamma_{osc} = \frac{1}{2}\left(\Gamma_\downarrow + \Gamma_{-+} + \Gamma_{+-}\right) + \Gamma_\varphi. \tag{4.32}$$

The rates without a superscript represent the sum of the respective rates for the qubit and TLS:

$$\begin{aligned}
\Gamma_\downarrow &= \gamma_\downarrow^f + \gamma_\downarrow^q, & \Gamma_\varphi &= \Gamma_\varphi^f + \Gamma_\varphi^q, \\
\Gamma_{-+} &= \Gamma_{-+}^f + \Gamma_{-+}^q, & \Gamma_{+-} &= \Gamma_{+-}^f + \Gamma_{+-}^q.
\end{aligned}$$

The purely decaying part is given by a slightly more complicated expression. Defining

$$A = \Gamma_{1-} + \Gamma_{-+} \quad , \quad B = \Gamma_{1+} + \Gamma_{+-} \ ,$$
$$C = \sqrt{(A - B)^2 + 4\Gamma_{-+}\Gamma_{+-}} \ ,$$

we obtain

$$a_{\downarrow,1/2} = \frac{1}{2} \left(1 + \cos^2 \xi\right)$$
$$\mp \frac{2 \, \cos\xi \, (A - B) + (\Gamma_{12} + \Gamma_{21}) \sin^2 \xi}{2\, C}$$
$$\Gamma_{\downarrow,1/2} = \frac{1}{2} \left(A + B \pm C\right)$$

In the limit $\beta_{q,\parallel} = \beta_{f,\parallel} = \beta_{q,\perp} = 0$, we reproduce the results of the previous section.

The decay of the average is again characterized by

$$a_{av} = a_{\downarrow,1} + a_{\downarrow,2} = 1 + \frac{\delta\omega^2}{v_\perp^2 + \delta\omega^2} \ , \tag{4.33}$$

$$\Gamma_{av} = \frac{a_{\downarrow,1} + a_{\downarrow,2}}{\frac{a_{\downarrow,1}}{\Gamma_{\downarrow,1}} + \frac{a_{\downarrow,2}}{\Gamma_{\downarrow,2}}} \ . \tag{4.34}$$

We work in the experimentally relevant limit $\omega_{osc} \ll T$. Then we obtain

$$\Gamma^f_{-+} = \Gamma^f_{+-} = \sin^2 \xi \, \Gamma^f_v \ ,$$
$$\Gamma^q_{-+} = \Gamma^q_{+-} = \sin^2 \xi \, \Gamma^q_v \ ,$$

where

$$\Gamma^f_v \equiv \frac{1}{4} \, \beta^2_{f,\parallel} \, S_{f,\parallel} \left(\omega_{osc}\right) \ ,$$

$$\Gamma^q_v \equiv \frac{1}{4} \, \beta^2_{q,\parallel} \, S_{q,\parallel} \left(\omega_{osc}\right) \ . \tag{4.35}$$

The decay rate of the average then reads

$$\Gamma_{av} = \frac{v_\perp^2 + 2\delta\omega^2}{2\left(v_\perp^2 + \delta\omega^2\right)} \left\{ \Gamma_\downarrow - \frac{4(\gamma^f_\downarrow)^2 \, \delta\omega^2}{v_\perp^2 \, (\Gamma_\downarrow + 4\Gamma_v) + 4\gamma^f_\downarrow \, \delta\omega^2} \right\} \ , \tag{4.36}$$

where $\Gamma_v = \Gamma^f_v + \Gamma^q_v$.

At resonance the resulting relaxation rate Γ_{av} is the mean of the decay rates of the qubit and TLS. Thus, if the TLS relaxes slower than the qubit (as was the case in Ref. [34]), Γ_{av} decreases. Fig. 4.8 shows the average decay rate Γ_{av} for the two cases with $\gamma^f_\downarrow$ bigger (solid blue) and smaller (dotted red) than $\gamma^q_\downarrow$. The double-peaked

structure in the first case is due to the contribution Γ_v of the longitudinal coupling to the baths. Exactly in resonance and far away from resonance the effect of Γ_v vanishes, while for $\delta\omega \sim v_\perp$ it produces somewhat faster relaxation.
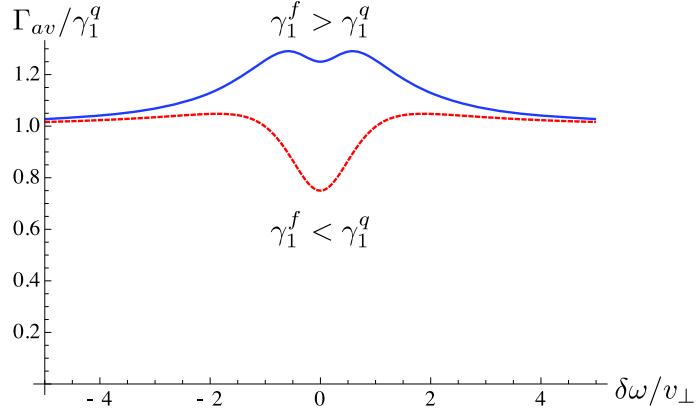
Figure 4.8.: Γ_{av} *as a function of the detuning $\delta\omega$ (rates in units of the qubit's relaxation rate γ_1^q, detuning in units of the coupling strength $v_\perp$) for the general case when the TLS's relaxation rate γ_1^f is higher (solid blue, $\gamma_1^f = 1.5\gamma_1^q$) / lower (dashed red, $\gamma_1^f = 0.5\gamma_1^q$) than the qubit's relaxation rate γ_1^q. The parameters in this plot are $\Gamma_v^q = \Gamma_v^f = 0.3$, $v_\perp = 5$ (in units of γ_1^q).*

For non-zero temperature, the excitations rates out of the ground-state for both qubit and TLS become important. We define

$$\gamma_\uparrow^f = \frac{1}{4}\beta_{f,\perp}^2 C_{f,\perp}(\omega \approx \epsilon_{01}), \qquad \gamma_\uparrow^q = \frac{1}{4}\beta_{q,\perp}^2 C_{q,\perp}(\omega \approx \epsilon_{01})$$
$$\gamma_1^f = \gamma_\downarrow^f + \gamma_\uparrow^f, \qquad \gamma_1^q = \gamma_\downarrow^q + \gamma_\uparrow^q \tag{4.37}$$

Then we recover the results of Sec. 4.3.1, now with effective decay rates given by the sum of qubit and TLS rates. For the oscillations, eq. (4.25) holds exactly for the amplitude, while their decay rate is now given by $\Gamma_{osc} = 1/2\Gamma_1$ with $\Gamma_1 = \gamma_1^f + \gamma_1^q$.

For the decay of the average, we can reproduce eq. 4.33 for the amplitude. Assuming again $\omega_{osc} \ll T$ and therefore $\Gamma_{+-} = \Gamma_{-+}$, we get for the decay rate

$$\Gamma_{av} = \frac{v_\perp^2 + 2\delta\omega^2}{2(v_\perp^2 + \delta\omega^2)} \left\{ \Gamma_1 - \frac{4(\gamma_1^f)^2 \, \delta\omega^2}{v_\perp^2 \, (\Gamma_1 + 4\Gamma_v) + 4\gamma_1^f \, \delta\omega^2} \right\}, \tag{4.38}$$

with the definitions given above.

Effects of Non-Markovian Baths

In the previous section we have shown (i.e. Eq. (4.32)) that pure dephasing affects only the decay rate of the oscillations of $\langle\sigma_z\rangle$. The result (4.32) is valid for a short-correlated (Markovian) environment. More specifically the relations $\Gamma_\varphi^q = \cos^2\xi \, \gamma_\varphi^q$

with $\gamma_\varphi^q = \frac{1}{2}\,\beta_{q,\parallel}^2\,S_{q,\parallel}\,(\omega = 0)$ and $\Gamma_\varphi^f = \cos^2\xi\,\gamma_\varphi^f$ with $\gamma_\varphi^f = \frac{1}{2}\,\beta_{f,\parallel}^2\,S_{f,\parallel}\,(\omega = 0)$ are valid only in the Markovian case. The generalization of these results to the case of non-Markovian noise, e.g., $1/f$ noise, is straightforward [63]. Assuming that at low frequencies $S_{q,\parallel} = A_{q,\parallel}/\omega$ and $S_{f,\parallel} = A_{f,\parallel}/\omega$, we obtain

$$\langle \sigma_z(t)\rangle = \langle\sigma_z\rangle_\infty + a_{\downarrow,1}\,e^{-\Gamma_{\downarrow,1}\,t} + a_{\downarrow,2}\,e^{-\Gamma_{\downarrow,2}\,t}$$
$$+ a_{osc}\,\cos\left(\omega_{osc}t\right) f_{1/f}(t)\,e^{-\Gamma'_{osc}\,t}\ , \tag{4.39}$$

where $\ln f_{1/f}(t) \sim -t^2\cos^2\xi\left(\beta_{q,\parallel}^2 A_{q,\parallel} + \beta_{f,\parallel}^2 A_{f,\parallel}\right)$ and Γ'_{osc} now includes only Markovian contributions.

In resonance, $\delta\omega = 0$, we have $\cos\xi = 0$ and therefore it seems at the first sight that the $1/f$ noise does not cause any dephasing. Yet, as shown in Ref. [85], in this case the quadratic coupling becomes relevant. The instantaneous splitting between the middle levels of the coupled qubit-TLS system, $|1-\rangle$ and $|1+\rangle$, is given by

$$\omega_{osc}(X_{q,\parallel}, X_{f,\parallel}) = \sqrt{v_\perp^2 + (\beta_{q,\parallel}X_{q,\parallel} + \beta_{f,\parallel}X_{f,\parallel})^2}$$
$$\approx v_\perp + \frac{1}{2}\frac{(\beta_{q,\parallel}X_{q,\parallel} + \beta_{f,\parallel}X_{f,\parallel})^2}{v_\perp}\ .$$

This dependence produces a random phase between the states $|1-\rangle$ and $|1+\rangle$ and, as a result, additional decay of the oscillations of $\langle\sigma_z\rangle$. We refer the reader to Ref. [85] for an analysis of the decay laws and times. Thus slow $(1/f)$ fluctuations make the decay of the coherent oscillations of $\langle\sigma_z\rangle$ faster without considerably affecting the average relaxation rate Γ_{av}.

For strong $1/f$ noise, thus, a situation arises in which the oscillations decay much faster than the rest of $\langle\sigma_z\rangle$. In experiments with insufficient resolution this may appear as a fast initial decay from $\langle\sigma_z\rangle = 1$ to $\langle\sigma_z\rangle = 1 - a_{osc}$ followed by a slower decay with the rate Γ_{av}.

4.3.2. Coupling to Two TLS

As a first step towards the analysis of the effect of many TLS's, we examine now the case when two fluctuators are simultaneously at resonance with the qubit. This situation in the weak coupling regime was considered, e.g., in Ref [86]. In this regime the fluctuators act as independent channels of decoherence and thus the contributions from different TLS are additive. However, in the regime of strong coupling between the qubit and the fluctuators, which is the focus of this paper, we do not expect the decoherence effects of the two fluctuators to simply add up. This means that the resulting relaxation rate will not be given by the sum of two single-fluctuator rates. The Hamiltonian of the problem reads

$$\hat{H} = -\frac{1}{2}\,\epsilon_{01}\,\sigma_z - \frac{1}{2}\sum_{n=1}^{2}\epsilon_{f,n}\,\tau_{z,n} + \frac{1}{2}\,\sigma_x\sum_{n=1}^{2}v_{\perp,n}\,\tau_{x,n} + \hat{H}_{\text{Bath}}\ , \tag{4.40}$$

where $\hat{H}_{\text{Bath}}$ contains now the coupling of each of the fluctuators to its respective bath. In the regime of our interest, $\epsilon_{01} \approx \epsilon_{f,1} \approx \epsilon_{f,2} \gg v_{\perp,1}, v_{\perp,2}$, the spectrum splits into four parts. The ground state is well approximated by $|0gg\rangle$. Analogously, the highest excited state is close to $|1gg\rangle$. The coupling $v_{\perp,n}$ is mainly relevant within two almost degenerate triplets. The first triplet is spanned by the states with one excitation: $\{|1gg\rangle, |0eg\rangle, |0ge\rangle\}$. In the second triplet, spanned by $\{|0ee\rangle, |1eg\rangle, |1ge\rangle\}$, there are two excitations. At low temperatures and for the initial state in which the qubit is excited and the fluctuators are in their ground states, only the first triplet and the global ground state are relevant. Within the first triplet the Hamiltonian reads

$$\frac{1}{2} \begin{pmatrix} 2\epsilon_{01} & v_{\perp,1} & v_{\perp,2} \\ v_{\perp,1} & 2\epsilon_{f,1} & 0 \\ v_{\perp,2} & 0 & 2\epsilon_{f,2} \end{pmatrix},$$

where the energy is counted from the ground state.

First, we consider the two fluctuators exactly in resonance with each other, $\epsilon_{f,1} = \epsilon_{f,2} = \epsilon_f$, and approximately at resonance with the qubit: $\epsilon_{01} \approx \epsilon_f$. We perform a rotation in the two-state subspace spanned by the states, where one of the TLS is excited, by applying the unitary transformation

$$U = \begin{pmatrix} 1 & 0 & 0 \\ 0 & \cos\alpha & \sin\alpha \\ 0 & -\sin\alpha & \cos\alpha \end{pmatrix}. \tag{4.41}$$

Choosing the angle $\alpha = \arccos \frac{v_{\perp,1}}{\sqrt{v_{\perp,1}^2 + v_{\perp,2}^2}}$, we arrive at the transformed Hamiltonian

$$\frac{1}{2} \begin{pmatrix} 2\epsilon_{01} & \sqrt{v_{\perp,1}^2 + v_{\perp,2}^2} & 0 \\ \sqrt{v_{\perp,1}^2 + v_{\perp,2}^2} & 2\epsilon_f & 0 \\ 0 & 0 & 2\epsilon_f \end{pmatrix}.$$

Fig. 4.9 gives an illustration of what happens. After the rotation (4.41) the qubit is coupled to only one effective state $|b\rangle$, whereas it is completely decoupled from the "dark" state $|d\rangle$. For symmetric coupling $v_{\perp,1} = v_{\perp,2}$ the states $|b\rangle$ and $|d\rangle$ are just symmetric and antisymmetric superpositions of $|0eg\rangle$ and $|0ge\rangle$. Thus, the rotation demonstrates that the situation is equivalent to only one effective TLS coupled to the qubit with the coupling strength

$$\tilde{v}_\perp = \sqrt{v_{\perp,1}^2 + v_{\perp,2}^2}.$$

Analyzing the coupling of the effective TLS to the dissipative baths (of both fluctuators), we conclude that the effective TLS is characterized by the relaxation rate

$$\tilde{\gamma}_1^f = \frac{1}{v_{\perp,1}^2 + v_{\perp,2}^2} \left(v_{\perp,1}^2 \, \gamma_1^{f,1} + v_{\perp,2}^2 \, \gamma_1^{f,2} \right).$$
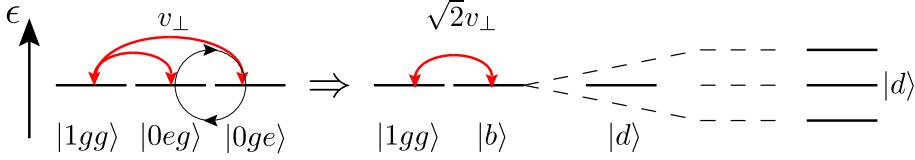
Figure 4.9.: *Illustration of the performed transformation in the one-excitation subspace of the Hamiltonian for the case of equal couplings $v_{\perp,1} = v_{\perp,2} = v_\perp$. Applying the rotation (4.41) we arrive first in a situation where the state $|d\rangle$ (the dark state) is completely decoupled from the other two states. The renormalized coupling then splits the remaining two states, giving a situation analogous to the coupling to one TLS.*

At this point we can apply all the results of Sec. 4.3.1 with $v_\perp$ replaced by the renormalized $\tilde{v}_\perp$ and the relaxation rate γ_1^f replaced by $\tilde{\gamma}_1^f$. In particular, using the formulas (4.20) and (4.21) we introduce

$$\Gamma_{av}^{(2)}(\delta\omega) = \Gamma_{av}(\delta\omega)\big|_{v_\perp \to \tilde{v}_\perp, \gamma_1^f \to \tilde{\gamma}_1^f} \ . \tag{4.42}$$

Here the superscript (2) stands for coupling to two fluctuators. The function $\Gamma_{av}^{(2)}(\delta\omega)$ is peaked around $\delta\omega = 0$. The height and the width of the peak depend on the relations between the coupling strengths and the relaxation rates of the two fluctuators. In the limiting cases of 'clear domination', e.g., for $v_{\perp,1} \gg v_{\perp,2}$ and $\gamma_1^{f_1} \gg \gamma_1^{f_2}$, everything is determined by a single fluctuator. In the opposite limit of identical fluctuators, i.e., for $v_{\perp,1} = v_{\perp,2}$ and $\gamma_1^{f_1} = \gamma_1^{f_2}$, the height of the peak (4.42) is given by $\gamma_1^{f_1}/2 = \gamma_1^{f_2}/2$, exactly as in the case of a single fluctuator. The width of the peak is, however, $\sqrt{2}$ times larger since $\tilde{v}_\perp = \sqrt{2}v_{\perp,1} = \sqrt{2}v_{\perp,2}$. Clearly, the relaxation rate of the qubit is not given by a sum of two relaxation rates due to the two fluctuators.

If the fluctuators are not exactly in resonance, this result still holds as long as their detuning $\delta\epsilon_f = \epsilon_{f,1} - \epsilon_{f,2}$ is smaller than the renormalized coupling $\tilde{v}_\perp$. For much larger detuning, the rate is given by the sum of two single-TLS contributions.

Many Degenerate TLS

For a higher number of fluctuators in resonance, i.e., $\epsilon_{f,n} = \epsilon_f$, the argument presented above is still valid, and the resulting decoherence of the qubit's state is the same as for a single TLS with a renormalized coupling strength of

$$\tilde{v}_\perp = \sqrt{\sum_n v_{\perp,n}^2}$$

and an effective TLS relaxation rate

$$\tilde{\gamma}_1^f = \frac{1}{\tilde{v}_\perp^2} \sum_n v_{\perp,n}^2 \, \gamma_1^{f,n} \; .$$

It should be stressed that this equivalence holds only within the one-excitation subspace of the system.

If the system with many fluctuators is excited more than once it is no longer equivalent to a system with one effective TLS. Multiple excitation could be achieved e.g., by following the procedure used in Ref. [87] or that of Ref. [34] repeatedly, i.e., exciting the qubit while out of resonance, transferring its state to the TLS's, exciting the qubit again and so forth. The simplest case is when all the fluctuators have equal couplings to the qubit $v_{\perp,n} = v_\perp$. The system's Hamiltonian then reads

$$H = -\frac{1}{2}\,\epsilon_{01}\sigma_z - \epsilon_f S_z + v_\perp \sigma_x S_x \; , \tag{4.43}$$

where $S_\alpha \equiv (1/2)\sum_n \tau_{\alpha,n}$.

For procedures of the type used in Ref. [34, 87], i.e., when only the qubit can be addressed, the TLS's will remain in the spin representation of S_α in which they were originally prepared. If the TLS's are all initially in their ground states, the accessible part of the Hilbert space is that of a qubit coupled to a spin $N/2$, where N is the number of TLS's. For the procedure of [34] the oscillation periods in the subspace with k excitations would be given by $2\pi/\tilde{v}_{\perp,k}$, where $\tilde{v}_{\perp,k} = \sqrt{k\,(N+1-k)} \cdot v_\perp$.

4.4. Coupling to an Ensemble of TLS

We now analyze decoherence of a qubit due to multiple TLS's. For this purpose, we introduce an ensemble of TLS's with energy splittings $\epsilon_{f,n}$, distributed randomly. For each fluctuator n we assume a uniform distribution of its energy splitting $\epsilon_{f,n}$ in a wide interval ΔE, with probability density $p_n = 1/\Delta E$. The overall density of fluctuators is given by $\nu_0 \equiv N/\Delta E$, where N is the total number of fluctuators in the interval ΔE. For simplicity we assume all the fluctuators to have the same coupling to the qubit $v_\perp$ and the same relaxation rate γ_1^f. The interval is much wider than a single peak, $\Delta E \gg v_\perp$, and the total number of TLS's in the interval is $N = \nu_0\,\Delta E \gg 1$.

We find that the physics is controlled by the dimensionless parameter $\bar{\nu} \equiv \nu_0\, v_\perp$. For $\bar{\nu} \ll 1$ the probability for two fluctuators to be in resonance with each other is low. Once the qubit is in resonance with one of the TLS's, the decay law of the qubit's $\langle \sigma_z \rangle$ takes the form (4.16). In this regime we take Γ_{av} to characterize the decay. We expect that in most situations the oscillations in (4.16) will decay fast due to the pure dephasing, and one will observe a very fast partial (down to half an amplitude) decay of $\langle \sigma_z \rangle$ followed by further decay with rate Γ_{av}. Thus the relaxation rate is given by a sum of many well separated peaks, each contributed by a

single fluctuator. Since the positions of the peaks are random, we expect, for $\bar{\nu} \sim 1$, a randomly looking dependence of the qubit's relaxation rate on the qubit's energy splitting (and a collection of rare peaks for lower densities, $\bar{\nu} \ll 1$). To characterize the statistical properties, we determine in Sec. 4.4.1 the relaxation rate, averaged over realizations, and its variance.

For larger $\bar{\nu} > 1$ the situation changes, as the peaks become dense, and the probability to have two or more fluctuators in resonance with each other is high. We conclude that it is not reasonable anymore to characterize the decay of $\langle \sigma_z \rangle$ by Γ_{av}. In this limit the coherent oscillations turn into much faster relaxation. The excitation energy is transferred from the qubit to the TLS's on a new, short time scale, $\sim (\bar{\nu} v_\perp)^{-1}$, which we now call the relaxation time. The energy remains in the TLS's for much longer time ($\sim 1/\gamma_1^f$) before it is released to the dissipative baths. Yet, if a strong enough fluctuation of the TLS's spectral density occurs, coherent oscillations appear again. A set of TLS's almost at resonance with each other form an effective strongly coupled fluctuator. The decay time of the oscillations is due to the background density of TLS's rather than due to the coupling to the baths. This could be an alternative explanations for the findings of Refs. [29, 30, 34]. In Sec. 4.4.2 we describe these two situations.

4.4.1. Independent TLS, $\bar{\nu} \ll 1$.

In this regime the relaxation rate Γ is given by a sum of single-fluctuator contributions. For a given realization of the ensemble we obtain

$$\Gamma(\epsilon_{01}) = \sum_n \Gamma_n \, , \tag{4.44}$$

where we use the notation $\Gamma_n = \Gamma_{av}(\epsilon_{01} - \epsilon_{f,n})$ and Γ_{av} is the average decay rate due to coupling to a single fluctuator, i.e. eq. (4.36). Integrating over the TLS energy splittings $\epsilon_{f,n}$, we obtain the average relaxation rate

$$\langle \Gamma \rangle = \int d^N \epsilon \, p^{(N)} \sum_n \Gamma_n = \gamma_1^f \, a_1 \, \bar{\nu} \, . \tag{4.45}$$

Here $d^N \epsilon = d\epsilon_{f,1} \dots d\epsilon_{f,N}$, and the probability distribution $p^{(N)} = \prod_n p_n$ is given by the product of single-TLS distribution functions, $p_n = \frac{1}{\Delta E} = \frac{\nu_0}{N}$. The second moment of the rate then follows as

$$\langle \Gamma^2 \rangle_0 = \int d^N \epsilon \, p^{(N)} \sum_{n,m} \Gamma_n \Gamma_m = (\gamma_1^f)^2 \left(a_2 \, \bar{\nu} - \frac{N-1}{N} a_1^2 \, \bar{\nu}^2 \right) . \tag{4.46}$$

The numerical factors a_1 and a_2 are calculated from the integrals

$$\int d\epsilon_{f,n} \, p_n \Gamma_n = \frac{1}{N} a_1 \, \gamma_1^f \, \bar{\nu} \,,$$

$$\int d\epsilon_{f,n} \, p_n \, (\Gamma_n)^2 = \frac{1}{N} \, a_2 \, (\gamma_1^f)^2 \, \bar{\nu} \,.$$

From this we directly find the variance

$$\langle\langle \Gamma^2 \rangle\rangle = \langle \Gamma^2 \rangle - \langle \Gamma \rangle^2 \sim (\gamma_1^f)^2 \bar{\nu} \,, \tag{4.47}$$

and thus

$$\frac{\langle\langle \Gamma^2 \rangle\rangle}{\langle \Gamma \rangle^2} \sim \frac{1}{\bar{\nu}} \tag{4.48}$$

This result can be expected. In the regime $\bar{\nu} \ll 1$ in each realization of the environment the function $\Gamma(\epsilon_{01})$ is a collection of rare peaks of height $\frac{1}{2}\gamma_1^f$ and width $v_\perp$. The average value of Γ is, thus, small, but the fluctuations are large. As expected, the relative variance decreases as the effective density $\bar{\nu}$ increases.

As we have seen in Sec. 4.3.2, the contribution from two TLS's in resonance differs from the sum of two single-TLS contributions. This effect leads to modifications of Eqs. (4.45) and (4.47) for a further increase of the spectral density $\bar{\nu}$ of the fluctuators. The relaxation rate becomes lower than the result (4.45) in the approximation of independent fluctuators, and the straightforward estimate gives:

$$\langle \Gamma \rangle \propto \gamma_1^f \, (\bar{\nu} - c_1 \bar{\nu}^2) \,, \tag{4.49}$$

Similarly, for the variance (which is close to the mean square) we find

$$\langle\langle \Gamma^2 \rangle\rangle \propto (\gamma_1^f)^2 \, (\bar{\nu} - c_2 \bar{\nu}^2) \,. \tag{4.50}$$

Here both pre-factors $c_1, c_2 \sim 1$. For example, $c_1 = 2 - \sqrt{2}, c_2 \approx 1.71$ in the rough approximation, when we (i) account for correlations by using the rate (4.42) for two resonant TLS's to describe the joint effect of two fluctuators, n and m, in a certain range around resonance, i.e., when their energy splittings differ by less than the coupling strength, $|\epsilon_{f,n} - \epsilon_{f,m}| < v_\perp$; (ii) neglect correlations for larger detunings $|\epsilon_{f,n} - \epsilon_{f,m}|$. In this approximation, we correct eq. (4.44) by an additional term $\sum_n \sum_{m \neq n} \theta_{i,j} \left(\frac{1}{2} \Gamma_n^{(2)} - \Gamma_n \right)$, with the unit-step $\theta_{n,m} = \Theta(\epsilon_{f,n} - \epsilon_{f,m} + v_\perp) \Theta(\epsilon_{f,m} + v_\perp - \epsilon_{f,n})$, where the $\Theta(\epsilon)$ are Heavyside step-functions. The rate $\Gamma_n^{(2)} = \Gamma_{av}^{(2)}(\epsilon_{f,n})$ is the average decay rate of the qubit due to coupling to two resonant TLS as given by the expression (4.42).

Fig. 4.10 shows the resulting relaxation rate Γ for one possible realization of the TLS distribution at $\bar{\nu} = 0.5$. The solid blue line corresponds to the approximation of independent fluctuators (4.44), while the dashed red line is calculated using the approximation described above.
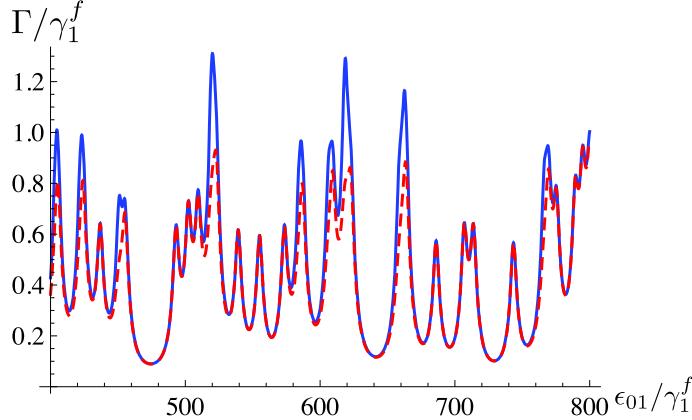
Figure 4.10.: Γ *as a function of the qubit's level splitting* ϵ_{01} *in units of the TLS relaxation rate* γ_1^f *for one possible realization of the fluctuator distribution with* $\bar{\nu} = 0.5$ *and* $v_\perp = 5\gamma_1^f$. *Solid blue line: approximation of independent fluctuators (4.44). Dashed red line: with account for correlations, see text. The corrections are most pronounced in areas, where more than one fluctuator is in resonance* $(\Gamma > \frac{1}{2}\gamma_1^f)$.

We see, that the experimental data, where "random" behavior of the relaxation rate as function of the qubit's energy splitting was observed [27, 63], could be consistent with the situation depicted in Fig. 4.10, i.e, with $\bar{\nu} \sim 1$.

## 4.4.2. Spectrally Dense Fluctuators, $\bar{\nu} \gg 1$.

For higher densities $\bar{\nu}$ the calculations above are no longer valid. In this section we discuss the limit of very high spectral densities, $\bar{\nu} \gg 1$. In the following considerations we restrict ourselves to the one-excitation subspace of the system and neglect the couplings to the baths. Thus we consider the one-excitation subspace of the following Hamiltonian

$$\hat{H} = -\frac{1}{2} \epsilon_{01} \sigma_z - \frac{1}{2} \sum_n \epsilon_{f,n} \tau_{z,n} + \frac{1}{2} \sigma_x \sum_n v_{\perp,n} \tau_{x,n} . \qquad (4.51)$$

Our purpose is to diagonalize the Hamiltonian in the one-excitation subspace and to find the overlap of the initial state $|i\rangle$ (qubit excited, all fluctuators in the ground state) with the eigenstates $|\phi_k\rangle$, labeled by an index k and having the eigenenergies E_k. This allows us to obtain the time evolution of the initial state:

$$|i(t)\rangle = \sum_k |\phi_k\rangle \langle \phi_k | i\rangle e^{-iE_k t} . \qquad (4.52)$$

We begin with the case of a completely uniform spectral distribution. This case is well known in quantum optics as the Wigner-Weisskopf theory [88]. We obtain a

(a)

(b)
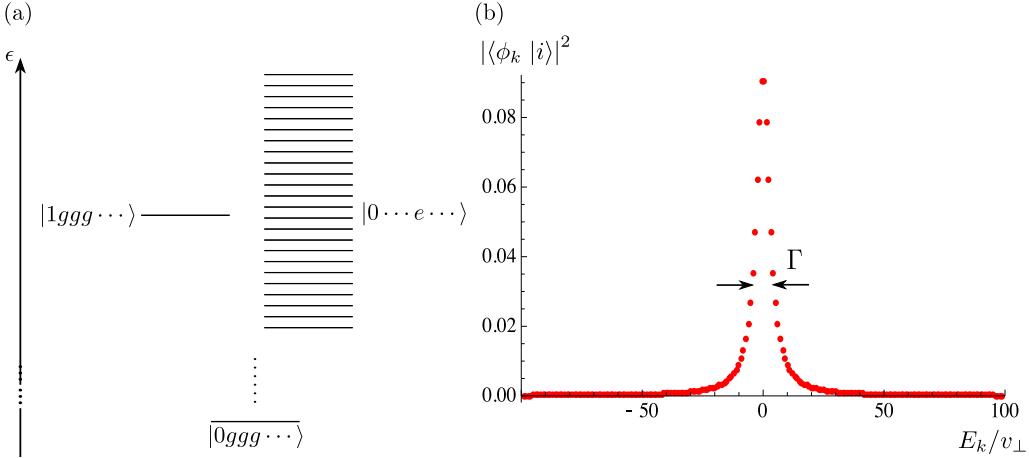
Figure 4.11.: *(a) Level structure of a qubit coupled to a uniform spectral distribution of fluctuators. The one-excitation subspace is shown. The state, where the qubit is excited, $|1ggg\cdots\rangle$, is coupled with strength $v_\perp$ to all other levels in this subspace. The ground state $|0ggg\cdots\rangle$ is energetically well separated from the subspace with one excitation. (b) Overlap of the initial state $|i\rangle = |1ggg\cdots\rangle$ with the eigenstates of the coupled system $|\phi_k\rangle$ for a uniform distribution of TLS's with an effective density $\bar{\nu} = 1$ as depicted above. The energy is counted from the energy of the initial state.*

Lorentzian shape of the overlap function. Fig. 4.11 shows the overlap $|\langle\phi_k|i\rangle|^2$ for an effective density $\bar{\nu} = 1$ as a function of E_k. We arrive at the probability amplitude to find the qubit still excited after time $t > 0$:

$$
\begin{aligned}
\langle i|i(t)\rangle &= \sum_k |\langle\phi_k|i\rangle|^2 \, e^{-iE_k t} \\
&= \int dE \sum_k |\langle\phi_k|i\rangle|^2 \, \delta(E - E_k) e^{-iEt} \\
&= \int \frac{dE}{2\pi} \frac{\Gamma}{\left(\frac{\Gamma}{2}\right)^2 + E^2} e^{-iEt} = e^{-\frac{\Gamma}{2}t} \,,
\end{aligned}
\tag{4.53}
$$

where $\Gamma = \frac{\pi}{2}\bar{\nu} \cdot v_\perp$. Thus the decay of the initially excited qubit in this situation is described by a simple exponential decay, $|\langle i|i(t)\rangle|^2 = e^{-\Gamma t}$. The width Γ of the Lorentzian in Fig. 4.11 determines the decay rate of the excited state.

Note, that we did not include here the coupling of either the qubit or the fluctuators to the dissipative baths. These couplings will broaden each of the eigenstates by an amount $\sim \gamma_1^f$. As long as this broadening is smaller than the resulting decay rate $\Gamma = \frac{\pi}{2}\bar{\nu} \cdot v_\perp$ (for strongly coupled fluctuators ($v_\perp \gg \gamma_1^f$) and $\bar{\nu} > 1$ this is always the case), the dissipative broadening has little effect. Thus the system of the coupled qubit and fluctuators remains for a long time ($\sim 1/\gamma_1^f$) in the one-excitation subspace, but the qubit relaxes much faster and the energy resides in the fluctuators.
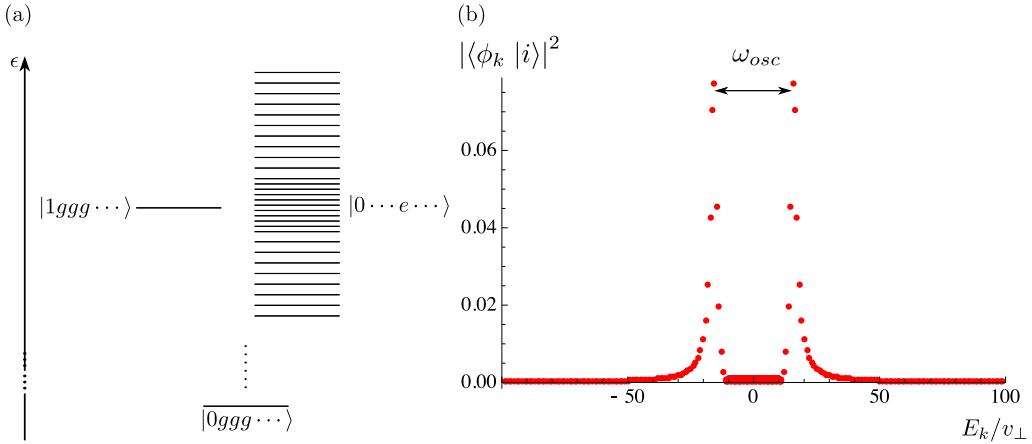
Figure 4.12.: *(a) Level structure for a non-homogeneous spectral distribution of TLSs. At energies near the qubit's level splitting ϵ_{01} the density is increased. The state $|1ggg\cdots\rangle$ is coupled equally to each level in the one-excitation subspace. (b) Overlap of the initial state with the eigenstates of the coupled system with a higher local density $\bar{\nu}_{local} = 10$ between $\epsilon = -10$ and $\epsilon = 10$ (in units of $v_\perp$). Out of resonance the effective density is $\bar{\nu} = 1$.*

Further, we analyze the situation with a large number of TLS's, whose energy splittings are accumulated near some value. For instance, this behavior may originate from the microscopic nature of the fluctuators. As we have seen above, a collection of resonant TLS's is equivalent, within the single-excitation subspace, to one effective TLS with a much stronger coupling to the qubit. This results in two energy levels, separated by this new strong effective coupling constant. As we discussed above, this may be the origin of the visible properties of strongly coupled TLS's. To illustrate this setting, we show typical numerical results in Fig. 4.12. The data are shown for the situation, where instead of many resonant TLS's we have a large collection of TLS's distributed in a certain energy range. On top of the homogeneous distribution with density $\bar{\nu} = 1$, we assume, locally, a higher density ($\bar{\nu} = 10$) of fluctuators with energies close to that of the qubit. We obtain a double-peak structure for the overlap $|\langle \phi_k |i\rangle|^2$. Performing again a calculation along the lines of Eq. (4.53), we obtain oscillations with frequency given by the energy splitting of the two peaks in Fig. 4.12. The widths of the peaks (set at this level by the local density) determine the decay rate of the oscillations. If these peaks are wider than the dissipative broadening, the latter can be neglected. Thus, the effect of the fluctuator bath with strong density variations on the qubit is equivalent to that of a single TLS with an effective coupling strength $\tilde{v}_\perp$, much stronger than the couplings $v_{\perp,n}$ between the qubit and the individual physical TLS's.

4.4.3. Dephasing due to Strongly Coupled TLS

Ensembles of TLS are a commonly used model for slow-noise in solid state systems [18] and thus attributed to pure dephasing processes. In the above we have shown that ensembles of TLS might be responsible for the seemingly random behavior of the relaxation rate of superconducting qubits as a function of their level splitting (cf. [27, 63]). In some experiments, a relation between low and high-frequency noise was observed [27], which can be explained when both regimes originate from the same ensemble of weakly coupled TLS [25]. In Ref. [25], the Markovian (short time-correlated) noise contributions of a set of weakly coupled TLS on the dephasing of a qubit were analyzed. Here, we show that we can reproduce their results even when assuming strong coupling and non-Markovian dynamics. In this case, the decay of the qubits density matrix coherences can be described by $\rho_{01}(t) \propto f(t)\mathrm{e}^{-\Gamma_\varphi t}$ (cf. Sec. 4.3.1), where Γ_φ is the Markovian dephasing rate and the decay function $f(t)$ includes the non-markovian contributions.

We follow the arguments of Ref. [65] to calculate the decay function $f(t)$. For this we consider an additional longitudinal coupling component between qubit and TLS of the form

$$H_\parallel = \frac{1}{2}\sum_n v_{\parallel,n}\sigma_z\tau_{z,n} \,. \tag{4.54}$$

This form of the coupling leads to a dependence of the qubit level splitting on the state of the TLS and for random fluctuations of the TLS therefore to pure dephasing. For the free induction (Ramsey) decay and coupling to one TLS the function $f(t)$ follows as

$$f_{R,n} = \mathrm{e}^{-\frac{1}{2}\gamma_n t}\left(\cos\mu_n t + \frac{\gamma_n}{\mu_n}\sin\mu_n t\right) \,, \tag{4.55}$$

with $\mu_n = \sqrt{v_{\parallel,n}^2 - \gamma_n^2}$ and the switching rate γ_n characterizing the timescale of switching events of an individual TLS. Similar, for an echo experiment, one finds

$$f_{E,n} = \mathrm{e}^{-\frac{1}{2}\gamma_n t}\left(1 + \frac{\gamma_n}{\mu_n}\sin\mu_n t + \frac{\gamma_n^2}{\mu_n^2}\left(1 - \cos\mu_n t\right)\right) \,. \tag{4.56}$$

In the limit of strong coupling $v_{\parallel,n} \gg \gamma_n$ and short timescales $v_{\parallel,n}t < 1$ one can approximate the above result as

$$\ln f_{R,n} \approx -\frac{1}{2}\,v_{\parallel,n}^2\,t^2 \tag{4.57}$$

$$\ln f_{E,n} \approx -\frac{1}{6}\,\gamma_n\,v_{\parallel,n}^2 t^3 \tag{4.58}$$

Relevant for dephasing processes are TLS with energies below the temperature T since these TLS will show random switching behavior. For an arbitrary distribution

function $\nu(\omega)$ we get their number as

$$N_< = \int_0^T d\omega \, \nu(\omega) \,. \tag{4.59}$$

For these TLS we can assume the temperature to be effectively infinite and the switching rate will be given by half the TLS relaxation rate $\gamma_n = \frac{1}{2} \gamma_1^f$.

The decay function due to more than one TLS is obtained by multiplication of single TLS contributions $f = \prod_i f_i$. We assume self averaging properties for the distributions of $v_\parallel, n$ and γ_n and finally arrive at the decay function

$$f_R = e^{-\frac{1}{2} N_< v_\parallel^2 t^2} \,,$$
$$f_E = e^{-\frac{1}{6} N_< \gamma \, v_\parallel^2 t^3} \,, \tag{4.60}$$

where $v_\parallel$ and γ are now given by the average longitudinal coupling and switching rate respectively. Identifying pure dephasing rates from Eq. (4.60) we arrive at

$$\Gamma_{R,2}^* = \frac{v_\parallel}{\sqrt{2}} \sqrt{N_<} \,,$$
$$\Gamma_{E,2}^* = \sqrt[3]{\frac{N_< \gamma \, v_\parallel^2}{6}} \,. \tag{4.61}$$

For a fluctuator density linear in energy $\nu(\omega) = \alpha \, \omega$ we get for the number of contributing TLS $N_< = \frac{1}{2} \alpha \, T^2$. For tunneling TLS such a distribution follows naturally (cf. [19, 20, 25]). The dephasing rate for a Ramsey type experiment is then given by $\Gamma_{R,2} = \frac{v_\parallel T}{2} \sqrt{\alpha}$ which would correspond to a $1/f$-spectrum $\propto \alpha T^2$. For the same distribution of TLS Eq. (4.45) becomes $\langle \Gamma \rangle \propto \alpha \, \omega$. Comparing with Ref. [25] we see that we can reproduce their results.

4.5. Coupling to Multi-Level Systems

We will now speculate on possible explanations of the experimental findings concerning the coherence properties of single TLS. This part is still work in progress [89], we only want to give a short introduction into some of the possibilities.

One puzzle is the clear asymmetry obvious is the dependence of the TLS relaxation time on detuning from the qubit (cf. Fig. 3.9). The theory developed in this chapter, involving a two-level qubit coupled to one or several TLS does predict a symmetric shape around zero detuning. We note that the dip in the relaxation time of the TLS in Fig. 3.9 is centered around negative detuning $\delta\omega$, meaning the TLS relaxation time is smaller it the qubit splitting ϵ_{01} is bigger than the defect splitting ϵ_f. For this detunings, higher qubit transitions ϵ_{nm} might become resonant with the TLS. Due to the negative anharmonicity in the phase qubit circuit, we have $\epsilon_{01} > \epsilon_{12} > \ldots$. Under the assumption that the qubit circuit is at least partly excited in the experiment,

resonance between the TLS and a higher transitions in the qubit circuit will influence the TLS dynamics in a similar way as seen earlier. This can be understood as due to the opening of additional relaxation channels in the dynamics. For each successive resonance condition, $\epsilon_f = \epsilon_{nm}$, we will then get a dip in the relaxation time along the lines shown in Sec. 4.3. If the dips are sufficiently broad, they will give an effective overall T_1 similar to Fig. 3.9.
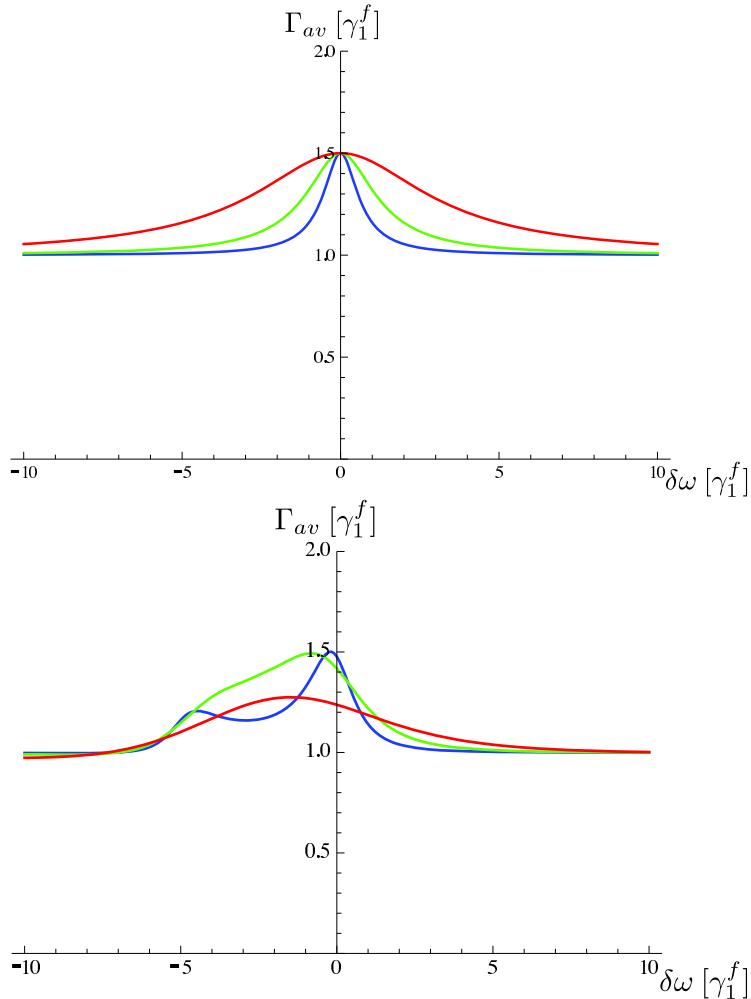
Figure 4.13.: *Average rate Γ_{Av} as a function of detuning $\delta\omega = \epsilon_{01} - \epsilon_f$ of a TLS coupled to a three level qubit. The top part shows the situation for an initial state of $|\Psi_{Init}\rangle = |0e\rangle$ and the lower part shows results from the same calculation but with an initial state of $|\Psi_{Init}\rangle = |1e\rangle$. The three lines are calculated for different coupling strength $v_\perp = 1, 2, 5$ (blue, green and red lines). Parameters are (in units of γ_1^f): $\gamma_1^q = 2$, anharmonicity $\Delta = 5$.*

To confirm this speculations, we have performed a calculation similar to what has been shown above. We are now interested in the dynamics of a two-level system coupled strongly to a multi-level qubit. As simplest such model, we calculate the dy-
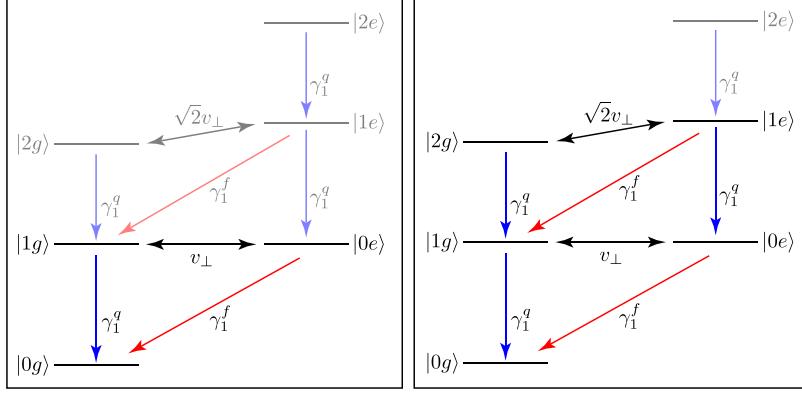
Figure 4.14.: *Illustration of the level structure of Hamiltonian Eq. (4.62) including the transitions due to transversal coupling to the baths. Blue arrows indicate qubit relaxation with rate γ_1^q, red arrows the TLS relaxation with rate γ_1^f. The left panel shows the situation for an initial state of $|\Psi_{Init}\rangle = |0e\rangle$ where the dynamics stays confined to the one-excitation subspace and the common ground-state $|0g\rangle$, while for the situation depicted in the right panel, with an initial state of $|\Psi_{Init}\rangle = |1e\rangle$, also the two-excitation subspace takes part in the dynamics and additional decoherence channels are opened. States and transitions not taking part in the dynamics are partly opaque in the illustration.*

namics of a three level qubit coupled purely transversally to a TLS. The Hamiltonian is given by

$$\hat{H} = \epsilon_{01} |1\rangle \langle 1| + (2\epsilon_{01} - \Delta) |2\rangle \langle 2| + \frac{1}{2}\tau_z \epsilon_f + \frac{1}{2}v_\perp \hat{q}\tau_x \,, \qquad (4.62)$$

with the principal qubit splitting ϵ_{01} and its anharmonicity Δ. The TLF has level splitting ϵ_f and is coupled to the qubit circuit purely transversally $\propto \hat{q}\,\tau_x$ with the coupling strength $v_\perp$. We assume zero temperature and both qubit and TLS coupled purely transversally to independent baths by the operator

$$\hat{H}_{Bath} = \frac{1}{2}\beta_{f,\perp}\tau_x \cdot \hat{X}_{f,\perp} + \frac{1}{2}\beta_{q,\perp}\hat{q} \cdot \hat{X}_{q,\perp} \,, \qquad (4.63)$$

with coupling strengths given again by β. We define the intrinsic relaxation rates of the qubit, γ_1^q, and the TLS, γ_1^f, as given in Eqs. (4.28) and (4.29). We then solve the Bloch-Redfield equations in secular approximation for the coupled system of three-level qubit and TLS for different initial states $|\Psi_{Init}\rangle$. The effective decay of the TLS is then characterized by its average decay rate Γ_{av}, as defined in Sec. 4.3.

Fig. 4.13 shows the average relaxation rate Γ_{av} of a TLS coupled to a three level qubit as a function of detuning $\delta\omega = \epsilon_{01} - \epsilon_f$ for different values of the transversal coupling strength $v_\perp$ (indicated by colors). The top panel is the result for an initial state $|\Psi_{Init}\rangle = |0e\rangle$, the TLS excited and the qubit in the ground-state. In this case

we exactly reproduce the results of Sec. 4.3, i.e. the average decay function is given by a quasi-Lorentzian function of width proportional to the qubit-TLS coupling strength $v_\perp$, centered around zero detuning. Since the initial state $|0e\rangle$ is part of the one-excitation subspace of the system, and we consider zero temperature (no excitations from the bath), the situation is exactly equivalent to the case of two strongly coupled coherent two-level systems, the case considered in Sec. 4.3.

For the initial state $|\Psi_{Init}\rangle = |1e\rangle$, both qubit and TLS in the first excited state, on the other hand, we get a different result. The lower panel in Fig. 4.13 shows the average TLS decay rate for this case. For small qubit-TLS coupling $v_\perp$ (blue line) we see a double peak structure with the second peak centered around $\delta\omega = \Delta$. At this detuning, the levels of the two-excitation subspace of the coupled system (i.e. the states $|2g\rangle$ and $|1e\rangle$) are resonant with each other and due to their coupling, additional decay channels are opened. The width of these peaks is again proportional to the coupling strength $v_\perp$, so that for stronger coupling (green and red lines) we can no longer distinguish between them and the overall rate is well described by a single peak centered around negative detunings. This behavior is general, meaning that we can include even higher qubit levels and will, for appropriately chosen initial states, get additional peaks in the average rate centered around energies corresponding to resonance of the levels in the n-excitation subspace. Fig. 4.14 shows an illustration of the relevant states and transitions for the two different initial states. As one can see in the right panel, the initial state $|1e\rangle$ gives the possibility to open additional decoherence channels.

The experimental data shown in Fig. 3.9 could thus be explained by this picture of a TLS interacting with a multi-level qubit under the explicit assumption that the higher qubit states are initially at least partly excited by the driving pulse. This assumption relies on the relatively high driving strength needed to excite the TLS. Even a small excitation probability of the high lying qubit states will significantly change the dynamical behavior of the TLS, due to the opening of additional decoherence channels.

This picture might also explain the anomalous temperature dependence. In experiment, the TLS was detuned by the amount of $\delta\omega = 0.5$ GHz while measuring the temperature dependence of the decoherence. If higher lying qubit states play a role in the dynamics, this detuning might not be sufficient to fully isolate qubit circuit and TLS. The temperature dependence of the decoherence rate will then be a superposition of the individual dependencies for each decoherence channel (cf. Sec. 4.3). The right inset in Fig. 3.10 shows the temperature dependence of the relaxation time for the qubit circuit. This also does not follow closely the theoretical expectation $T_1 \propto \tanh(\epsilon_{01}/2T)$ [90] and the total temperature dependence might be very complicated.

4.6. Collective Effects in Decoherence

An interesting new field of research of the last years is the study of so-called quantum meta-materials. This term is generally used to describe any kind of material whose properties have been engineered with a specific task in mind, often reaching parameters where no naturally occurring materials are known. This materials often consist of arrays of small functional building blocks whose effects on the material properties will then be described in a mean-field description. In quantum meta-materials, these building blocks are in general coherent systems, and their effects can be described in a collective state picture.

One such effect is the appearance of super- and sub-radiant states traditionally associated with ensembles of atoms of the same species in quantum optics [91]. Super- and sub-radiance describes the phenomenon that in coherently coupled ensembles of atoms, the coherence times of some of the coupled states differ strongly from the initial, uncoupled situation. The same situation can in principle be realized in superconducting systems, and here especially for two-level systems coupled to a superconducting qubit or a transmission line.

The use of the Bloch-redfield equations to describe decoherence of the coupled system allows for a very intuitive and simple understanding of the origin of this effect, which we give in the following. For simplicity we consider a system of only two two-level systems coupled purely transversally to each other, which is the minimal system in which super- and sub-radiance can be observed. The following considerations can easily be generalized to bigger systems.

The system is described by the Hamiltonian

$$\hat{H} = \frac{1}{2}\epsilon_1\sigma_z^{(1)} + \frac{1}{2}\epsilon_2\sigma_z^{(2)} + \frac{1}{2}v_\perp\left(\sigma_+^{(1)}\sigma_-^{(2)} + \sigma_-^{(1)}\sigma_+^{(2)}\right) + \hat{H}_{Bath}\,, \qquad (4.64)$$

with the level-splittings ϵ_i and the pauli-matrices σ. The coupling is written in the RWA and has strength $v_\perp$. The operator $\hat{H}_{Bath}$ describes the coupling of the two-level systems to their baths. In the previous sections we always considered every individual quantum system coupled to its own separate bath. In general it is also possible that decoherence is mediated by a common bath acting simultaneously on all the quantum systems. In quantum optical ensembles this common bath is given by the oscillator mode of the electromagnetic environment. Again for simplicity we here only consider transversal coupling to the baths and we give the general case, where we have both coupling to an individual bath as well as to a common bath. The bath coupling operator then has the form

$$\hat{H}_{Bath} = \frac{1}{2}\left(\beta_{1,C}\,\sigma_x^{(1)} + \beta_{2,C}\,\sigma_x^{(2)}\right)\hat{X}_C + \frac{1}{2}\sum_i \beta_i\sigma_x^{(i)}\hat{X}_i\,, \qquad (4.65)$$

where the β give the coupling strengths to the baths. The bath operator $\hat{X}_C$ characterizes the shared bath while the $\hat{X}_i$ are operators of the individual baths. We consider the situation where the two-level systems are near resonant $\epsilon_1 \approx \epsilon_2 \gg v_\perp$.

In this case the two states with either one of the two systems excited are degenerate. Due to the coupling term in Eq. (4.64) this degeneracy is lifted and analogous to the situation depicted in Fig. 4.3 a symmetric and antisymmetric superposition of the initial states is formed. We find the eigenstates of the coupled system $|-\rangle = -\cos\frac{\xi}{2}|ge\rangle + \sin\frac{\xi}{2}|eg\rangle$ and $|+\rangle = \sin\frac{\xi}{2}|ge\rangle + \cos\frac{\xi}{2}|eg\rangle$ where $|g/e\rangle$ are the ground / excited state of the individual two-level system. We denote the common ground-state as $|0\rangle = |gg\rangle$ and the fully excited state as $|3\rangle = |ee\rangle$. The angle ξ is defined as $\arctan\xi = v_\perp/\delta\omega$ with the detuning $\delta\omega = \epsilon_1 - \epsilon_2$. It is the decay of the two states $|\pm\rangle$ into the ground-state $|0\rangle$ which will show super- and sub-radiance, so we will take a close look at their relaxation rates in the Bloch-Redfield framework.

In the construction of the Redfield tensor Eq. (1.24), we add terms of the form

$$\Lambda_{nmlk} = \frac{1}{2}z_{nm}z_{lk}C_X(\omega = \omega_{kl}),\tag{4.66}$$

where z_{nm} are the matrix elements of the systems coupling operator $\hat{z}$ while C_X is the correlation function of the bath part of the coupling Hamiltonian $\hat{X}$. We also take the temperature to be small compared to the level splitting $T \ll \epsilon_i$ so that we can neglect excitations.

Our interest in the decay rates of the states $|-\rangle$ and $|+\rangle$ into the ground-state translates to calculating the Redfield-tensor elements $\mathcal{R}_{--00}$ and $\mathcal{R}_{++00}$. Analyzing them for the situation described above, we find that each is given by only one non-vanishing term of the form (4.66) and we find $\mathcal{R}_{ii00} = \Lambda_{0ii0}$, for $i = \pm$. Using Eq. (4.66) we can easily calculate the decay rates as $\mathcal{R}_{ii00} = \Lambda_{0ii0} = \frac{1}{2}|z_{0i}|^2 C_X(\omega = \omega_{i0})$. It is important to remember that for each independent bath we have to calculate separate Redfield-tensors and therefore separate rates. The complete decoherence dynamics will be given by the sum of the individual contributions from each of the baths. In the coupled eigenbasis of $\{|0\rangle, |-\rangle, |+\rangle, |3\rangle\}$ the bath coupling Hamiltonian reads

$$\hat{H}_{Bath,1} = \frac{1}{2}\beta_1 \begin{pmatrix} 0 & \cos\frac{\xi}{2} & \sin\frac{\xi}{2} & 0 \\ \cos\frac{\xi}{2} & 0 & 0 & -\sin\frac{\xi}{2} \\ \sin\frac{\xi}{2} & 0 & 0 & \cos\frac{\xi}{2} \\ 0 & -\sin\frac{\xi}{2} & \cos\frac{\xi}{2} & 0 \end{pmatrix},\tag{4.67}$$

for coupling of the first two-level system to its own bath, while for the second one we have

$$\hat{H}_{Bath,2} = \frac{1}{2}\beta_2 \begin{pmatrix} 0 & -\sin\frac{\xi}{2} & \cos\frac{\xi}{2} & 0 \\ -\sin\frac{\xi}{2} & 0 & 0 & \cos\frac{\xi}{2} \\ \cos\frac{\xi}{2} & 0 & 0 & \sin\frac{\xi}{2} \\ 0 & \cos\frac{\xi}{2} & \sin\frac{\xi}{2} & 0 \end{pmatrix}.\tag{4.68}$$

The coupling angle ξ is again defined by $\tan\xi = v_\perp/\delta\omega$. The coupling to the common bath we write as

$$\hat{H}_{Bath,C} = \hat{H}_{Bath,1} + \hat{H}_{Bath,2},\tag{4.69}$$

where we replaced the β_i by $\beta_{i,C}$. Calculating now the relevant matrix elements we can immediately understand the phenomenon of super- and sub-radiance. The rates are given by two contributions, one from the separate baths, which is the same for the decay of both states,

$$\mathcal{R}^{Sep}_{\pm\pm 00} = \frac{1}{4}\beta_1^2 \cos^2\frac{\xi}{2}C_{X_1} + \frac{1}{4}\beta_2^2 \sin^2\frac{\xi}{2}C_{X_2}\,, \tag{4.70}$$

and one from the common bath

$$\mathcal{R}^{C}_{\pm\pm 00} = \frac{1}{4}\left(\beta_{1,C}\cos\frac{\xi}{2} \pm \beta_{2,C}\sin\frac{\xi}{2}\right)^2 C_{X_C}\,. \tag{4.71}$$

Here all correlation functions C_X are evaluated at the frequency of the two-level systems ϵ. For the case when the coupling to the environment is constant $\beta_{1,C} = \beta_{2,C} = \beta_1 = \beta_2 = \beta$ and exact resonance of the two-level systems $\xi = \pi/2$ we find $\mathcal{R}^{C}_{--00} = 0$ and $\mathcal{R}^{C}_{++00} = \mathcal{R}^{Sep}_{\pm\pm 00} + 1/2\beta^2 C_{X_C}$. The decay rate of the state $|+\rangle$, known as super-radiant, is therefore faster than the decay of the state $|-\rangle$, which is is also called the sub-radiant state. Similarly for unequal coupling to the common bath, $\mathcal{R}^{C}_{--00}$ will always be smaller than $\mathcal{R}^{C}_{++00}$ by the factor $\beta_{1,C}\beta_{2,C}C_{X_C}$. The effect can in this way also be understood as constructive and destructive interference of the decoherence processes via the shared bath.

The calculations above are easily generalized to the case of an arbitrary number of two-level systems coupled to a common bath. The coupled system will in each of the n-excitation manifolds form a fully symmetric as well as a fully antisymmetric state which, due to the properties of the coupling to the environment, will show super- and sub-radiance.

These effects are notoriously difficult to observe since disorder in the couplings to the bath will average the effect to zero [91]. It has been observed in artificial crystals of single ions [92] interacting with an optical cavity. In this case the environment is given by the electromagnetic modes of the cavity into which the ions can decay spontaneously.

For solid state systems, the situation is more complicated due to the possible individual decoherence channels for each circuit. As we have seen above, the difference in super- and sub-radiance is only manifested in the coupling to a common bath. If this coupling is much weaker than individual decoherence channels, the effect might not be visible. Experimental evidence for TLS suggest that coupling to a possible common bath is very weak compared to intrinsic decoherence, and therefore the effect could to date not be seen in the data. An alternative superconducting system where these effects can be observed is the case where several transmon or flux qubits are coupled to a superconducting cavity and decay mainly via the Purcell effect [93] (which gives the exact analogue to the quantum optics case).

It is important to note that from the theory viewpoint, such an effect can only be observed in the framework of the Bloch-Redfield equations, since they describe the system in its eigenbasis. In a Lindblad description, with only individual decoherence

channels for each system, the effect does not appear.

Conclusions

In this chapter we have analyzed the effects of interactions on the dynamics of a quantum bit. We have considered the case of weak coupling to single and ensembles of TLS which we describe in an effective bath picture. In this picture each TLSs influence on the qubit can be characterized by an effective correlation function. This description enables us to describe the ubiquitous $1/f$-noise spectra as stemming from an ensemble of tunneling two-level systems. Ohmic, high-frequency noise might also be caused by the same ensemble of TLS.

Additionally we analyzed the case of strong qubit-TLS coupling in the case where both qubit and TLS are coherent. In this case we solve for the dynamics of the coupled systems and characterize the evolution by effective decoherence rates. We find that multiple TLS in resonance will emulate a single, strongly coupled TLS in the qubit dynamics. This results shows that the strong anti-crossings observed in qubit spectroscopy might also be caused not by single TLS but by an ensemble of near resonant, weakly coupled ones. However, the experimental results contradict this findings and point in the direction of single two-level systems.

Further, we calculated the effects when coupling a TLS to a multi-level qubit. The results allow us to speculate on the explanation for recently observed asymmetric decoherence properties of a TLS near resonance with a phase qubit.

Finally, we provided some calculations regarding the effects of super- and subradiance. These are collective effects which might be observable in quantum metamaterials, fabricated using superconducting transmon or flux qubit coupled to a common transmission line resonator.

5. Holonomies in Superconducting Systems

In this chapter we develop a way to realize holonomic, topologically protected gates for quantum information processing in a superconducting circuit quantum electrodynamics architecture. We consider a transmission line resonator coupled off-resonantly to three transmon qubits while driving each qubit individually via its flux bias. We will demonstrate that this scheme can be described by the tripod Hamiltonian introduced in Ch. 1 and demonstrate the operation of standard gates in this system for experimentally feasible parameters.

Introduction

This chapter presents a deviation from the main theme of this thesis. As we have seen in the above, all solid state devices in general and especially superconducting qubits, with their need for long decoherence times, suffer from the inevitable coupling to a decohering environment. An additional problem are imprecise gate controls, either because experimental parameters of the circuits are not known with sufficient precision or because of restrictions on the pulse shape. As a possible solution to overcoming these problems in quantum information processing, holonomic quantum computing was proposed [58] (cf. Sec. 1.4).

Abelian holonomies, also called geometric phases or Berry phases, have been observed in a wide variety of systems including superconducting qubits [94, 95] The situation is quite different for non-Abelian holonomies necessary for universal geometric quantum computing. Despite a variety of theoretical proposals [96–100], to date no such transformation has been experimentally observed in superconducting qubits.

Here we propose a way to implement a non-trivial holonomic gate in a superconducting circuit. We use the architecture know as circuit quantum electrodynamics (cQED) [101] in which superconducting qubits, or artificial atoms, are coupled to a common cavity resonance. The most successful realizations of this architecture rely on either phase or transmon qubits coupled to superconducting transmission line resonators. For both implementations, three-qubit entanglement has recently been shown successfully [102, 103].

In the relevant parameter regime, these systems are well described by the well-

known Tavis-Cummings Hamiltonian

$$\hat{H} = \omega\hat{a}^\dagger\hat{a} + \frac{1}{2}\sum_n \epsilon_n \sigma_z^{(n)} + \frac{1}{2}\sum_n g_n\left(\sigma_+^{(n)}\hat{a} + \sigma_-^{(n)}\hat{a}^\dagger\right), \tag{5.1}$$

where ω is the frequency of the cavity mode, ϵ_n the level-splitting of the n-th qubit and g_n is its coupling strength to the cavity. The σ are pauli-matrices and $\hat{a}$ is the bosonic annihilation operator of cavity photons. The above Hamiltonian Eq. (5.1) is restricted to the case where the couplings are much smaller than all level-splittings, $g \ll \omega, \epsilon$, in order for the rotating wave approximation to be valid. Most experiments with the cQED architecture are performed in this parameter regime.

In our proposal, we will focus on transmon qubits as artificial atoms, but the employed method can easily be generalized to phase or also flux-qubits. A transmon qubit [14] is a variation on the cooper-pair box design [5] adding a large shunting capacitor with the goal to flatten the charge dispersion. As a result, this circuit is virtually immune to charge noise, which manifests in its long relaxation times $T_1 \sim \mu s$ and T_1-limited dephasing $T_2 \approx 2T_1$ [104]. Additional tuneability is added by replacing the single Josephson junction with a double JJ SQUID design [105], where the effective Josephson energy can be tuned with an external flux line.

This chapter is organized as follows: In the first part we will introduce the physical system in which we propose to implement a holonomic transformation. The second section will then show how we can realize the tripod Hamiltonian, introduced in Sec. 1.4, in this system. The last part will be dedicated to the actual implementation of the gate. We will show a pulse sequence realizing a holonomic NOT-gate and verify our results using numerical simulations.

5.1. Physical Realization

The physical system we will consider is given by a cavity coupled to three transmon qubits. Each transmon is detuned from the cavity by an amount $\Delta_n = \epsilon_n - \omega$. In the relevant parameter regime, this system is well described by the Hamiltonian Eq. (5.1). Furthermore, we restrict ourselves to the one-excitation subspace of this systems, spanned by the states $\{|1ggg\rangle, |0egg\rangle, |0geg\rangle, |0gge\rangle\}$. Here, $|n\rangle$ denotes the n-photon Fock-state in the cavity while $|g/e\rangle$ denotes ground- / excited state of the transmons. An illustration of the level structure of this system, including the common ground state $|0ggg\rangle$, is given in Fig. 5.1.

In the one-excitation subspace, the Hamiltonian can be written as

$$\hat{H} = \begin{pmatrix} 0 & g_1 & g_2 & g_3 \\ g_1 & \Delta_1 & 0 & 0 \\ g_2 & 0 & \Delta_2 & 0 \\ g_3 & 0 & 0 & \Delta_3 \end{pmatrix}, \tag{5.2}$$

with g and Δ as defined above. For all transmons resonant with the cavity $\Delta = 0$,
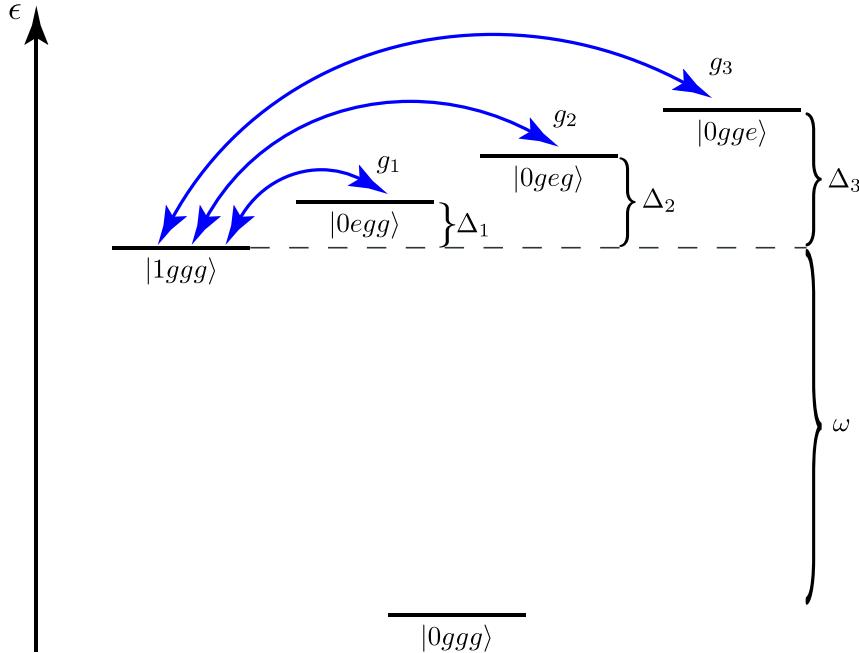
Figure 5.1.: *Illustration of the level structure of an electromagnetic cavity mode coupled to three transmon qubits. Each transmon is detuned from the cavity resonance ω by the detuning Δ_i and coupled to it with the coupling strength g_i. Only the ground state and the one-excitation subspace is shown here.*

we would obtain a tripod structure, but would have no way of changing the coupling strengths g and therefore could not realize any Holonomies. Our scheme now relies on driving each of the transmon qubits individually via its flux line while keeping them detuned from the cavity and also detuned from each other. This will give us the desired tripod structure of the Hamiltonian in a rotation frame where the effective Rabi-frequencies will be given by a combination of second order transitions induced by the driving and contributions from the direct transmon-cavity coupling g.

Varying the external flux Φ_{Ext} through a transmon SQUID loop changes the effective Josephson energy of the circuit according to $E_J(\phi_{Ext}) = E_{J,0} \cos \phi_{Ext}/2$. Here the phase drop corresponding to the external flux has been defined as $\phi_{Ext} = (2\pi/\Phi_0) \Phi_{Ext}$, with the flux quantum $\Phi_0 = h/2e$. $E_{j,0}$ is the maximum Josephson energy of the loop, for equal junctions it is exactly twice the single JJ E_J.

A change of the external flux applied to one of the transmons therefore changes its effective Josephson energy and through this, its level-splitting ϵ_n. Since the coupling to the electromagnetic field of the cavity is via the dipole moment d of the transmon, and we have $d \propto \sqrt{\epsilon}$, a change in the level-splitting will also modify the coupling.

Explicitly, we have [14]

$$\epsilon_n(\phi_{Ext,n}) = \sqrt{8E_C^{(n)} E_{J,0}^{(n)} |\cos \phi_{Ext,n}/2|}$$

$$g_n(\phi_{Ext,n}) = k_n \left[\cos \phi_{Ext,n}/2\right]^{\frac{1}{4}} \tag{5.3}$$

where the constant k_n depends on the physical parameters of the particular experiment and can be determined experimentally.

In order to reach a necessary working point, each of the transmons will have to be biased with an initial constant external flux $\phi_{Ext}^{(0)}$. On top of this constant driving, we will apply a small time dependent drive with a frequency that will be determined below. We denote the initial bias point with the superscript (0) and write

$$\phi_{Ext,n}(t) = \phi_{Ext,n}^{(0)} + \delta\phi_{Ext,n}(t) \,,$$
$$\Delta_n(t) = \Delta_n^{(0)} + \delta\Delta_n(t) \,,$$
$$g_n(t) = g_n^{(0)} + \delta g_n(t) \,,$$
$$\hat{H}(t) = \hat{H}^{(0)} + \delta\hat{H}(t) \,. \tag{5.4}$$

We assume the flux modulation to be small compared to the flux quantum, i.e. $\delta\phi_{Ext,n}(t) \ll 2\pi$, and use a first order expansion in $\delta\phi_{Ext,n}$ to obtain the time dependent quantities. Because the cavity frequency ω is independent of the flux, we have $\delta\Delta_n = \delta\epsilon_n$. Together with $g_n(\phi) \propto \sqrt{\epsilon_n(\phi)}$ we find a useful relation between the change in coupling and the change in detuning

$$\frac{\delta g_n}{g_n^{(0)}} = \frac{\delta\Delta_n}{2\epsilon_n^{(0)}} \,, \tag{5.5}$$

which is valid to first order in $\delta\phi_{Ext,n}$. Since typically $g_n \ll \epsilon_n$, the driving via the flux has a much smaller relative effect on the transmon-cavity coupling g_n than on the detuning $\delta\Delta_n$.

5.2. Effective Tripod Hamiltonian

In a first step towards obtaining the desired tripod structure, we assume that the driving $\delta\hat{H}(t)$ will lead to transitions between the eigenstates of the Hamiltonian $\hat{H}$. We therefore diagonalize $\hat{H}(t)$ up to first order in $g_n^{(0)}/\Delta_n^{(0)}$ and obtain

$$\hat{H}^D(t) = \begin{pmatrix} 0 & \delta_1(t) & \delta_2(t) & \delta_3(t) \\ \delta_1(t) & E_1 + \delta\Delta_1(t) & 0 & 0 \\ \delta_2(t) & 0 & E_2 + \delta\Delta_2(t) & 0 \\ \delta_3(t) & 0 & 0 & E_3 + \delta\Delta_3(t) \end{pmatrix} \,, \tag{5.6}$$

where $\delta_n(t) = \delta g_n(t) - \frac{g_n^{(0)}}{\Delta_n^{(n)}}\delta\Delta_n(t)$ and the eigenenergies to first order can be found as

$$E_n = \Delta_n^{(0)} + \frac{2(g_n^{(0)})^2}{\Delta_n^{(0)}} + \sum_{m \neq n} \frac{2(g_m^{(0)})^2}{\Delta_m^{(0)}} \, . \tag{5.7}$$

We now assume the time dependent fluxes $\delta\phi_{Ext,n}(t)$ to oscillate at frequencies ω_n and write

$$\begin{aligned}
\delta\phi_{Ext,n}(t) &= F_n(t)\cos\left(\omega_n t + \varphi_n(t)\right), \\
\delta\Delta_n(t) &= L_n(t)\cos\left(\omega_n t + \varphi_n(t)\right), \\
\delta g_n(t) &= T_n(t)\cos\left(\omega_n t + \varphi_n(t)\right),
\end{aligned} \tag{5.8}$$

where later we will change the amplitude $F(t)$ and the relative phases $\varphi(t)$ adiabatically in time to realize the Holonomy. Looking at Eq. (5.3) we can find the relation between the amplitudes of energy and coupling L_n and T_n and the external flux drive F_n.

We insert the parametrisation Eq. (5.8) into the Hamiltonian Eq. (5.6) and transform into the rotating frame with respect to each of the transmon drives ω_n. It is then clear that the driving frequencies have to be equal to the eigenenergies Eq. (5.7) so that this transformation will rid us of the constant diagonal elements in the Hamiltonian Eq. (5.6). For the Hamiltonian of the one excitation subspace in the rotating frame we obtain

$$\begin{aligned}
\hat{H}^D(t) &= \sum_{n=1}^{3} \Omega_n(t)\left(1 + e^{-2i(\omega_n t + \varphi_n(t))}\right)|0\rangle\langle n| + \text{h.c.} \\
&+ \sum_{n=1}^{3} L_n(t)\cos\left(\omega_n t + \varphi_n(t)\right)|n\rangle\langle n| \, ,
\end{aligned} \tag{5.9}$$

where we already defined the effective Rabi-frequencies

$$\begin{aligned}
\Omega_n(t) &= \left(\frac{T_n(t)}{2} - \frac{g_n^{(0)}L_n(t)}{2\Delta_n^{(0)}}\right)e^{i\varphi_n(t)} \\
&= L_n(t)\left(\frac{g_n^{(0)}}{4\epsilon_n^{(0)}} - \frac{g_n^{(0)}}{2\Delta_n^{(0)}}\right)e^{i\varphi_n(t)} \, ,
\end{aligned} \tag{5.10}$$

and we used Eq. (5.5) in the second line. We see that we have two qualitatively different contributions to the effective Rabi frequencies Ω_n, one stemming from the direct coupling between transmons and cavity $\Omega_{Dir,n} \propto g_n^{(0)}/4\epsilon_n^{(0)}$ and the other one due to second order transitions induced by the flux driving $\Omega_{Ind,n} \propto g_n^{(0)}/2\Delta_n^{(0)}$.

We now perform another rotating wave approximation on the Hamiltonian Eq. (5.9) to finally arrive at the desired tripod Hamiltonian, Eq. (1.66), with the effective Rabi-frequencies $\Omega_n(t)$ as defined above. It is important to note here that the time

varying diagonal and off-diagonal parts in Eq. (5.9) oscillate at different frequencies so that we can neglect both contributions in the RWA.

For negative detunings, i.e. $\omega > \epsilon_n^{(0)}$, the direct coupling due to T_n (variation of the direct transmon-cavity coupling, Ω_{Dir}) and the indirect coupling due to L_n (variation of the detuning, Ω_{Ind}) add up, thus increasing the strength of the effective coupling. Depending on the ratio between the detuning and the transmon level-splittings we find two different regimes. For $|\Delta_n^{(0)}| \ll \epsilon_n^{(0)}$ the second contribution dominates. We will call this the small detuning regime. If $|\Delta_n^{(0)}| \gg \epsilon_n^{(0)}$ however, we are in the large detuning regime and the first contribution dominates. Both regimes yield the tripod form of the effective Hamiltonian, but require strongly different experimental parameters. Since the standard cQED setups are all in the small detuning regime [102, 103], we will focus on this range of parameters below.

We will say some words on the approximations made to derive the effective tripod Hamiltonian. Two main assumptions of the parameters are needed for the derivation. First, we assumed $g_n^{(0)}/\Delta_n^{(0)} \ll 1$ in order to arrive at the Hamiltonian in the rotating frame, Eq. (5.9). There exist higher order terms in $g_n^{(0)}/\Delta_n^{(0)}$ which might seem to destroy the ideal tripod structure, but they can all be removed by the RWA. However, higher order terms will lower the effective coupling, Eq. (5.10), and also lead to a slight change in the optimal driving frequencies, Eq. (5.7). Second, the RWA requires $L_n \ll \omega_n \approx \Delta_n^{(0)}$. These relations limit the available effective coupling strength of the indirect coupling term in Eq. (5.10). The direct coupling is in turn bound by the requirement $g_n^{(0)} \ll \epsilon_n^{(0)}$, which is necessary for the Tavis-Cummings model, Eq. (5.1), to hold.

To realize a holonomic gate with the currently available experimental parameters (decoherence times, transmon-cavity coupling strength, magnitude of flux driving), the detuning $\Delta_n^{(0)}$ will have to be strongly reduced and we will reach the limit of the above approximations. If they still hold for realistic parameters will be investigated in the following section.

5.3. Implementation of the Holonomic NOT-Gate

In this section we will introduce a particular implementation of a holonomic gate and then verify our derivation of the effective tripod structure of the Hamiltonian. We do this by comparing the operation of the gate fro the effective tripod Hamiltonian with a full numerical integration of the Hamiltonian Eq. (5.2) for the same parameters.

We first give the adiabatic pulse sequence for a specific gate, the holonomic NOT-gate. We choose to work with a particular implementation of non-Abelian operators proposed in Refs. [60, 61], in which the effective Rabi frequencies Ω_i in Eq. (5.10)
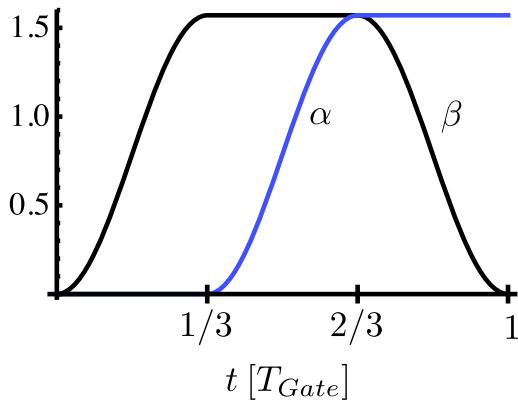
are real (i.e., $\varphi_n = 0$) and parameterized as

$$\begin{aligned}
\Omega_1 &= \Omega \sin \beta \cos \alpha \,, \\
\Omega_2 &= \Omega \sin \beta \sin \alpha \,, \\
\Omega_3 &= \Omega \cos \beta \,,
\end{aligned} \tag{5.11}$$

where we assume the amplitude Ω to be constant and change the angles α and β adiabatically in time. In this parametrisation, the two zero-energy dark states of the tripod Hamiltonian are given by

$$\begin{aligned}
|d_1\rangle &= \cos \beta \left(\cos \alpha \, |1\rangle + \sin \alpha \, |2\rangle \right) - \sin \beta \, |3\rangle \,, \\
|d_2\rangle &= \cos \alpha \, |2\rangle - \sin \alpha \, |1\rangle
\end{aligned} \tag{5.12}$$

where $|i\rangle$ are the states in which the tripod Hamiltonian Eq. (1.66) is written.

Figure 5.2.: *Pulse scheme for the parameters α (blue) and β (black) as a function of time in units of the total gate time T_{Gate}. This pulse with the parametrisation Eq. (5.11) in the tripod Hamiltonian will lead to a holonomic NOT-gate.*

The evolution in parameter space begins and ends at the point $(\Omega_1, \Omega_2, \Omega_3) = (0, 0, \Omega)$. Writing the dark states of the tripod Hamiltonian explicitly, using Eq. (5.12), we obtain the initial zero-energy subspace. It is spanned by the states $\{|1\rangle, |2\rangle\}$ in the tripod basis. These states are the basis states of our logical qubit.

The change of the angles α and β according to

$$(\alpha(t), \beta(t)) : (0, 0) \to (0, \pi/2) \to (\pi/2, \pi/2) \to (\pi/2, 0), \tag{5.13}$$

will then result, up to a phase factor, in a holonomic NOT gate $U_{NOT} = |1\rangle \langle 2| - |2\rangle \langle 1|$ for this logical qubit. Assuming an initial state $|\Psi(t = 0)\rangle = |1\rangle$, the application of this gate leads ideally to a final state of $|\Psi(t = T_{Gate})\rangle = |2\rangle$. Note that because of the spherical parameterization, Eq. (5.11), our Hamiltonian is cyclic under the transformation eq. (5.13). The enclosed solid angle in the (α, β) parameter space is simply 1/8 of a full sphere [106]. To achieve stronger adiabaticity, we will

change the angles smoothly using sine functions and constants. The pulse scheme we employ in our simulations is shown in Fig. 5.2.

To implement this loop in our setup, one has to change the flux driving amplitudes $L_n(t)$ adiabatically and for each transmon individually. Together with the relations Eq. (5.10) one finds the necessary adiabatic change in the Rabi frequencies.

The computational state are given by the eigenstates of the Hamiltonian in the one-excitation subspace, Eq. (5.2). For small $g_n^{(0)}/\Delta_n^{(0)}$, the logical states are simply $|1\rangle = |0egg\rangle$ and $|2\rangle = |0geg\rangle$ as defined above. This enables particularly easy initialization and readout in this scheme, since we only have to manipulate and characterize the state of two of the transmons to determine the gate operation.

In order to quantify the operation of the holonomic gate, we define a fidelity $F(t) = |\langle \Psi_{Ideal}(t)|\Psi(t)\rangle|^2 = |\langle 2|\Psi(t)\rangle|^2$, simply given by the population of state $|2\rangle$ in the final state after time t.
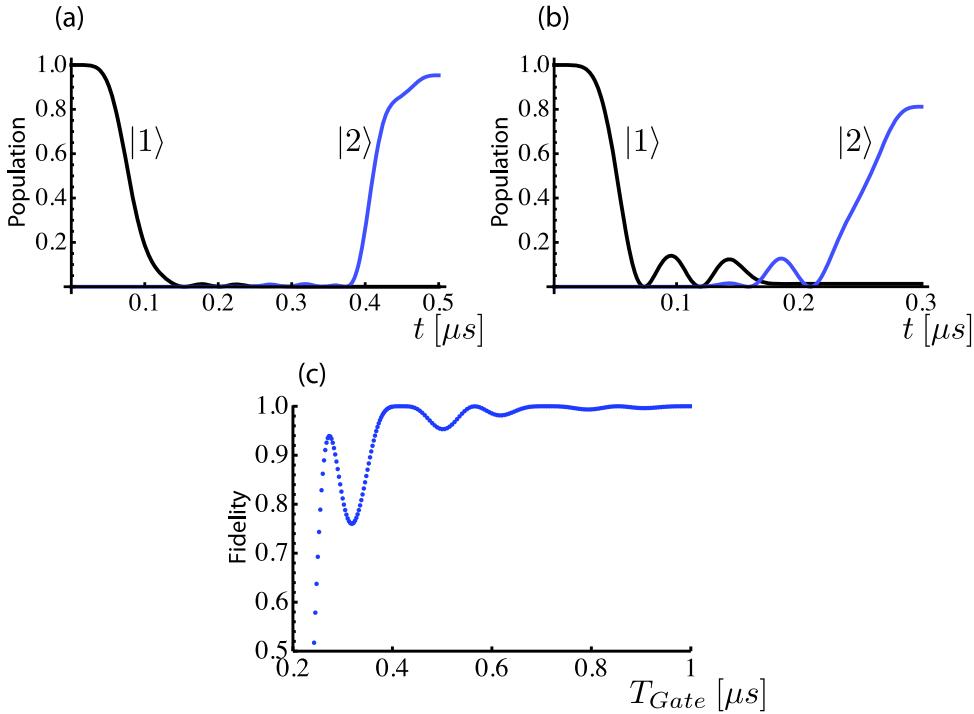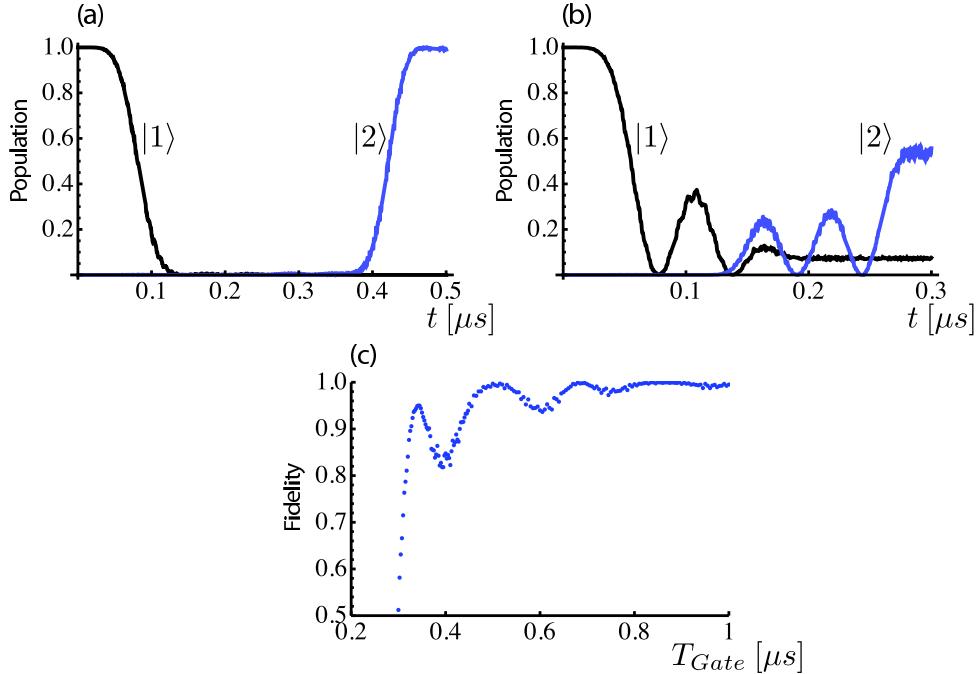

Figure 5.3.: *Results from numerical integration of the Schrödinger equation using the effective tripod Hamiltonian, Eq. (1.66), with effective Rabi amplitudes of $\Omega/2\pi = 10.5$ MHz. Panels (a) and (b) show the population of the logical qubit states $|1\rangle$ (black) and $|2\rangle$ (blue). For a total gate time of $T_{Gate} = 0.5 \ \mu s$ (a) we see good transfer of population while for $T_{Gate} = 0.3 \ \mu s$ (b) the transfer is no longer complete. Panel (c) shows the fidelity of the gate as a function of the gate time T_{Gate}.*

In Fig. 5.3 we show the integrated dynamics of the ideal tripod Hamiltonian, Eq. (1.66), with the Rabi frequencies determined using experimentally feasible parameters. Specifically, we use a cavity frequency of $\omega/2\pi = 5$ GHz, detunings

of the individual transmons of $\Delta_1^{(0)}/2\pi = -300$ MHz, $\Delta_2^{(0)}/2\pi = -400$ MHz and $\Delta_3^{(0)}/2\pi = -500$ MHz, transmon cavity coupling strengths of $g_1^{(0)}/2\pi = 60$ Mhz, $g_2^{(0)}/2\pi = -80$ Mhz and $g_3^{(0)}/2\pi = 100$ Mhz. The magnitude of the longitudinal driving is restricted to $L_n(t) \leq 100$ MHz. With these parameters we arrive at Rabi amplitudes of $\Omega = 10.5$ MHz, where the main contribution comes from the indirect coupling $\Omega_{Ind} = 10$ MHz while the direct coupling part contributes $\Omega_{Dir} = 0.5$ MHz.

Fig. 5.3 (a) and (b) show the time evolution of the logical qubit states $|1\rangle$ and $|2\rangle$ as a function of time for two different total gate times T_{Gate}. For longer gate times, adiabaticity is better and the the population is transferred with high probability. Fig. 5.3 (c) shows the gate fidelity as defined above as a function of total gate time T_{Gate} using the same parameters. We see that for gate times $T_{Gate} > 0.6$ μs, the fidelity approaches unity. Note that the oscillatory behavior of the fidelity is typical for adiabatic gates [106].

Figure 5.4.: *Results from numerical integration of the Schrödinger equation using the exact Hamiltonian Eq. (5.2). Panels (a) and (b) show the population of the logical qubit states $|1\rangle$ and $|2\rangle$ for total gate times of $T_{Gate} = 0.5$ μs (a) and $T_{Gate} = 0.3$ μs (b). Panel (c) shows again the fidelity as a function of the gate time T_{Gate}. The results are in good agreement with the calculations in the effective tripod picture, Fig. 5.3.*

In Fig. 5.4 we show the results of a numerical integration of the exact Hamiltonian Eq. (5.2) for comparison. We use the same parameters as in Fig. 5.3 above to be able to quantify the approximations we used in the derivation of the tripod structure. The result show good agreement with the calculations for the effective

tripod Hamiltonian, Fig. 5.3. The main difference is a rescaling of the gate time to reach maximum fidelity in Fig. 5.4 (c) as compared to Fig. 5.3 (c). The reason for this rescaling is that for our parameters we have $g_n^{(0)}/\Delta_n^{(0)} = 0.2$, a value which is not small enough to perfectly justify the approximation $g_n^{(0)}/\Delta_n^{(0)} \ll 1$. Therefore the effective coupling Ω is somewhat smaller than given in Eq. (5.10), as described in the previous section. In total this still shows that the approximations we made in obtaining the tripod Hamiltonian are well justified in the experimentally accessible parameter range.
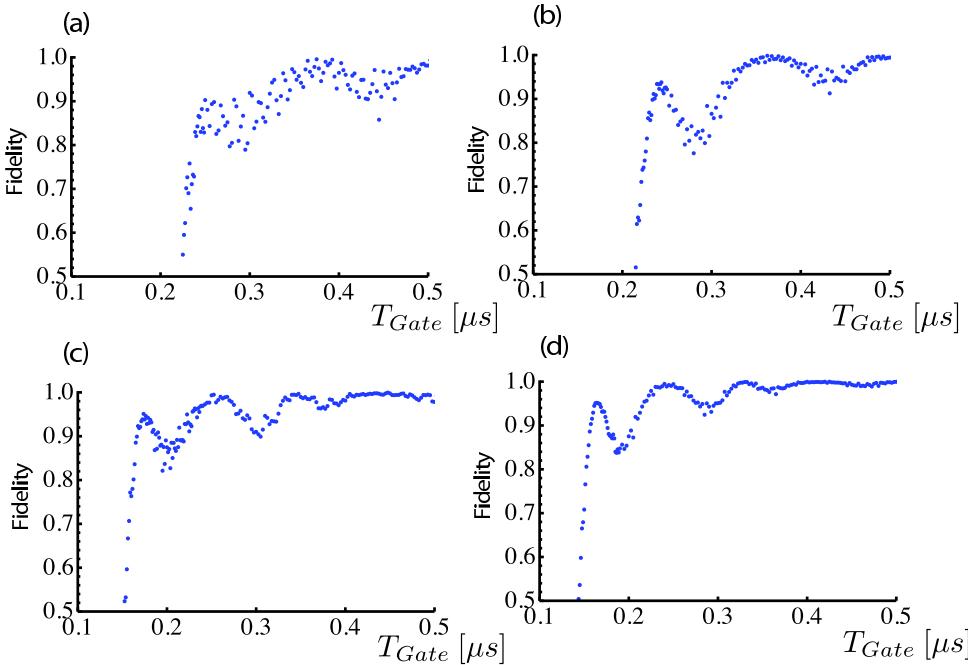
Figure 5.5.: *Fidelity as a function of time obtained from numerical integration of the exact Hamiltonian, Eq. (5.2) for stronger effective coupling Ω. This is achieved by using (a) half the detuning $\Delta_n^{(0)}$, $\Omega = 20.5$ MHz, (b) double transmon-cavity coupling $g_n^{(0)}$, $\Omega = 21$ MHz, (c) twice the magnitude of flux driving L_n, $\Omega = 21$ MHz and (d) twice of all of these parameters, $\Omega = 22$ MHz. For each case, the minimum gate time to reach acceptable fidelities is effectively halved as compared to the previous case.*

A note on decoherence in this scheme: In general it is desirable to perform holonomic gates in the ground-state manifold of a Hamiltonian. Then for small enough temperatures the resulting gates are not affected by decoherence, since relaxation will not take us out of the ground-state and dephasing is equivalent to variations of the control parameters to which our gate is to first order insensitive. Our scheme presented here, however, performs the computation in the one-excitation subspace of the Tavis-Cummings model, and will therefore be susceptible to relaxation into the common ground-state $|0ggg\rangle$ of the system. Since the relaxation times of trans-

mons to date are of the order of $\sim \mu$s, one will have to perform the computation in times which are significantly smaller than the relaxation time T_1 of the transmons. In Fig. 5.5 we show the fidelity as a function of gate time T_{Gate} for various scenarios where the effective coupling strength is always roughly double the value of the previous simulations. The experimentally most easily accessible situation is the one depicted in Fig. 5.5 (a), where we simple decrease the detunings $\Delta_n^{(0)}$ ba a factor of two. However, the fidelity in this case is not very good. The reason for this is simply that the conditions $\Delta_n^{(0)} \gg g_n^{(0)}, L_n$, necessary in the derivation of the tripod structure, are no longer fulfilled. The situation is somewhat better in Fig. 5.5 (b) and (c) where the increase in effective coupling is achieved by increasing the transmon-cavity couplings $g_n^{(0)}$ and the amplitude of the flux drive L_n, respectively. The only way to increase the effective couplings without affecting any of the necessary approximations is to simultaneously increase $g_n^{(0)}$, L_n and $\Delta_n^{(0)}$, which is depicted in Fig. 5.5 (d). However, it might be experimentally challenging to achieve such high values of coupling strength g and flux driving L.

Conclusions

We presented a scheme to implement a non-abelian holonomic gate in superconducting circuits. The scheme uses three transmon qubit coupled to a common cavity resonance. Each transmon is driven longitudinally and the driving is changed adiabatically to achieve the holonomy. This scheme is experimentally feasible using current state-of-the-art techniques. Unfortunately it may only serve as proof of principle, since the system we propose is still affected by decoherence. However, it may show that geometric quantum computation is possible in superconducting circuits.

Conclusion

The interaction of superconducting circuits with additional quantum systems is a topic that has found extensive study in the recent past. In the limit where the added system are incoherent, this is the standard field of decoherence and the system dynamics can be described by a simple master equation. In the other limit however, when the additional parts are coherent, the resulting time-evolution can become more complicated.

In this thesis we have investigated the interaction of superconducting circuits with coherent and incoherent two-level defects. We have shown theoretical calculations characterizing this interaction for all relevant parameter regimes. In the weak coupling limit, the interaction can be described in an effective bath picture, where the TLS act as parts of a large, decohering environment. For strong coupling, however, the coherent dynamics of the full coupled system has to be considered. We show the calculations of the coupled time-evolution and again characterize the interaction by an effective decoherence rate.

We also used experimental data to characterize the microscopic origin of the defects and the details of their interaction with the circuits. The results obtained by analyzing spectroscopic data allow us to place strong constraint on several microscopic models for the observed TLS. However, these calculations are not yet fully conclusive as to the physical nature of the TLS. We propose additional experiments to fully characterize the interaction part of the Hamiltonian, thus providing the answer to the question of the physical origin of the coupling.

Additionally we have developed a method to directly drive individual defect states via virtual excitation of the qubit. This method allows one to directly probe the properties of single TLS and possibly make use of their superior coherence times for quantum information purposes.

The last part of this thesis provided a way for a possible implementation of geometric quantum computation in superconducting circuits. The proposal is focused on three transmons in a cQED architecture and is experimentally feasible with current parameters. This scheme provides the possibility for a first demonstration of non-abelian holonomies in physical systems.

Bibliography

[1] M. A. Nielsen and I. L. Chuang. *Quantum computation and Quantum information*. Cambridge University Press, 2005.

[2] J. L. O'Brien. Optical quantum computing. *Science*, 318:1567–1570, 2007.

[3] J. I. Cirac and P. Zoller. Quantum computation with cold trapped ions. *Phys. Rev. Lett.*, 74:4091–4094, 1995.

[4] M. Anderlini, P. J. Lee, B. L. Brown, J. Sebby-Strabley, W. D. Phillips, and J. V. Porto. Controlled exchange interaction between pairs of neutral atoms in an optical lattice. *Nature*, 448:452–456, 2007.

[5] A. Shnirman, G. Schön, and Y. Makhlin. Quantum manipulations of small josephson junctions. *Phys. Rev. Lett.*, 79:2371–2374, 1997.

[6] J. E. Mooij, T. P. Orlando, L. Levitov, L. Tian, C. H. van der Waal, and S. Lloyd. Josephson persistent current qubit. *Science*, 285:1036, 1999.

[7] J. Clarke, A. N. Cleland, M. H. Devoret, D. Esteve, and J. M. Martinis. Quantum mechanics of a macroscopic variable: The phase difference of a josephson junction. *Science*, 239:992, 1988.

[8] Quantum computation roadmap. URL http://qist.lanl.gov/qcomp_map.shtml.

[9] A. Aspect, P. Grangier, and G. Roger. Experimental test of realistic local theories via bell's theorem. *Phys. Rev. Lett.*, 47:460–463, 1981.

[10] C. Roos, G. P. T. Lancaster, M. Riebe, H. Häffner, W. Hänsel, S. Gulde, C. Becher, J. Eschner, F. Schmidt-Kaler, and R. Blatt. Bell states of atoms with ultralong lifetimes and their tomographic state analysis. *Phys. Rev. Lett.*, 92:220402, 2004.

[11] M. Ansmann, H. Wang, R. C. Bialczak, M. Hofheinz, E. Lucero, M. Neeley, A. D. O'Connell, D. Sank, M. Weides, J. Wenner, A. N. Cleland, and J. M. Martinis. Violation of bell's inequalities in josephson phase qubits. *Nature*, 461:504–506, 2009.

[12] B. D. Josephson. Possible new effects in superconductive tunneling. *Physics Letters*, 1:251–253, 1962.

[13] D. Vion, A. Aassime, A. Cottet, P. Joyez, H. Pothier, C. Urbina, D. Esteve, and M. H. Devoret. Manipulating the quantum state of an electrical circuit. *Science*, 296:886, 2002.

[14] J. Koch, T. M. Yu, J. Gambetta, A. A. Houck, D. I. Schuster, J. Majer, A. Blais, M. H. Devoret, S. M. Girvin, and R. J. Schoelkopf. Charge-insensitive qubit design derived from the cooper pair box. *Phys. Rev. A*, 76:042319, 2007.

[15] M. Sandberg, C. M. Wilson, F. Persson, T. Bauch, G. Johansson, V. Shumeiko, T. Duty, and P. Delsing. Tunig the field in a microwave resonator faster than the photon lifetime. *Applied Physics Letters*, 92:203501, 2008.

[16] R. Vijay, D. H. Slichter, and I. Siddiqi. Observation of quantum jumps in a superconducting artificial atom. *Phys. Rev. Lett.*, 106:110502, 2011.

[17] J. Clarke. private communication, 2011.

[18] P. Dutta and P. M. Horn. Low-frequency fluctuations in solids: 1/f noise. *Rev. Mod. Phys.*, 53:497–516, 1981.

[19] W. A. Phillips. Tunneling states in amorphous solids. *Journal of Low Temperature Physics*, 7:351, 1972.

[20] P. W. Anderson, B. I. Halperin, and C. M. Varma. Anomalous low-temperature thermal properties of glasses and spin glasses. *Philosophical magazine*, 25:1–9, 1972.

[21] P. Esquinazi, editor. *Tunneling Systems in Amorphous and Crystalline Solids.* Springer, Berlin, 1998.

[22] O. Arcizet, R. Rivière, A. Schliesser, G. Anetsberger, and T. J. Kippenberg. Cryogenic properties of optomechanical silica microcavities. *Phys. Rev. A*, 80: 021803(R), 2009.

[23] A. Venkatesan, K. J. Lulla, M. J. Patton, A. D. Armour, C. J. Mellor, and J. R. Owers-Bradley. Dissipation due to tunneling two-level systems in gold nanomechanical resonators. *Phys. Rev. B*, 81:073410, 2010.

[24] C. Kaiser, S. T. Skacel, S. Wünsch, R. Dolata, B. Mackrodt, A. Zorin, and M. Siegel. Measurement of dielectric loss in amorphous thin films at gigahertz frequencies using superconducting resonators. *Supercond. Sci. Technol.*, 23: 075008, 2010.

[25] A. Shnirman, G. Schön, I. Martin, and Y. Makhlin. Low- and high-frequency noise from coherent two-level-systems. *Phys. Rev. Lett.*, 94:127002, 2005.

[26] L. Kakuyanagi, T. Meno, S. Saito, H. Nakano, K. Semba, H. Takayanagi, F. Deppe, and A. Shnirman. Dephasing of a superconducting flux qubit. *Phys. Rev. Lett.*, 98:047004, 2007.

[27] O. Astafiev, Y. A. Pashkin, Y. Nakamura, T. Yamamoto, and J. S. Tsai. Quantum noise in the josephson charge qubit. *Phys. Rev. Lett.*, 93:267007, 2004.

[28] A. Shnirman, G. Schön, I. Martin, and Y. Makhlin. Josephson qubits as probes of 1/f noise. In *Proceedings of the CFN Summer School "Nanoelectronics"*, 2005.

[29] R. W. Simmonds, K. M. Lang, D. A. Hite, S. Nam, D. P. Pappas, and J. M. Martinis. Decoherence in josephson phase qubits from junction resonators. *Phys. Rev. Lett.*, 93:077003, 2004.

[30] K. B. Cooper, M. Steffen, R. McDermott, R. W. Simmonds, S. Oh, D. A. Hite, D. P. Pappas, and J. M. Martinis. Observation of quantum oscillations between a josephson phase qubit and a microscopic resonator using fast readout. *Phys. Rev. Lett.*, 93:180401, 2004.

[31] A. Lupascu, P. Bertet, E. F. C Driessen, C. J. P. M Harmans, and J. E Mooij. One- and two-photon spectroscopy of a flux qubit coupled to a microscopic defect. *Phys. Rev. B*, 80:172506, 2009.

[32] Z. Kim, V. Zaretskey, Y. Yoon, J. F. Schneiderman, M. D. Shaw, P. M. Echternach, F. C. Wellstood, and B. S. Palmer. Anomalous avoided level crossing in a cooper-pair box spectrum. *Phys. Rev. B*, 78:144506, 2008.

[33] P. Bushev, C. Müller, J. Lisenfeld, J. H. Cole, A. Lukashenko, A. Shnirman, and A. V. Ustinov. Hybrid quantum system surveyed using multi-photon spectroscopy. *Phys. Rev. B*, 82:134530, 2010.

[34] M. Neeley, M. Ansmann, R. C. Bialczak, M. Hofheinz, N. Katz, E. Lucero, A. O'Connel, H. Wang, A. N. Cleland, and J. M. Martinis. Process tomography of quantum memory in a josephson-phase qubit coupled to a two-level state. *Nat. Phys.*, 4:523–526, 2008.

[35] J. Lisenfeld, C. Müller, J. H. Cole, P. Bushev, A. Lukashenko, A. Shnirman, and A. V. Ustinov. Measuring the temperature dependence of individual two-level systems by direct coherent control. *Phys. Rev. Lett.*, 105:230504, 2010.

[36] A. M. Zagoskin, S. Ashhab, J. R. Johansson, and F. Nori. Quantum two-level systems in josephson junctions as naturally formed qubits. *Phys. Rev. Lett.*, 97:077001, 2006.

[37] J. Lisenfeld, C. Müller, J. H. Cole, P. Bushev, A. Lukashenko, A. Shnirman, and A. V. Ustinov. Rabi spectroscopy of a qubit-fluctuator system. *Phys. Rev. B*, 81:100511(R), 2010.

[38] C. Müller, A. Shnirman, and Y. Makhlin. Relaxation of josephson qubits due to strong coupling to two-level systems. *Phys. Rev. B*, 80:134517, 2009.

[39] J. H. Cole, C. Müller, P. Bushev, G. J. Grabovskij, J. Lisenfeld, A. Lukashenko, A. V. Ustinov, and A. Shnirman. Quantitative evaluation of defect-models in superconducting phase qubits. *Applied Physics Letters*, 97:252501, 2010.

[40] L. Faoro and L. B. Ioffe. Microscopic origin of critical current fluctuations in large, small, and ultra-small area josephson junctions. *Phys. Rev. B*, 75: 132505, 2007.

[41] L. Ku and C. C. Yu. Decoherence of a josephson qubit due to coupling to two-level systems. *Phys. Rev. B*, 72:024526, 2005.

[42] L. Faoro, J. Bergli, B. L. Altshuler, and Y. M. Galperin. Models of environment and T_1 relaxation in Josephson Charge Qubits. *Phys. Rev. Lett.*, 95:046805, 2005.

[43] R. de Sousa, K. B. Whaley, Th. Hecht, J. von Delft, and F. K. Wilhelm. Microscopic model of critical current noise in josephson-junction qubits: Subgap resonances and andreev bound states. *Phys. Rev. B*, 80:094515, 2009.

[44] I. Martin, L. Bulaevskii, and A. Shnirman. Tunneling spectroscopy of two-level systems inside a josephson junction. *Phys. Rev. Lett.*, 95:127002, 2005.

[45] J. M. Martinis, K. B. Cooper, R. McDermott, M. Steffen, M. Ansmann, K. D. Osborn, K. Cicak, S. Oh, D. P. Pappas, R. W. Simmonds, and C. C. Yu. Decoherence in josephson qubits from dielectric loss. *Phys. Rev. Lett.*, 95: 210503, 2005.

[46] S. Sendelbach, D. Hover, A. Kittel, M. Mück, J. M. Martinis, and R. McDermott. Magnetism in squids at millikelvin temperatures. *Phys. Rev. Lett.*, 100: 227006, 2008.

[47] H. Bluhm, J. A. Bert, N. C. Koshnick, M. E. Huber, and K. A. Moler. Spin-like susceptibility of metallic and insulating thin films at low temperature. *Phys. Rev. Lett.*, 103:026805, 2009.

[48] A. G. Kofman, Q. Zhang, J. M. Martinis, and A. N. Korotkov. Theoretical analysis of measurement crosstalk for coupled josephson phase qubits. *Phys. Rev. B*, 75:014524, 2007.

[49] F. Bloch. Nuclear induction. *Phys. Rev.*, 70:460, 1946.

[50] J. Schriefl. *Dekohärenz in Josephson Quantenbits*. PhD thesis, Institut für Theoretische Festkörperphysik, Universität Karlsruhe, 2005.

[51] F. Bloch. Generalized theory of relaxation. *Phys. Rev.*, 105:1206–1222, 1957.

[52] A. G. Redfield. On the theory of relaxation processes. *IBM Journal of Research and Development*, 1:19–31, 1957.

[53] C. W. Gardiner and P. Zoller. *Quantum noise.* Springer, Berlin Heidelberg New York, Jan 2004.

[54] G. Lindblad. On the generators of quantum dynamical semigroups. *Communications in Mathematical Physics*, 48:119–130, 1976.

[55] R. S. Whitney. Staying positive: going beyong lindblad with perturbative master equations. *J. Phys. A: Mathematical and Theoretical*, 41:175304, 2008.

[56] T. Dittrich, P. Hänggi, G.-L. Ingold, B. Kramer, G. Schön, and W. Zwerger. *Quantum transport and dissipation.* Wiley-VCH, 1998.

[57] J. H. Shirley. Solution of the schrödinger equation with a hamiltonian periodic in time. *Phys. Rev.*, 138:B979, 1965.

[58] P. Zanardi and M. Rasetti. Holonomic quantum computation. *Physics Letters A*, 264:94 – 99, 1999.

[59] G. de Chiara and G. M. Palma. Berry phase for a spin 1/2 particle in a classical fluctuation field. *Phys. Rev. Lett.*, 91:090404, 2003.

[60] R. G. Unanyan, B. W. Shore, and K. Bergmann. Laser-driven population transfer in four-level atoms: Consequences of non-abelian geometrical adiabatic phase factors. *Phys. Rev. A*, 59:2910–2919, 1999.

[61] L. M. Duan, J. I. Cirac, and P. Zoller. Geometric manipulation of trapped ions for quantum computation. *Science*, 292:1695–1697, 2001.

[62] A. Shnirman, Y. Makhlin, and G. Schön. Noise and decoherence in quantum two-level systems. *Physica Scripta*, T102:147, 2002.

[63] G. Ithier, E. Collin, P. Joyez, P. J. Meeson, D. Vion, D. Esteve, F. Chiarello, A. Shnirman, Y. Makhlin, J. Schriefl, and G. Schön. Decoherence in a superconducting quantum bit circuit. *Phys. Rev. B*, 72:134519, 2005.

[64] T. A. Palomaki, S. K. Dutta, R. M. Lewis, A. J. Przybysz, H. Paik, B. K. Cooper, H. Kwon, J. R. Anderson, C. J. Lobb, F. C. Wellstood, and E. Tiesinga. Multilevel spectroscopy of two-level systems coupled to a dc squid phase qubit. *Phys. Rev. B*, 81:144503, 2010.

[65] J. Schriefl, Y. Makhlin, A. Shnirman, and G. Schön. Decoherence from ensembles of two-level fluctuators. *New J. Phys.*, 8:1, 2006.

[66] C. M. Wilson, T. Duty, F. Persson, M. Sandberg, G. Johansson, and P. Delsing. Coherence times of dressed states of a superconducting qubit under extreme driving. *Phys. Rev. Lett.*, 98:257003, 2007.

[67] J. Hausinger and M. Grifoni. Dissipative two-level system under strong ac driving: A combination of floquet and van vleck perturbation theory. *Phys. Rev. A.*, 81:022117, 2010.

[68] C. M. Wilson, G. Johansson, T. Duty, F. Persson, M. Sandberg, and P. Delsing. Dressed relaxation and dephasing in a strongly driven two-level system. *Phys. Rev. B*, 81:024520, 2010.

[69] A. D. Bain and R. S. Dumont. Introduction to floquet theory: The calculation of spinning sideband intensities in magnetic-angle spinning NMR. *Concepts in Magnetic Resonance*, 13:159–170, 2001.

[70] M. Hofheinz. private communication, 2009.

[71] Jürgen Lisenfeld. private communication, 2009.

[72] S. J. Devitt, J. H. Cole, and L. C. L. Hollenberg. Scheme for direct measurment of a general two-qubit hamiltonian. *Phys. Rev. A*, 73:052317, 2006.

[73] M. Constantin and C. C. Yu. Microscopic model of critical current noise in josephson junctions. *Phys. Rev. Lett.*, 99:207001, 2007.

[74] Y. M. Galperin, D. V. Shantsev, J. Bergli, and B. L. Altshuler. Rabi oscillations of a qubit coupled to a two-level system. *Europhysics Letters*, 71:21, 2005.

[75] S. Ashhab, J. R. Johansson, and F. Nori. Rabi oscillations in a qubit coupled to a two-level systemi. *New J. Phys.*, 8:103, 2006.

[76] L. Tian and K. Jacobs. Quantum manipulation of low-frequency fluctuators by superconducting resonantor. *Phys. Rev. B*, 79:144503, 2009.

[77] A. J. Leggett, S. Chakravarty, A. T. Dorsey, Matthew P. A. Fisher, Anupam Garg, and W. Zwerger. Dynamics of the dissipative two-state system. *Rev. Mod. Phys.*, 59:1–85, 1987.

[78] Y. Nakamura. private communication, 2009.

[79] Y. M. Galperin, B. L. Altshuler, J. Bergli, and D. V. Shantsev. Non-gaussian low-frequency noise as a source of qubit decoherence. *Phys. Rev. Lett.*, 96: 097009, 2006. doi: doi:10.1103/PhysRevLett.96.097009.

[80] E. Paladino, L. Faoro, G. Falci, and R. Fazio. Decoherence and 1/f noise in josephson qubits. *Phys. Rev. Lett.*, 88:228304, 2002.

[81] R. de Sousa, K. B. Whaley, F. K. Wilhelm, and J. von Delft. Ohmic and step noise from a single trapping center hybridized with a fermi sea. *Phys. Rev. Lett.*, 95:247006, 2005.

[82] A. Grishin, I. V. Yurkevich, and I. V. Lerner. Low-temperature decoherence of qubit coupled to background charges. *Phys. Rev. B*, 72:060509(R), 2005.

[83] U. Weiss. *Quantum Dissipative Systems*. World Scientific, Singapore, Jan 2008.

[84] Yuriy Makhlin, Gerd Schön, and Alexander Shnirman. Dissipation in josephson qubits. In Rosario Fazio, V. F. Gantmakher, and Y. Imry, editors, *New Directions in Mesoscopic Physics (Towards Nanoscience)*, pages 197–224, Dordrecht, 2003. Kluwer.

[85] Y. Makhlin and A. Shnirman. Dephasing of solid-state qubits at optimal points. *Phys. Rev. Lett.*, 92:178301, 2004.

[86] S. Ashhab, J. R. Johansson, and F. Nori. Decoherence dynamics of a qubit coupled to a quantum two-level system. *Physica C*, 444:45, 2006.

[87] M. Hofheinz, H. Wang, M. Ansmann, R. C. Bialczak, E. Lucero, M. Neeley, A. D. O'Connell, D. Sank, J. Wenner, J. M. Martinis, and A. N. Cleland. Synthesizing arbitrary quantum states in a superconducting resonator. *Nature*, 459:546–549, 2009.

[88] V. Weisskopf and E. Wigner. Berechnung der natürlichen linienbreite auf grund der diracschen lichttheorie. *Z. Phys.*, 63:54, 1930.

[89] D. Mischek. Coherent defects in superconducting qubits. Master's thesis, Institut für Theorie der Kondensierten Materie, Karlsruhe Institute of technology, 2011.

[90] J. Lisenfeld, A. Lukashenko, M. Ansmann, J. M. Martinis, and A. V. Ustinov. Temperature dependence of coherent oscillations in josephson phase qubits. *Phys. Rev. Lett.*, 99:170504, 2007.

[91] K. Härkönen, F. Plastina, and S. Maniscalco. Dicke model and environment-induced entanglement in ion-cavity qed. *Phys. Rev. A*, 80:033841, 2009.

[92] R. G. DeVoe and R.G. Brewer. Observation of superradiant spontaneous emission of two trapped ions. *Phys. Rev. Lett.*, 76:2049, 1996.

[93] A. A. Houck, J. A. Schreier, B. R. Johnson, J. M. Chow, J. Koch, J. M. Gambetta, D. I. Schuster, L. Frunzio, M. H. Devoret, S. M. Girvin, and R. J. Schoelkopf. Controlling the spontaneous emission of a superconducting transmon qubit. *Phys. Rev. Lett.*, 101:080502, 2008.

[94] P. J. Leek, J. M. Fink, A. Blais, R. Bianchetti, M. Göppl, J. M. Gambetta, D. I. Schuster, L. Frunzio, R. J. Schoelkopf, and A. Wallraff. Observation of berry's phase in a solid state qubit. *Science*, 318:1889–1892, 2007.

[95] M. Möttönen, J.J. Vartiainen, and J. Pekkola. Experimental determination of the berry phase in a superconducting charge punp. *Phys. Rev. Lett.*, 100: 177201, 2008.

[96] M.-S. Choi. Geometric quantum computation on solid-state qubits. *Journal of Physics: Condensed Matter*, 15:7823, 2003.

[97] L. Faoro, J. Siewert, and R. Fazio. Non-abelian holonomies, charge pumping and quantum computation with josephson junctions. *Phys. Rev. Lett.*, 90: 028301, 2003.

[98] V. Brosco, R. Fazio, F. W. J. Hekking, and A. Joye. Non-abelian superconducting pumps. *Phys. Rev. Lett.*, 100:027002, 2008.

[99] J.-M. Pirkkalainen, P. Solinas, J. P. Pekkola, and M. Möttönen. Non-abelian geometric phases in ground-state josephson devices. *Phys. Rev. B*, 81:174506, 2010.

[100] P. Solinas, J.-M. Pirkkalainen, and M. Möttönen. Ground-state geometric quantum computing in superconducting systems. *Phys. Rev. A*, 82(5):052304, 2010.

[101] A. Blais, R.-S. Huang, A. Wallraff, S. M. Girvin, and R. J. Schoelkopf. Cavity quantum electrodynamics for superconducting electrical circuits: an architecture for quantum computation. *Phys. Rev. A*, 69:062320, 2004.

[102] M. Neeley, R. C. Bialczak, M. Lenander, E. Lucero, M. Mariantoni, A. O'Connell, D. Sank, H. Wang, M. Weides, J. Wenner, Y. Yin, T. Yamamoto, A. N. Cleland, and J. M. Martinis. Generation of three-qubit entangled states using superconducting phase qubits. *Nature*, 467:570–573, 2010.

[103] L. DiCarlo, M. D. Reed, L. Sun, B. R. Johnson, J. M. Chow, J. M. Gambetta, L. Frunzio, S. M. Girvin, M. H. Devoret, and R. J. Schoelkopf. Preparation and measurement of three-qubit entaglement in a superconducting circuit. *Nature*, 467:574–578, 2010.

[104] A. A. Houck, Jens Koch, M. H. Devoret, S. M. Girvin, and R. J. Schoelkopf. Life after charge noise: recent results with transmon qubits. *Quantum Information Processing*, 8:105–115, 2009.

[105] Y. Makhlin, G. Schön, and A. Shnirman. Josephon-junction qubits with controlled couplings. *Nature*, 398:305–307, 1998.

[106] G. Florio, P. Facchi, R. Fazio, G. Vittorio, and P. Saverio. Robust gates for holonomic quantum computation. *Phys. Rev. A*, 73:022237, 2006.

Acknowledgements

I want to thank the many people whose help contributed to the successful completion of this work.

First of all, many thanks go to my advisor Sasha Shnirman for accepting me as his student and always patiently answering my many questions. I also want to thank Alexey Ustinov, who agreed to referee this work and who provided us with the opportunity to work closely with his group and profiting from the view of our experimental colleagues. Additionally I want to mention Prof. Gerd Schön with whom we had many fruitful discussions and exchanges.

Many thanks also to all colleagues in the institutes of TKM, TFP and PI for helping to turn all this work into a lot of fun. This is especially, but not limited to, Jared, Michael, Burkhard, Ingo, Susanne, Jin, and Jürgen.

Special mention goes to my mother for always being there. Also to my father, who supported me a lot during these last years. And to Matilda, who showed me that life does not have to be so complicated.

And to the many friends, family and colleagues I did not mention by name. You are not written here, but present in my heart and thoughts.

A. Circuit Model of Charge TLS

Introduction

In this part we will present some additional calculation concerned with the circuit model of superconducting devices presented in Sec. 1.1. We start by deriving the Hamiltonian for a standard three junction flux qubit. In particular we will show a circuit representation of a charge TLS inside a Josephson junction and apply this to both phase and flux qubit circuits. We will give the physical motivation for this model and discuss its implications.

A.1. Three-Junction Flux Qubit
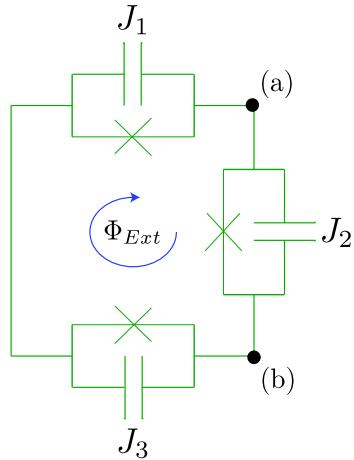
Figure A.1.: *Circuit diagram of three-Josephson junction flux qubit. The self-inductance of the loop is neglected. Junction J_2 is smaller than the junctions $J_{1/3}$ by a factor α. The potential is controlled by the external flux Φ_{Ext}. The current balance at the points (a) and (b) is evaluated to arrive the equations of motion.*

We start by deriving the Hamiltonian of a standard three-junction flux qubit [6]. It is build out of a superconducting ring interrupted by three Josephson junctions. The difference to the previously discussed case of the phase qubit (Sec. 1.1) is mainly the size of the ring and the junctions, which are smaller for a flux qubit as compared to the phase qubit. The circuit diagram of a such a superconducting flux qubit is show

in Fig. A.1. For simplicity we neglect the inductance of the loop [6]. The junctions J_1 and J_3 are assumed to be equal with critical current I_C and capacitance C. Junction J_2 is smaller by a factor α, decreasing both critical current and capacitance by the same factor. The qubit is controlled by applying an external flux Φ_{Ext} through the loop. For simplicity of presentation, we will only use dimensionless phase variables denoted by lowercase ϕ. The external flux through the loop will generate a phase of $\phi_{Ext} = \frac{2\pi}{\Phi_0}\Phi_{Ext}$ with the flux quantum $\Phi_0 = \frac{2e}{h}$.

The canonical variables describing the dynamics of the circuit depicted in Fig. A.1 are the phase differences across the three junctions ϕ_n and the corresponding charges $q_n = \frac{\partial \mathcal{L}}{\partial \dot\phi_n}$. The ring geometry enables us to express one pair of variables by the other two. We chose to use $\phi_2 = \phi_1 + \phi_3 - \phi_{Ext}$, and additionally adopt the common notation $\phi_\pm = 1/2\,(\phi_1 \pm \phi_3)$. For the Hamiltonian of the flux qubit we then get

$$
\hat{H} = \frac{1}{C}\left(q_+^2 + q_-^2\right) - \frac{\alpha}{2C(1+2\alpha)}\left(2q_+ - q_{Ext}\right)^2
$$
$$
- E_J\left(2\cos\frac{\phi_+}{2}\cos\frac{\phi_-}{2} + \alpha\cos\left(\phi_+ - \phi_{Ext}\right)\right), \tag{A.1}
$$

where $q_\pm = \frac{\partial \mathcal{L}}{\partial \dot\phi_\pm}$ and $q_{Ext} = C\dot\phi_{Ext}$. Here the first two terms describe the kinetic energy of a particle moving in the two dimensional potential

$$
U(\phi_+, \phi_-) = E_J\left(2\cos\frac{\phi_+}{2}\cos\frac{\phi_-}{2} + \alpha\cos\left(\phi_+ - \phi_{Ext}\right)\right). \tag{A.2}
$$

For $\alpha < 1$ and near the degeneracy point $\Phi_{Ext} = 1/2\Phi_0$ this is the well known double well potential with the barrier height depending on α.

A.2. TLS Circuit Model

We now include the coupling to charge fluctuators in our discussion. In many types of superconducting qubits, including phase [29], flux [31] and charge [32] qubits, avoided crossings can be found in spectroscopy. These are attributed to additional quantum systems being resonantly coupled to the qubit circuit. In general they are considered detrimental to the operation of the qubit [38], but their exact microscopic nature remains unclear [39].

One possibility is for them to be formed as charged dipoles sitting inside the oxide layer of the qubits Josephson junction. In this case we have developed a toy model which allows us to derive the form of their interaction with the qubit circuit in an a priori fashion. The parameters of the model will have to be adjusted according to experiment.

The idea is to model the TLSs as two superconducting islands, separated by another Josephson junction and capacitively coupled to the two sides of the circuits Josephson junction (cf. Fig. A.2). Each of the two islands will be charged and hold
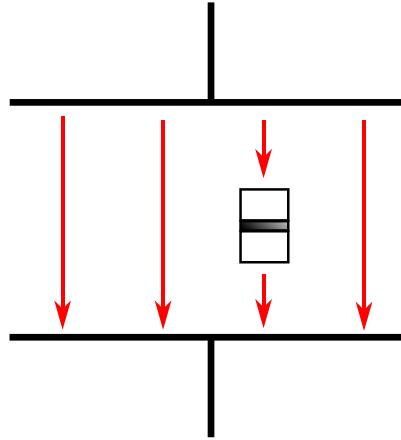
Figure A.2.: *Illustration of the toy model for a charged dipole sitting inside the Josephson junction of a superconducting circuit. Two superconducting islands separated by a Josephson junction are coupled capacitively to the electric field.*

some charge q_i. Then the total charge $q_N = q_1 + q_2$ on the islands is conserved and quantized and can therefore be chosen at will. The charge imbalance, $q_n = q_1 - q_2$ between the two islands will give the strength of the dipole element while the Josephson energy of the junction $E_{J,f}$ will determine the switching dynamics. Lastly, the coupling to the circuit is determined by the coupling capacitors C_C.

A.2.1. Phase Qubit and Charge TLS
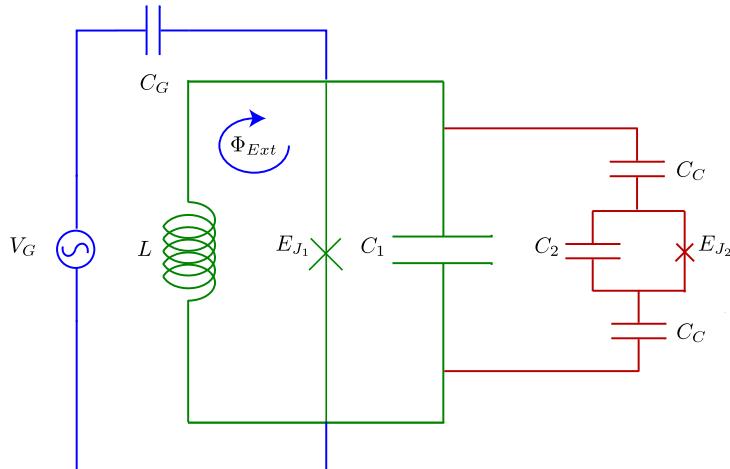
Figure A.3.: *Circuit diagram of a phase qubit including the toy model representation of a charge defect sitting inside the Josephson junction. Two superconducting islands separated by a JJ are coupled to the two sides of the external junctions with coupling capacitors C_C.*

As a simple example we first show the case of a charge fluctuator sitting inside the Josephson junction of a superconducting phase qubit. The circuit diagram, including the representation of the charge defect, is shown in Fig. A.3.

The variables describing the charge defect we denote as ϕ_N and ϕ_n, where ϕ_N is the sum of the phase differences across the two islands, while ϕ_n is the difference. The conjugated momenta q_N and q_n then correspond to the sum and difference in charge on the two islands, as described above.

The Hamiltonian looks as

$$\hat{H} = \frac{1}{C_q}\left(n_G + \tilde{q}\right)^2 + \frac{1}{C_n}q_n^2 + \frac{1}{C_I}\left(n_G + \tilde{q}\right)q_n$$
$$- E_{J_1}\cos\phi - E_{J_2}\cos\tilde{\phi}_n + \frac{1}{2L}\left(\frac{\Phi_0}{2\pi}\right)^2\left(\phi - \phi_{Ext}\right)^2\,, \qquad (A.3)$$

where constant terms have been neglected. The capacitances above are defined by

$$C_q = \frac{2C_\Sigma^2}{2C_2 + C_C} \approx C_1 + C_G\,,$$
$$C_n = \frac{2C_\Sigma^2}{2C_1 + 2C_G + C_C} \approx 2C_2 + C_C\,,$$
$$C_I = \frac{C_\Sigma^2}{C_C}\,,$$

with $C_\Sigma^2 = \left(C_1 + C_G\right)\left(2C_2 + C_C\right) + C_2 C_C$.

For simplicity of presentation we again performed a canonical transformation from the original variables defined in the text to the new variables

$$\tilde{q} = q + q_n \qquad \tilde{\phi}_n = \phi - \phi_n\,.$$

The coupling between qubit and TLS is given by the second part of the third term $\propto \tilde{q}\,q_n$, so the coupling is of the form dipole moment of the TLS times electric field across the junction.

To other part of this term is of particular interest and serves to illustrate the limitations of this model. The coupling term $\propto n_G\,q_n$ describes a direct coupling between the dipole moment of theTLS and the externally applied voltage. We can, however, transform the above Hamiltonian into new variables, namely $\tilde{q} \to q' = \tilde{q} + n_G$ and canonical conjugate, where no such direct coupling is observed. The remaining structure of Eq. (A.3) remains the same. The nature of the coupling to the TLS seems to depend solely on the choice of canonical variables we use to describe the circuit. As of yet, it is unclear which description corresponds to the physical picture.
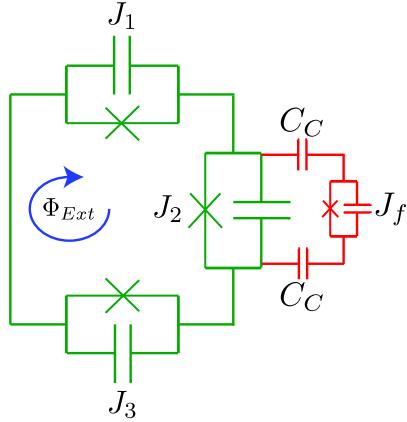
Figure A.4.: *3-junction flux qubit with the circuit representation of a charge fluctuator residing in the α-junction. Two superconducting islands separated by a Josephson junction J_F are coupled capacitively with coupling capacitance C_C to the electric field in the α-junction J_2.*

A.2.2. Three-Junction Flux Qubit - TLS in α-Junction

As the name implies, a three-junction flux qubit contains a total of three Josephson junction. two of them are equivalent, and the third one is smaller by the factor α. Inserting a charge TLS into the circuit, we therefore have two distinct possibilities leading to different Hamiltonians.

The case when the TLS is sitting inside the α-junction of a standard three-junction flux qubit is due to symmetry reasons easier to treat compared to the TLS sitting in one of the other two junctions. The circuit diagram for this case is shown in Fig. A.4 with the labels the same as described above.

We find the Hamiltonian as

$$\hat{H} = \frac{1}{C}\left(q_+^2 + q_-^2\right) - \frac{C_q}{2C_\Sigma^2}\left(2q_+ - q_{Ext}\right)^2 + \frac{C_n}{2C_\Sigma^2}q_n^2 - \frac{C_f}{C_\Sigma^2}\left(2q_+ - q_{Ext}\right)q_n$$
$$- E_J\left(2\cos\frac{\phi_+}{2}\cos\frac{\phi_-}{2} + \alpha\cos\left(\phi_+ - \phi_{Ext}\right)\right) - E_{J,f}\cos\left(\phi_{Ext} - \phi_n - \phi_+\right) \quad \text{(A.4)}$$

with the capacitances

$$C_q = \frac{C_C C_f}{C} + \alpha(C_C + C_f)$$
$$C_n = C(1 + 2\alpha) + 2C_f$$
$$C_\Sigma^2 = 2C_C C_f + C\left(C_C + C_f\right)\left(1 + 2\alpha\right)$$

and $q_{Ext} = C\dot{\phi}_{Ext}$. Constant parts, which do not contribute to the dynamics, have been neglected again.

We see additional kinetic energy terms as compared to the case without TLS,

Eq. (A.1). In the flux qubit, these terms should be small and their influence on the dynamics negligible. The coupling between qubit and TLS is given by the last term in the potential $\propto \cos{(\phi_{Ext} - \phi_n - \phi_+)} = \cos{(\phi_2 + \phi_n)}$, where $\phi_2 = \phi_+ - \phi_{Ext}$ is the phase difference across the α-junction. We can rearrange this further to get $\cos{(\phi_2 + \phi_n)} = \cos{\phi_2} \cos{\phi_n} + \sin{\phi_2} \sin{\phi_n}$. The potential can thus be written as

$$E_J \left(2 \cos{\frac{\phi_+}{2}} \cos{\frac{\phi_-}{2}} + \alpha' \cos{\phi_2} \right) + E_{J,f} \sin{\phi_2} \sin{\phi_n} \qquad (A.5)$$

with $\alpha' = \alpha + E_{J,f}/E_J \cos{\phi_n}$. Since the flux qubits level-splitting depends exponentially on the value of α, this expression implies a very strong coupling between qubit and TLS. Assuming a two state approximation for the TLS (e.g., if there is in total one charge on the two islands, which can either be on the upper or on the lower island), we can write $\cos{\phi_n} \equiv \sigma_x$ and $\sin{\phi_n} \equiv \sigma_y$. The effective α of the qubit can then be expressed as

$$\alpha' = \alpha + \frac{E_{J,f}}{E_J} \sigma_x , \qquad (A.6)$$

implying very strong influence of the TLS on the qubits dynamics.

We now rewrite Eq. (A.4) in new variables, to compare with the previous part on coupling to the phase qubit. With

$$\phi_n \rightarrow \tilde{\phi}_n = \phi_n + \phi_+ - \phi_{Ext} ,$$
$$q_+ \rightarrow \tilde{q}_+ = q_+ - q_n ,$$
$$q_{Ext} \rightarrow \tilde{q}_{Ext} = q_{Ext} + q_n ,$$

we can rewrite the Hamiltonian (A.4) to get:

$$
\begin{aligned}
\hat{H} = & \frac{1}{C} \left(\tilde{q}_+^2 + q_-^2 \right) + (1 + 2\alpha) \frac{C}{2 C_\Sigma^2} q_n^2 \\
& - \frac{2 C_q}{C_\Sigma^2} \left(\frac{1}{2} q_n + \tilde{q}_+ - \frac{1}{2} \tilde{q}_{Ext} \right)^2 - \frac{C_f}{C_\Sigma^2} (\tilde{q}_+ - \frac{1}{2} \tilde{q}_{Ext}) p_n \\
& - E_J \left(2 \cos{\frac{\phi_+}{2}} \cos{\frac{\phi_-}{2}} + \alpha \cos{(\phi_+ - \phi_{Ext})} \right) - E_{J,f} \cos{(\tilde{\phi}_n)} \qquad (A.7)
\end{aligned}
$$

where we now do not find a variation in the effective α. The coupling written in this set of variables is again a simple charge-type coupling and we would not expect a strong influence on the qubit dynamics.

A.2.3. Three-Junction Flux Qubit - TLS in Normal Junction

Placing the TLS inside one of the other two junctions (here we choose junction #1), we get

$$
\begin{aligned}
\hat{H} = {}& \frac{1}{C}\left(q_+^2 + q_-^2\right) - \alpha\frac{C_C + C_f}{2C_\Sigma^2}\left(2q_+ - q_{Ext}\right)^2 + \frac{C_n}{2C_\Sigma^2}q_n^2 \\
& + \frac{C_f}{C_\Sigma^2}\left((q_+ + q_-) + \alpha(2q_- + q_{Ext})\right)q_n \\
& - \frac{C_C C_f}{C}\left\{\alpha\left(q_+ - q_- - q_{Ext}\right)^2 + (1+\alpha)\left(q_+ + q_-\right)^2\right\} \\
& - E_J\left(2\cos\frac{\phi_+}{2}\cos\frac{\phi_-}{2} + \alpha\cos\left(\phi_+ - \phi_{Ext}\right)\right) - E_{J,f}\cos\left(\frac{1}{2}\left(\phi_+ + \phi_-\right) - \phi_n\right)
\end{aligned}
$$

$$(A.8)$$

with the capacitances

$$
\begin{aligned}
C_n &= (1 + 2\alpha)C + (1 + \alpha)C_f \\
C_\Sigma^2 &= C_C C_f\left(1 + \alpha\right) + C\left(C_C + C_f\right)\left(1 + 2\alpha\right)
\end{aligned}
$$

Here the coupling between TLS and qubit is mainly given by the term in the potential $\propto \cos\left(1/2(\phi_+ + \phi_-) - \phi_n\right) = \cos\left(\phi_1 - \phi_n\right)$, as could be expected. By the appropriate choice of variables, this can again be transformed into a pure charge-type coupling as has been shown in the previous part.

A.3. Extended Circuit Model

Here we give some discussion on how to include additional degrees of freedom into our circuit model of a charge TLS. We discuss the effect of dipole rotations, i.e. when the dipole axis and the electric field enclose an angle θ and also the effect of a change in TLS position, i.e. when it is located not directly in the middle of the junction. Last, we discuss the predictions of the model if two TLS are simultaneously in the same junction.

A.3.1. Effects of Dipole Rotations

We can extend our simple picture of the TLS do accommodate a possible angle θ between the dipole axis and the electric field in the capacitor. The microscopic picture for this case is show in Fig. A.5.

We still assume the electric field to be homogeneous, and in this case both islands representing the dipole couple capacitively to both sides of the junction. The circuit Fig. A.3 would then be modified by additional coupling capacitors. The new circuit diagram is shown in Fig. A.6.
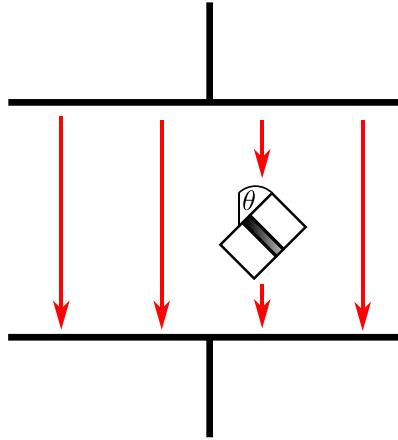
Figure A.5.: *Illustration of the effective model for the charged dipolar TLS. The dipole is represented by two superconducting islands separated by a Josephson junction. The charge on the islands couples to the electric field of the qubit. The dipole axis encloses the angle θ with the electric field lines.*
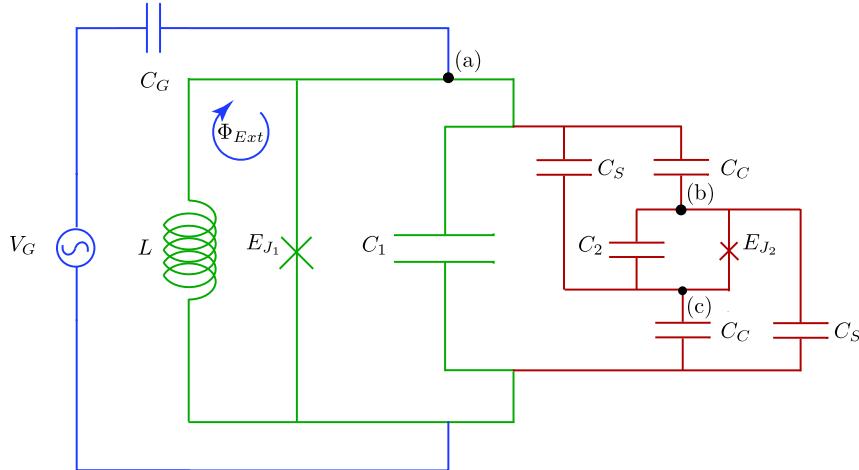
Figure A.6.: *Effective circuit describing the charge TLS model now with a possible angle θ between dipole axis and electric field. The Josephson junction defining the TLS (in red) has capacitance C_2 and Josephson energy E_{J_2}. The two islands are coupled to the outside with the capacitors C_C and C_S. The ratio C_C/C_S defines the angle θ. At the three points (a) - (c) the current balance is evaluated to arrive at the Lagrangian.*

The dynamics of the circuit in Fig. A.6 are described using 10 circuit elements and therefore 10 pairs of variables. Using loop constraints in the circuit we can reduce this number to 3 independent pairs. For these we use the phase across the qubits capacitor ϕ_1 and its time derivative $\dot{\phi}_1$ and the phase across each of the two coupling capacitors $C_{C_{1/2}}$, $\phi_{C_{1/2}}$ together with their time derivatives $\dot{\phi}_{C_{1/2}}$.

For the same choice of variables as in Eq. (A.3), we get the Hamiltonian

$$
\hat{H} = \frac{1}{C_q}(n_G + \tilde{q}_1)^2 + \frac{1}{C_n}q_n^2 + \frac{1}{C_I}(n_G + \tilde{q}_1)q_n
$$
$$
- E_{J_1} \cos\left(\frac{2\pi}{\Phi_0}\phi_1\right) - E_{J_2} \cos\left(\frac{2\pi}{\Phi_0}\tilde{\phi}_n\right) + \frac{1}{2L}\left(\phi_1 - \phi_{Ext}\right)^2 , \qquad (A.9)
$$

where we neglected constant terms and defined the capacitances

$$
C_q = \frac{2C_\Sigma^2}{2C_2 + C_C + C_S} \approx C_1 ,
$$
$$
C_n = \frac{2C_\Sigma^2}{2C_1 + 2C_G + C_C + C_S} \approx C_2 ,
$$
$$
C_I = \frac{C_\Sigma^2}{C_C - C_S} ,
$$
$$
C_\Sigma^2 = C_1(2C_2 + C_C + C_S) + C_2(2C_G + C_C + C_S) + C_G(C_C + C_S) + 2C_C C_S
$$

The angle θ is related to the TLS coupling capacitors as $\sin\theta \propto C_S/C_C$. As is expected from the physical picture, the coupling of the TLS to the outside world $\propto 1/C_I$ will go to zero for $\theta \to \pi/2$, i.e. when the dipole is oriented perpendicular to the electric field.

A.3.2. Spatial Dependence of the Coupling - Unequal TLS Coupling Capacitors

Since the two coupling capacitors C_C in Fig. A.3 are equal, the model for the fluctuator introduced above translates into microscopic picture as the TLS being located exactly in the middle of the junctions insulating oxide.

We can replace the two coupling capacitors C_C in Fig. A.3 with unequal capacitors C_{C_1} and C_{C_2} and repeat derivation to arrive at

$$
\hat{H} = \frac{1}{C_q}(n_G + \tilde{q}_1)^2 + \frac{1}{C_n}q_n^2 + \frac{1}{C_I}(n_G + \tilde{q}_1)p_n
$$
$$
- E_{J_1} \cos\left(\frac{2\pi}{\Phi_0}\phi_1\right) - E_{J_2} \cos\left(\frac{2\pi}{\Phi_0}\tilde{\phi}_n\right) + \frac{1}{2L}\left(\phi_1 - \phi_{Ext}\right)^2 , \qquad (A.10)
$$

with the capacitances

$$C_q = \frac{2C_\Sigma^3}{C_2(C_{C_1} + C_{C_2}) + C_{C_1}C_{C_2}} \approx C_1 + C_G$$

$$C_n = \frac{2C_\Sigma^3}{(C_1 + C_2 + C_G)(C_{C_1} + C_{C_2}) + C_{C_1}C_{C_2}} \approx C_2$$

$$C_I = \frac{2C_\Sigma^3}{2C_{C_1}C_{C_2}}$$

$$C_\Sigma^3 = (C_{C_1} + C_{C_2})(C_1C_2 + C_2C_G) + C_{C_1}C_{C_2}(C_1 + C_2 + C_G)$$

In order to see the spatial dependence of the coupling between qubit and TLS, we assume a simple plane-parallel capacitor model for the two coupling capacitances C_{C_1} and C_{C_2}. The areas of the capacitors will be given by the spatial extent A of the TLS and the maximum height is given by the thickness h of the insulating oxide. The capacitance are the given by $C_{C_1} = \epsilon_0 A/d$ and $C_{C_2} = \epsilon_0 A/(h - d)$. For the capacitance defining the coupling between qubit and TLS in the Hamiltonian (A.10) we then get

$$C_I = (C_1 + C_2 + C_G) + \frac{h}{\epsilon_0 A}C_2 (C_1 + C_G) \tag{A.11}$$

which is independent of the position of the TLS. This result is in agreement with the expectations regarding our simple model since we assume a constant electric field across the whole Josephson junction.

A.3.3. Two TLS inside One Junction

To determine if the model predicts a natural coupling between several TLS in the same qubit circuit, we repeat the derivation for two charge defects. One of them is characterized by capacitance C_2 and Josephson energy E_{J_2}, the other by C_3 and E_{J_3}. The capacitance C_1 and energy E_{J_1} again describe the qubit. The TLS are coupled by the capacitances C_{C_2} and C_{C_3} to the outside circuit, analogous to the situation in Fig. A.3.

We find the Hamiltonian as

$$\begin{aligned}
\hat{H} = {} & \frac{1}{C_q} (n_G + \tilde{q}_1)^2 + \frac{1}{C_{f_1}}q_{n_1}^2 + \frac{1}{C_{f_2}}q_{n_2}^2 \\
& + \frac{1}{C_{I_1}} (n_G + \tilde{q}_1) q_{n_1} + \frac{1}{C_{I_2}} (n_G + \tilde{q}_1) q_{n_2} + \frac{1}{C_{I_{12}}}q_{n_1}q_{n_2} \\
& - E_{J_1} \cos\left(\frac{2\pi}{\Phi_0}\phi_1\right) - E_{J_2} \cos\left(\frac{2\pi}{\Phi_0}\tilde{\phi}_{n_1}\right) - E_{J_3} \cos\left(\frac{2\pi}{\Phi_0}\tilde{\phi}_{n_2}\right) + \frac{1}{2L} (\phi_1 - \phi_{Ext})^2
\end{aligned}$$

$$\tag{A.12}$$

with the capacitances defined by

$$C_q = \frac{2C_\Sigma^3}{4C_2C_3 + 2C_2C_{C_3} + 2C_3C_{C_2} + C_{C_2}C_{C_3}} \approx C_1 + C_G \,,$$

$$C_{f_i} = \frac{2C_\Sigma^3}{C_{C_2}C_{C_3} + 2C_j\left(C_{C_2} + C_{C_3}\right) + 2C_1\left(2C_j + C_{C_j}\right)} \approx C_i \,,$$

$$C_{I_i} = \frac{C_\Sigma^3}{C_{C_i}\left(2C_j + C_{C_j}\right)} \,,$$

$$C_{I_{12}} = \frac{C_\Sigma^3}{C_{C_2}C_{C_3}} \,,$$

$$C_\Sigma^3 = (C_1 + C_G)\left(2C_2 + C_{C2}\right)\left(2C_3 + C_{C_3}\right) + 2C_2C_3\left(C_{C_2} + C_{C_3}\right) + C_{C_2}C_{C_3}\left(C_2 + C_3\right) \,,$$

where $i, j = 2, 3$ for TLS 1 and vice versa for TLS 2. The model provides a mutual coupling between the two TLS $\propto 1/C_{I_{12}}$.

Conclusions

This chapter illustrates a simple and intuitive model for a charge TLS inside a Josephson junction. This model in the circuit description provides for a natural coupling of TLS and circuit dynamics. However, the choice of canonical coordinates to describe the system seems to strongly influence the form of the coupling. Since a coordinate transform cannot change the physics of the model, it is unclear what is the origin of this change. Until this can be understood, the model should not be taken too serious.

B. Additional Information on Evaluation of Defect Models

Here we give some additional information on the fitting and the calculations performed to obtain the results of Sec. 2.3. We start by giving the exact form of the fitting results and defining the steps taken to obtain the microscopic parameters. We then give the details of the calculation for the four different coupling models considered in Sec. 2.1.2. We assume linear error regression for all parameters througout this calculations.

B.1. Results of the Fitting

The fitting was performed for an interaction Hamiltonian of the form

$$H_I = \hat{o} \left(\tilde{v}_\perp \tau_x + \tilde{v}_\parallel \tau_z \right) , \tag{B.1}$$

where the qubit operator $\hat{o}$ is given by the actual operator of the interaction and the $\tilde{v}$ are free parameters. In terms of the Eq. (2.31) the fitting parameters $\tilde{v}$ can be identified as

$$\tilde{v}_\perp = v_o \cos \theta_o \qquad \tilde{v}_\parallel = v_o \sin \theta_o . \tag{B.2}$$

The spectroscopy experiment is only sensitive to purely transversal $\propto \sigma_x \tau_x$ and purely longitudinal $\propto \sigma_z \tau_z$ coupling. Mixed terms (e.g. $\propto \sigma_z \tau_x$ or $\propto \sigma_x \tau_z$) are not visible in the spectrum. If we were to ignore the higher lying qubit states, in the two state basis for the qubit we can write the relevant coupling Hamiltonian as

$$H_I = v_\perp \sigma_x \tau_x + v_\parallel \sigma_z \tau_z . \tag{B.3}$$

We then use the fitted values of $\tilde{v}$ to obtain the transversal and longitudinal coupling strengths

$$v_\perp = \langle \hat{o} \rangle_\perp \tilde{v}_\perp , \qquad v_\parallel = \langle \hat{o} \rangle_\parallel \tilde{v}_\parallel , \tag{B.4}$$

where the factors $\langle \hat{o} \rangle$ are given by

$$2 \langle \hat{o} \rangle_\perp = \langle 1 | \hat{o} | 0 \rangle + \langle 0 | \hat{o} | 1 \rangle ,$$
$$2 \langle \hat{o} \rangle_\parallel = \langle 1 | \hat{o} | 1 \rangle - \langle 0 | \hat{o} | 0 \rangle . \tag{B.5}$$

Tab. B.1 gives the fitting results for two TLSs that were found on the same chip

TLS1	ϵ_{TLS}	$v_\perp$	$v_\parallel$	χ_r^2
$H_I^{(p)}$	7944.49 ± 0.08	35.65 ± 0.08	$----$	0.998
$H_I^{(\phi)}$	7944.41 ± 0.08	35.55 ± 0.09	0.23 ± 0.12	0.997
$H_I^{(c)}$	7944.38 ± 0.08	35.52 ± 0.13	0.27 ± 0.12	0.997
TLS2	ϵ_{TLS}	$v_\perp$	$v_\parallel$	χ_r^2
$H_I^{(p)}$	7734.0 ± 0.2	23.2 ± 0.2	$----$	0.994
$H_I^{(\phi)}$	7734.5 ± 0.2	23.3 ± 0.2	0.5 ± 0.2	0.992
$H_I^{(c)}$	7734.4 ± 0.3	23.3 ± 0.2	0.5 ± 0.2	0.992

Table B.1.: *Estimates for the TLS resonance frequency and qubit-TLS coupling which were obtained from the fitting procedure, including 1-σ uncertainties. The parameters for two different TLSs on the same chip are shown and all values are in MHz. The reduced χ^2 value is also given for each fit, showing good convergence with minimal over-fitting.*

during one cooldown. Since the dataset for the second is smaller, the resulting uncertainties are bigger.

Because the momentum operator $\hat{q}$ has no diagonal components, $\langle \hat{q} \rangle_\parallel = 0$, no purely longitudinal coupling term exists in this case and we have no information on $\tilde{v}_\parallel$.

B.2. Coupling to Charge n_G

Analogous to the treatment in Ref. [45] (cf. Sec. 2.1.2) we calculate the fractional size d of the aligned dipole moment in the direction of the electric field as

$$d/x = v_\perp \sqrt{\frac{2C}{e^2 \epsilon_{01}}} , \qquad \text{(B.6)}$$

where x ist the thickness of the junction, C its capacitance and e the electron charge. The qubit level splitting ϵ_{01} is taken in resonance with the TLS ($\epsilon_{01} = \epsilon_{\text{TLS}}$) and $v_\perp$ is the transversal coupling strength from the fitting.

For the two TLSs under consideration we obtain

$$d_1/x = 0.0837 \pm 0.0002 ,$$
$$d_2/x = 0.0551 \pm 0.0004 ,$$

where the subscript $1, 2$ denotes TLS 1 / TLS 2 respectively.

For a junction thickness x of $\propto$ nm, this results in an aligned dipole-size of the order of atomic distances.

B.3. Coupling to External Flux Φ_{Ext}

We express the coupling operator in the Hamiltonian in the qubits 2-state representation as

$$\frac{\partial H}{\partial \phi_{Ext}} \delta\phi_{Ext} = \delta\phi_{Ext} \left(\eta_x \sigma_x + \eta_z \sigma_z \right) , \tag{B.7}$$

which we calculate using the full numeric qubit potential. For the numerical values of the parameters we obtain

$$\eta_{z,1} = 3.57 \pm 0.04 \ \ \text{GHz} \ \hbar/2\text{e} ,$$
$$\eta_{x,1} = 24.36 \pm 0.05 \ \ \text{GHz} \ \hbar/2\text{e} ,$$
$$\eta_{z,2} = 3.89 \pm 0.04 \ \ \text{GHz} \ \hbar/2\text{e} ,$$
$$\eta_{x,2} = 24.69 \pm 0.04 \ \ \text{GHz} \ \hbar/2\text{e} .$$

Comparing this with the results from the fitting to the operator $H_I^\phi = v_\phi \hat{\phi} \left(\cos\theta_\phi \tau_x + \sin\theta_\phi \tau_z \right)$ we can identify

$$v_\perp = \delta\phi_{Ext} \eta_x \cos\theta_\phi ,$$
$$v_\parallel = \delta\phi_{Ext} \eta_z \sin\theta_\phi ,$$

with the definitions of $v_\perp$ and $v_\parallel$ given above. We solve this set of equations to get estimates for the change in magnetic flux $\delta\phi_{Ext}$ and the TLS orientation angle θ_ϕ:

$$\delta\phi_{Ext,1} = 232.5 \pm 1.2\mu\Phi_0 ,$$
$$\delta\phi_{Ext,2} = 151.5 \pm 2.5\mu\Phi_0 ,$$

and

$$\tan\theta_{\phi,1} = 0.04 \pm 0.02 ,$$
$$\tan\theta_{\phi,2} = 0.14 \pm 0.06$$

To estimate the magnetic moment needed to generate this change in external flux, we assume the moment to be located on the surface of the current carrying wire. The magnetic field on the surface of a wire of radius R is given by

$$B = \frac{\mu_0}{2\pi} \frac{I}{R} , \tag{B.8}$$

with the direction parallel to the wire surface. The energy of a magnetic moment μ in a magnetic field is

$$U = -\vec{\mu} \cdot \vec{B} , \tag{B.9}$$

so the energy difference for the two possible orientations (parallel and anti-parallel) is given by

$$\delta E = 2\mu B . \tag{B.10}$$

A switching magnetic moment μ will induce a change in magnetic flux $\delta\Phi$ through a nearby ring. In order to calculate this change, we make use of Newton's third law, that a change $\delta\Phi$ in the magnetic flux through the loop induces an electromotive force due to Lenz' rule, which in turn gives an energy change of

$$\delta E = I\delta\Phi\,. \tag{B.11}$$

We compare the two energies and find the magnitude of the magnetic moment needed for a change in magnetic flux $\delta\Phi$ as

$$\mu = \frac{\pi R}{\mu_0}\delta\Phi\,, \tag{B.12}$$

which for our fits and a wire radius of $\propto 1\mu m$ gives us

$$\begin{aligned}
\mu_1 &= 129700 \pm 700\,\mu_B\,, \\
\mu_2 &= 84500 \pm 1400\,\mu_B\,,
\end{aligned}$$

in units of the electron magnetic moment μ_B.

B.4. Coupling to Critical Current I_C

As in the case of the coupling to the external flux, we express the coupling operator in the Hamiltonian in the qubits 2-state representation as

$$\frac{\partial H}{\partial I_c}\delta I_c = \delta I_c\left(\lambda_x\sigma_x + \lambda_z\sigma_z\right)\,. \tag{B.13}$$

For the numerical values of the parameters we get

$$\begin{aligned}
\lambda_{z,1} &= 8.91 \pm 0.07\ \text{GHz}/\mu\text{A} \\
\lambda_{x,1} &= 51.32 \pm 0.16\ \text{GHz}/\mu\text{A} \\
\lambda_{z,2} &= 9.45 \pm 0.07\ \text{GHz}/\mu\text{A} \\
\lambda_{x,2} &= 52.45 \pm 0.13\ \text{GHz}/\mu\text{A}
\end{aligned}$$

Again comparing this with the results from the fitting to the operator $H_I^c = v_c\cos\hat{\phi}\left(\cos\theta_c\tau_x + \sin\theta_c\tau_z\right)$ we can identify

$$\begin{aligned}
v_\perp &= \delta I_c\lambda_x\cos\theta_c\,, \\
v_\parallel &= \delta I_c\lambda_z\sin\theta_c\,,
\end{aligned}$$

and obtain estimates for the change in critical current δI_c:

$$\delta I_{c,1} = 693 \pm 5 \times 10^{-12} \mathrm{A}\,,$$
$$\delta I_{c,2} = 447 \pm 7 \times 10^{-12} \mathrm{A}\,,$$

where the critical current is obtained via our fitting procedure,

$$I_{c,1} = 984 \pm 2 \times 10^{-9} \mathrm{A}\,,$$
$$I_{c,2} = 976 \pm 1 \times 10^{-9} \mathrm{A}\,.$$

The angle θ_c can be found as

$$\tan \theta_{c,1} = 0.04 \pm 0.02\,,$$
$$\tan \theta_{c,2} = 0.12 \pm 0.05$$

Using these estimates for the angle θ we can place further constraints on the microscopic model. We can write the Hamiltonian in its physical basis, in which the coupling to the qubit is diagonal, (e.g., the position basis for a bistable atomic defect) as

$$H_{\mathrm{TLS}} = \frac{1}{2}\epsilon_0 \tilde{\tau}_z + \frac{1}{2}\Delta_0 \tilde{\tau}_x\,, \tag{B.14}$$

where ϵ_0 gives the splitting in the physical basis and Δ_0 the tunneling element between the two states. The coupling operator in the eigenbasis is then given by $\tilde{\tau}_z \to \cos\theta\, \tau_x + \sin\theta\, \tau_z$ with $\tan\theta = \epsilon_0/\Delta_0$, while the level splitting of the TLS is calculated as $\epsilon_{\mathrm{TLS}} = \sqrt{\epsilon_0^2 + \Delta_0^2}$. Therefore, an angle of $\theta = \pi/2$ would correspond to exact degeneracy of the TLS-states in the original basis. Using the above estimates yields

$$\epsilon_{0,1} = 0.34 \pm 0.16 \, \mathrm{GHz}\,,$$
$$\Delta_{0,1} = 7.937 \pm 0.007 \, \mathrm{GHz}\,,$$
$$\epsilon_{0,2} = 0.97 \pm 0.38 \, \mathrm{GHz}\,,$$
$$\Delta_{0,2} = 7.89 \pm 0.05 \, \mathrm{GHz}\,.$$

B.5. Andreev Level Fluctuator

Ref. [43] gives a general model for coupling between a qubit and an Andreev level fluctuator (ALF), formed when an impurity level in the Josephson junction is hybridised with the superconducting leads. The Hamiltonian for this model is given as

$$
\begin{aligned}
H = {}& \frac{1}{2}\epsilon_q \sigma_z + E_b \tau_z \\
& + (v_z \sigma_z + v_x \sigma_x)\left(2\sqrt{a_+ a_-}\,\tau_x + (a_+ - a_-)\tau_z\right)
\end{aligned}
\tag{B.15}
$$

(Eq. (35) in Ref. [43]), where we slightly adapted their notation to our convention. The operators σ and τ are the pauli-matrices for qubit and TLS, respectively. Comparing Eq. (B.15) with Eq. (B.15) we can identify

$$2\sqrt{a_+ a_-} = \cos\theta$$
$$(a_+ - a_-) = \sin\theta \tag{B.16}$$

The amplitudes $a_\pm$ are given by

$$a_\pm = \frac{(\Delta_{\mathrm{BCS}}^2 - E_b^2)\left[(\epsilon_d \pm E_b)^2 + \gamma^2\right]}{2\left[(2\Delta_{\mathrm{BCS}}^2 - E_b^2)(\epsilon_d^2 + \gamma^2) - E_b^4\right]}, \tag{B.17}$$

while the Andreev level splitting E_b is the solution to

$$E_b^2\left(1 + \frac{2\gamma}{\sqrt{\Delta_{\mathrm{BCS}}^2 - E_b^2}}\right) - \epsilon_d^2 - \gamma^2 = 0. \tag{B.18}$$

Here Δ_{BCS} is the superconducting gap ($\Delta_{\mathrm{BCS}} \approx 300\mu\mathrm{eV}$ for thin Al-films), ϵ_d is the impuritiy level energy and γ is the hybridisation parameter characterizing the interaction with the leads. The ALF splitting E_b is related to the TLS energy splitting ϵ_f in our model by $2E_b = \epsilon_f$. Inserting Eq. (B.18) into Eq. (B.17) we can express the amplitudes $a_\pm$ as function of only one unknown variable, the impurity level energy ϵ_d. The relations Eq. (B.16) therefore connect the angle θ in this model to the impurity level energy ϵ_d.

In the model of Ref. [43] the coupling between qubit and ALF is via a modulation of the critical current I_c. The coupling paramteters $v_{x/z}$ in Eq. (B.15) are then given by $v_{x/z} = \delta I_c \lambda_{x/z}$, with $\lambda_{x/z}$ defined by Eq. (B.13).

Comparing now Eq. (B.15) with our fitted results we find the system of coupled equations

$$v_\perp = 2\lambda_x \delta I_c \sqrt{a_+ a_-}\,,$$
$$v_\parallel = \lambda_z \delta I_c (a_+ - a_-)\,, \tag{B.19}$$

which we can solve for the two unknowns critical current variation δI_c and the impurity level energy ϵ_d. Solving these equations will give us a multitude of possible solutions, from which we will only show the largest values. Fig. B.1 shows the full spectrum of solutions.

For the values of $v_\perp$ and $v_\parallel$ we obtain in the fitting we get a change in critical current of

$$\delta I_{c,1} \leq 1.46 \pm 0.01 \times 10^{-9}\mathrm{A}$$
$$\delta I_{c,2} \leq 0.94 \pm 0.01 \times 10^{-9}\mathrm{A}$$

and an impurity level energy of

$$\epsilon_{d,1} \leq 101.6 \pm 46.5 \text{ MHz}$$
$$\epsilon_{d,2} \leq 278.4 \pm 109.6 \text{ MHz}$$
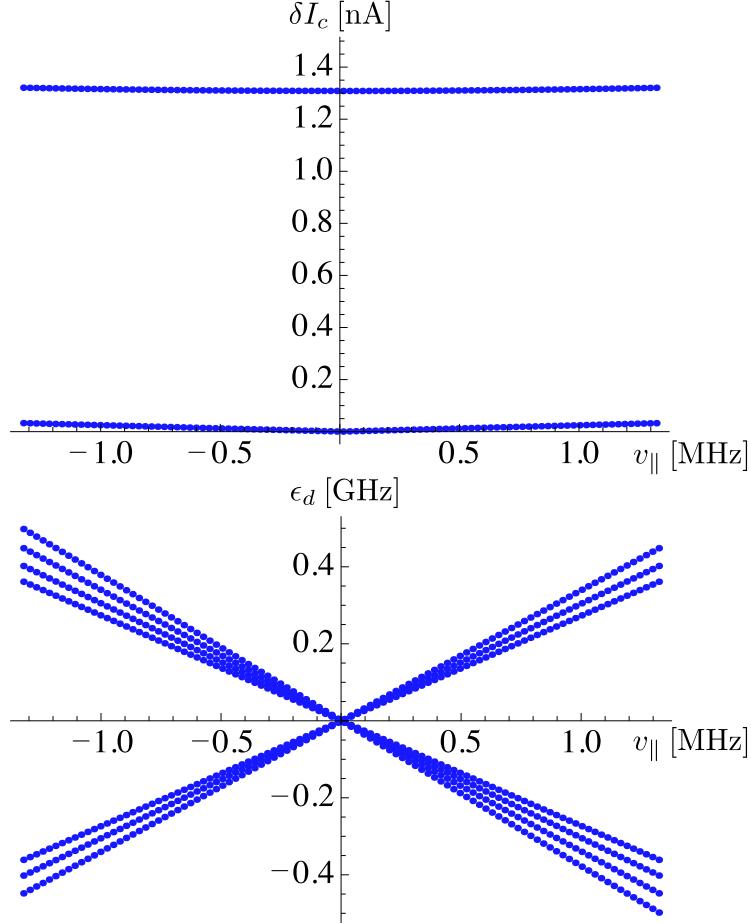
Figure B.1.: *Change in critical current δI_c (upper plot) and impurity level energy ϵ_d (lower plot) as a function of longitudinal coupling $\tilde{v}_\parallel$ and for constant transversal coupling strength $\tilde{v}_\perp$. Numbers are taken from the fitted values for TLS 1. The range in longitudinal coupling is ± 5 times the fitted result.*

To illustrate the dependence of these two variables on the longitudinal coupling $v_\parallel$, we plot their values as a function of $v_\parallel$ in a range of $[-5, 5]$ times the fitted value. The result is shown in Fig. B.1.

C. List of Publications

- I. Kamleitner, P. Solinas, C. Müller, A. Shnirman and M. Möttönen, *Geometric quantum gates with superconducting qubits,* arXiv.quant-phys:1104.0159 (2011), accepted in Phys. Rev. B

- G. J. Grabovskij, P. Bushev, J. H. Cole, C. Müller, J. Lisenfeld, A. Lukashenko, and A. V. Ustinov, *Entangling microscopic defects via a macroscopic quantum shuttle,* New J. Phys. **13**, 063015 (2011)

- J. H. Cole, C. Müller, P. Bushev, G. J. Grabovskij, J. Lisenfeld, A. Lukashenko, A. V. Ustinov and A. Shnirman, *Quantitative evaluation of defect models in superconducting phase qubits,* Appl. Phys. Lett. **97**, 252501 (2010)

- J. Lisenfeld, C. Müller, J. H. Cole, A. Lukashenko, A. Shnirman and A. V. Ustinov, *Measuring the temperature dependence of individual two-level systems by direct coherent control,* Phys. Rev. Lett. **105**, 230504 (2010)

- P. Bushev, C. Müller, J. Lisenfeld, J. H. Cole, A. Lukashenko, A. Shnirman and A. V. Ustinov, *Multi-photon spectroscopy of a hybrid quantum system,* Phys. Rev. B **82**, 134530 (2010)

- J. Lisenfeld, C. Müller, J. H. Cole, P. Bushev, A. Lukashenko, A. Shnirman and A. V. Ustinov, *Rabi-spectroscopy of a strongly driven qubit-fluctuator system,* Phys. Rev. B **81**, 100511(R) (2010)

- C. Müller, A. Shnirman and Y. Makhlin, *Relaxation of Josephson qubits due to strong coupling to two-level systems,* Phys. Rev. B **80**, 134517 (2009)